University of Bath

PHD

Biomimetic templating in materials chemistry

Patel, Harish M.

Award date:
1998

Awarding institution:
University of Bath

Link to publication

Alternative formats
If you require this document in an alternative format, please contact:
openaccess@bath.ac.uk

Copyright of this thesis rests with the author. Access is subject to the above licence, if given. If no licence is specified above, original content in this thesis is licensed under the terms of the Creative Commons Attribution-NonCommercial 4.0 International (CC BY-NC-ND 4.0) Licence (https://creativecommons.org/licenses/by-nc-nd/4.0/). Any third-party copyright material present remains the property of its respective owner(s) and is licensed under its existing terms.

Take down policy
If you consider content within Bath's Research Portal to be in breach of UK law, please contact: openaccess@bath.ac.uk with the details. Your claim will be investigated and, where appropriate, the item will be removed from public view as soon as possible.

Download date: 05. May. 2023

BIOMIMETIC TEMPLATING IN MATERIALS CHEMISTRY

submitted by **HARISH M. PATEL**

for the degree of Doctor of Philosophy

of the University of Bath

1998

COPYRIGHT

Attention is drawn to the fact that copyright of this thesis rests with its author. This copy of the thesis has been supplied on condition that anyone who consults it is understood to recognise that its copyright rests with its author and that no quotation from the thesis and no information derived from it may be published without prior written consent of the author.

This thesis may be made available for consultation within the University Library and may be photocopied or lent to other libraries for the purposes of consultation.

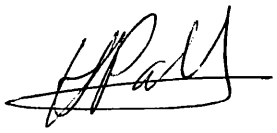

UMI Number: U601404

All rights reserved

INFORMATION TO ALL USERS
The quality of this reproduction is dependent upon the quality of the copy submitted.

In the unlikely event that the author did not send a complete manuscript
and there are missing pages, these will be noted. Also, if material had to be removed,
a note will indicate the deletion.

UMI U601404
Published by ProQuest LLC 2013. Copyright in the Dissertation held by the Author.
Microform Edition © ProQuest LLC.
All rights reserved. This work is protected against
unauthorized copying under Title 17, United States Code.

ProQuest LLC
789 East Eisenhower Parkway
P.O. Box 1346
Ann Arbor, MI 48106-1346

UNIVERSITY OF BATH
LIBRARY
21 10 JUN 1998
PHD
S122063

"Where nature finishes producing its own species, man begins using natural things and with the help of this nature, to create an infinity of species"

Leonardo da Vinci

FOREWORD

Among the numerous challenges awaiting to be taken up by synthetic chemists, the construction of molecular objects presenting unusual structures, in terms of shape or topology, may still be considered to be an art, as is the preparation of elaborate large molecular assemblies composed of molecular units, which is another largely unexplored area of research.

In terms of structure, topology, and function, an elegant and efficient way of constructing simple to extremely elaborate molecules involves a templating strategy. This is based upon the pre-assembly and organisation of several molecular fragments around a templating core using a number of construction principles. Covalent connection of the individual components affords a molecular entity, the high degree of complexity of which would have discouraged any non-template classical approach. An example of this is the template directed synthesis of mesoporous silica sieves. Using such a strategy, the size of the molecular objects lies typically within the nanoscale range.

Another viable approach to the construction of highly complex molecular entities is based on non-covalent links, as opposed to the strategy using covalent links, mentioned above. The construction of large size molecules in the order of 10^{-6} - 10^{-4} cm in scale, with predicted and programmed structures can hardly be envisaged through stepwise classical synthesis using covalent linkages. However, the preparation of such higher-order materials may be attained through iterative assembling of individual modules, which still remains a challenge to chemists. A strict control of the self-assembly of molecular modules in the solid state should lead to structurally strictly controlled assemblies.

The ultimate goal of the approaches mentioned is to convert molecular functions, built in within the framework of the individual modules, into macroscopic properties expressed at the level of the molecular assemblies and thus leading to the production of addressable devices.

ACKNOWLEDGEMENTS

Firstly, I would like to thank Professor Stephen Mann for giving me the opportunity to work within this field which I have found most enjoyable, and for his continued interest and guidance.

I would also like to express my upmost gratitude to all the people I have worked with in the research group in the last three years: Dr Kim Wong for his help, guidance and support; Dr Dominic Walsh for his helpful discussions; Dr Sandi Burkett for her expertise on mesoporous silica materials; Dr Sean Davis for his great knowledge of bionites and not forgetting our "working" holiday to Mexico for the 4th ICAM conference on materials chemistry; Steve Sims, Wayne Shenton, Eric Mayes and more recently Christabel Fowler and Simon Hall for making the working environment a happy place to be.

I thank also the external scientists with whom I have worked with during my stay in Bath: Dr Andreas Hirsch for the fullerene malonic acid sample; Dr Neil Mendelson for the bacterial thread; Dr Christine Göltner for SAXRD; Dr David Apperley for solid state NMR measurements and Micheal Breulmann for TGA analysis.

I am indebted to the support staff especially Ursula Potter for endless hours on the microtome, and Hugh Perrot of the electron microscopy unit; Alan Carver for XRD and CHN analysis; Syliva Hodges, Ahmed and Robert from the chemistry department.

I must also thank ESPRC for financial assistance and allowing me to attend the 4th ICAM conference in Cancún, Mexico.

Finally, I would like to thank Claire Beddows for her continued support, patience and time throughout the entirety of this project. Cheers Claire Bear !!!!

CONTENTS

APPENDICIES

CHAPTER ONE

BIOMIMETIC TEMPLATING IN MATERIALS CHEMISTRY

1.1 Introduction

Biological organisms are known to produce a variety of inorganic-organic composite materials known as biominerals.[1] Common examples include bones, shells, and teeth. These biominerals are of interest because they exhibit a high degree of structural complexity and are often constructed under ambient conditions. Studies have shown that these biominerals are based upon the ordering of molecular interactions, occurring between supramolecular assemblies and inorganic counterparts, which lead to the fabrication of a variety of forms and functional shapes. Biominerals are more often than not a mixture of molecules or microstructures in which the organic molecules and the formed inorganic phase coexist with one another. This manipulation of form takes into account supramolecular processes such as assembly, templating, and organisation.[1]

In the past, the major area of research has focused on the design of biominerals by mechanical means because numerous "bioceramics" such as bone and shell, exhibit unusual strength and toughness for materials which contain a high percentage proportion of an inorganic phase.[2] An example of this is the mother-of-pearl or nacre layer of seashells.[1] This layer comprises of thin laminate calcium carbonate crystals, in the aragonite polymorph, sandwiched between nanometre-thick sheets of biomolecules. Having the arrangement, the structure will prevent any cracks propagating through the shell wall, by dissipating the energy associated with crack formation, within the organic layers of the shell.

More recently, the research emphasis has shifted somewhat, with chemists and material researchers becoming more and more interested in the role of the organic matrix, and what its function or purpose is in the construction of the highly organised biominerals. The lessons learnt from this area of research, together with the study of biomineralisation, are of real importance to the technological sector, since valuable information and insight into the nature of materials chemistry at the inorganic-organic interface can be gained.[3-7] From this, the knowledge and the ability for man to fabricate organised materials, on the nanoscale, microscopic, macroscopic or bulk scale will be of great importance within the material world for producing sensory devices, catalysis and electronics. A pioneer in this field is Professor Stephen Mann, who summarised the relationship that exists between biomineralisation and materials chemistry, as shown in Figure 1.1.[2]

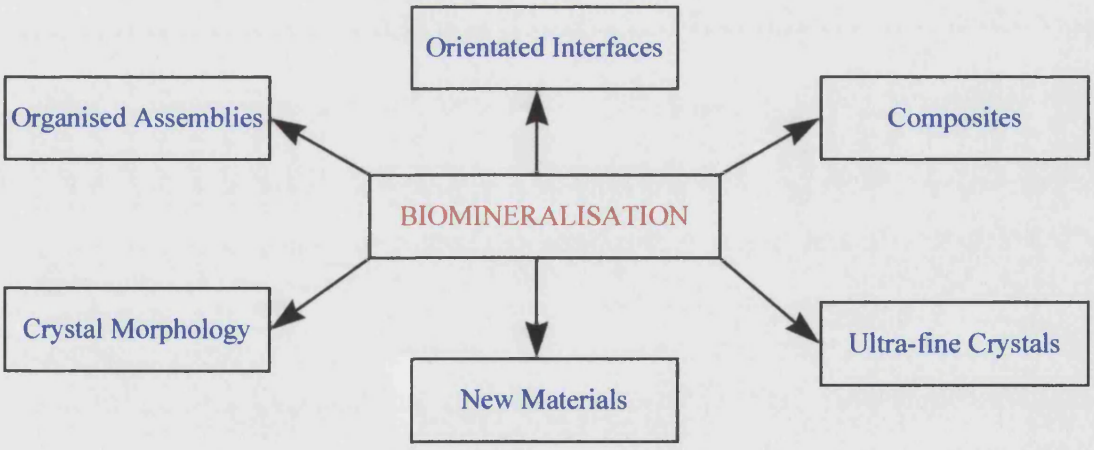

Figure 1.1 *The relationships between biomineralisation and materials chemistry.*[2]

Mann stated[1] "*A pivotal feature of biomineralisation is the use of organic supramolecular assemblies to control the synthesis and construction of inorganic-based materials and composites. This is a very surprising, yet logical, fusion of inorganic and organic materials chemistry. It is well accepted that biological systems are replete with examples of organic supramolecular assemblies (double and triple helices, multisubunit proteins, membrane-bound reaction centres, vesicles, tubules, etc.), some of which (collagen, cellulose and chitin) extend to microscopic dimensions in the form of hierarchical structures. However, less well known is that organic architectures can be utilised to direct and control the structure, size, shape, orientation, texture and assembly of inorganic minerals. What captures the imagination is how relatively simple inorganic minerals such as $CaCO_3$, SiO_2, Fe_3O_4, and so on, can be constructed into such precise architectures compared with the limited shapes offered by purely chemical or geological processes. Moreover, the resulting materials are highly functional - not only as tough, durable and adaptive polymer-ceramic composites but as specialised sensing devices, for example, of ambient magnetic and gravitational fields*".

This introductory chapter begins with an section on how biomimetic design leads to new approaches in materials design (section 1.2) and will highlight several approaches including templating synthesis, synergistic synthesis,[10] and synthesis-with construction, with some examples. Then, the chapter will proceed by summarising an approach termed Integrative synthesis,[11] defined as a collection of two or more of the approaches mentioned above. Finally, the chapter will close with an overview of the work presented in this thesis.

1.2 Approaches to Biomimetic Materials Design

In nature, the elaborate and elegant structures produced have arisen from organic components, such as polysaccharides and proteins, self-assembling into enclosed lipid vesicles, protein cages and extended organic networks, which form the reaction centres or environments that are the basis for the construction of biominerals. Generally the organised organic surfaces in these reaction centres dictate the nucleation and hence the crystal growth of the inorganic phase. The resulting biominerals display organised textures, unusual crystal habits, and defined structures and compositions. One of the most striking features of biomineralisation is the preferential crystallographic alignment of biominerals relative to the organised organic matrix. Subsequent ordering of the individual organised inorganic-organic composites, results in the construction of hierarchical microstructures such as a diatom frustule (Figure 1.2) and the coccosphere of *Emiliania huxleyi* (Figure 1.3).

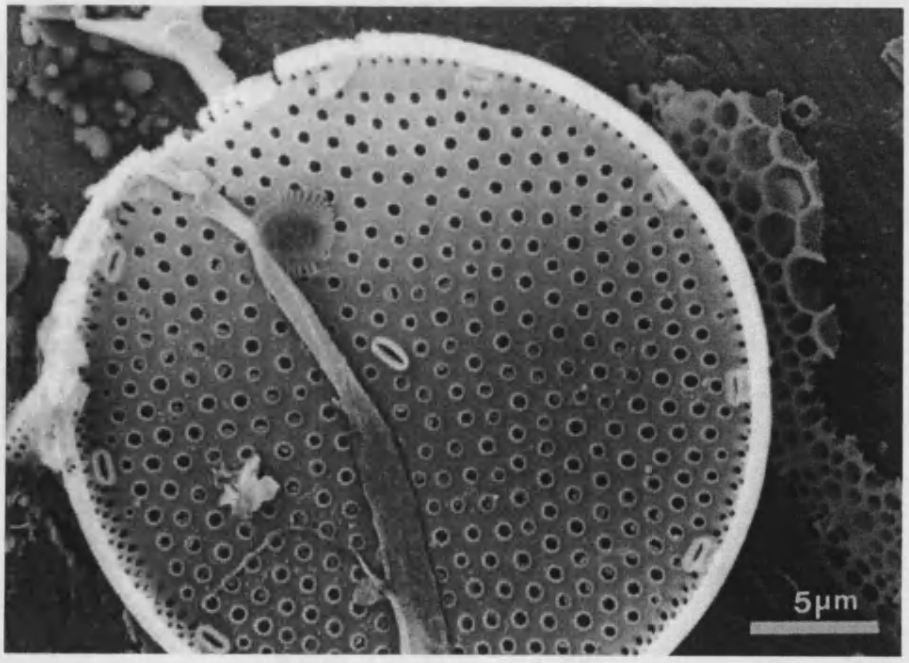

Figure 1.2 *SEM micrograph of the porous siliceous structure of a diatom frustule (courtesy of S.A. Davis, University of Bath).*

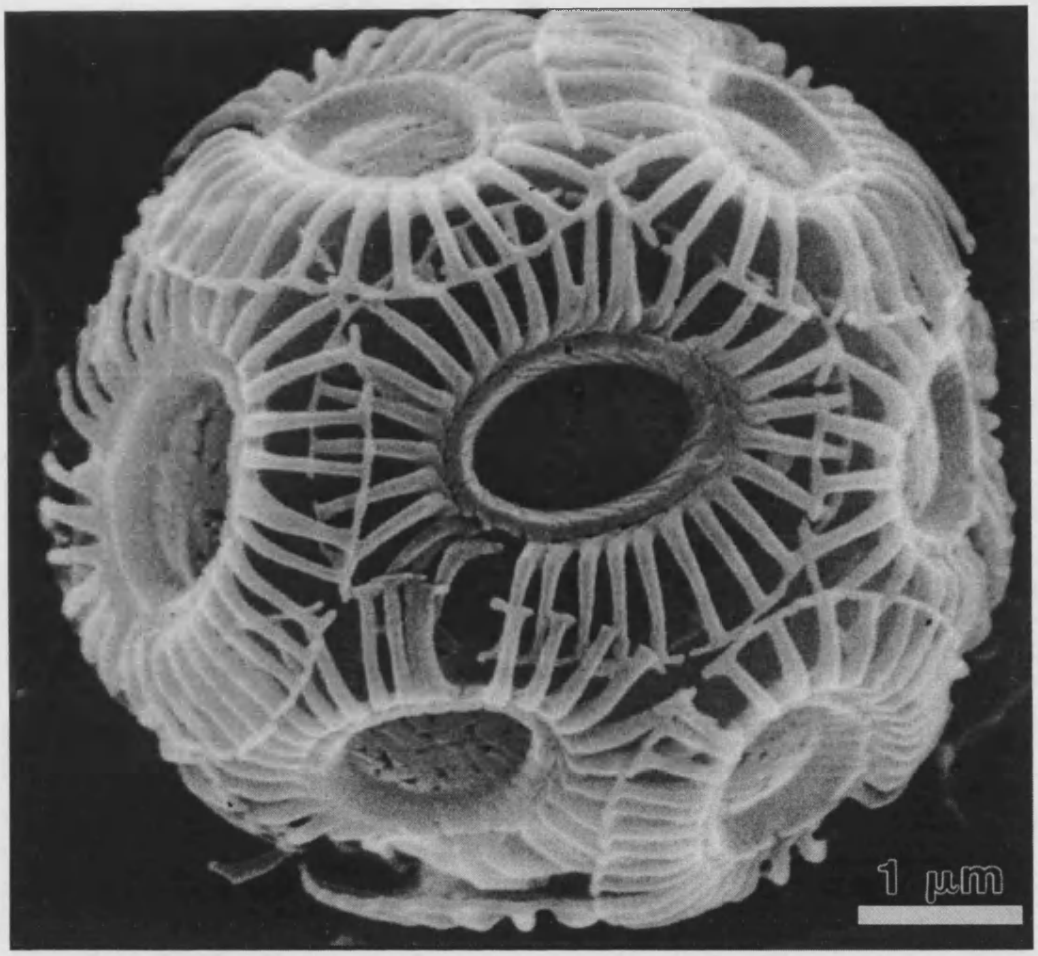

Figure 1.3 *SEM Micrograph of coccosphere, Emiliania huxleyi, showing the assembly of individual coccolith scales against the cell wall (courtesy of J. Young, Natural History Museum, London).*

The major goal for biomimetic materials chemists is to attempt to mimic nature's approaches to biomineral construction for the fabrication of materials which exhibit novel properties and complex form across a range of length scales.[8] Recent studies by Mann *et al.*[9] indicates that interactions at the inorganic-organic interface are paramount to understanding the physicochemical processes that result in the controlled nucleation and subsequent growth of inorganic crystals. The synthetic systems utilised in these studies have highlighted the importance of factors such as

electrostatic association or binding, geometric matching and stereochemical correspondence in the recognition processes. Adhering to these design principles, the development of novel strategies is currently underway for controlling the synthesis of inorganic phases, crystal engineering of bulk solids and the assembly of organised composite and ceramic materials.

The main body of work carried out recently has focused on the use of organic templating agents such as molecules, micelles, vesicles, for the fabrication of inorganic materials at the micro-,meso-, and macro-scale. The composite materials produced have arisen from specific molecular interactions occurring between organic and inorganic entities. Spatially controlled and organised inorganic structures are left once the template has been removed after mineralisation is complete.

1.2.1 Templating Synthesis

This process was highlighted by Mann and Ozin in 1996,[10] and showed that the formation of organised inorganic materials, in terms of pattern and form, closely corresponds to that of the self-assembled architecture, and can be described by the following sequence:

self-assembly → *transcription* → *replication*

Generally, the pre-organised organic template, which is in place prior to the formation of the inorganic phase, should be relatively stable throughout materials synthesis, with chemical and morphological information 'transcribed' into the surface structure. The interactions at the organic surface should ideally be competitive over analogous processes occurring in bulk solution, in order to obtain inorganic replicas with high fidelity. This is achieved by the incorporation of surface functional groups

that will direct interfacial events such as nucleation from supersaturated solutions and adsorption of preformed or incipient nanoclusters from colloidal sols. High specificity templates can be seen as chemically coded surfaces, which are transcribed into the nuclei of the inorganic phase at the molecular level with precise structural, orientational and positional properties. In association with outgrowth along and within the template, repetition of these molecular processes results in inorganic replication of the organic architecture. By this method the synthesis of inorganic-organic hybrids with meso-, micro-, and macro-scale patterns is possible.

Such templation strategies can fall into one of two categories, firstly, synthetic templates and secondly, biological templates.

Synthetic Templates

Synthetic templates are usually made up of surfactant organic molecules, which have been compressed to form Langmuir monolayers on aqueous subphases. Numerous studies have probed the use of Langmuir monolayers[12,13] and also functionalised self-assembling monolayers[14,15] as pre-organised templates in the oriented nucleation of two-dimensional arrays of inorganic crystals and thin films. These studies highlighted that for many cases, the electrostatic, stereochemical and geometric properties of the surfactant headgroup are transcribed within the primary layer of the inorganic crystal nuclei through molecular recognition between the pre-organised organic template and the inorganic crystal nuclei, resulting in the control of orientated inorganic nucleation.

An extension of this principle to produce a higher degree of complexity involves the use of pre-formed, self-assembled bilayer templates in the form of

vesicles. These lipid templates remain intact during and after inorganic mineralisation. These lipid structures can be utilised as three-dimensional templates for the controlled crystallisation of hollow silica tubes,[16] helical strings of gold crystals,[17] and iron oxide coated cylinders.[18] For example, sugar-based galactocerebroside lipids self-assemble into tubular microstructures in the presence of an anionic sulphated derivative, present in order to provide nucleation sites, resulting in the nucleation of non-magnetic/magnetic iron oxides 'decorating' the external surface of the lipid template. The presence of the functionalised headgroups on the lipid facilitate site-directed nucleation as well as patterned architectures for materials nucleation. In this example, electrostatic, structural and stereochemical complementarity at the inorganic-organic interface governs the assembly of the mineral nuclei.

Several studies have highlighted the use of pre-organised assemblies for direct synthetic control over the size of inorganic crystals; use of reverse micelles,[19,20] polymer matrices,[21] phospholipid vesicles,[22] and protein cages.[23] Having reaction environments with variable diameters ranging from 1 - 500 nm, and surface functional groups which can be tailored to specific needs *via* molecular engineering, makes these systems very versatile. For example, a range of sulphide and metal oxide nanocomposites have been synthesised using phospholipid vesicles (Figure 1.4).[22,24-27]

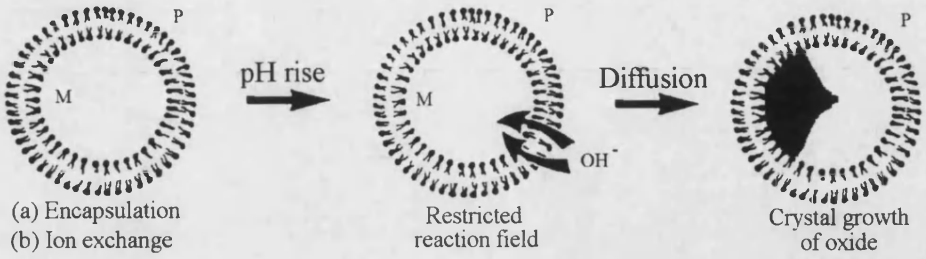

Figure 1.4 *Use of phospholipid vesicles in the membrane-mediated precipitation of metal oxides (redrawn from Mann, S.).* [2]

Unilamellar phosphatidylcholine vesicles, which have a diameter of ~30 nm, can be easily prepared by sonicating dispersions of the lipid in aqueous media at a temperature above the gel-liquid transition point. If these systems are prepared in the presence of metal ions, the internal cavity will encapsulate these ions which can subsequently undergo crystallisation reactions with membrane species such as OH^- and H_2S gas. Figure 1.4 also illustrates that the cations (M) are encapsulated by sonication and replaced in the external phase by inert cations (P) by ion exchange chromatography. Increases in the extravesicular pH results in a slow OH^- influx and therefore subsequent nucleation of the oxide on the inner surface of the membrane.

As each synthesised particle is housed within a 4.5 nm thick bilayer membrane, particle-particle interactions are insignificant and rates of reaction can be controlled by diffusion. The primary aim of this type of work focuses on the range of nanoparticles that can be synthesised in confined vesicular environments and the control mechanisms exerted by these chemically well-defined supramolecular assemblies.

However, these lipid-based assemblies often have limited stability with regards to hydrolysis and aggregation. An alternative approach has been to use the

protein ferritin. This biomolecular cage used for iron storage, is a more robust environment for the synthesis of inorganic materials (Figure 1.5).[28,29] *In-situ* chemical reaction of the native iron oxide cores readily produces nanoscale iron sulphides, whilst the reconstitution of the demetallated protein in aqueous salt solutions gives a range on non-native oxide materials, one of which is magnetite (Fe_3O_4) which endows the protein (magnetoferritin) with permanent magnetic properties.[29] An advantage of this method is that loading of the metal within the ferritin cavity can be more precisely controlled, as can the stoichiometry of the reaction mixtures, enabling nanophase cores of various particle sizes to be prepared. Additionally, the synthesis of mixed-metal oxide cores (*e.g.* FeOOH/MnOOH) can be achieved by sequential reconstitution of the protein cage with different solutions containing the metal salt.[23] In all of these examples the resulting materials are nanocomposites of mineral and protein which form stable sols of discrete particles. The biocompatibility of the polypeptide shell suggests that materials such as magnetoferritin will have potential applications as contrast agents in magnetic resonance imaging.[30] A detailed review of the use of ferritin in nanoscale synthesis is presented by Douglas.[31]

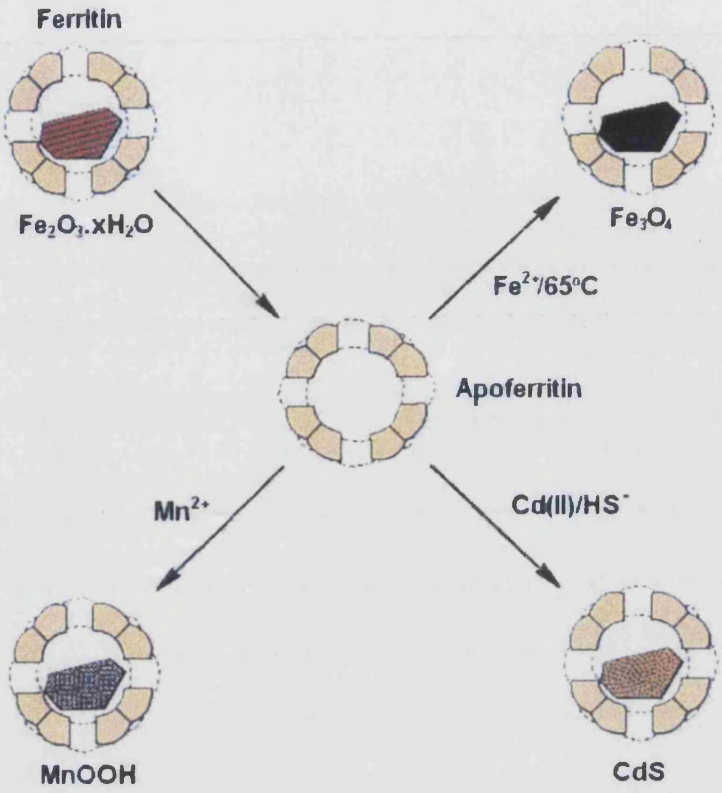

Figure 1.5 *Use of protein cages in biomimetic nanoscale synthesis of inorganic materials (redrawn from Sims, S.).*[32]

The materials formed from these approaches are reproducible and have been fabricated from relatively simple methods based on spatially discrete organic architectures such as single monolayer sheets, vesicle spheres, lipid tubes and surfactant rods. However, the templates required for the fabrication of more complex inorganic patterns need to have extended phases, such as, liquid crystals, polymerised bicontinuous microemulsions, and polysaccharide networks.[10]

Biological Templates

Generally, it is reasonable to assume that transcripitive methods will lead to a direct correspondence in size and shape between the template and inorganic replica. By this rationale, supramolecular assemblies are therefore of limited use for the chemical construction of micrometer-scale and macroscale structures. An increase in length scale requires templates with higher-order architectures, as well as larger building blocks. This is because the larger volume fraction of mineralised material is difficult to achieve from molecular precursors unless the system is under flow rather than batch conditions. A strategy to overcome this difficulty is to use inorganic nanoparticles as preformed building blocks for the infiltration and mineralisation of organised organic micro- and macroarchitectures.[11]

The work carried out by Davis *et al.*[33] utilises the strategy outlined above. In the study, the macroscale organic template is an organised bacterial superstructure consisting of coaligned multicellular filaments of mutant *Bacillus subtilis*. This bacterial superstructure is formed by the slow drawing of a macroscopic thread from a web culture,[34] and resembles the arrangement of surfactant cylinders in the H_1 liquid-crystal phase. The notable difference being that there is an increase in length scale of 2 orders of magnitude. The interfilament spaces within the bacterial superstructure are large enough (100-200 nm wide) to accommodate a large scale constructional unit, (i.e.) preformed silica nanoparticles. Infiltration of the silica nanoparticles within the bacterial supracellular template is a direct consequence of the increase in volume associated with swelling of the thread, when placed in aqueous solutions. When the thread dries, contraction and large increases in ionic strength occur within the interfilament regions. This has the effect of shielding the surface

charge on the silica nanospheres such that a continuous mineral framework is formed by particle-particle aggregation (Figure 1.6).

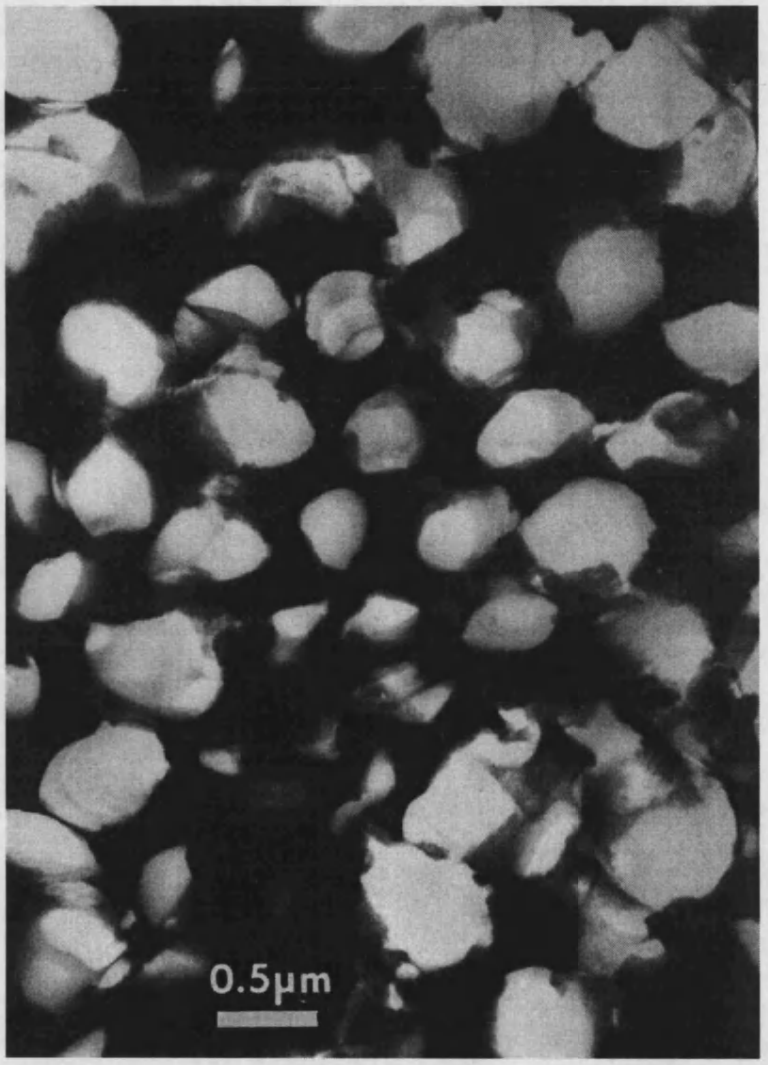

Figure 1.6 *High magnification TEM of mineralised thread showing the formation of the continuous silica walls (darkest regions) and encapsulated multicellular filaments (courtesy of S.A. Davis, University of Bath).*

1.2.2 Synergistic Synthesis

Synergistic synthesis implies the development of mineralised patterns based on the co-operative interactions between inorganic and organic constituents present in the reaction media.[10] A general feature of this process is the coadaptation of independent self-assembled systems with the formation of new organisational states replicated by materials deposition. The process is best described as a three-step sequence:

coadaptation → *coassembly* → *replication*

In the nano-region, inorganic building blocks can be assembled around single organic molecules, for example, silicate anions assembled around quaternary ammonium cations in the synthesis of zeolites.[35] The association and subsequent ordering of the two components is dependant upon the degree of chemical and structure complementarity at the inorganic-organic interface. The mechanism of zeolite formation has been proposed by Anderson *et al.*[36] to involve the assembly of silicate and aluminate building blocks on curved, periodic minimal-energy surfaces possessing zeolite-like topologies. Some surfaces have their origin in density fluctuations of transient local order delineated by the organic template in a synthesis mixture.

This concept can be extended to the mesoscale by utilising supramolecular aggregates of surfactant molecules,[37,38] for example, the synthesis of mesoporous and mesolamellar silica's at the cationic headgroups of quaternary ammonium surfactant molecules in weakly associated micellar and lamellar mesostructures, respectively.[39] The result of these co-operative interactions is a change in the spatial charge density

and steric requirements at the headgroup-silicate interface. Mann *et al.*[11] stated that the extent of coadaptation is extremely sensitive to the stoichiometry and relative chemical potentials of the reactants, that is, to the balance of thermodynamic and kinetic driving forces within the system. Therefore, a high supersaturation of silicate species will induce phase separation *via* inorganic precipitation of amorphous silica, as opposed to low silicate concentrations which yield soluble products. At conditions in between these two extremes, the interfacial energetics dominate so that lamellar, hexagonal (MCM-41) or cubic (MCM-48) arrays of the inorganic and organic constituents are formed by rearrangement and subsequent aggregation of coadapted micelles. At this stage, the assembled architecture closely mimics a liquid crystalline inorganic salt of the cationic surfactant. Pattern replication occurs which is then followed by further condensation and polymerisation of silica within the interstitial spaces of the co-assembled template. Post-synthesis removal of the organic template by solvent extraction or calcination affords an ordered mesoporous inorganic material with channels dimensions commensurate with the width of the rod-like surfactant micelles. The resulting mesoporous silica is a kind of 'crystalline glass' with ordered mesopores whose inorganic walls are amorphous - an observation that highlights the hierarchical nature of these materials.

Another example of synergistic synthesis, is the recent discovery that chiral lipid molecules, together with silicate anions, co-assemble synergistically to yield a biphasic material with complex microscale morphology.[40] The reaction conditions are very similar to those used for conventional room temperature, acid-catalysed synthesis of MCM-41, but with replacement of the surfactant by an unsaturated phospholipid, diacetylenic phosphatidylcholine. In this experiment the phospholipid crystallisation

and silica polymerisation occurred simultaneously, resulting in a helical silica-lipid multilamellar microstructure (Figure 1.7). In the absence of the silica precursor, the phospholipid self-assembles to form closed tubules, rather than the open ribbon structure of the biphase, therefore suggesting that co-assembly leads to stabilisation of the metastable form.[11]

Figure 1.7 *TEM micrograph of a helical ribbon of a silica-phospholipid multilamellar biphase. Scale bar = 500 nm.*

1.2.3 Synthesis-with-Construction

Mann and Ozin[10] reported that it may be possible that the synergistic synthesis of co-assembled inorganic materials could be coupled ineractively with the surrounding reaction medium. The principle is based on nucleation and initial growth of an inorganic phase within an organised multi-component system. Such a system is a water/surfactant/oil microemulsion, which can induce changes within the local structure and phase behaviour, such that new morphological patterns develop from existing architectures. The synthesis process has been summarised by the following sequence:

co-assembly → *replication* → *reconstruction*

These changes of patterns replicated during mineralisation can be relatively small to large in scale and form. However, these changes do not have to occur over a great length scale, since they can be confined to localised reconstruction of the initial motif. For example, a silica mesoporous material may exhibit an increase in the pore diameter from 3 to 7 nm due to mild hydrothermal treatment of the surfactant biphasic products.[41]

For the fabrication of a more complex nanostructured composite, a different approach has been utilised with the construction of inorganic frameworks directing the use of a reaction medium for the fabrication of microscopic mesh-like architectures of silica,[42] or calcium phosphate.[43] The reaction medium, a reticulated biocontinuous microemulsion, can be readily formed from mixtures of the cationic surfactant, didodecyldimethylammonium bromide (DDAB), water and a long chain alkane mixture *e.g.* tetradecane and hexadecane. The microstructure of this system is

based on a dynamically fluctuating reticulated network of nanoscale water conduits within an oil matrix. The surfactant DDAB resides at the oil/water interface, therefore stabilising the framework from phase separation (Figure 1.8).

The reasoning behind using such a system is that it permitted the use of a supersaturated solution of calcium phosphate instead of water. This would allow crystals to nucleate more slowly at the surfactant headgroups and grow along the spatially delineated aqueous channels. Additionally, the junctions between channels would provide intergrowth sites for individual crystals, such that a replica of the biocontinous framework is established. SEM microscopy (Figure 1.9) showed the presence of a highly reticulated microstructure of interconnecting needle-like crystals, 0.2-1.0 μm in length, of hydroxyapatite ($Ca_{10}(OH)_2(PO_4)_6$). The material was macroporous with pore diameters up to several micrometres and wall thickness' of 50-130 nm, depending upon storage conditions and composition of the microemulsion mixture.

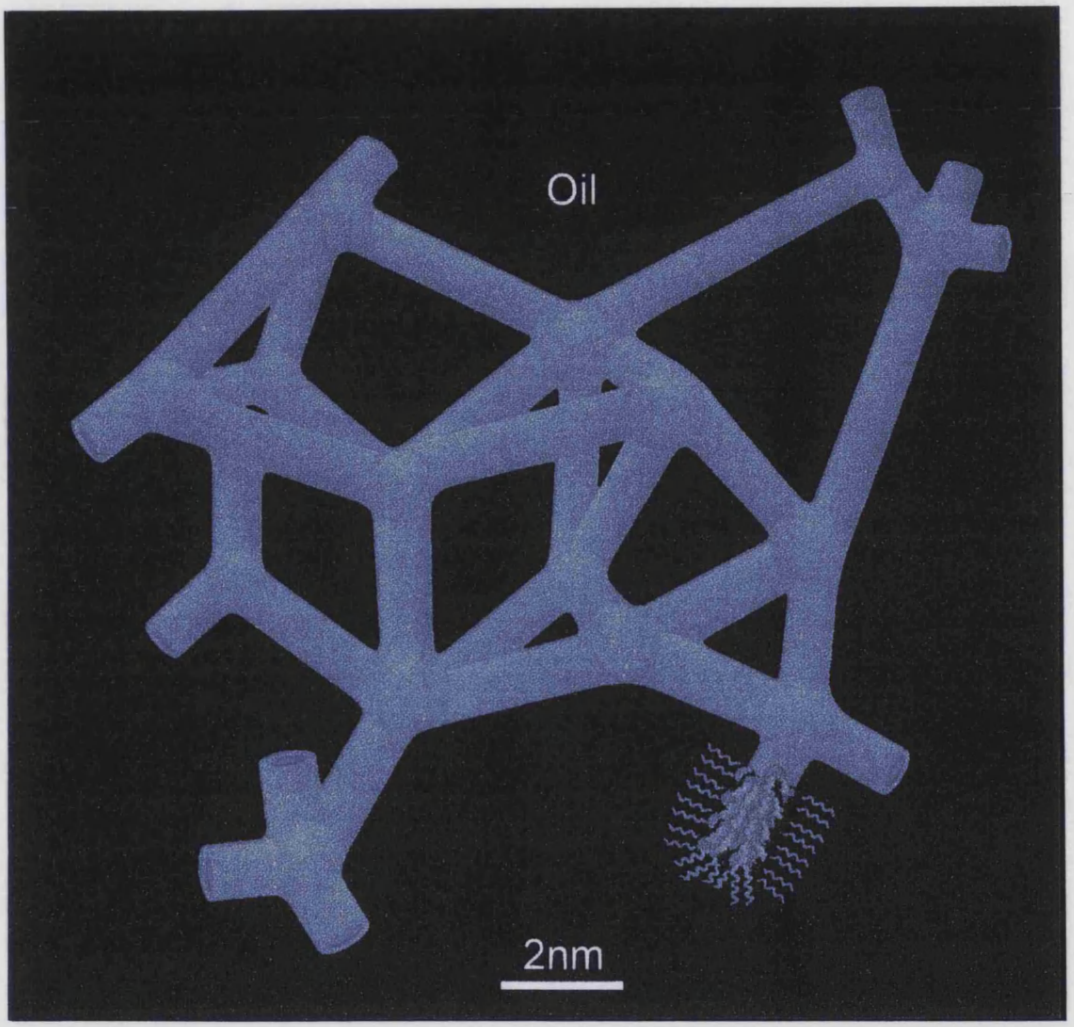

Figure 1.8 *Schematic showing the reticulated microstructure of water-in-oil bicontinuous microemulsion used in mineralisation experiments (redrawn from Hyde S.T. et al.).* [44]

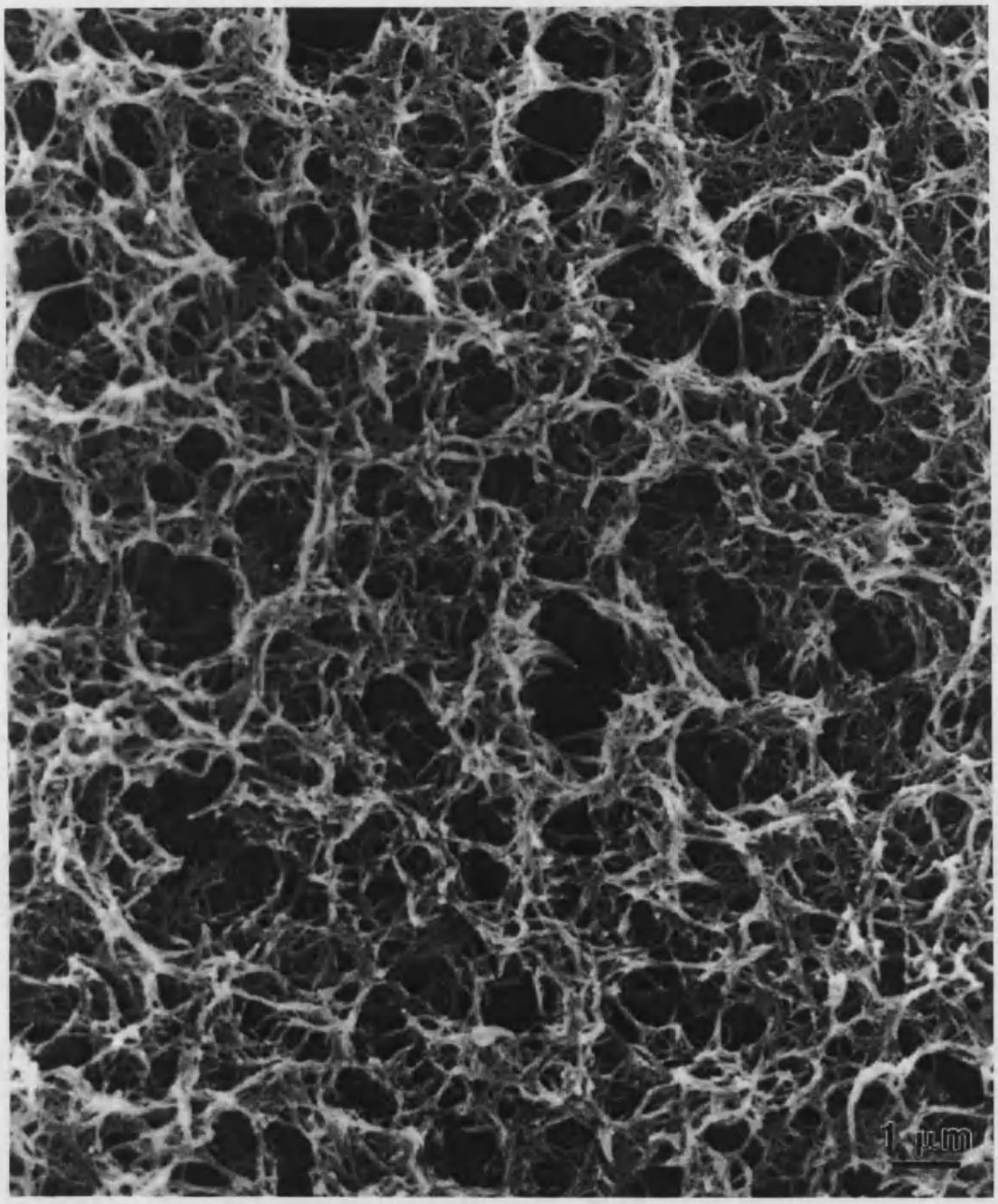

Figure 1.9 *SEM micrograph of reticulated calcium phosphate grown within a bicontinuous microemulsion (courtesy of D. Walsh, University of Bath).*

The results shown suggest that the microskeletal inorganic form 'evolves' *via* localised disruption and subsequent reordering of the microemulsion due to incipient crystallisation. The construction of the reticulated framework depends upon the ability of the self-organised reaction environment to undergo restructuring or 'metamorphosis' during inorganic crystallisation. Implicit in this transformability is that the surfactant headgroups initially act as the boundaries of nanoscale containers and templates, but become growth directors as crystallisation proceeds.[10] Analogous experiments with CdS and calcite, which do not adopt acicular habits, failed to produce macroporous materials.

Another approach to 'synthesis with construction' strategy involves the materials replication of transitory reaction fields.[11] This approach involves the induction of localised microphase separation in multicomponent reaction systems, such as microemulsions, foams and vesicles, to generate boundary surfaces and imprints for the sculpting of complex form in organic materials. An important factor to bear in mind is that the formation of the microphase architectures has to be synchronised with the onset of deposition of the inorganic phase, so that self-organised patterns are replicated before they disintegrate. This strategy has been utilised for the preparation of honeycomb frameworks of macroporous calcium carbonate (aragonite).[45] In this example, solvent extraction of oil and surfactant from a supersaturated microemulsion film spread on to metal substrates, results in a thin cellular film of porous aragonite. When micrometer-size polystyrene beads are coated with a thin film of the supersaturated microemulsion and subsequently washed with hot solvent, spherical shells of perforated calcium carbonate are formed (Figure 1.10).

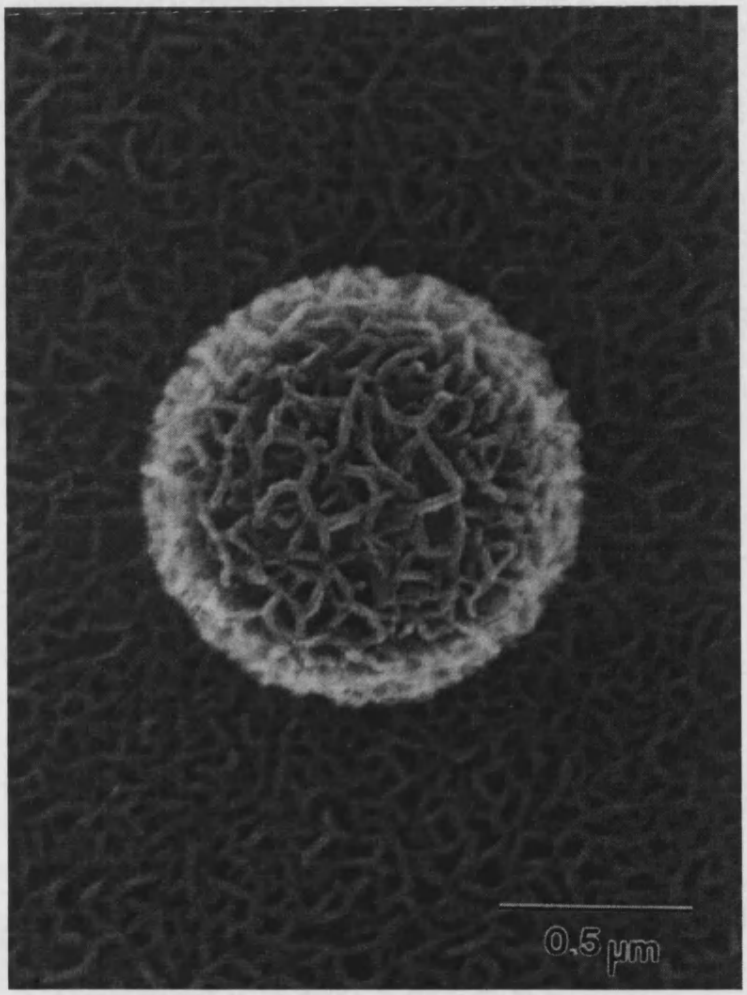

Figure 1.10 *Micrograph of an intact hollow shell of macroporous aragonite (courtesy of D. Walsh, University of Bath).*[39]

1.2.4 Integrative Synthesis

Integrative synthesis is a strategy that can possibly encompass some, if not all of the strategies mentioned above, for example the fabrication of materials displaying hierarchical structure and morphology. To date, research has concentrated on the development of systems which contain templates/directing agents which are expressed simultaneously on at least two different length scales.[11] For example, this strategy involves the synergistic synthesis of silica-surfactant mesophases with higher order transcriptive patterning. Two examples of this are the fabrication of hollow macroscopic spheres of mesoporous silica from an oil/water emulsion,[46] and the bacterial templating of ordered macrostructures in silica and silica-surfactant mesophases.[33]

In the example of the hollow macroscopic spheres of silica,[46] the hierarchical structure is formed by the co-assembly of the silica and surfactant at the surface of the dispersed oil droplets, which have a diameter of several micrometers. Contained within these oil droplets is the silica precursor, tetraethoxysiloxane (TEOS) and surfactant molecules. As the reaction proceeds TEOS is hydrolysed and the surfactant molecules are present in greater numbers at the oil/water interface, such that the emulsion droplets are acting as macroscopic templates for the nucleation of the silica-surfactant biphase.

The second example illustrates how supramolecular and supracellular templates can be combined for the fabrication of inorganic materials with structural hierarchy.[33] This approach utilises two synthesis strategies as before, but differ as in this example in that co-assembly of a silica-surfactant mesophase is patterned within a

biological superstructure consisting of coaligned cellular filaments of mutant *Bacillus subtilis*. The bacterial thread is dipped into a alkaline reaction media containing TEOS and surfactant (hexadecyl-trimethylammonium bromide). Removal of the thread and subsequent drying produces a product that was extensively mineralised throughout, with the multicellular filaments being encased in an extended polycrystalline framework of the silica-surfactant mesophase. Removal of the surfactant *via* calcination, afforded a intact fibre, consisting of a macroporous framework of co-aligned channels, which are 0.5 μm in width, and which are enclosed in mesoporous silica walls. Electron microscopy of a fractured sample (Figure 1.11) showed the presence of discrete hollow cylinders of mesoporous silica, suggesting that the organised composite is assembled *via* templating the mesophase onto the surface of the bacterial thread.

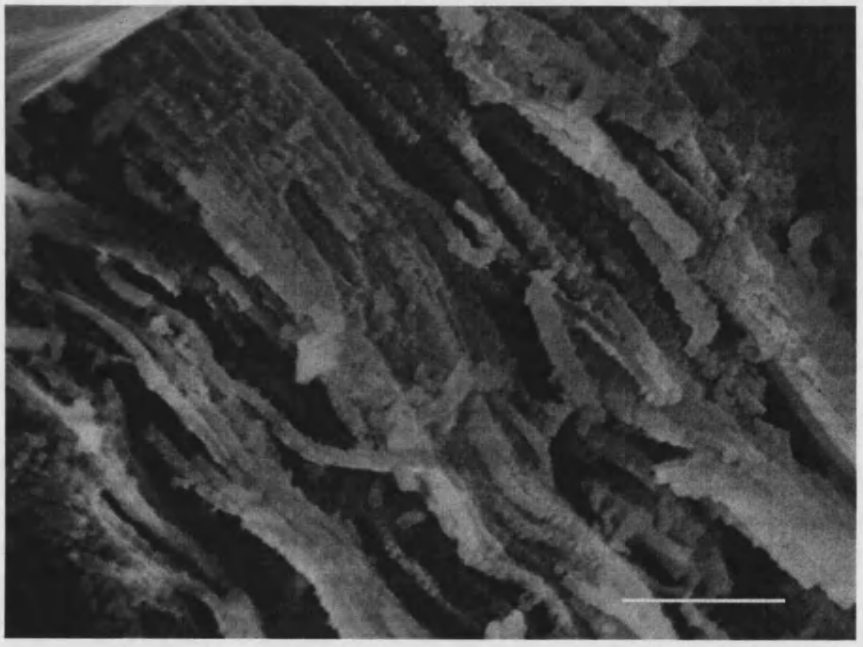

Figure 1.11 *SEM micrograph of MCM-41 infiltrated bacterial thread after calcination showing intact hollow cylinders of mesoporous silica. Scale Bar 10 μm (courtesy of S.A. Davis, University of Bath).*

1.3 Overview of Thesis

The work described within this thesis concentrates on the study of templating, or transcriptive synthesis systems. Two types of templating systems were studied; firstly, synthetic templating in two-dimensions with a length scale ranging from nm (10^{-9} m) to Å (10^{-10} m), and secondly biological templating in three-dimensions with a length scale of μm (10^{-6} m). The opening experimental chapter (chapter three) concerns itself with integrative synthesis, for the formation of mesostructured films of silica (MCM-41) under a compressed lipid monolayer spread at the air/water interface. This approach is a example of integrative synthesis, since it combines both templating and synergistic synthesis. The former involves the use of a lipid monolayer to aid the nucleation of a MCM-41 thin film, whereas the latter is involved in the self-assembly of the mesostructured silica frameworks from bulk solution. Chapter four is a study of the growth of these mesostructured silica films using x-ray reflectance in an attempt to elucidate the mechanism of formation of these films. Chapter five is a study using biological templating in the form of the supracellular bacterial thread of mutant *Bacillus subtilis*. This study shows two possible routes to the fabrication of a cadmium sulphide bionite, firstly using an *in-situ* reaction, highlighting that these bionites can be further chemically processed, and secondly using a preformed cadmium sulphide colloid for direct infiltration. Chapter six highlights the use of a synthetic template, focusing on the formation of fullerene malonic acid monolayers. Subsequent research on the monolayer focuses mainly on the interactions of divalent cations with the monolayer, termed 'fullerates', and the possibility of calcium carbonate crystallisation experiments under this monolayer.

1.4 References

1. Mann, S. (1996). Self-assembly in biomineralisation and biomimetic materials chemistry. **In**: *Comprehensive supramolecular chemistry* (Sauvage, J-P., and Hosseini, M.W. eds.), **9**, pp 529-564. Oxford: Elsevier Science (UK) Ltd.

2. Mann, S. (1996). Biomineralisation and biomimetic materials chemistry. **In**: *Biomimetic materials chemistry* (Mann, S. ed.), pp 1-37. Cambridge: VCH Publishers (UK) Ltd.

3. Calvert, P.D., and Mann, S. (1988). Synthetic and biological composites formed by *in-situ* precipitation, *Journal of Material Science*, **23 (11)**, 3801-3815.

4. Mann, S., Archibald, D.D., Didymus, J.M., Heywood, B.R., Meldrum, F.C., and Wade, V.J. (1992). Biomineralisation - Biomimetic potential at the inorganic-organic interface, *Material Research Society Bulletin*, **17 (10)**, 32-36.

5. Heuer, A.H., Fink, D.J., Laraia, V.J., Arais, J.L., Calvert, P.D., Kendall, K., Messing, G.L., Blackwell, J., Rieke, P., Thompson, D.H., Wheeler, A.P., Veis, A., and Caplan, A.I. (1992). Innovative materials processing strategies - A biomimetic approach, *Science*, **225 (5048)**, 1098-1105.

6. Addai, L., and Weiner, S. (1992). Control and design principles in biological mineralisation, *Angewandte Chemie, International Edition in English*, **31 (2)**, 153-168.

7. Mann, S., Archibald, D.D., Didymus, J.M., Douglas, T., Heywood, B.R., Meldrum, F.C., and Reeves, N.J. (1993). Crystallisation at inorganic-organic interfaces - Biominerals and biomimetic synthesis, *Science*, **261 (5126)**, 1286-1292.

8. Mann, S. (1993). Biomineralisation - The hard part of bioinorganic chemistry, *Journal of the Chemical Society, Dalton Transaction*, **1**, 1-9.

9. Mann, S., Archibald, D.D., Didymus, J.M., Heywood, B.R., Meldrum, F.C., and Wade, V.J. (1992). Biomineralisation - Biomimetic potential at the inorganic-organic interface, *Material Research Society Bulletin*, **17 (10)**, 32-36.

10. Mann, S., and Ozin, G.A. (1996). Synthesis of inorganic materials with complex form, *Nature*, **382 (6589)**, 313-318.

11. Mann, S., Burkett, S.L., Davis, S.A., Fowler, C.E., Mendelson, N.H., Sims, S.D., Walsh, D., and Whilton, N.T. (1997). Sol-gel synthesis of organised matter, *Chemistry of Materials*, **9 (11)**, 2300-2310.

12. Heywood, B.R., and Mann, S. (1994). Template-directed nucleation and growth of inorganic materials, *Advanced Materials*, **6 (1)**, 9-20.

13. Fendler, J.H., and Meldrum, F.C. (1995). The colloid-chemical approach to nanostructured materials, *Advanced Materials*, **7 (7)**, 607-632.

14. Feng, S., and Bein, T. (1994). Growth of orientated molecular-sieve crystals on organophosphonate films, *Nature*, **368 (6474)**, 834-836.

15. Shin, H., Collins, R.J., de Guire, M.R., Heuer, A.H., and Sukenik, C.N. (1995). Synthesis and characterisation of TiO_2 thin-films on organic self-assembled monolayers. 2. Film formation *via* an organometallic route, *Journal of Materials Research*, **10 (3)**, 699-703.

16. Baral, S., and Schoen, P. (1993). Silica-deposited phospholipid tubules as a precursor to hollow submicron-diameter silica cylinders, *Chemistry of Materials*, **5 (2)**, 145-147.

17. Burkett, S.L., and Mann, S. (1996). Spatial-organisation and patterning of gold nanoparticles on self-assembled biolipid tubular templates, *Journal of the Chemical Society, Chemical Communications*, **3**, 321-322.

18. Archibald, D.D., and Mann, S. (1993). Template mineralisation of self-assembled anisotropic lipid microstructures, *Nature*, **364 (6436)**, 430-433.

19. Meyer, M., Wallberg, C., Kurihara, K., and Fendler, J.H. (1984). Photosensitised charge separation and hydrogen production in reversed micelle entrapped platinised colloidal cadmium sulphide, *Journal of the Chemical Society, Chemical Communications*, **2**, 90-91.

20. Petit, C., Lixon, P., and Pileni, M.P. (1993). In-situ synthesis of silver nanoclusters in AOT reverse micelles, *Journal of Physical Chemistry*, **97 (49)**, 12974-12983.

21. Bianconi, P.A., Lin, J., and Strezlecki, A.R. (1991). Crystallisation of an inorganic phase controlled by a polymer matrix, *Nature*, **349 (6307)**, 315-317.

22. Mann, S., Hannington, J.P., and Williams, R.J.P. (1986). Phospholipid-vesicles as a model for biomineralisation, *Nature*, **324 (6097)**, 565-567.

23. Meldrum, F.C., Wade, V.J., Nimmo, D.L., Heywood, B.R., and Mann, S. (1991). Synthesis of inorganic nanophase materials in supramolecular protein cages, *Nature*, **349 (6311)**, 684-687.

24. Youn, H.-C., Baral, S., and Fendler, J.H. (1988). Dihexadecyl phosphate, vesicle stabilised and *in-situ* generated mixed CdS and ZnS semi-conductor particles - Preparation and utilisation for photosensitised charge separation and hydrogen generation, *Journal of Physical Chemistry*, **92 (22)**, 6320-6327.

25. Mann, S., and Williams, R.J.P. (1983). Precipitation within unilamellar vesicles 1. Studies of silver (I) oxide formation, *Journal of the Chemical Society, Dalton Transactions*, **2**, 311.

26. Bhandarkar, S., and Bose, A. (1990). Synthesis of nanocomposite particles by intravesicular coprecipitation, *Journal of Colloidal and Interface Science*, **135 (2)**, 541-550.

27. Heywood, B.R., and Eanes, E.D. (1987). An ultrastructural study of calcium phosphate formation in multilamellar liposome suspensions, *Calcified Tissue International*, **41 (4)**, 192-201.

28. Meldrum, F.C., Heywood, B.R., and Mann, S. (1992). Magnetoferritin - *In-vitro* synthesis of a novel magnetic protein, *Science*, **257 (5069)**, 522-523.

29. Bulte, J.W.M., Douglas, T., Mann, S., Frankel, R.B., Moskovitz, B.M., Brooks, R.A., Baumgarner, C.D., Vymazel, J., Strub, M.-P., and Frank, J.A. (1994). Magnetoferritin - Characterisation of a novel superparamagnetic magnetic resonance contrast agent, *Journal of Magnetic Resonance Imaging*, **4 (3)**, 497-505.

30. Bulte, J.W.M., Douglas, T., Mann, S., Frankel, R.B., Moskovitz, B.M., Brooks, R.A., Baumgarner, C.D., Vymazel, J., and Frank, J.A. (1994). Magnetoferritin - Biomineralisation as a novel molecular approach in the design of iron oxide based magnetic-resonance contrast agents, *Investigative Radiology*, **29 (S2)**, S214-S216

31. Douglas, T. (1996). Biomimetic synthesis of nanoscale particles in organised protein cages. **In**: *Biomimetic materials chemistry* (Mann, S. ed.), pp 91-112. Cambridge: VCH Publishers (UK) Ltd.

32. Sims, S.D. (1997). Template directed synthesis of hybrid silica materials, PhD thesis, University of Bath.

33. Davis, S.A., Burkett, S.L., Mendelson, N.H., and Mann, S. (1997). Bacterial templating of ordered macrostructures in silica and silica-surfactant mesophases, *Nature*, **385 (6615)**, 420-423.

34. Mendelson, N.H. (1978) *Proceedings of the National Academy of Science USA,* **75**, 2478.

35. Zones, S.I., and Davis, M.E. (1996). Zeolite Materials - Recent discoveries and future prospects, *Current Opinion in Solid State and Materials Science*, **1 (1)**, 107-117.

36. Anderson, S., Hyde, S.T., Larsson, K., and Lidin, S. (1988). Minimal surfaces and structures - From inorganic and metal crystals to cell membranes and biopolymers, *Chemical Reviews*, **88 (1)**, 221-242.

37. Kresge, C.T., Leonowicz, M.E., Roth, W.J., Vartuli, J.C., and Beck, J.S. (1992). Ordered mesoporous molecular sieves synthesised by a liquid-crystal template mechanism, *Nature*, **359 (6397)**, 710-712.

38. Huo, Q.S., Marglose, D.I., Ciesla, U., Demuth, D.G., Feng, P.Y., Gier, T.E., Sieger, P., Firouzi, A., Chmelka, B.F., Schüth, F., and Stucky, G.D. (1994). Organisation of organic molecules with inorganic molecular species into nanocomposite biphase arrays, *Chemistry of Materials*, **6 (8)**, 1176-1191.

39. Firouzi, A., Kumar, D., Bull, L.M., Besier, T., Sieger, P., Huo, Q., Walker, S.A., Zasadzinski, J.A., Glinka, C., Nicol, J., Margolese, D., Stucky, G.D., and Chemelka, B.F. (1995). Co-operative organisation of inorganic-surfactant and biomimetic assemblies, *Science*, **267 (5201)**, 1138-1143.

40. Patel, H.M., Burkett, S.L., and Mann, S. *Unpublished data.*

41. Khushalani, D., Kuperman, A., Ozin, G.A., Tanaka, K., Garces, J., Olken M.M., and Coombs, N. (1995). Metamorphic materials - Siliceous restructuring mesoporous materials, *Advanced Materials*, **7 (10)**, 842-847.

42. Watzke, H.J., and Dieschbourg, C. (1994). Novel silica biopolymer nanocomposites - The silica sol-gel process in biopolymer organogels, *Advances in Colloid and Interface Science*, **50**, 1-14.

43. Walsh, D., Hopwood, J.D., and Mann, S. (1994). Crystal tectonics - Construction of reticulated calcium phosphate frameworks in biocontinuous reverse microemulsions, *Science*, **264 (5265)**, 1576-1578.

44. Hyde, S.T., Ninham, B.W., and Zemb, T. (1989). Phase boundaries for ternary microemulsions - Predictions of a geometric model, *Journal of Physical Chemistry*, **93 (4)**, 1464-1471.

45. Walsh, D., and Mann, S. (1995). Fabrication of hollow porous shells of calcium carbonate from self-organising media, *Nature*, **377 (6547)**, 320-323.

46. Schacht, S., Huo, Q., Voigt-Martin, I.G., Stucky, G.D., and Schüth, F. (1996). Oil-water interface templating of mesoporous macroscale structures, *Science*, **273 (5276)**, 768-771.

CHAPTER TWO

GENERAL EXPERIMENTAL METHODS

Water Purification

Local tap water, of high hardness, was initially fed into an Aquatron A4D commercial still with dual boilers to produce double-distilled water. The output from the still was then further upgraded by using a Purite Standard Stillplus™ clean-up system, which contains a 0.2 μm bacterial filter, activated carbon cartridge and a mixed bed ion exchange column. The combination of these two procedures produced very high quality water (BS 3978 Grade 1) of typical conductivity much better than 1 $\mu S\ cm^{-1}$ and a pH of 5-6.

Preparation of Glassware

All glassware was first soaked in hot detergent solution. Then after rinsing with double-distilled water, re-soaked in dil. HCl (2 mol dm^{-3}). Finally, it was rinsed with high quality Purite™ distilled water and then oven dried, prior to use.

Measurement of pH

Various instruments were used, such as a Kent Industrial EIL 7045/46 digital and Radiometer PHM 84 and PHM 82 pH meters. Standard electrodes were used with each meter. Before use, each meter was calibrated using standard buffers covering the range of interest (Fisons phthalate pH 4.0; Fisons phosphate pH 7.0; BDH borate pH 10.0).

Infrared Spectroscopy (IR)

Analysis of materials was performed using a Nicolet 510P Fourier Transform Infrared Spectrometer, with an attached computer interface. The sample (1 mg) was ground together with IR-grade KBr (200 mg) to make 1 wt% solid solutions, which were then pressed to form 12 mm discs. Each sample was routinely scanned from 4000-400 cm^{-1}, with a resolution of 1 cm^{-1}. Precise peak locations were determined using a Nicholet software package.

Optical Microscopy (OM)

Two compound instruments were used; a Zeiss Axioskop and a Leitz Orthoplan capable of magnification from ×100 to ×1000 at the eyepiece. Both were equipped for photomicrography producing 35 mm negatives with magnification from ×25 to ×250. The Zeiss was fitted with special objectives (×10, ×20, ×50, ×100) that gave better than usual depth of field and obviated the need for cover glasses.

Scanning Electron Microscopy (SEM)

Because of the limitations in resolution and depth of field with OM, more detailed morphological examinations were carried out with scanning electron microscopy. Routine imaging of samples was performed using a JEOL 6310 scanning electron microscope operated at 15 kV. Samples were examined at magnifications between ×50 - ×20 000. The absolute limit resolution for a gold specimen was quoted as 7 nm, but in practice the resolution was found to be very dependent on the sample.

Transmission Electron Microscopy (TEM)

Detailed examination of materials was performed using either a JEOL 1200 EX or JEOL 2000 FX Transmission Electron Microscopes. These were operated at 120 and 200 kV respectively, but on some occasions it was necessary to operate below these kV values in order to preserve the sample. Both TEM's were capable of routine magnification of up to ×200 000, with an absolute limit in point to point resolution better than 5 Å. Samples were prepared for TEM on formvar-covered, carbon coated, 3 mm copper grids.

A description of the operational procedures in transmission electron microscopy can be found in Appendix One.[1]

Energy Dispersive X-ray Analysis (EDXA)

Qualitative elemental analysis was performed on both the JEOL 6310 scanning electron microscope and the JEOL 2000 FX transmission electron microscope using an energy dispersive X-ray analysis (EDXA) technique. The detector used was a Link lithium-drifted, silicon type cooled with liquid nitrogen. The limit of detection was dependent upon the element under study, but was generally of the order of 1-5 wt%. The JEOL 6310 scanning electron microscope was fitted with a removable Be window, which allowed the detection of lighter elements such as oxygen and carbon. The JEOL 2000 FX transmission electron microscope was windowless. Link AN10000 X-ray microanalysis systems were used on both machines to accumulate and then process the data.

Selected Area Electron Diffraction(SAED)[2]

Selected area electron diffraction patterns were taken of images magnified at × 120 000, using a camera length of 80 cm. Beam damage was occasionally a problem and so adjustments to the focus and astigmatism controls were made on areas adjacent to the area of interest. The patterns were indexed using d-spacings which were measured for each spot/ring using the formula:

$$d = \frac{2.\lambda.L_{mm}}{D_{mm}}$$

where λ is the relativistic wavelength of the electron beam, equal to 0.0334 Å and 0.0251 Å at 120 KeV and 200 KeV, respectively. L_{mm} is the camera length in mm and D_{mm} is the distance in mm between like spots/rings on opposite sides of the central spot.

X-ray Diffraction (XRD)

Milligram samples were assayed using a Phillips PW 1130 X-ray diffractometer fitted with a Debeye-Scherrer camera (diameter = 11.4592 cm), employing the Straumanis method of mounting. The samples were finely ground, placed in a Lindeman capillary tube (highly amorphous lithium glass) and exposed to Cu K_α radiation (α_1 = 1.54050 Å, α_2 = 1.544534 Å, weighted mean = 1.5418 Å) at 40 kV, 20 mA for 3-4 hours on average. In this arrangement, the distance between the entrance and exit holes represented 180° 2θ. The d-spacings were calculated from the Bragg equation: $n\lambda = 2d\sin\theta$ and compared to standard values obtained from the ASTM (JCPDS) cards.[3]

Small Angle X-ray Diffraction (SAXRD)

Small angle X-ray diffraction studies were performed at the following outside institutions:

California Institute of Technology (CalTech), USA

Analyses were performed using a Scintag XDS-2000 diffractometer equipped with a liquid nitrogen-cooled germanium solid-state detector. Samples were examined from 1° to 10° (2θ). Data were received as a plot of intensity versus 2θ.

Max Plank Institute, Teltow, Germany

Measurements were made using a Kratky camera (Otto Paar, Graz) and a Phillips stepscan detector, equipped with an impulse-height descriminator. Data were received as a file of intensity versus 1/d-spacing, allowing simple replotting to yield intensity versus 2θ.

All of the methods described used an X-ray source emitting Cu K_α radiation (α_1 = 1.54050 Å, α_2 = 1.544534 Å, weighted mean = 1.5418 Å).

^{13}C and ^{29}Si Magic Angle Spinning Nuclear Magnetic Resonance Spectroscopy (MAS NMR)

All solid state nuclear magnetic resonance measurements were performed using the ESPRC service based at Durham University, UK. Experiments were conducted using a Varian UNITY+ 300 spectrometer fitted with a Doty Scientific MAS probe. The spectrometer rotor had an outer diameter of 7 mm and was made of

zirconia with Kel-F end caps. Referencing was to an external sample of tetramethylsilane (TMS). Deconvolution of the spectra was performed using Varian software, which determined position and intensity of each peak.

CHN Microanalysis[4]

Elemental analysis was performed on a Carlo Erba 1106 Elemental Analyser. Samples of approximately 5 mg were burnt in a combustion tube at 1020 °C in O_2 alongside a reference. The products of combustion (such as carbon dioxide, water and nitrogen containing oxides) were then passed down a chromium (III) oxide column containing a silver-coated, mixed valence cobalt oxide to remove any sulphur and halogens. In addition, heated copper removed any remaining oxygen and reduced the nitrogen containing oxides to nitrogen gas. The outflow of the column was connected to a gas chromatograph employing helium as the carrier gas. Analyses were usually performed in duplicate, and were found to have a reproducibility of better than 0.05 wt%.

Thermogravimetric Analysis (TGA)

Thermogravimetric analyses were carried out by Micheal Breulmann at the Max Planck Institute, Teltow, Germany, using a NETZSCH TG 209 system fitted with a computer interface. Samples were loaded into an alumina crucible and heated at 50 K min^{-1} in a constant flow of compressed air.

2.1 References

1. Didymus, J.M. (1991). Morphological studies of morphological recognition in calcite ($CaCO_3$) crystallisation, PhD Thesis, University of Bath.

2. Hopwood, J.D. (1996). Barium sulphate crystallisation in synthetic and biological systems, PhD Thesis, University of Bath.

3. ASTM cards, *Annual Report to the Joint Committee on Powder Diffraction Standards*.

4. Sims, S.D. (1997). Template directed synthesis of hybrid silica materials, PhD thesis, University of Bath.

CHAPTER THREE

FORMATION AND CHARACTERISATION OF A MESOSTRUCTURED MCM-41 FILM AT THE AIR/WATER INTERFACE

3.1 Introduction

Mesoporous materials are complex inorganic frameworks with pore sizes in the range 20-100 Å in diameter. This compares with microporous materials which have pore diameters of < 20 Å. Until recently efforts to obtain mesoporous molecular sieves with regular, well defined channel systems had been unsuccessful. Mesoporous materials are typically amorphous such as silicas or aluminosilicates, and generally have pores which are irregularly spaced and broadly distributed in size.

However, back in 1992, Kresge *et al.*[1] and Beck *et al.*[2] who were Mobil workers reported on the preparation of M41S, a novel family of mesoporous molecular sieves made from aluminosilicates. These nanostructured ceramic oxides were prepared by the hydrothermal conversion of aluminosilicate gels in the presence of alkylammonium surfactant templates, and contained ordered arrays of pores. The process of forming M41S materials is reminiscent of that for the production of zeolites, in that the size of the system of pores and shape is directed by an auxiliary reagent or template. Within this family, the material Mobil Composition of Matter number **41**, or commonly abbreviated to MCM-41[3] exhibits a regular, hexagonally-ordered arrangement of pores with dimensions which can be measured from 20 Å to greater than 100 Å. Another member of the family of similar structure, except with cubic symmetry, was later designated MCM-48. Following the formation of these types of materials, removal of the surfactant template either by solvent extraction or

calcination revealed a porous silica material. The discovery of this new family of materials has lead to major advances in the synthesis and understanding of the mechanism of formation of similar materials.

The first synthesis of solid M41S materials involved a variety of silica sources to give silicate or aluminosilicate frameworks.[1,2] For example, hydrolysis followed by full condensation of tetraethylorthosilicate (TEOS) leads to a silica network around the organised surfactant micelles. The reaction scheme for hydrolysis and full condensation is shown in Figure 3.1.

Hydrolysis:

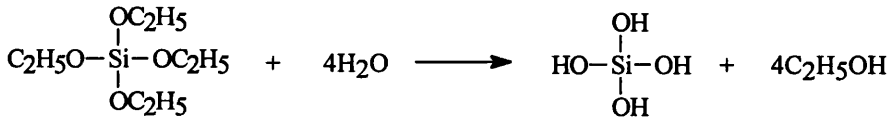

Condensation:

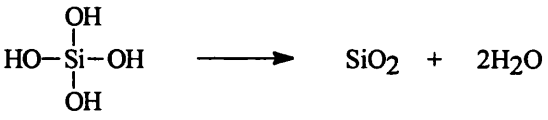

Figure 3.1 *Reaction scheme for silicate inorganic frameworks using TEOS.*

The surfactants initially used to form the micelles were quaternary ammonium surfactants such as hexadecyltrimethylammonium chloride $[C_{16}H_{33}(CH_3)_3N^+Cl^-$ (CTACl), which when placed in water can adopt one of two basic states. Firstly, if the carbon chain is small *i.e.* 2 - 3 unit long, the molecules will remain isolated in solution, but if the carbon chain becomes large, *i.e.* 15 units long then the molecules can spontaneously self-assemble into molecular aggregates. These aggregates, or

micelles, arise from the organisation of the hydrocarbon chains to form a hydrophobic inner area, whilst the polar head groups are at the surface, and are in contact with the aqueous phase.[4] The as-synthesised products can be formed over a large time and temperature range, and are isolated by filtration and washing with water. The final mesoporous material is obtained by calcination of the as-synthesised product in nitrogen and air, which removes most of the surfactant templating molecules. This stage causes a lattice contraction of around 3 Å. It has since been shown that the formation of these ordered materials from the M41S family does not always require hydrothermal treatment, and can be achieved by alkoxide hydrolysis (Figure 3.1) in the presence of a surfactant. The synthesis, physical properties and proposed mechanism of formation of the M41S family of mesoporous materials have been extensively investigated.[1-3,5] The mechanism by which these M41S materials are produced involves a co-operative self-assembly of a silica precursor with an ionic surfactant into a siliceous mesophase. The nature of the mesoporous product is dependent on the surfactant types, chain length, concentration, surfactant/silica ratio, and reaction conditions. The effect of these factors will be discussed in more detail later on.

The most extensively studied member of the M41S family is MCM-41,[1] which possesses a regular hexagonal array of uniform pores whose dimensions can be engineered in the range 15 - >100Å. A TEM micrograph of MCM-41 is shown in Figure 3.2.

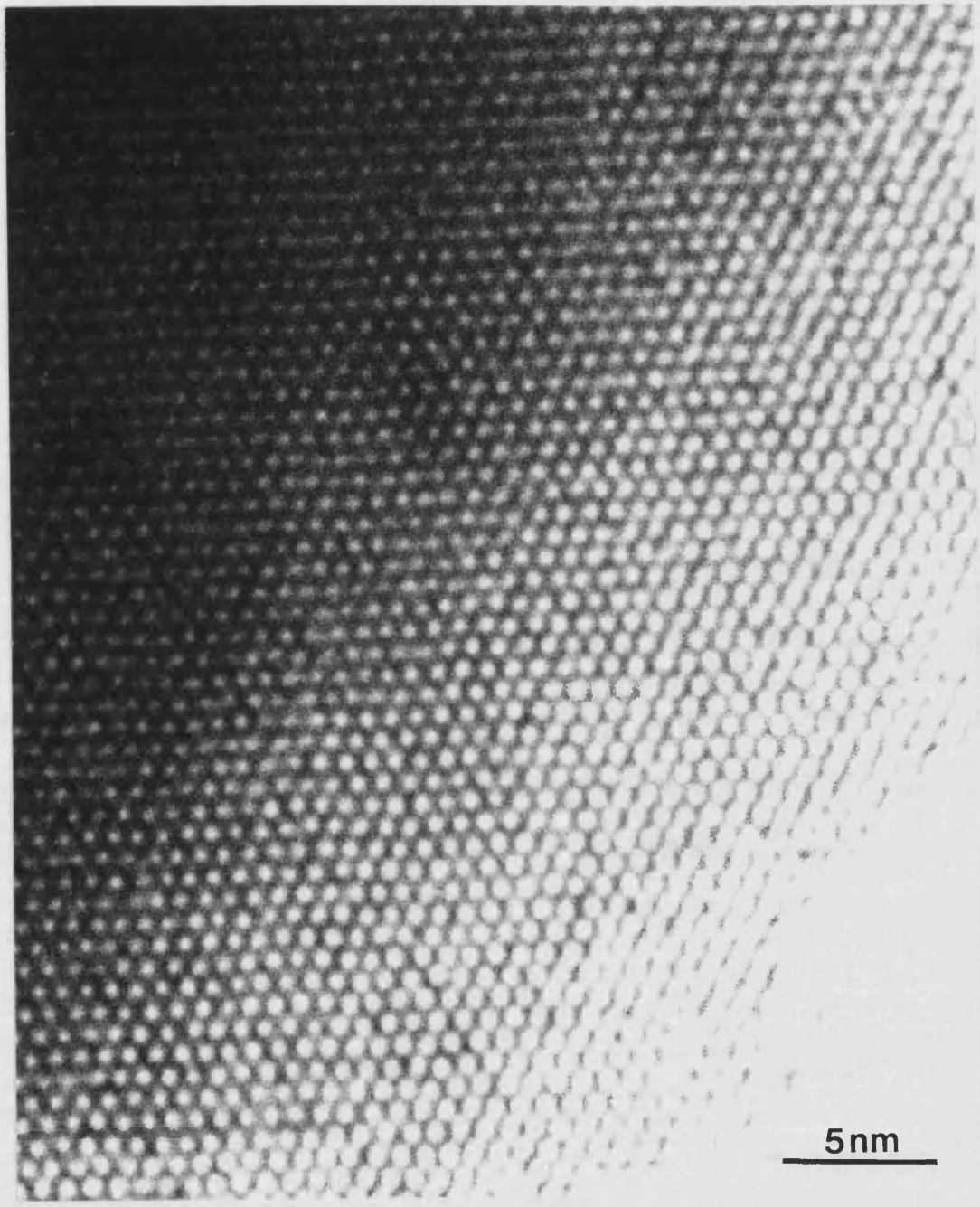

Figure 3.2 *TEM micrograph of MCM-41 material (courtesy of C.E. Fowler, University of Bath).*

From the micrograph, it can be seen that smaller pore size materials, < 40 Å, tend to give more regular hexagonal arrangements , with each pore surrounded by six other pores. Synthesis of MCM-41 materials with pore sizes greater than 40 Å requires an organic auxiliary added to the reaction mixture. MCM-41 with large pores of greater than 40 Å can have surface areas above 700 m^2 g^{-1}, and hydrocarbon sorption capacities of 0.7 cm^3 g^{-1}. The nature of the ordering in the walls of MCM-41, *i.e.*, the arrangement of atoms, is not yet fully understood, but is believed to have long range hexagonal regularity.

3.1.1 Mechanism of MCM-41 Formation

It was proposed by Kresge *et al.*[1] and Beck *et al.*[2] that the formation of MCM-41 takes place by means of a liquid-crystal templating (LCT) mechanism, in which supramolecular assemblies of surfactants serve as organic templates for the formation of inorganic walls (Figure 3.3).

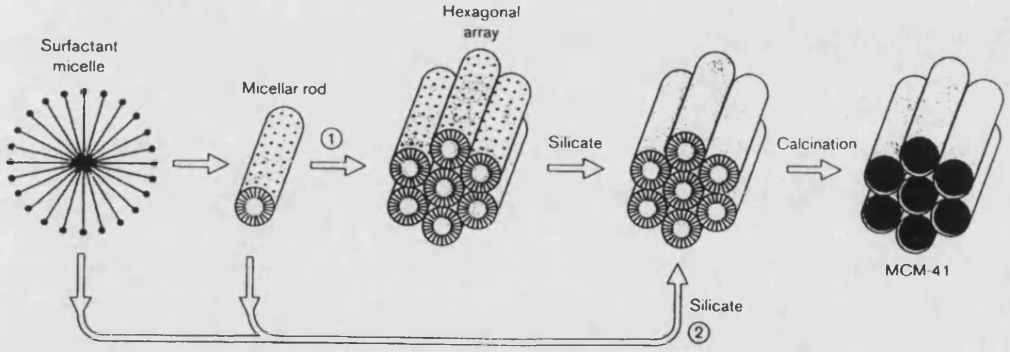

Figure 3.3 *Possible mechanistic pathways for the formation of MCM-41 (redrawn from Beck et al.).*[2]

Route 1 in Figure 3.3 involves the surfactant molecules forming organised aggregates, or micelles independently of the inorganic silicate crystallisation, the siliceous framework then polymerises around the organic material. Route 2 involves the addition of silicate resulting in the ordering of the subsequent silicate encased surfactant micelles. In both cases, the resulting surfactant/silicate composite mimics that of known liquid crystal phases.

The concept of using groups of molecules (micelles) as structure directing or templating devices expands on the idea of using a single molecule, as in zeolite synthesis. The initial use of supramolecular cationic surfactant aggregates and anionic silicate species to form mesoporous matter has opened the door to a range of novel molecular sieve materials. By tailoring the surfactant assemblies, the structure, pore diameter and composition of these materials can be engineered to meet a range of potential applications such as catalysis and sorption media. In this mechanism, hexagonally-ordered surfactant liquid-crystal structures served as the organic template. These liquid-crystal structures can exist as either a hexagonal phase (H_1), or reversed hexagonal phase (not used for MCM formation). The H_1 phase consists of rod-shaped micelles of indefinite length in an hexagonal arrangement, separated by a continuous water region. The micelle diameter is again approximately 10-30% less than the length of two all trans-molecules. The distance between the micelles is dependent on the water content and can vary between 8-50 Å. In the reversed hexagonal phase the hydrophobic ends of the surfactant molecules face outwards and hence occupy the spaces between the hexagonal micelles. Water lies at the centre of the micelles, in contact with the hydrophilic end of the surfactant chain. The proposed mechanism uses the H_1 hexagonal phase.

Further elucidation of the synthesis pathway by Chen *et al.*[6,7] utilising the technique of *in-situ* ^{14}N NMR and Edler *et al.*[8] using *in-situ* small angle neutron scattering, discounted this mechanism. At no point during MCM-41 formation was the proposed hexagonal liquid-crystalline phase, H_1, present in the synthesis medium. Data accumulated from the ^{14}N NMR studies showed evidence that the surfactant phase was most likely to be present in the form of elongated, flexible rod-like micelles. X-ray diffraction and ^{29}Si NMR investigations show that once the micelles have formed, and have long range order, the silanol groups encapsulating the micelles are still condensing to form the silica framework. Complete condensation does not occur because some SiO^- groups are necessary to charge balance the quaternary ammonium cations.

Small angle X-ray diffraction studies by Monnier *et al.*[9] suggested a different mechanism of formation involving an intermediate lamellar phase. This phase was thought to form in the initial stages, and then with time transform into a hexagonal structure. This mechanism was once again discounted, by Chen *et al.*,[7] who proved that the lamellar phase was formed as an artefact of the drying process when the samples were collected for analysis during the synthesis.

Of the two mechanisms mentioned above, that proposed by Chen *et al.*[6,7] is now considered the best description of how the template-directed process occurs. In this mechanism, randomly ordered rod-like micelles form in the synthesis mixture and interact with the silicate species to give silica encapsulated micelles (stages 1 and 2 of Figure 3.4). This interaction is favourable as the negatively charged silicate species interact with the positively charged quaternary ammonium ions *via* coulombic interactions. The randomly ordered tubes then spontaneously assemble into a

hexagonal arrangement, which is the lowest energy configuration (stage 3). Finally, the silicate species from different rods undergo base-catalysed condensation. Further heating allows the silicate species in the interstitial spaces of the ordered inorganic-organic phase to continue to condense (stage 4). Further condensation of the silicate species fuses the ordered hexagonal array to give coherent wall structure of 1 nm thickness. Removal of the surfactant template, either by solvent extraction or calcination, yields the mesoporous MCM-41 type material. The long range order found in MCM-41 is thus observed and the driving force for its formation is the condensation of the silicate species. The resemblance between the hexagonal liquid-crystal phase and the hexagonal arrangement of pores in MCM-41 may only be coincidence. This mechanism is proposed for MCM-48 and other members of the M41S family of mesoporous materials.

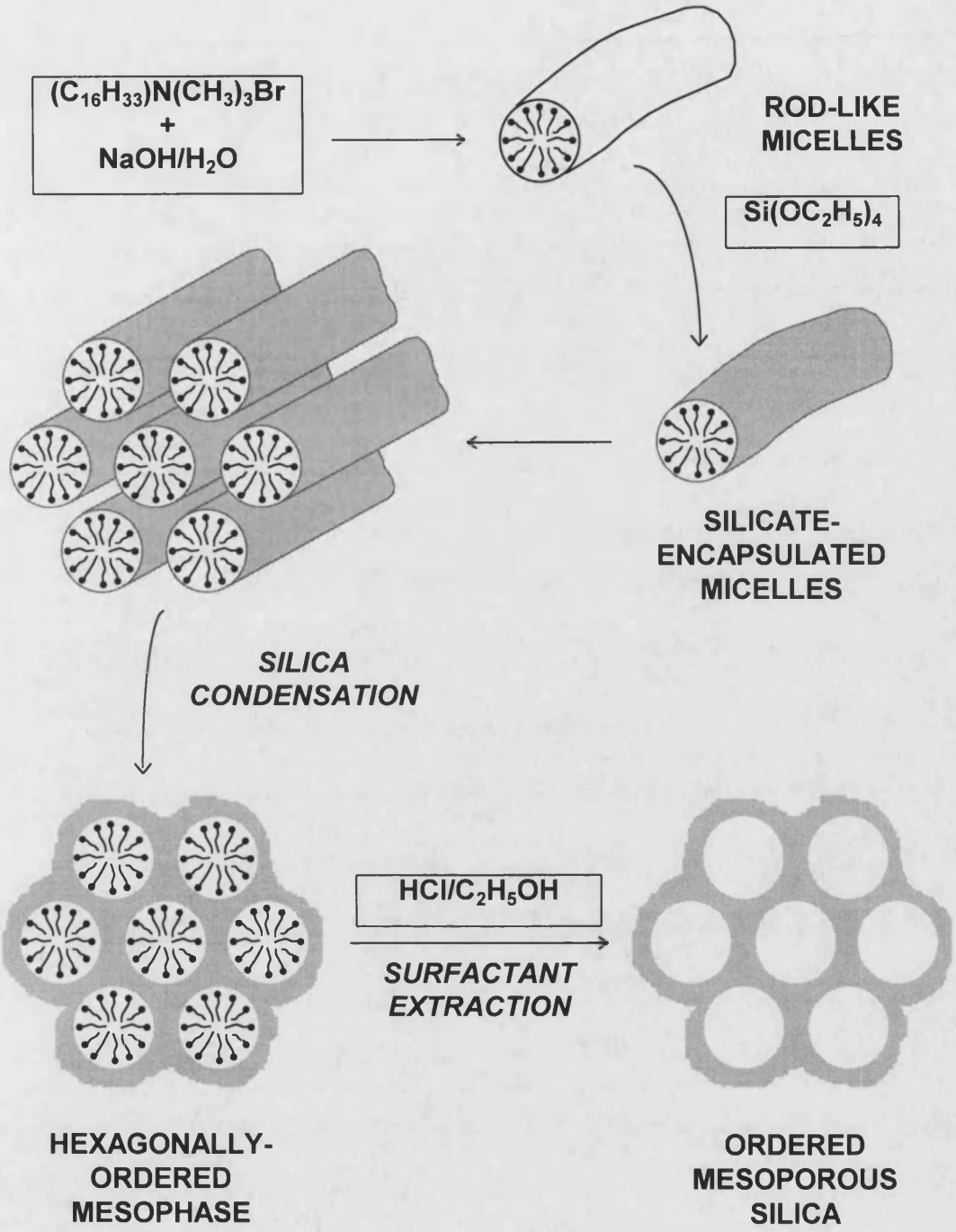

Figure 3.4 *Schematic diagram of the mechanism for formation of MCM-41 type silica material (redrawn from Sims, S.).*[10]

The pore size of MCM-41 can be increased by using an organic auxiliary to swell the micelles, at any time prior to the silica encapsulation. The inorganic framework resembles that of amorphous silicas or aluminosilicates in terms of atomic structure and bonding. The Si-O bond length is typically 1.6 Å and the Si-O-Si bond angle is 150°, resulting in a wall thickness of about 10 Å (Figure 3.5), commensurate to each micelle being approximately encapsulated by two or three layers of silica.[11]

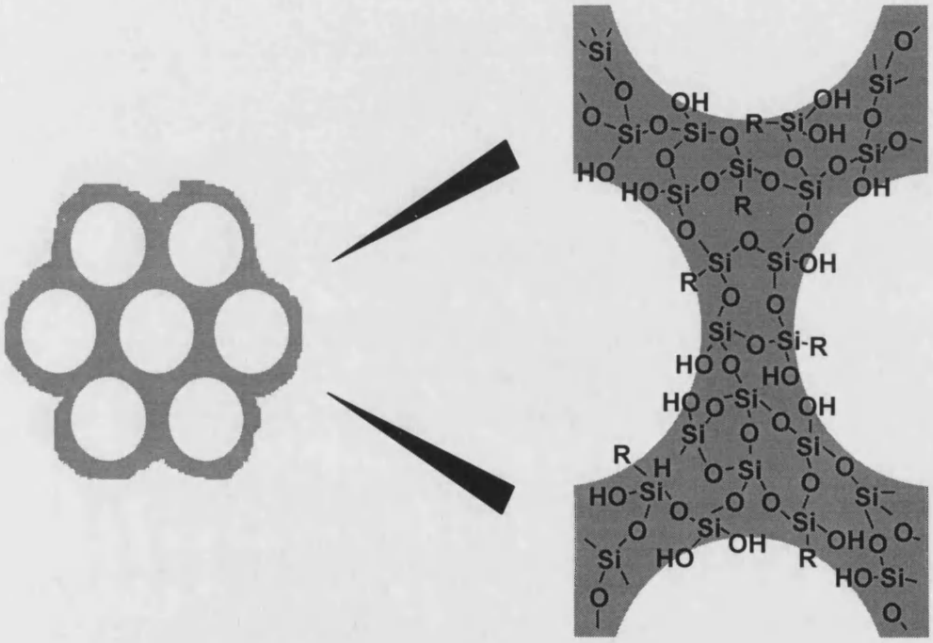

Figure 3.5 *Schematic diagram of the pore structure in MCM-41 material (redrawn from Sims, S.).*[10]

Interestingly, Davis and Burkett[4] also discuss the fact that MCM-41 type materials can be prepared with $C_{12}H_{25}N(CH_3)_3Cl$ (a surfactant which does not form rod-like micelles) and with 1 wt % $C_{16}H_{33}(CH_3)_3^+$ solutions (this concentration is well below that required for rod-like micelle formation). Hence, the presence of rod-like

micelles does not appear to be a necessary requirement for the formation of mesoporous materials. It does however highlight the key point that silica and surfactant species are both present in the reaction media. The presence of silica aq. NaOH and aq. NaBr each have a dramatic effect on the phase diagram of $C_{16}H_{33}(CH_3)_3^+$,[7] and so it is possible that surfactants, not capable of forming rod-like structures under normal aqueous conditions, may well do so in two-phase silicate media of these systems.

Since the initial studies on these type of materials, there has been a vast number of similar studies focusing on different aspects of the MCM-41 formation. It has been shown that pure silica MCM-41 type materials can be made using a variety of different silica sources *e.g.* tetramethylammonium silicate, sodium silicate, tetraethoxysilane and tetramethoxysilane.[1,12,13,6] In each case, the source of silica undergoes hydrolysis and condensation to form small silicate oligomers. At the low pH values commonly used in these preparations, the silicate species carry a net negative charge. It is these small negatively charged species which interact with the positively charged quaternary headgroups on the surfactant to form ordered silica-surfactant aggregates.

Studies have also shown that different surfactants can be used as the template for these structures. The most commonly used surfactant is the cationic surfactants in the form $(C_nH_{2n+1})N(CH_3)_3X$ (n = 8 ~ 22, X = Br, Cl). However, examples do exist where dimeric cationic surfactants like $[(C_mH_{2m+1})N(CH_3)_2\text{-}C_sH_{2s}\text{-}(CH_3)_2N(C_mH_{2m+1})]Br_2$ (m = 16, s = 2 ~ 12) have been shown to produce hexagonally-ordered mesophases.[4] In these examples, cationic surfactants are templating anionic silicate solution species, however examples do exist where this relationship is reversed. The

anionic surfactant $C_{16}H_{33}SO_3H$ has been used to produce hexagonally-ordered lead (II) oxide phases.[4] Tanev and Pinnavaia[14] have shown an example using an electronically neutral species. They showed that hexagonally-ordered, mesoporous silica can be synthesised using amines at a pH where the surfactant is neutral. In this instance it is proposed that hydrogen bonding, rather than electrostatic interactions causes the association between the surfactant template and the silicate species. The structures produced from these experiments have thicker silicate walls, smaller X-ray scattering domains, and poor textural mesoporosity when compared with conventional mesoporous silicates, prepared *via* charge balance templating.

The concept of charge-balancing to direct synthesis allows us to work with either anionic or cationic surfactants to effect the formation of anionic and cationic frameworks, respectively. Thus, although the main emphasis has been on silica structures, many other transition and main group elemental oxides have also been investigated.

Further extension of this area of work into the synthesis of non-silicate analogues using oxides of Sb, W, Pb,[4] and Nb,[15] shows that the many different methods for formation of MCM-41 type materials may afford the possibility to produce an ever expanding range of materials.

Reviews which cover the current range of systems are by Beck and Vartuli,[16] Huo *et al.*,[17] Ramsey,[18] and Göltner and Antonietti.[19]

3.1.2 Effect of Chain Length on MCM-41 Formation

The pore size of MCM-41 can be controlled by varying the alkyl chain length of the cationic surfactant used in the preparation. It was found that as the surfactant chain length is increased, the pore diameter of the material also increases (Table 3.1). This data was supported by benzene sorption studies. The uptake of benzene is increased as the surfactant chain length increases, indicating the filling of larger pores.

Table 3.1 *Effect of surfactant chain length on pore size of MCM-41.*[10]

Surfactant Chain Length*	Pore Size	Total Benzene Uptake
n =	Å	wt% at 50 Torr
Siliceous Products:		
10	22	32
12	22	36
14	30	54
16	37	64
Aluminosilicate products:		
14	34	40
16	38	61

* Chain length for $C_nH_{2n+1}(CH_3)_3N^+$

3.1.3 Effect of Organic Auxiliaries in MCM-41 Reaction Mixtures

The pore diameter of MCM-41 can also be altered by the addition of auxiliary hydrocarbons such, as alkylated benzenes *e.g.*, mesitylene, [1,3,5-trimethylbenzene]. These organic molecules are solubilised into the hydrophobic regions of the micelles, causing an increase in cell diameter. For the organic molecule to have any effect, it must be added in the early stages of the synthesis. As the mesitylene to surfactant ratio increases, so too does the pore size (Table 3.2). The surfactant chain length is kept constant in this case. For ratios of mesitylene: $C_nH_{2n+1}(CH_3)_3N^+$ greater than 3, the pores tend to be irregular with a broader distribution of sizes, but generally still hexagonally arranged. Pore sizes up to 100 Å have been synthesised.

Table 3.2 *Effect of mass of mesitylene added on the pore size of MCM-41.*[10]

Mass of Mesitylene added	Pore Size
g	Å
0	40
6	45
9	50
22	65

3.1.4 Effect of Surfactant : Silicon Ratio - Formation of Other Phases

Variation of the surfactant : silicon ratio leads to the isolation of other members of the M41S family. If the surfactant hexadecyltrimethylammonium chloride is used, then the hexagonal MCM-41 geometry is formed when the surfactant : silicon ratio is 1. On increasing the ratio, the MCM-48 cubic phase is formed. Variation of the ratio results in products that can be grouped into four main categories as shown in Table 3.3 and shown in Figure 3.6.

Table 3.3 *Effect of surfactant : silicon ratio.*

Surfactant : Silicon ratio	Phase
< 1	Hexagonal (MCM-41)
1 - 1.5	Cubic (MCM-48)
1.2 - 2	Thermally unstable phases (includes lamellar)
2	Cubic Octamer

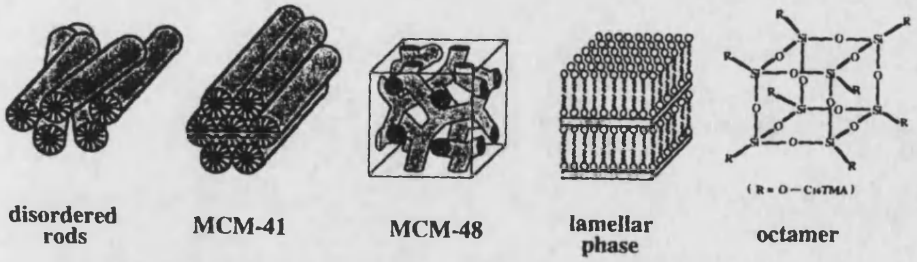

Figure 3.6 *Phases formed from variations in the surfactant:silicon ratio (redrawn from Davis, M.E. et al.)*[4]

At ratios of 1.2 - 2, the as-synthesised products formed have the appearance of a lamellar type phase, which collapses upon calcination. Hence the hexagonal, cubic and other less well defined phases give rise to the M41S family of mesoporous molecular sieves. At ratios above 2, an organic octamer is formed, namely $[(C_{16}H_{33}(CH_3)_3N)SiO_{2.5}]_8$, which does not form part of the M41S family.

3.1.5 Orientated Films of Mesoporous Silica

The synthesis of thin ordered films of thickness 0.2-1.0 μm of mesoporous silica on mica[20] brought a new dimension to the technological importance since it is thought that these structures may be applied to sensors, and optical and electronic materials, to which powdered forms of randomly orientated mesoporous silica are not accessible. The mica serves to orientate the micelles of surfactant, which in turn bring order to the developing film. Upon removal from the solid substrate the mesoporous film is stable.

The synthesis of the mesoporous film occurs under acidic conditions,[19] with freshly cleaved mica held horizontally in the synthesis vessel. Muscovite mica, $[KAl_2(AlSi_3O_{10})(OH)_2]$, is made up of double layers of tetrahedral SiO_4/AlO_4 building blocks sandwiching a single layer of octahedral AlO_6 units. When freshly cleaved, atomically flat, aluminosilicate six-rings sites are exposed. Under aqueous acidic conditions, the potassium counterions are exchanged with protons, hence providing SiOH sites on the mica for the silanol groups of the inorganic/surfactant micellar precursor to bind.

A model for the formation of the hexagonal mesoporous films has been suggested. Interfacial interactions between silica, surfactant and mica initiate nucleation and the organisation of silica-surfactant micellar seeds on the mica. SEM studies reveal that micrometre islands of mesoporous silica/micelles grow in a preferential direction, indicating that growth is regulated by charge and structure matching at the mica/silica/surfactant interface. The islands then coalesce to form a continuous film. TEM analysis indicate the presence of mesoporous steps providing

evidence for the deposition of further silica-surfactant miceller layers. The mesoporous films are formed on the lower side of the horizontal solid mica substrate.

Having formed, the films are washed with water and then calcined to remove the surfactant templates. This causes a lattice contraction of 2-5 Å due to the removal of the micelles and further condensation of silanol groups. The mesoporous silica film can then be removed from the mica substrate.

3.1.6 Free-Standing and Orientated Mesoporous Silica Films

The disadvantage of the mesoporous silica films grown at the mica/water interface is that the mica surface does not remain atomically smooth under the synthesis conditions, this affects the orientated film formation. The problem can be overcome by surfactant templating at the air/water interface.[21] The films formed are continuous and resilient enough to be bent and transferred onto substrates of various shapes.

The mesoporous films studied by polarised optical microscopy show that they are optically isotropic. Liquids and gases are isotropic phases,[22] which means the molecules are completely disordered in all directions, and thus all directions are equivalent. A solid can also be isotropic if it is amorphous. In an amorphous solid, the molecules are unable to diffuse throughout the substance because they are fixed in place. There is no overall arrangement of the molecules, they are positioned randomly as in a liquid. Liquid crystals on the other hand are anisotropic, not isotropic. At every point in the liquid crystal the molecules define a special direction by spending more time pointing along this direction (*i.e.* there is order in at least one direction and if there is order in more than one direction, the orders are different).

These results suggest that the silica framework is amorphous, and the channels which were previously filled with micellar surfactant template are not behaving as liquid crystals. This also enforces Burkett and Davis hypothesis,[7,23,24] which states that the resemblance between the hexagonal liquid crystal phase and the hexagonal arrangement of pores in MCM-41 may only be coincidental.

A model for growth of the free-standing mesoporous silica film is based on the formation of a hemi-micellar surfactant layer formed at the air/water interface.[25-27] The film grows into the solution as micelles, encapsulated by silicate, which assemble in a hexagonal close packed arrangement beneath the hemi-micellar over-structure. Condensation of the silicate groups of adjacent micelles leads to the formation of the mesoporous thin film. The micelles or channels of the mesoporous film lie parallel to the air/water interface. The surface at the air/water interface is believed to mimic that of the surfactant over-structure and has a roughness of about 2-3 Å, hence it is relatively smooth. Any defects in the surface are attributed to inhomogenities in the silicate condensation process. The roughness of the film/solution (*i.e.* the interface growing into the solution), is on the mesoscopic scale. This represents the arrangement of silica encapsulated micelles as they are deposited on the lower side of the film.

In conclusion, a preorganised hemi-micellar overlayer of surfactant molecules at the air/water interface interacts with underlying silicate building blocks and micellar solution species to form a mesoporous silica film. This film then grows into the solution. The proposed mechanism is graphically illustrated in Figure 3.7.[21]

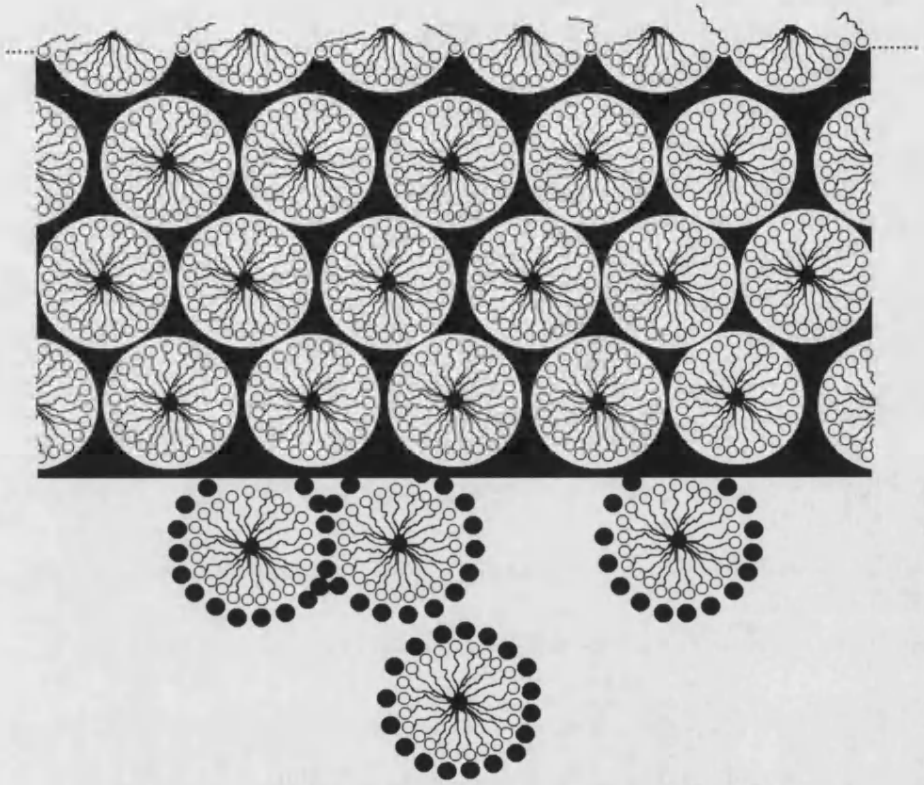

Figure 3.7 *Graphical illustration of the proposed model for formation of free-standing orientated mesoporous silica film at the air/water interface (redrawn from Yang, H. et al.).*[21]

3.1.7 Application of Mesoporous Molecular Sieves

Mesoporous Adsorbents[28]

This application utilises the large pore volumes possessed by mesoporous materials. An example is the use of mesoporous adsorbents in the removal of volatile organic compounds.

Catalysts

Mesoporous aluminosilicates have been used in the catalysis of large organic molecules. Aluminosilicate MCM-41 can catalyse the alkylation of 2,4-di-tert-butylphenol to form 6,8-di-tert-2-phenyl-2,3-dihydrobenzopyran.[29] The reaction could not be catalysed by zeolites due to their small pore size. Mesoporous transition metal oxides such as titanium and vanadium also have catalytic activity, and have reported uses in the oxidation of large molecules. In addition, metals and metal complexes have been incorporated into the mesoporous materials, and used as catalysts. Aluminosilicate MCM-41 containing nickel and molybdenum has been used in the hydrocracking of vacuum gas oils.[30] Its catalytic activity was attributed to the high surface acidity, (due to the presence of alumina), and large uniform mesopores.

Mesoporous Mini-reactors for Electron Transfer Reactions

MCM-41 can be converted into an efficient electron transfer material by incorporation of the 2,4,6-triphenylpyrilium ion (TP^+).[31] This material was used as a sensitiser to convert *cis*-stilbene to *trans*-stilbene. Hence mesoporous materials can be used as hosts for photo-induced electron transfer reactions.

Mesoporous Hosts

An organometallic complex such as trimethyl tin-molybdenum carbonyl, can be sorbed into the pores of a mesoporous material and then anchored in place by ligand loss (*i.e.* protons from silanol groups combine with methyl ligands to form methane).[32] Subsequent thermal treatment causes decomposition of the anchored complex to Sn-Mo clusters, which have potential catalytic activity in the hydrogenation of olefins.

Shape Selective Polymerisation

The controlled polymerisation of styrene, methylmethacrylate and vinyl acetate can be carried out by the use of mesoporous silicates as hosts.[33] Smaller pore sizes produced higher molecular weight polymers. This may have been due to the increase in confinement of the polymer chain, which prevents it from reacting with other chains, resulting in termination.

3.2 Experimental

Production of Mesoporous Silica

MCM-41 type materials were synthesised at room temperature[11] from a dilute basic solution containing the organosiloxane, tetraethoxysilane (TEOS) and the surfactant hexadecyl-trimethylammonium bromide (C_{16}TMABr) (molar composition = 0.01 C_{16}TMABr : 1.19 NaOH : 0.09 TEOS : 402.06 H_2O). The structures of C_{16}TMABr and TEOS are shown in Figure 3.8.

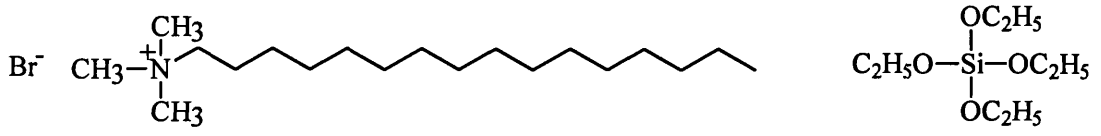

C_{16}TMABr TEOS

Figure 3.8 *Structure of C_{16}TMABr and TEOS.*

In a typical experiment, the solution is prepared as follows: 0.16 g of C_{16}TMABr was dissolved in 318.0 g of H_2O and stirred continuously. To this solution 2.0 g of 1M NaOH was added, followed by 0.828 ml of TEOS. This solution was placed into clean crystallisation dishes and sealed with parafilm and left for 3 days.

In the experiments involving the templating monolayer of phosphatidylcholine (PC), the TEOS/C_{16}TMABr solution was placed into a clean crystallisation dish and a known volume of PC in chloroform was dropped onto the air/water interface, drop by drop, *via* a microsyringe to form a monolayer. These dishes were also sealed with parafilm and left for 3 days.

After 3 days, the visible films at the air/water from both samples were sampled in two ways. Firstly, a 300 mesh copper, formvar coated grid was dipped through the interface and left to dry for 24 hours before being analysed by electron microscopy.

Secondly, the remainder of the film at the air/water interface was collected *via* suction pipette and filtered using Whatman 0.2 μm PTFE membrane filters, washed with water and dried for 10 hours at 100 °C *in vacuo*, before undergoing solid characterisation. These samples were termed as-synthesised samples.

The samples for solid characterisation were also characterised after the surfactant template had been removed. This was done by calcination, which involves heating the sample to a temperature of 500 °C to remove all volatile organic components. These samples were termed calcined samples.

C_{16}TMABr and TEOS were supplied from the Aldrich Chemical Company and were used as received. A solution of NaOH was prepared using 1.0 mol dm^{-3} $NaOH_{(aq)}$ standard solution from FSA.

The materials produced were characterised by small angle X-ray diffraction (SAXRD), transmission electron microscopy (TEM), ^{13}C cross-polarisation (CP) and ^{29}Si solid-state, magic angle spinning (MAS) NMR spectroscopy, Infra-red spectroscopy, CHN microanalysis and thermogravimetric analysis (TGA) described in Chapter Two.

In addition to the above characterisation techniques, two additional techniques of solution ^{13}C NMR and small angle X-ray reflectance (SAXR) were also employed.

Solution ^{13}C NMR on C_{16}TMABr were performed using a JEOL GX 270 MHz Spectrometer. A C_{16}TMABr sample was prepared as a 3% w/w solution in 99.8% $CDCl_3$ (Aldrich Chemical Company).

3.3 Results and Discussions

The mesostructured silica film grown at the air/water interface in the presence of a templating monolayer of PC (whose structure is shown in Figure 3.9) became visible to the naked eye after 8 hours, whereas the film without a templating monolayer of PC became visible to the naked eye after 12 hours. Therefore, the presence of a templating monolayer of PC promotes nucleation and hence growth of the mesostructured silica film at the air/water interface.

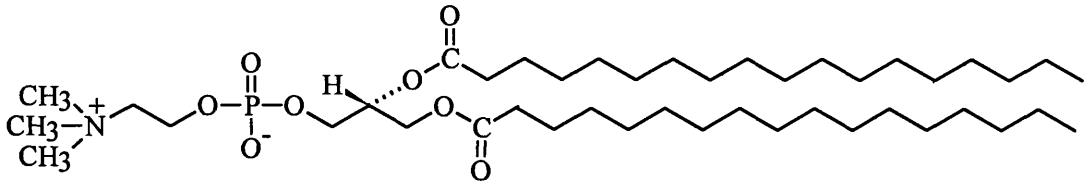

Figure 3.9 *Structure of egg-lecithin phosphatidylcholine (PC) supplied by Nutfield Nurseries, Surrey, U.K.*

Small Angle X-Ray Diffraction (SAXRD)

Small angle X-ray diffraction studies on the material produced at the air/water interface show that a single phase is formed for both the as-synthesised samples, as shown in Figure 3.10.

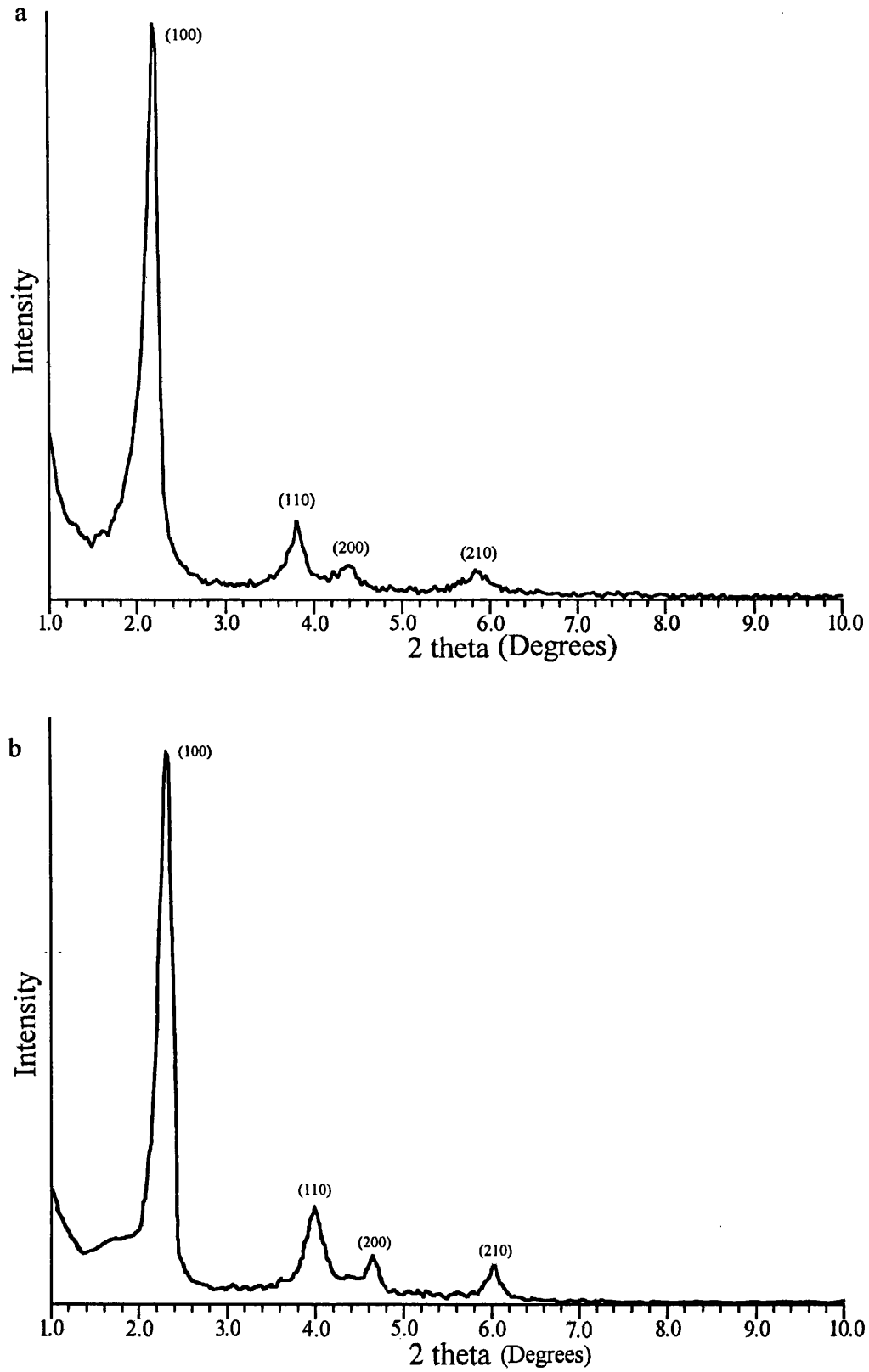

Figure 3.10 *SAXRD patterns for as-synthesised samples in a) the presence of a PC and b) without the presence of a PC templating monolayer, indexed to a hexagonal unit cell.*

Analysis of the d-spacing and associated Miller Indices (Table 3.4) indicated that the phase produced for each as-synthesised sample conforms to a hexagonal unit cell. This conformation was deduced by taking the main reflection, the (100) peak, and the subsequent higher order reflections at angular reflections √3 (110), 2 (200), √7 (210) and √12 (310) of this first-order maximum, and the resulting spacing sequence is indicative of a hexagonal unit cell. The relationship between the d_{100} spacing and the hexagonal unit cell parameter (*a*), is illustrated in Figure 3.11.

Table 3.4 *SAXRD data for as-synthesised samples.*

	XRD d-spacings and calculated hexagonal unit cell parameter, *a* (Å)				
	(100)	(110)	(200)	(210)	*a*
With PC monolayer	40.1	23.2	20.1	15.2	46.3
Without PC monolayer	38.1	22.0	19.0	14.4	43.9

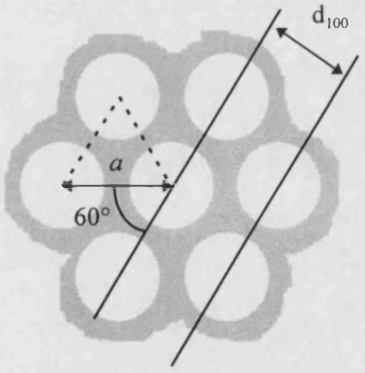

$d_{100} = a \times \text{Sin } 60°$

$\Rightarrow d_{100} = a \times \sqrt{3}/2$

$\Rightarrow a = d_{100} / \sqrt{3}/2$

$\Rightarrow a = 2d_{100} / \sqrt{3}$

Figure 3.11 *Schematic diagram illustrating the relationship between d_{100} spacing and the hexagonal unit cell parameter, a, (redrawn from Sims, S.).*[10]

The observation of higher order peaks in both the as-synthesised samples confirms the presence of long-range hexagonal order (Figure 3.12).

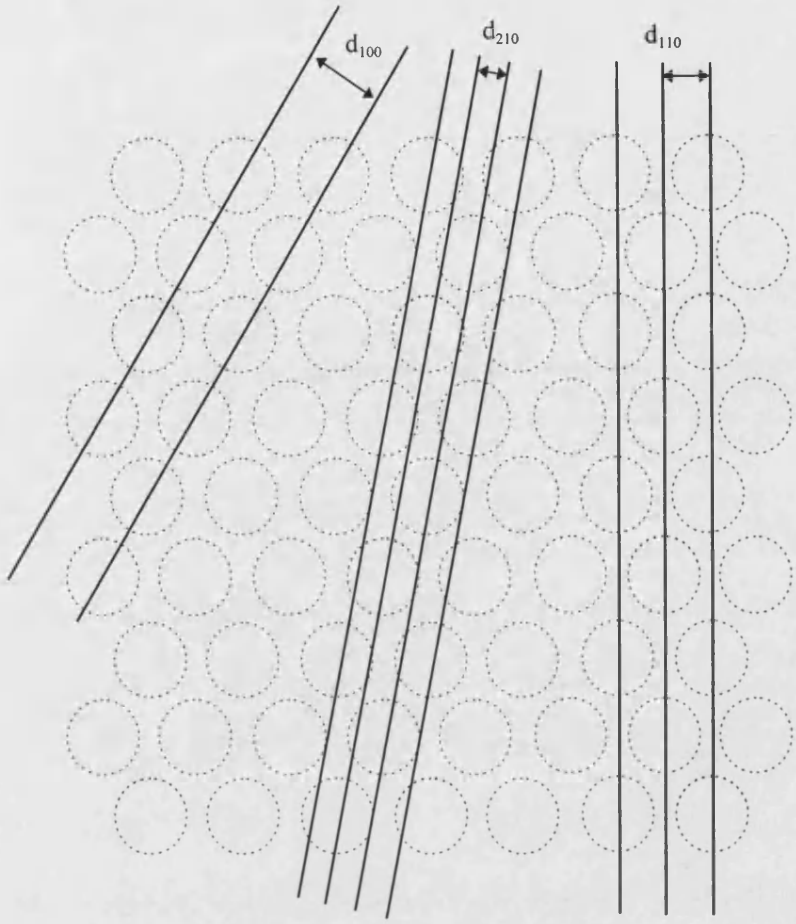

Figure 3.12 *Schematic diagram showing the relationship between long range hexagonal structures and the observed X-ray diffraction peaks for MCM-41 material (redrawn from Sims, S.).*[10]

As seen in Figure 3.12 and text[34] the relationship between the d-spacing and associated reflections of a hexagonal unit cell of length *a*, is given by the following equation:

$$d = \frac{a}{\sqrt{\frac{4}{3}(h^2 + k^2 + hk)}}$$

Small-angle x-ray reflectivity (SAXR) analysis of both calcined samples is shown in Figure 3.13.

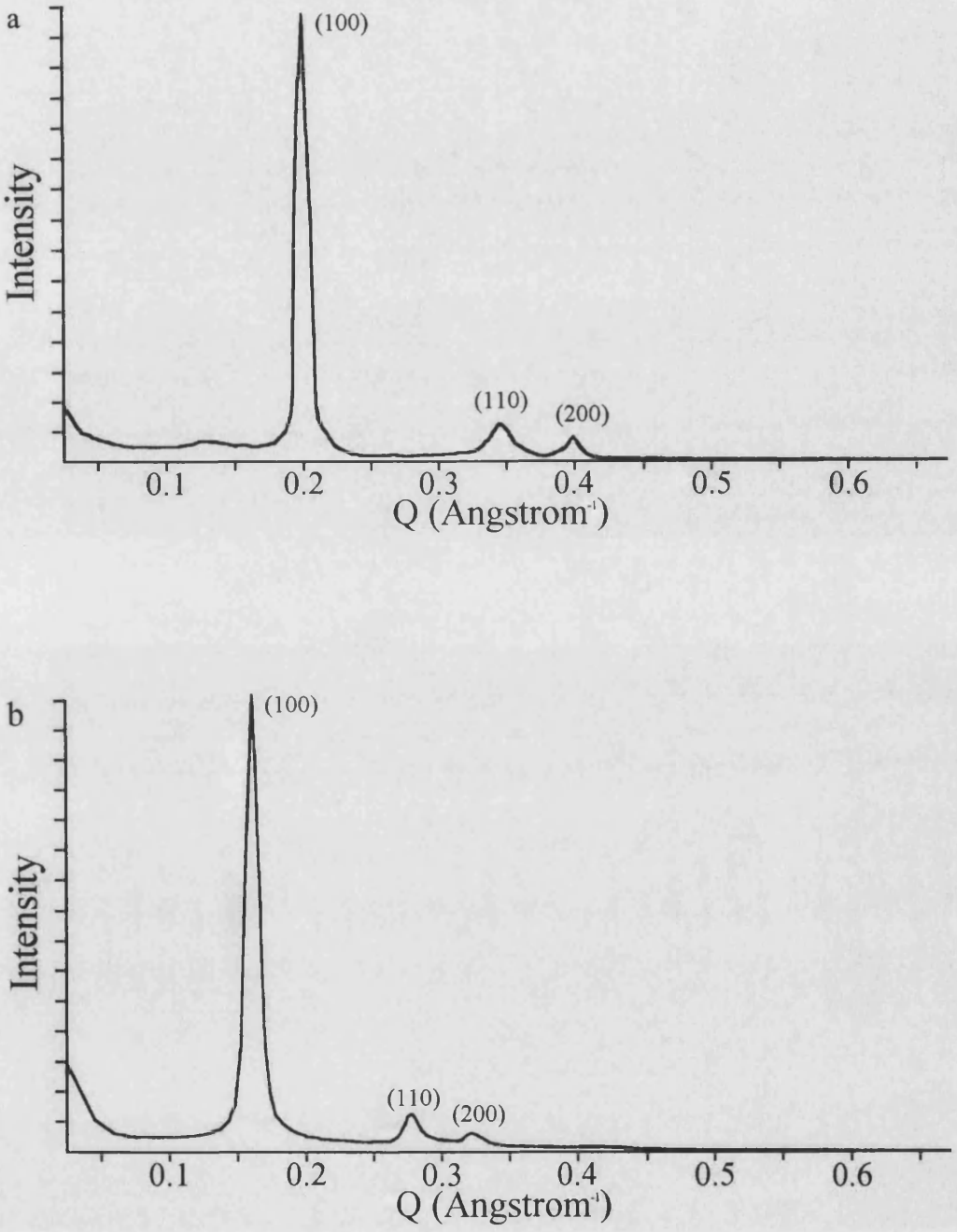

Figure 3.13 *SAXR patterns for the calcined samples in a) the presence of a PC and b) without the presence of a PC templating monolayer, indexed to a hexagonal unit cell.*

Table 3.5 shows the d-spacing values obtained by using the equation $d = 2\pi/\mathbf{Q}$. The results show that the hexagonal order within both calcined samples is maintained. Calculation of the hexagonal unit cell parameter *a*, showed that for each calcined sample a large contraction had occurred in the size of the hexagonal lattice.

Table 3.5 *SAXRD data for the calcined samples.*

	XRD d-spacings and calculated hexagonal unit cell parameter, *a* (Å)				
	(100)	(110)	(200)	(210)	*a*
With PC monolayer	31.4	18.3	15.7	-	36.3
Without PC monolayer	36.9	22.4	19.0	-	42.6

Contraction of the size of the hexagonal lattice occurs as a result of further condensation of Si-OH groups in the structure, under the conditions of calcination, a trend reported by Chen *et al.*[6] If a single peak is observed, then this is indicative of the formation of a disordered hexagonal phase.[6] This occurs where there are imperfections in the packing of the silicate coated tubules.

Transmission Electron Microscopy (TEM)

Examination of the as-synthesised samples, with and without the presence of the templating monolayer of PC revealed a hexagonal system of lattice fringes, shown in Figures 3.14 and 3.15, respectively. On further examination of both the as-synthesised samples, we can see images of parallel fringes, shown in Figures 3.16 and 3.17, respectively. Both of these observations for each of the four samples are commensurate with the presence of an hexagonally-ordered mesophase. D-spacings taken from both as-synthesised micrographs are shown in Table 3.6

The presence of parallel fringe structures has been demonstrated to be due to the effects of imaging the side-on view of the hexagonally ordered tubular structures.[35]

Table 3.6 *d-spacing data for the as-synthesised samples from TEM micrographs.*

	TEM d-spacings and calculated hexagonal unit cell parameter, *a* (Å)				
	(100)	(110)	(200)	(210)	*a*
With PC monolayer	40.0	22.5	20.0	-	46.2
Without PC monolayer	38.0	21.0	20.0	-	43.8

These d-spacings are in good agreement with those obtained from SAXRD analysis (Table 3.4).

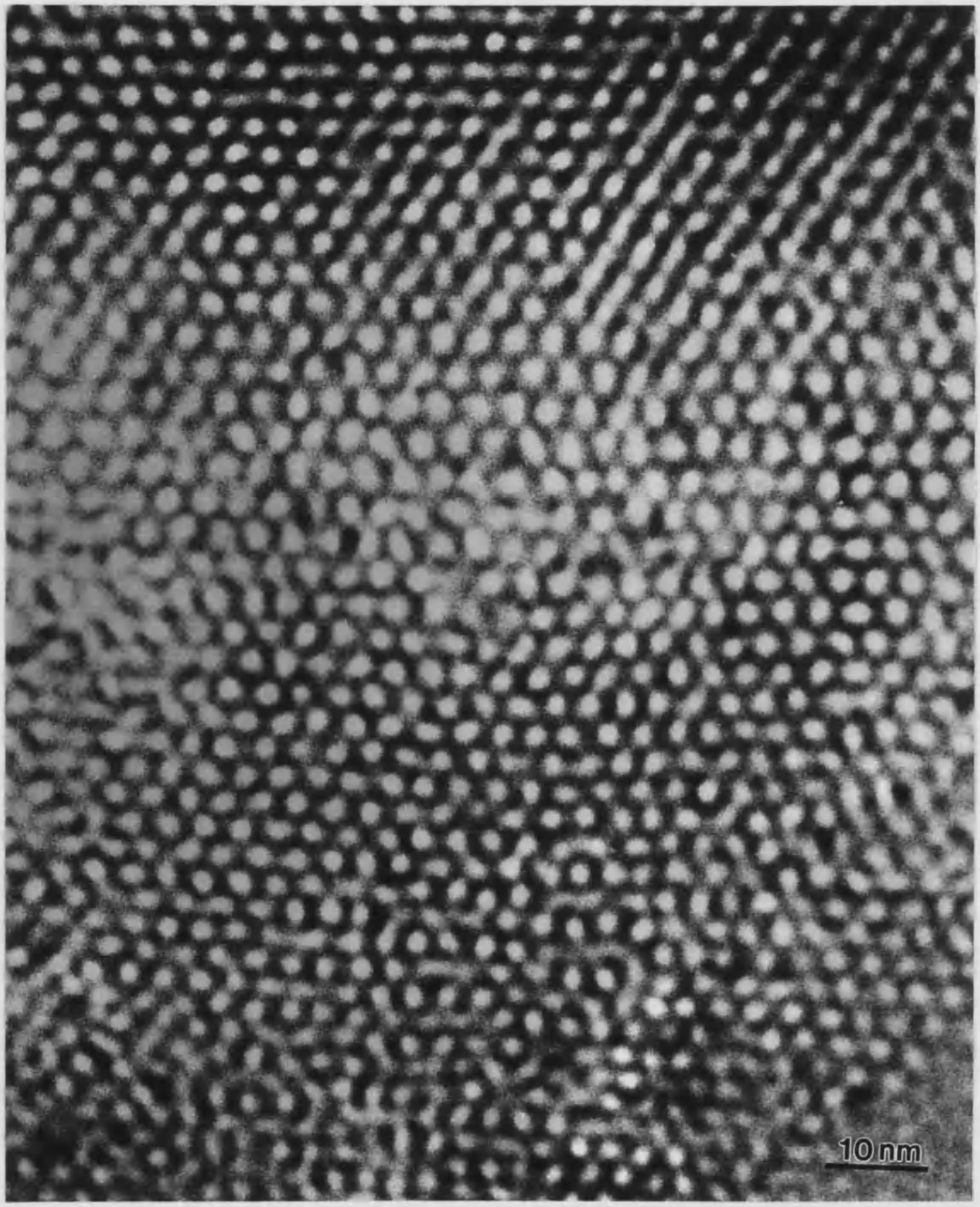

Figure 3.14 *TEM micrograph of as-synthesised sample in the presence of a templating monolayer of PC showing a hexagonal system of lattice fringes.*

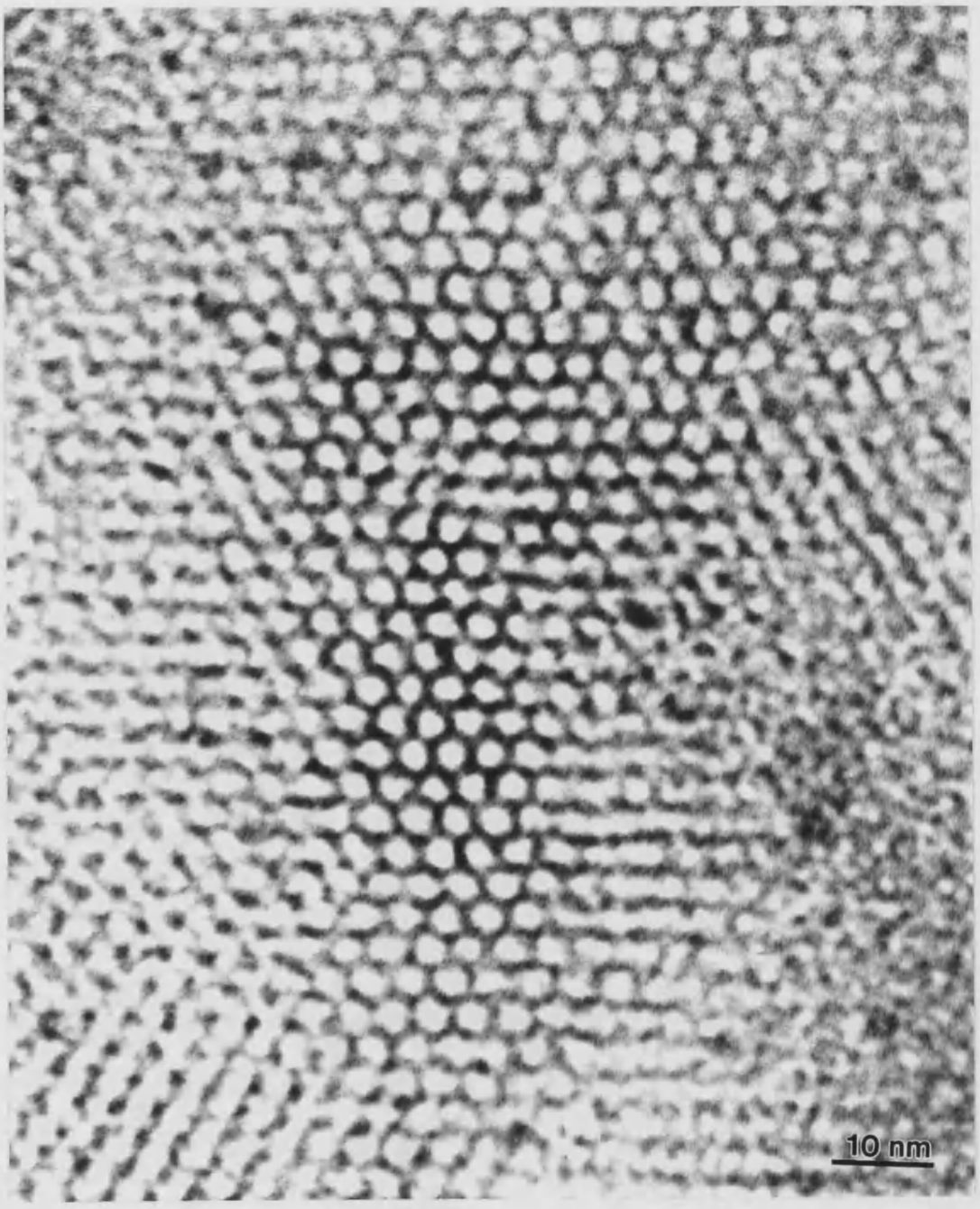

Figure 3.15 *TEM micrograph of as-synthesised sample without the presence of a templating monolayer of PC showing a hexagonal system of lattice fringes.*

Figure 3.16 *TEM micrograph of as-synthesised sample in the presence of a templating monolayer of PC showing a parallel system of lattice fringes.*

Figure 3.17 *TEM micrograph of as-synthesised sample without the presence of a templating monolayer of PC showing a parallel system of lattice fringes.*

Following calcination, TEM micrographs of the materials prepared with and without the presence of a templating monolayer of PC (Figures 3.18 and 3.19, respectively) show that the hexagonal structuring is still apparent in the samples. D-spacings taken from micrographs of both the calcined samples are shown in Table 3.7. This confirms that the hexagonally-ordered silica structure remains stable after removal of the C_{16}TMABr template.

Table 3.7 *d-spacing data for the calcined samples from TEM micrographs.*

	TEM d-spacings and calculated hexagonal unit cell parameter, *a* (Å)				
	(100)	(110)	(200)	(210)	*a*
With PC monolayer	30.0	18.0	15.0	-	34.6
Without PC monolayer	36.0	22.0	18.0	-	41.5

These d-spacings are in good agreement with those obtained from SAXRD analysis (Table 3.5).

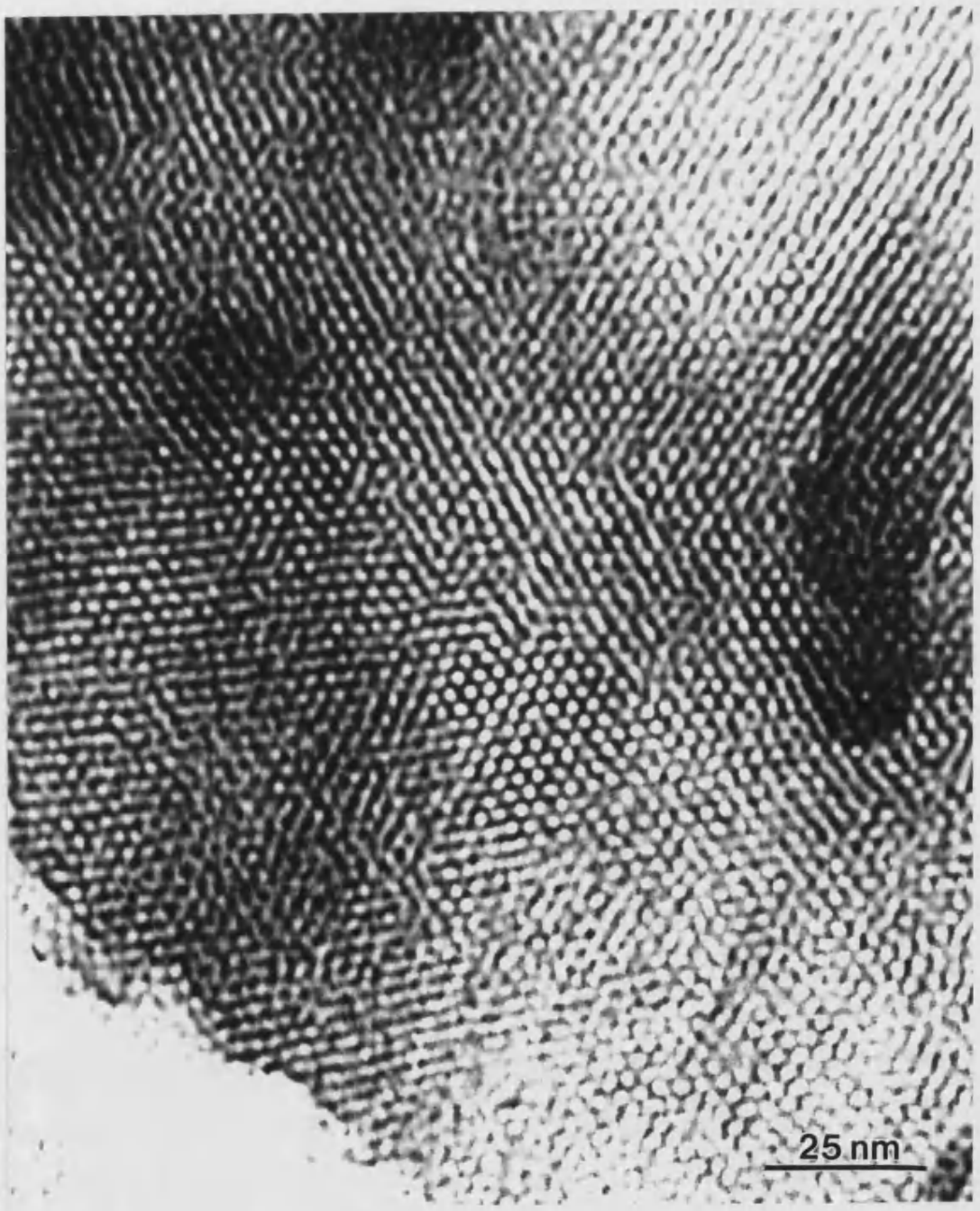

Figure 3.18 *TEM micrograph of the calcined samples with the presence of a templating monolayer of PC showing a hexagonal system of lattice fringes.*

Figure 3.19 *TEM micrograph of the calcined samples without the presence of a templating monolayer of PC showing a hexagonal system of lattice fringes.*

^{13}C Cross-Polarisation (CP) Magic Angle Spinning (MAS) NMR

^{13}C Cross-Polarisation (CP) Magic Angle Spinning (MAS) NMR spectroscopy was utilised to detect the presence of PC within the sample formed in the presence of the PC monolayer. The ^{13}C CP MAS NMR spectra for the as-synthesised samples formed in the presence and without the presence of the templating monolayer of PC (Figure 3.20) contained seven resolvable carbon resonances, shown in Table 3.8. These peaks are consistent with the presence of C_{16}TMABr surfactant, whose ^{13}C solution NMR is shown in Figure 3.21 and are assigned as shown in Figure 3.22. Several of the peaks are not resolved due to overlap. Both spectra are almost identical and no extra peaks which can be attributed to PC are visible in Figure 3.20a.

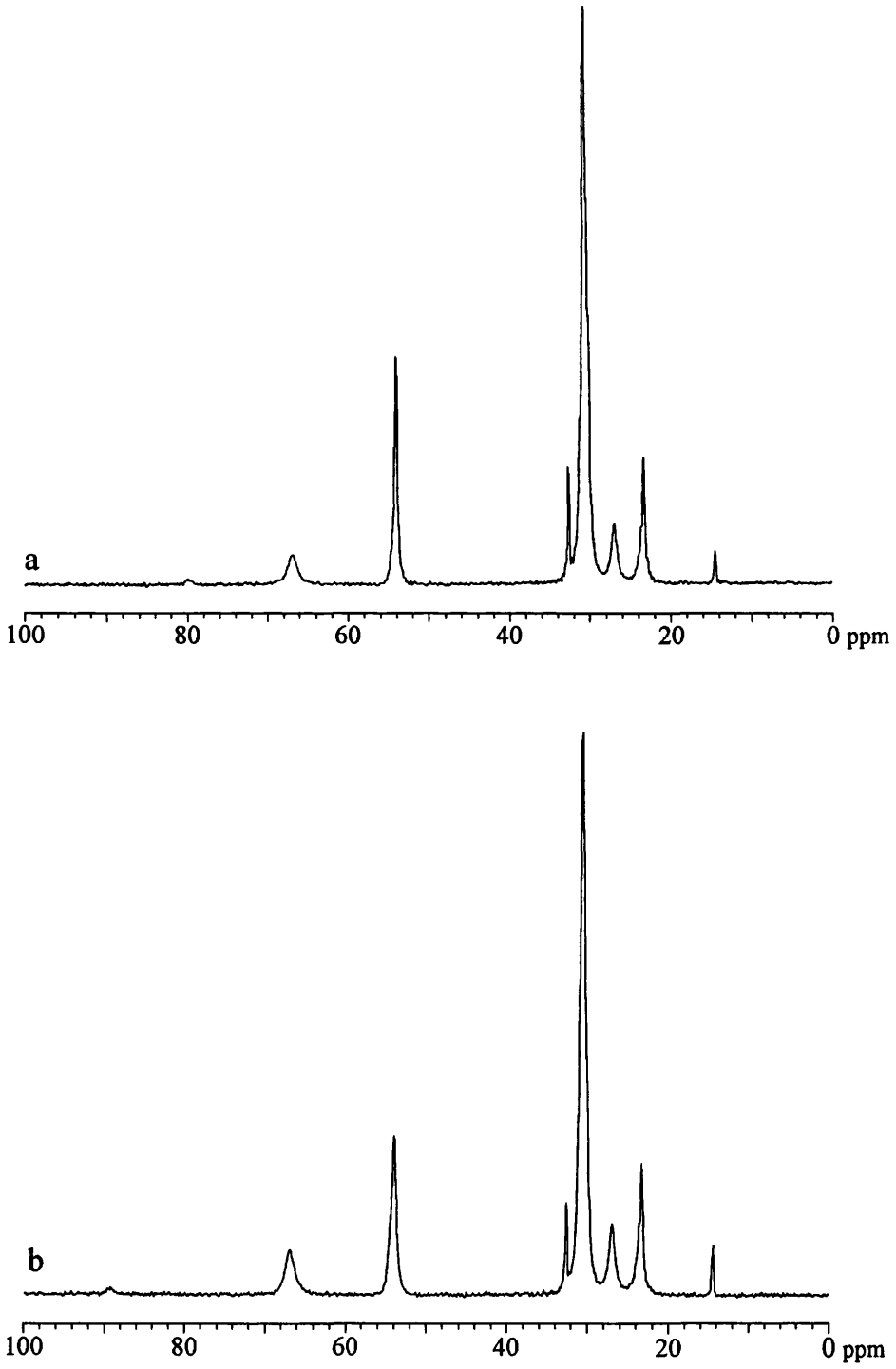

Figure 3.20 *^{13}C CP MAS NMR spectra of the as-synthesised samples a) with and b) without the presence of a templating monolayer of PC.*

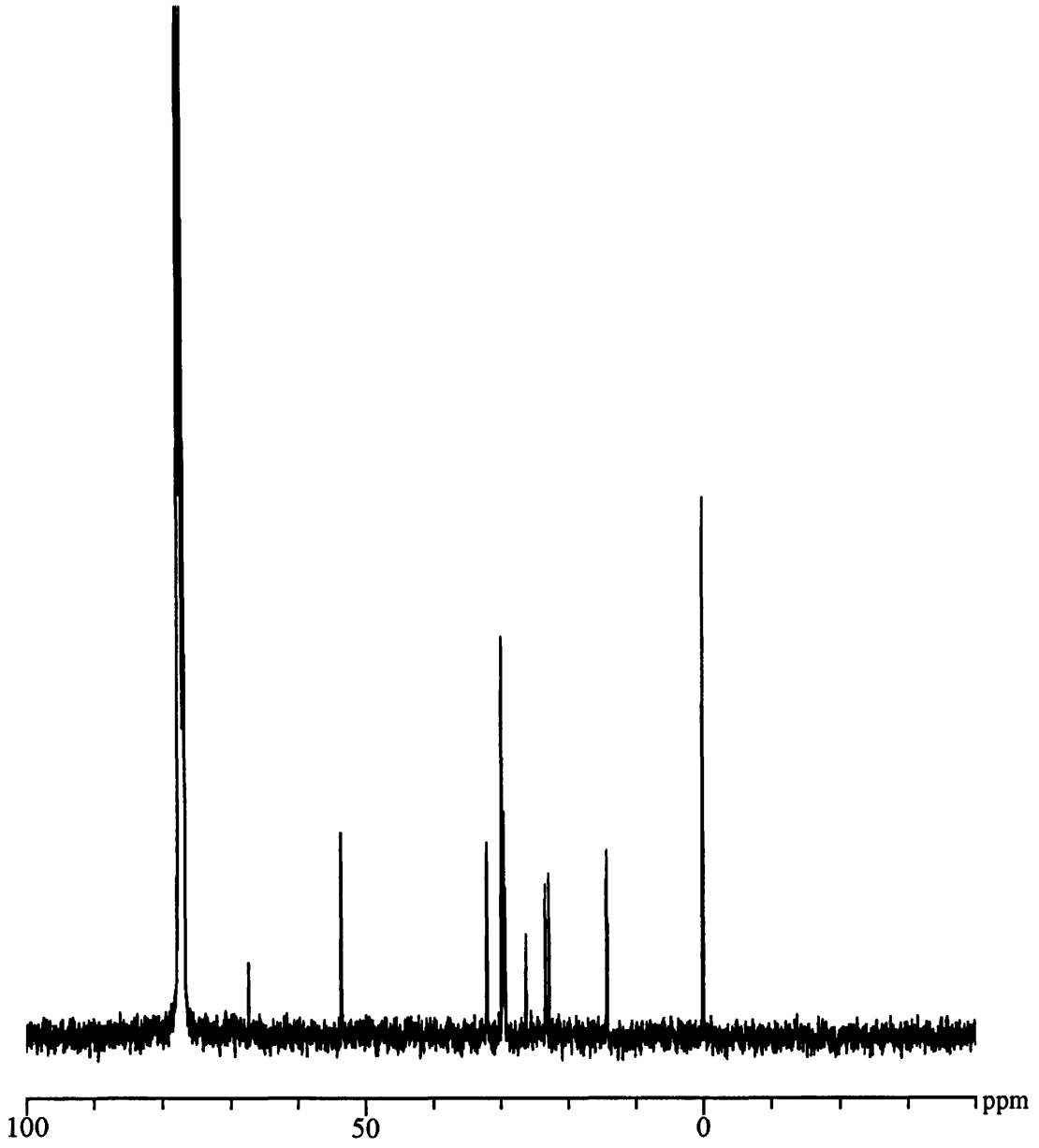

Figure 3.21 *^{13}C solution NMR spectra of $C_{16}TMABr$ in deuterated $CDCl_3$.*

Table 3.8 *^{13}C CP MAS NMR and solution data for as-synthesised samples and C_{16}TMABr.*[10]

Chemical Shift (ppm) relative to TMS [$Si(CH_3)_4$]			
With PC	Without PC	C_{16}TMABr	Assignment
14.46	14.46	14.12	C_{16}TMABr C_1
23.25	23.29	23.19	C_{16}TMABr C_2
26.99	26.98	26.15	C_{16}TMABr $C_{3\text{-}15}$
30.68	30.63	30.54	C_{16}TMABr $C_{3\text{-}15}$
32.62	32.61	32.50	C_{16}TMABr $C_{3\text{-}15}$
54.04	53.98	53.33	C_{16}TMABr C_{17}
66.91	66.90	67.12	C_{16}TMABr C_{16}

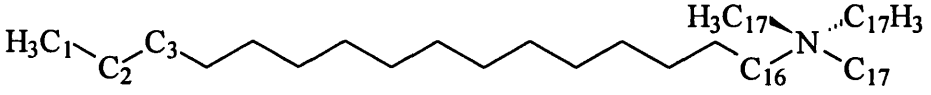

Figure 3.22 *Schematic diagram of C_{16}TMABr with NMR assignments.*

^{29}Si Magic Angle Spinning (MAS) NMR

^{29}Si Magic Angle Spinning (MAS) NMR spectroscopy of the as-synthesised samples with or without the presence of the templating monolayer of PC (Figure 3.23 and Table 3.9), indicated quantitatively the extent of organosiloxane incorporation into the silica samples. Resonances were observed for siloxane Q^2, Q^3 and Q^4 units where $Q^q = Si(OSi)_q(OH)_{4-q}$. The calculated peak area ratios of Q^2:Q^3:Q^4 are consistent with the presence of a highly condensed silica phase, with the great majority of silicon centres bonded to either 3 or 4 other silicon centres *via* oxygen bridges.

If organically functionalised organosiloxanes such as phenyltriethoxysilane and *n*-octyltriethoxysilane are used instead of TEOS in the reaction mixture then extra

resonances would be seen, corresponding to organosiloxane T^1, T^2 and T^3 units, where $T^t = RSi(OSi)_t(OH)_{3-t}$.[36] The relative amounts of $(Q^2 + T^1)$, $(Q^3 + T^2)$ and $(Q^4 + T^3)$ are equivalent to the respective $Q^2:Q^3:Q^4$ ratio in a sample prepared with 100 mol% TEOS (as in the case of the as-synthesised sample prepared without a templating monolayer of PC in this study). The T^t resonances are mentioned here in order to provide a detailed guide for all the possible structural information that may be obtained from utilising ^{29}Si MAS NMR spectroscopy. It should be noted that in the course of this study no organosiloxanes were used. The Q^q and T^t resonances are shown in Figure 3.24.

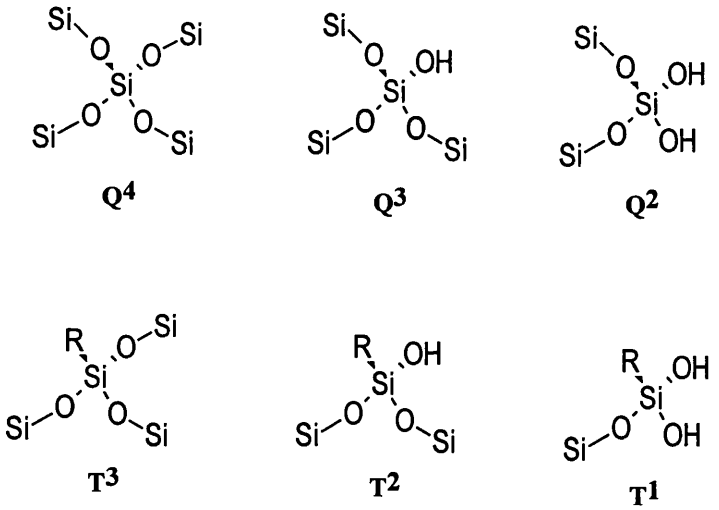

Figure 3.24 *The Q^q and T^t silicon centres that can be observed by ^{29}Si MAS NMR.*

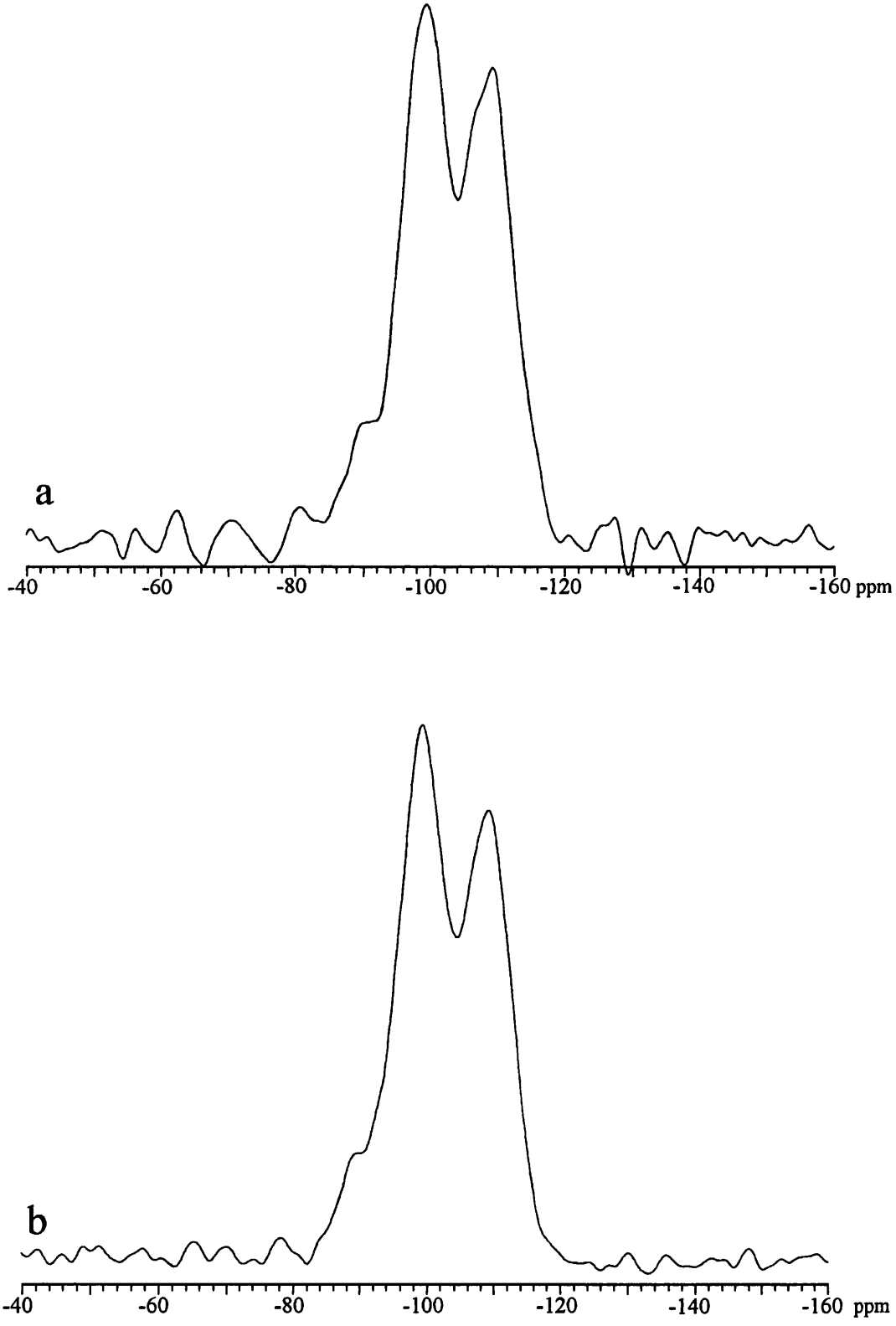

Figure 3.23 *^{29}Si MAS NMR spectra of the as-synthesised samples a) with and b) without the presence of a templating monolayer of PC.*

Table 3.9 *^{29}Si MAS NMR data for as-synthesised materials.*

	Chemical shift (ppm) relative to TMS $[Si(CH_3)_4]$ [Relative peak area]		
	Q^2	Q^3	Q^4
With PC monolayer	-89.7	-99.6	-109.4
	[6.5]	[52.5]	[41.0]
Without PC monolayer	-91.3	-99.3	-108.9
	[12.3]	[41.9]	[45.8]

Infra-red Spectroscopy (IR)

Infra-red spectroscopy of the as-synthesised and subsequent calcined materials formed with and without the presence of the PC templating monolayer indicated qualitatively the amount of organosiloxane incorporated within the silica framework, which is related to the initial composition of the synthesis mixture.[10] The spectra of the as-synthesised materials (Figure 3.25) indicated the presence of an amorphous silica phase. Characteristic range of vibrations were observed at 1300 - 400 cm^{-1}, corresponding to ν(Si-O) and associated ν(Si-O-Si) framework vibrations as reported by Chen *et al.*[6] Distinctive bands were also observed at 2950 - 2850 cm^{-1} and 1460 - 1490 cm^{-1}, which were attributed to the presence of the C_{16}TMABr surfactant.

After calcination, analysis of the material formed with and without the presence of the templating monolayer of PC showed all the peaks attributed to the presence of an amorphous silica phase (Figure 3.26). However the peaks attributed to C_{16}TMABr surfactant were observed only at trace levels on the baseline.

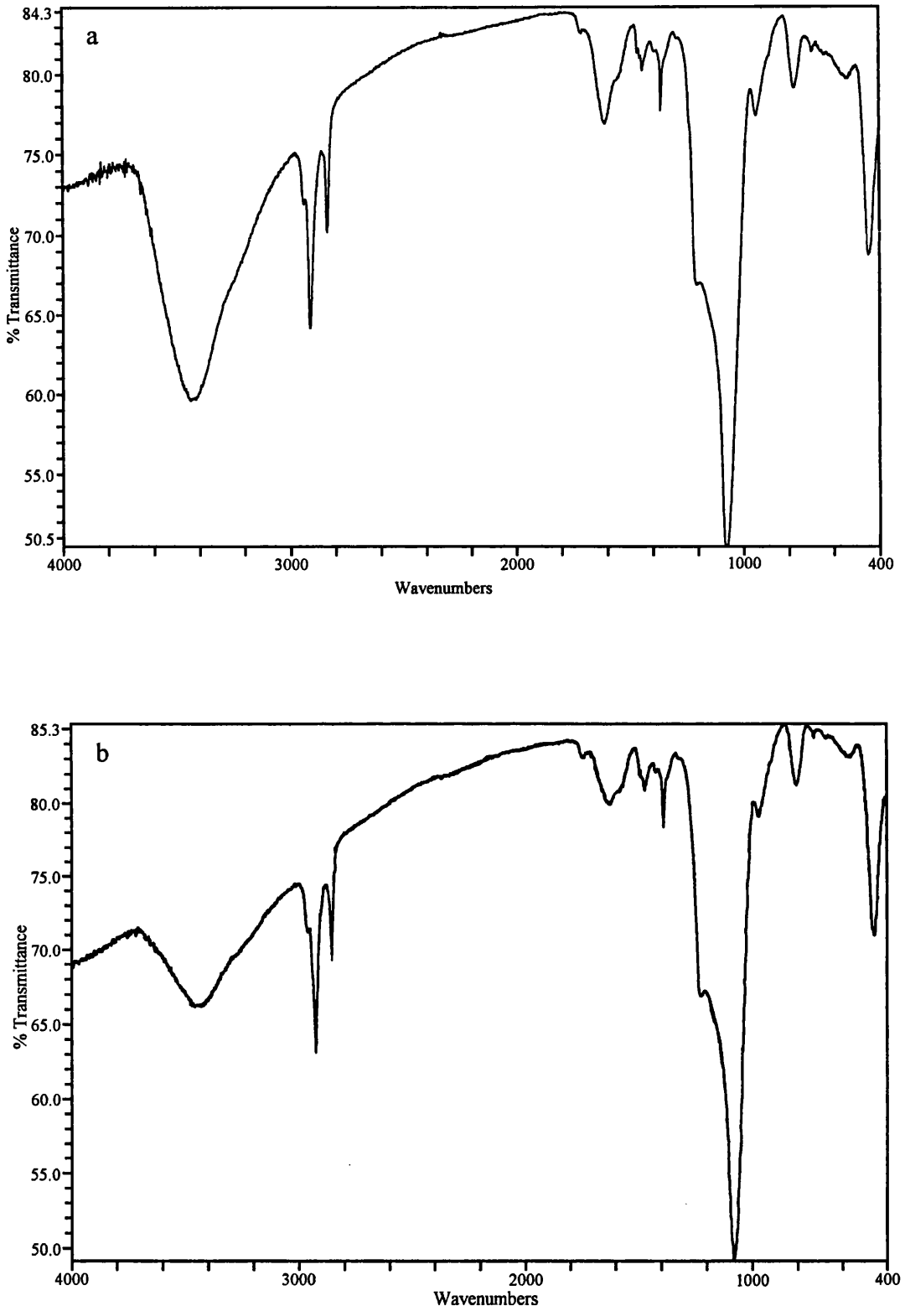

Figure 3.25 *Infra-red spectra for the as-synthesised material formed a) with and b) without the presence of a templating monolayer of PC.*

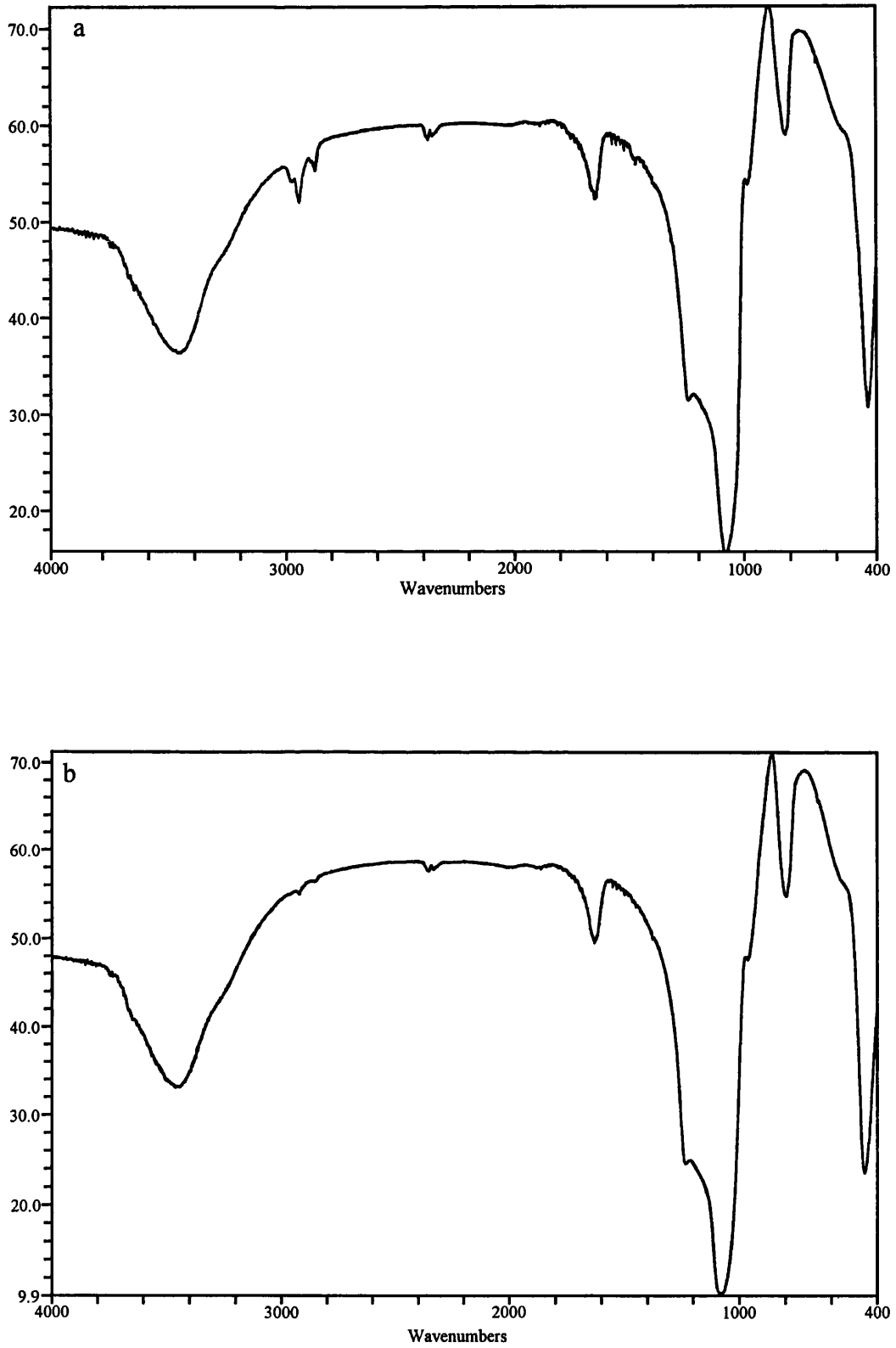

Figure 3.26 *Infra-red spectra for the calcined material formed a) with and b) without the presence of a templating monolayer of PC.*

CHN Microanalysis

Results from CHN microanalysis (Table 3.10) enabled a determination of the organic content for both the as-synthesised and both the calcined samples. Both the as-synthesised samples showed a consistently high organic carbon content, which is attributed to the presence of C_{16}TMABr templating surfactant. Analysis of both the calcined samples indicated that the organic carbon content was approximately 0.35 wt%, due to remaining traces of C_{16}TMABr templating surfactant.

Table 3.10 *CHN microanalysis for as-synthesised and calcined samples with and without the presence of a templating monolayer of PC.*

Samples	C (wt %)	H (wt %)	N (wt %)
As-synthesised			
With PC monolayer	37.5	7.84	2.18
Without PC monolayer	31.8	6.96	1.91
Calcined			
With PC monolayer	0.02	0.62	-
Without PC monolayer	0.05	0.77	-

Thermogravimetric Analysis

Thermogravimetric analysis (TGA) of the as-synthesised samples prepared with and without the presence of a PC templating monolayer (Figure 3.27) gave results in good agreement with those obtained from CHN microanalysis (Table 3.11).

Table 3.11 *Calculated weight loss from TGA of as-synthesised materials.*

Sample	Weight Loss (wt%)
With PC monolayer	56.23
Without PC monolayer	47.16

The calculated weight losses showed an weight loss of 50 %weight, following the heat treatment to 800 °C. The as-synthesised sample prepared in the presence of a templating PC monolayer showed a higher weight loss than the sample prepared without PC. This difference can be attributed to the presence of PC which will have an influence on the final weight loss value. Total weight losses can be attributed to the loss of water from continued condensation of Si-OH groups with in the silica framework, in addition to the combustion of the C_{16}TMABr surfactant.

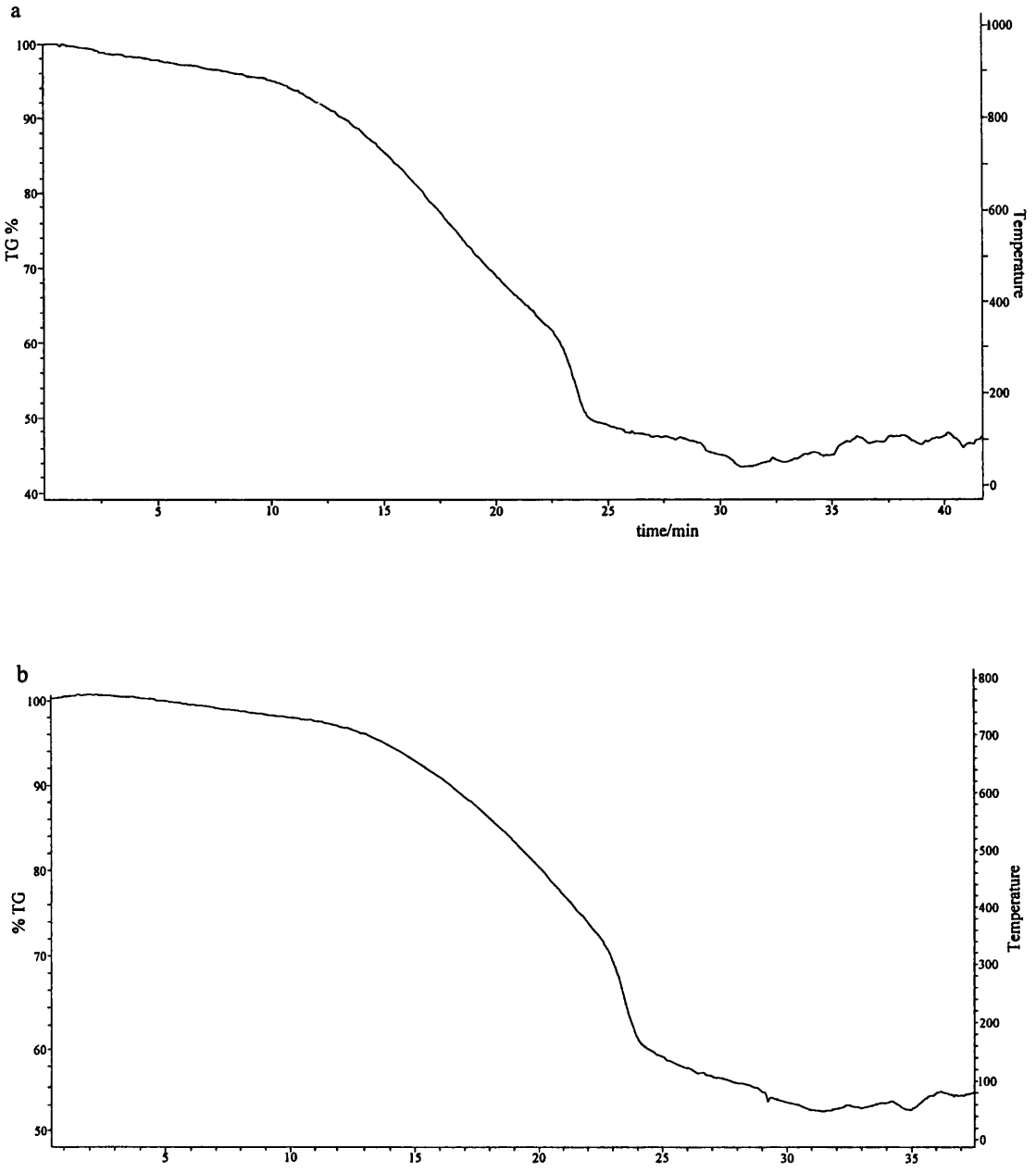

Figure 3.27 *TGA traces for the as-synthesised material formed a) with and b) without the presence of a templating monolayer of PC.*

Selected Area Electron Diffraction

Selected area electron diffraction (SAED) patterns were obtained for the as-synthesised materials formed with and without the presence of a templating PC monolayer (Figures 3.28a and b, respectively). The patterns show a hexagonal arrangement of six dots centred around a central dot, indicating ordering in three planes of direction. These patterns are similar with those obtained by Kresge *et al.*,[1] Huo *et al.*,[37] and Vartuli *et al.*,[38] confirming the presence of an MCM-41 silica film. Each of the six dots has another two or more 'sister' dots either side of them indicating that the sampled area has domains where there is slight orientation in the hexagonal structure. It is evident that the quality of Figure 3.28b is not as good as Figure 3.28a. This is due to structural irregularities within the sampled area.

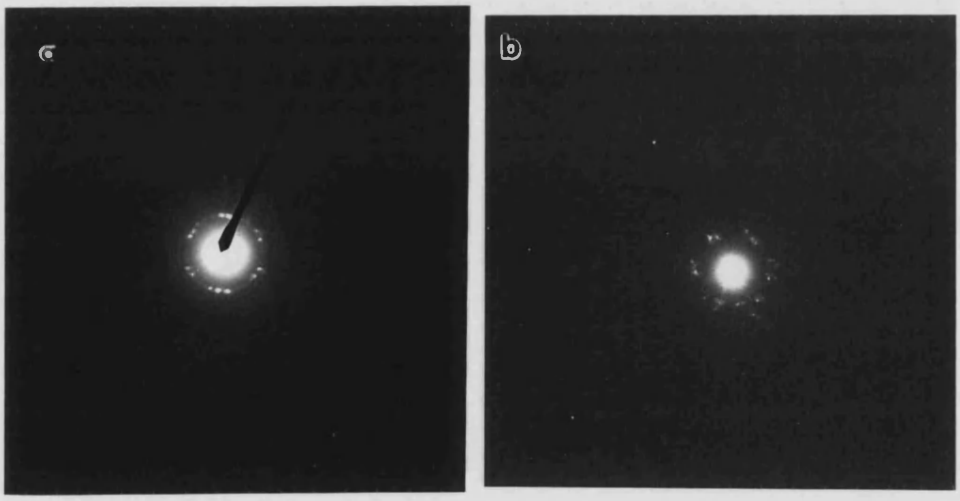

Figure 3.28 *SAED patterns for as-synthesised material formed a) with and b) without the presence of a templating monolayer of PC.*

From these SAED patterns, an interplanar d_{100} spacing of 40 and 41 Å was observed for the as-synthesised material formed with and without the presence of a templating monolayer of PC, respectively. These results are consistent with SAXRD data obtained for the as-synthesised materials.

A SAED pattern showing only two dots, one either side of the central dot was obtained as shown in Figure 3.29 for the as-synthesised material formed in the presence of a templating monolayer of PC. An interplanar spacing of 36 Å was observed. The presence of only two dots indicates ordering in one plane of direction and is attributed to viewing the MCM-41 rods side-on as shown in Figures 3.16 and 3.17.[37]

Figure 3.29 *SAED pattern of MCM-41 rods viewed side-on showing two dots.*

3.4 Conclusions

The results in this chapter show that the condensation of siloxanes in the presence of a surfactant template, such as hexadecyl-trimethylammonium bromide (C_{16}TMABr), is a viable route for the formation of mesostructured, hexagonally-ordered, MCM-41 silica film at the air/water interface, within a sealed glass container. Even though the growth of MCM-41 films at the air/water interface has already been reported by Yang *et al.*,[21] the reaction conditions we used varied from those used previously. The two main differences were that the films formed in this study were grown at room temperature, whilst Yang *et al.*[21] grew theirs at 80 °C and we used base catalysed reaction, as opposed to an acid catalysed reaction used by Yang *et al.*[21] In order to modify the reaction conditions still further, we utilised a insoluble lipid monolayer at the interface to act as a preformed site to induce nucleation. The lipid chosen in this study was phosphatidylcholine because it was readily available, produced a stable monolayer at the interface, and most importantly the charged groups would lie at the interface whilst the long carbon chains would be repelled by the water. The charged groups at the interface would promote a PC-C_{16}TMABr complex being formed, therefore we would have a greater concentration of C_{16}TMABr present at the interface than in the bulk solution without the PC monolayer. From the results shown, the film with the PC monolayer present became visible to the naked eye quicker than the film without, suggesting that the monolayer has served it purpose it that it allows a faster nucleation rate for the MCM-41 silica film.

SAXRD and TEM microscopy of both films show that they are hexagonally ordered with a higher degree of ordering for the film formed in the presence of the PC monolayer. After calcination, the hexagonal structure is retained, and a contraction in

the unit cell is observed as expected. ^{13}C CP MAS NMR spectroscopy showed the presence of the surfactant C_{16}TMABr in both films. ^{29}Si MAS NMR showed the extent of organosiloxane incorporation with the films, and that each silicon is bonded to two or more other silicon atoms, producing an Si-O-Si random network throughout the films. Infrared spectroscopy showed the characteristic Si-O and Si-O-Si framework vibrations reported by Chen *et al.*[6] for MCM-41 materials. Elemental microanalysis showed that after calcination the C_{16}TMABr template is burnt out, and only present in trace amounts. TGA showed a greater % weight loss for the film formed in the presence of a monolayer of PC due to the fact that the PC is also combusted. Of particular interest is the SAED patterns obtained for the as-synthesised films which show the characteristic six dots associated with the hexagonal MCM-41 structure. The presence of the 'sister' dots shows that there are domains where the hexagonal structure is slightly orientated from the majority of the sampled area, nevertheless by obtaining SAED patterns of the films it shows that they are stable and orientated to a high degree.

In summary, we have been able to produce an MCM-41 silica film at the air/water interface. The speed at which this film grows can be increased if an insoluble monolayer is present on the surface. The PC lipid used in this study is more than adequate for the faster formation of the MCM-41 silica film. The production of orientated silica films gives opportunities for tailoring their structure, varying the pore sizes and compositions and chemically modifying their surface reactivity with the incorporation of appropriate guest molecules such as organometallic compounds.[10] Ultimately these films may find uses as organised catalysts, sensors for large molecules, mesostructured semiconductors, and ordered ceramic matrix composites.[21]

3.5 References

1. Kresge, C.T., Leonowicz, M.E., Roth, W.J., Vartuli, J.C., and Beck, J.S. (1992). Ordered mesoporous molecular sieves synthesised by a liquid-crystal template mechanism, *Nature*, **359 (6397)**, 710-712.

2. Beck, J.S., Vartuli, J.C., Roth, W.J., Leonwicz, M.E., Kresge, C.T., Schmitt, K.D., Chu, C.T., Olsen, D.H., Sheppard, E.W., McCullen, S.B., Higgins, J.B., and Schlenker, J.L. (1992). A new family of mesoporous molecular sieves prepared with liquid-crystal templates, *Journal of the American Chemical Society*, **114 (27)**, 10834-10843.

3. Beck, J.S. (1991). Method for synthesising mesoporous crystalline material, U.S. Patent number 5 057 296.

4. Davis, M.E., and Burkett, S.L. (1995). Towards the rational design and synthesis of microporous and mesoporous silica-containing materials, *Zeoraito*, **12 (2)**, 33-47.

5. Vartuli, J.C., Schmitt, K.D., Kresge, C.T., Roth, W.J., Leonwicz, M.E., McCullen, S.B., Hellring, S.D., Beck, J.S., Schlenker, J.L., Olsen, D.H., and Sheppard, E.W. (1994). Effect of surfactant/silica molar ratios on the formation of mesoporous molecular sieves - Inorganic mimicry of surfactant liquid-crystal phases and mechanistic implications, *Chemistry of Materials*, **6 (12)**, 2317-2326.

6. Chen, C.-Y., Li, H.-X., and Davis, M.E. (1993). Studies on mesoporous materials I. Synthesis and characterisation of MCM-41, *Microporous Materials*, **2**, 17-26.

7. Chen, C.-Y., Li, H.-X., Burkett, S.L., and Davis, M.E. (1993). Studies on mesoporous materials II. Synthesis mechanism of MCM-41, *Microporous Materials*, **2**, 27-34.

8. Edler, K.J., Dougherty, J., Durand, R., Iton, L., Kirton, G., Lockhart, G., Wang, Z., Withers, R., and White, J.W. (1995). Small angle x-ray scattering from MCM-41 and its synthesis gels - Optimisation of the synthesis parameters, *Colloidal Surfactants*, **A102**, 213-230.

9. Monnier, A., Schuth, F., Huo, Q., Kumar, D., Margolese, D., Maxwell, R.S., Stuky, G.D., Krishnamurty, M., Petroff, P., Firouzi, A., Janicks, M., and Chemelka, B.F. (1993). Co-operative formation of inorganic-organic interfaces in the synthesis of silicate mesostructures, *Science*, **261 (5126)**, 1299-1303.

10. Sims, S.D. (1997). Template directed synthesis of hybrid silica materials, PhD thesis, University of Bath.

11. Fantell, K. (1990). *Colloidal Polymer Science*, **268**, 264.

12. Huo, Q.S., Marglose, D.I., Ciesla, U., Demuth, D.G., Feng, P.Y., Gier, T.E., Sieger, P., Firouzi, A., Chmelka, B.F., Schüth, F., and Stucky, G.D. (1994). Organisation of organic molecules with inorganic molecular species into nanocomposite biphase arrays, *Chemistry of Materials*, **6 (8)**, 1176-1191.

13. Ogawa, M. (1996). A simple sol-gel route for the preparation of silica surfactant mesostructured materials, *Journal of the Chemical Society, Chemical Communications*, **10**, 1149-1150.

14. Tanev, P.T., Chibwe, M., and Pinnavia, T.J. (1994). Titanium-containing mesoporous molecular sieves for catalytic oxidation of aromatic compounds, *Nature*, **368 (6469)**, 321-323.

15. Stein, A., Fendorf, M., Jarvie, T.P., Mueller, K.T., Benesi, A.J., and Mallouk, T.E. (1995). Salt-gel synthesis of porous transition metal oxides, *Chemistry of Materials*, **7 (2)**, 304-313.

16. Beck, J.S., and Vartuli, J.C. (1996). Recent advances in the synthesis, characterisation, and applications of mesoporous molecular sieves, *Current Opinion in Solid State and Materials Science*, **1**, 76-87.

17. Huo, Q., Margolse, D.I., and Stucky, G.D. (1996). Surfactant control of phases in the synthesis of mesoporous silica-based materials, *Chemistry of Materials*, **8 (5)**, 1147-1160.

18. Ramsey, J.D.F. (1996). Ceramics from templated gels, *Current Opinion in Colloid and Interface Science*, **1**, 208-213.

19. Göltner, C.G., and Antonietti, M. (1997). Mesoporous materials by Templating of liquid crystalline phases, *Advanced Materials*, **9 (5)**, 431-436.

20. Yang, H., Kuperman, A., Coombs, N., Mamiche-Afara, S., and Ozin, G.A. (1996). Synthesis of orientated films of mesoporous silica on mica, *Nature*, **379 (6567)**, 703-705.

21. Yang, H., Coombs, N., Sokolov, I., and Ozin, G.A. (1996). Free-standing and orientated mesoporous silica films grown at the air/water interface, *Nature*, **381 (6583)**, 589-592.

22. Collings, P.J. (1990). **In**: *Liquid crystals - Natures delicate phase of matter.* Bristol: Hiliger UK.

23. Davis, M.E., Chen, C.Y., Burkett, S.L., and LoBo, R.F. (1994). Synthesis of aluminosilicate materials using organic molecules and self-assembled organic aggregates as structure-directing agents, *Material Research Society, Symposium Proceedings*, **346**, 831-841.

24. Burkett, S.L., and Davis, M.E. (1996). Synthetic mechanism and strategies for zeolite synthesis. **In**: *Comprehensive Supramolecular Chemistry, volume* 7, Oxford: Pergamon Press UK.

25. Bocker, J., Schlenkrich M., Bopp, P., and Brickmann, J. (1992). Molecular dynamics simulation of a n-hexadecyltrimethylammonium chloride monolayer, *Journal of Physical Chemistry*, **96 (24)**, 9915-9922.

26. Lu, J.R., Li, Z.X., Smallwood, J., Thomas, R.K., and Penfold, J. (1995). Detailed structure of the hydrocarbon chain in a surfactant monolayer at the air/water interface - Neutron reflection form hexadecyltrimethylammonium bromide, *Journal of Physical Chemistry*, **99 (20)**, 8233-8243.

27. Braun, C., Lang, P., and Findnegg, G.H. (1995). Surface induced shift of the hexagonal to isotropic phase transition in the lyotropic system studied by x-ray reflectivity, *Langmuir*, **11 (3)**, 764-766.

28. Branton, P.J., Hall, P.G., Sing, K.S.W., Reichert, H., Schüth, F., and Unger, K.K. (1994). Physisorption of argon, nitrogen, and oxygen by MCM-41 - A model mesoporous adsorbent, *Journal of the Chemical Society, Faraday Transaction*, **90 (19)**, 2965-2967.

29. Armengol, E., Cano, M.L., Corma, A., Garcia, H., and Navarro, M.T. (1995). Mesoporous aluminosilicate MCM-41 as a convenient acid catalyst for friedel-crafts alkylation of a bulky aromatic compound with cinnamyl alcohol, *Journal of the Chemical Society, Chemical Communications*, **5**, 519-520.

30. Corma, A., Martinez, A., Martinez-Soria, V., and Monton, J.B. (1995). Hydrocracking of vacuum gasoil on the novel mesoporous MCM-41 aluminosilicate catalyst, *Journal of Catalysts*, **153 (1)**, 25-31.

31. Corma, A., Fornés, V., Garcia, H., Miranda, M.A., and Sabater, M.J. (1994). Highly efficient photo-induced electron transfer with 2,4,6-triphenylpyrylium cation incorporated inside extra large pore zeotype MCM-41, *Journal of the American Chemical Society*, **116 (21)**, 9767-9768.

32. Huber, C., Moller, K., and Bein, T. (1994). Reactivity of a trimethylstannyl molybdenum complex in mesoporous MCM-41, *Journal of the Chemical Society, Chemical Communications*, **22**, 2619-2620.

33. Llewellyn, P.L., Ciesla, U., Decler, H., Studier, R., Schüth, R., Schüth, F., and Unger, K. (1995). **In:** *Zeolites and related microporous materials.*

34. Smart, L., and Moore, E. (1995). **In**: *Solid state chemistry*. London: Chapman and Hall.

35. Chenite, A., Le Page, Y., and Sayari, A. (1995). Direct TEM imaging of tubules in calcined MCM-41 mesoporous materials, *Chemistry of Materials*, **7 (5)**, 1015-1019.

36. Lindner, E., Kemmler, M., Meyer, H.A., and Wegner, P. (1994). Polysiloxane-bound ether-phosphines and ruthenium complexes - A characterisation by solid-state NMR spectroscopy and catalysis, *Journal of the American Chemical Society*, **116 (1)**, 348-361.

37. Huo, Q., Leon, R., Petroff, P.M., and Stucky, G.D. (1995). Mesostructure design with gemini surfactants: Supercage formation in the three-dimensional hexagonal array, *Science*, **268 (5215)**, 1324-1327.

38. Vartuli, J.C., Kresge, C.T., Leonowicz, M.E., Chu, A.S., McCullen, S.B., Johnson, I.D., and Sheppard, E.W. (1994). Synthesis of mesoporous materials: Liquid-crystal templating versus intercalation of layered silicates, *Chemistry of Materials*, **6 (11)**, 2070-2077.

CHAPTER FOUR

X-RAY REFLECTANCE OF A MESOSTRUCTURED MCM-41 FILM AT THE AIR/WATER INTERFACE

4.1 Introduction

One of the most promising routes to new silica-based mesostructured materials with pore diameters greater than those of conventional materials such as zeolites involves the co-operative assembly of inorganic precursors with supramolecular organic templates.[1-7] The resulting silica-surfactant liquid crystalline mesophases can have a range of symmetries, including hexagonal (MCM-41) or cubic (MCM-48), and can be processed to produce mesoporous replicas consisting of an ordered array of channels with 1 nm thick silica walls. Several studies have recently shown that thin films of MCM-41 materials can be formed at the air/water,[8] mica/water,[9] or graphite/water interface,[10] as well as on gold substrates which have been chemically patterned.[11] In this chapter, having grown MCM-41 films at the air/water interface (described in the previous chapter), we use X-ray reflectivity to probe the nucleation and growth of MCM-41 at the air/water interface. We use this technique to investigate the effect of changes in the nature of the interface by studying the formation of MCM-41 under an insoluble lipid monolayer.

The relatively new technique of specular x-ray reflection is a powerful tool for studying surfaces and interfaces. Like neutron reflection, it is an non-destructive, *in-situ* method, yielding structural information perpendicular to the surface, to give density, thickness and roughness of an interface. The real power of this method is its

potential ability to examine a "buried" interface. That is an interface which is buried beneath another relatively thick interface so that the beam of x-rays has to penetrate the first layer in order to reach the interface. As a result its applications are varied and range from studies of film growth and morphology to molecular ordering at solid/liquid and free fluid interfaces.[12,13]

The high resolution of this technique makes it very attractive for surface analysis, since x-rays are very short wavelength beams of radiation, the wavelengths being comparable to the distance between molecules and between nuclei. Reflection of these beams from surfaces therefore gives spatial resolution as low as 1 nm (the wavelength of the beam).

The penetration of the surface of the sample is dependent upon the angle of incidence of the beam onto the surface, a higher angle penetrating the surface more deeply. It is possible to penetrate the surface and hence to study the structure of the surface for hundreds of nanometres.

The theory behind the technique of specular x-ray reflection is described in Appendix Two. As mentioned previously, x-ray reflection is similar to that of neutron reflection, with the main difference being that neutrons interact with the nuclei of the atoms or molecules, whereas x-rays interact with the electron cloud of molecules. This imposes a problem that is inherent to the use of x-ray reflection. Namely that x-ray reflection is limited by the inability of atoms of low atomic number and hence low electron density to scatter electrons strongly. With neutrons, the strength of scattering interaction, the scattering length is independent of the atomic number, giving random values across the periodic table of elements. Hence x-rays are more suited to the

study of samples containing heavy atoms, but neutrons can be more universally applied.

With neutrons, the values of scattering length are also different for isotopes of the same element due to varying neutron - nuclear interactions. This gives neutron reflection another advantage over x-ray reflection for the study of buried interfaces such as the liquid/liquid interface. The hydrogen:deuterium ratio of the upper layer can be adjusted so that the scattering density difference between the air and upper layer is reduced close to zero, whilst keeping the chemical structure of the upper layer the same. This means that the air/upper layer interface will no longer cause significant reflections and so the neutron beam will only "see" the upper layer/lower layer interface. This method is called contrast variation and will not work for x-rays, where the scattering from hydrogen and deuterium is small and almost exactly the same hence the reflectivity profile will be dominated by the big step in electron density from air to liquid.

Other advantages of neutron reflection are that neutrons interact weakly with matter. This means that they will be only weakly scattered in going through a container housing the sample under study. Hence the sample may be held in an furnace or low temperature cryostat chamber without affecting reflection. X-rays on the other hand are strongly scattered and so the choice of container is important and sometimes restricting.

Despite these problems with x-rays, they do have some advantages over neutrons for reflection at surfaces and interfaces. The most obvious is the large expense of conducting neutron experiments. Neutrons cannot be used in the

laboratory unlike x-rays, so if the experiments can be carried out with either x-rays or neutrons, x-rays would be the first choice.

X-ray reflection also has a much higher signal to noise ratio than neutron reflection and hence x-rays have an intrinsically higher resolution. This means that where high values of **Q** are required, *i.e*, Langmuir-Blodgett layers where there is a high degree of two dimensional order, x-ray reflection would be preferred over neutron reflection because of the high background scattering with neutrons. X-ray beams may also be produced with a much shorter wavelength than neutrons and hence are able to penetrate more deeply into a liquid phase due to their higher energy x-rays, which should be more useful in the study of buried interfaces.

Problems associated with x-ray and neutron reflection, include ambiguities in the analysis of the reflectivity profiles produces. This is due to the fact that a model must be fitted to the data and so a prior knowledge of the structure is useful if accurate, non-ambiguous information is to be elucidated. Although this technique provides out of plane structural information of surfaces and interfaces, it does not provide direct real-space images of surface structure. Therefore in reality a combination of reflection and spectroscopic techniques, such as microscopy, is often used to deduce information in and out of plane.

4.2 Experimental

X-ray reflectance was used to characterise the structural and kinetic parameters of the initial growth of silica at the air/water interface in the presence of the soluble surfactant hexadecyl trimethylammonium bromide, both with and without a compressed monolayer of phosphatidylcholine. Experiments and some initial data manipulation were carried out with Dr. Micheal Lovall. Later on Miss Jane Muir (final year BSc student) carried on with the data manipulation as part of her final year project. The graphs were produced by Dr. Steven J. Roser, University of Bath.

4.2.1 Instrumentation

X-Ray Reflectometer

The X-ray reflectometer (Figure 4.1) consists of an x-ray source and an x-ray detector. These are placed at opposite ends of two arms, which are each 700 mm in length, down which the x-rays are projected.[14] These arms are pivoted at a central point where the sample is to be placed and its height in the x-ray beam can be altered by a remote control. The arms enable the x-ray source and detector to be moved simultaneously or independently in a vertical plane, thus allowing the surface of the sample to remain level during the experiment. The height of the arms can be measured to the nearest micron (1×10^{-6} m) and can be altered *via* a stepper motor connected to the computer. When the arms are aligned with each other and with respect to the sample, their heights are set to zero to give a reference point.

The x-ray beam is focused by four horizontal slits placed at intervals along the reflectometer arms, two between the source and sample and the other two between the sample and detector. It is possible to alter the position of these slits along the arms.

The slits can be opened or closed to alter the intensity of the x-ray beam and the size of the x-ray footprint reaching the sample or detector. Each slit is made of tantalum (which absorbs x-ray radiation) mounted on aluminium.

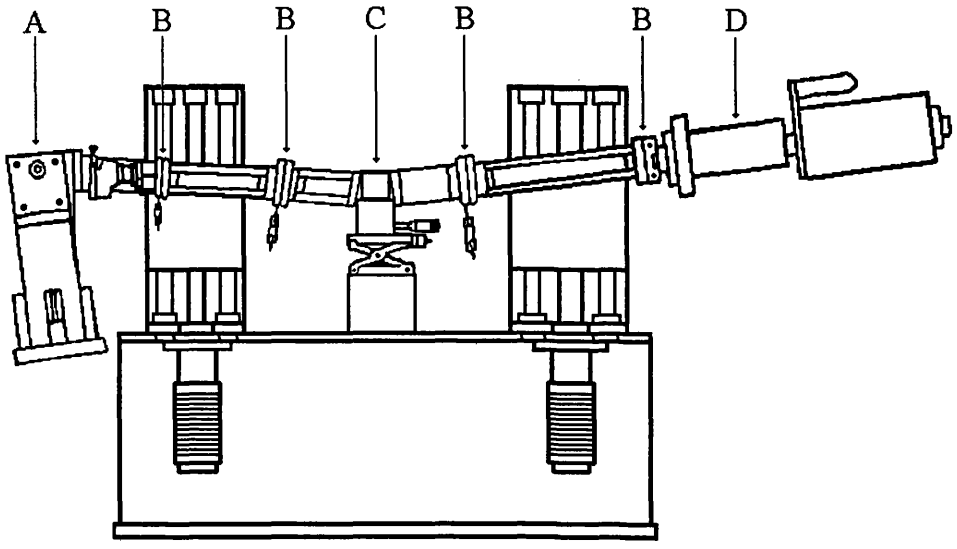

A X-Ray Source **C** Sample Position

B Focusing Slits **D** Detector

Figure 4.1 *Schematic plan of the x-ray reflectometer.*

X-Ray Source

The X-ray beam is generated using a Phillips PW 1825/00 X-ray generator. This generates a high tension (HT) supply to accelerate the electrons to a target metal in the x-ray tube. In this case the target metal is tungsten. This metal was chosen as it has secondary emission peaks at low energy and so does not interfere with the straight through beam, termed the white beam. Typical voltage and current values for the HT supply used in a reflectivity experiment are 50 kV and 10 mA, respectively. The

generator stabilises the current and voltage so that the intensities from different runs can be reliably inter-compared. The accelerating voltage controls the energy of the x-rays leaving the source (the higher the voltage, the higher the x-ray energies and thus the shorter the wavelengths) and the current affects the x-ray intensity. In the x-ray reflection experiments, no monochromator is necessary (as with x-ray diffraction) because the wavelengths are varied at a fixed angle. The x-ray wavelengths typically produced range from 0.3 to 1.4 Å. However, in order to obtain a large **Q** range, the reflectivity measurements are performed at three or four different angles. The reflectivity profiles measured at higher angles need to be recorded for longer periods of time. This is due to the decrease in reflectivity with increasing angle and ensures that the whole range of wavelengths are detected. The data for the three or four runs is normalised to give one reflectivity profile. The minimum reflectivity that can be measured depends on the diffuse background scattering from the sample and air.

X-Ray Detector

The x-ray detector used is a Gamma Gage Portable Spectrometer, by EG&G ORTEC with a high purity doped crystal of germanium as the detector. It is cooled by liquid nitrogen, housed in a dewar attached to the detector. The dewar must be filled with liquid nitrogen *via* a funnel attached to the valve and the detector allowed to cool for at least two hours. As a result of the x-rays hitting the crystal, the germanium emits electrons with energies corresponding to those of the reflected x-rays. The electrons are then captured and their energy converted, by windows-based software, into a pulse. The height of the pulse being proportional to the energy of the x-rays detected and thus their wavelengths.

Occasionally, when there are rapid changes in the reflectivity, the germanium detector produces echoes. These are formed when the energy from the detected x-rays is used to cause a germanium k_α transition. This results in an exact but less intense profile, shifted to lower energies by an amount E, where E is the energy of the k_α transitions. The echoes can be numerically removed from the data.

The information gained by the detector is then used to plot a graph of counts versus energy which is viewed using MAESTRO software. This is then saved and converted to a data file. This data is then imported into ORIGIN software, where it is manipulated to give a graph of reflectivity versus **Q**. The reflectivity curve is normalised by dividing the reflectivity at each **Q** by the reflectivity of a measured white beam.

If three reflectivity profiles are measured at different angles for the same sample, as in our experiments, further data manipulation is required. The lower angle reflectivity profile is the only one likely to show reflectivity at the critical angle. Therefore the middle angle reflectivity profile and then the higher angle profile is scaled to the lower angle reflectivity profile. The ranges of each of the reflectivity profiles are then edited to give a smooth reflectivity profile for the sample over a wide **Q** range.

4.2.2 Reflectometer Safety Controls

The use of x-rays is potentially dangerous and so many safety features are incorporated into the reflectometer. These are as follows:

1. Perspex windows shield the reflectometer. X-rays cannot be generated unless these windows are closed. These protect against accidental touching of the x-ray beam.

2. The x-ray tube has water supply to cool it whilst operational and will not operate unless the water is turned on.

3. Shutter No. 4 can only be opened with "Shutter" and "Enter" depressed simultaneously on the generator. This prevents accidental opening of the shutter.

4. The shutter closes automatically if no x-rays are being generated.

5. High voltage to the detector is shut off if the temperature reaches a critical value.

6. The detector will not detect very intense x-ray beams, the voltage switching off automatically.

4.2.3 X-Ray Reflection Technique[14]

Arms Alignment

Both source and detector arms must be aligned in order for the reflected x-rays to be detected. This is achieved by holding the source constant and varying the height of the detector (no sample is present). A typical range may be from + 10 mm to - 10 mm in increments of 1 mm. However this will vary depending on how well the source and detector are already aligned. To aid this task, the buffer is used which measures the total number of counts reaching the detector every two seconds. This means it is easy to compare the counts recorded at different detector positions. A graph of counts versus detector height can then be plotted and a gaussian distribution taken. This leads to the detector height that gives the most counts and therefore the most aligned position of the detector to the source. These heights are the reference points and are therefore labelled zero. This procedure is usually run at 15 kV and 10 mA with slit widths S_1=10, S_2=10, S_3=30 and S_4=50 μ. A typical number of counts recorded every two seconds is 10 000. The size of the voltage must be sufficient to produce X-rays with high enough energies to pass the glass or perspex container holding the sample (if there is one), while still being sensitive to the surface under study.

The slit size is important because they control the size of the x-ray footprint reaching the sample and the intensity of x-rays reaching the detector. At low angles just above the critical angle, the rate of change of the reflectivity is greater compared to higher angles, and thus good resolution is necessary. Slits S_1 and S_2 should be relatively small, so that the footprint of the beam is small and thus the angles of the x-rays in the beam hitting the sample vary only slightly from the angle of incidence of

the beam. Slits S_3 and S_4 can be made wider or narrower depending on whether too many or too little x-rays are being detected. When there are too many x-rays reaching the detector at any one time, the detector will have difficulty in detecting them all and thus the "Dead" time will be high. The dead time should never exceed about 20%. Conversely, to increase the x-ray intensity the current from the HT supply can be increased.

Sample Alignment

Although the x-ray source and detector are aligned to each other, they also have to be aligned with respect to the sample, so that the x-ray beam is parallel to the surface of the sample. The sample is placed on a stand at the central pivot. The height of the stand can be altered by an automatic height adjuster. Firstly, the counts produced by a straight through beam are recorded and the sample is raised by remote control to "half height". This is the height at which the beam is reduced to half its straight through value and hence the number of counts will be half their initial value. The rotation spot on the central pivot is useful as a guide to the half height position of the sample. The voltage, current and slit size values are the same as those used to align the arms and results in a half height of around 5 000 counts every two seconds (where the straight through beam is 10 000 counts).

To check that the beam and sample are parallel to each other, the sample is kept in this half height position and a "rocking" procedure performed. The x-ray arm is moved down and the detector arm moved up by equivalent amounts. If the sample is aligned with respect to the beam the number of counts should decrease. Similarly, if the x-ray arm is moved up and the detector arm down, then the counts should again

decrease. In both cases the sample is interrupting more of the beam. However, if the beam and sample are not aligned, rocking one way will decrease the counts, but rocking the other way will increase the counts.[15] This is illustrated in Figure 4.2.

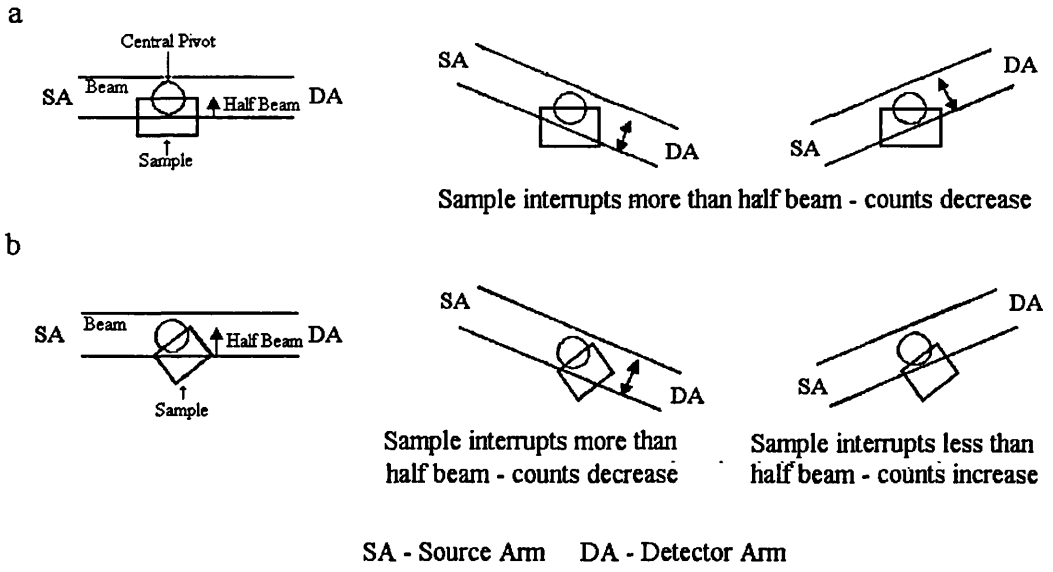

Figure 4.2 *a) beam and sample aligned and b) beam and sample not aligned.*

To align the sample with the beam, a gaussian plot of counts versus detector arm height can be taken which leads to the height of the detector arm (and corresponding source arm) that gives the most counts and thus the best alignment of the beam with the sample. These heights are then re-zeroed and the half height checked. This may be repeated several times in order to obtain a gaussian value which is within 20 μm of the current detector arm height.

On completion of the procedure outlined above, the apparatus is ready to perform a reflection from the sample surface. Both the source and detector arms are

raised by the same height to give the required incident angle and the slits, voltage and current set at values which account for factors such as sensitivity and resolution.

4.2.4 Formation of Mesostructured Silica

MCM-41 type materials were synthesised at room temperature[5] from a dilute basic solution containing the organosiloxane, tetraethoxysilane (TEOS) and the surfactant hexadecyl-trimethylammonium bromide (C_{16}TMABr) (molar composition = 0.01 C_{16}TMABr : 1.19 NaOH : 0.09 TEOS : 402.06 H_2O).

In a typical experiment, the solution is prepared as follows: 0.16 g of C_{16}TMABr was dissolved in 318.0 g of H_2O and stirred continuously. To this solution 2.0 g of 1M NaOH was added, followed by 0.828 cm^{-3} of TEOS. This solution was left to stir for a further 3 minutes before being placed in the teflon trough of the X-ray reflectometer.

In the experiments involving the templating monolayer of phosphatidylcholine (PC), a known volume of PC in chloroform was dropped onto the air/water interface, drop by drop, *via* a micro-syringe in order to form a monolayer.

The samples were grown at the surface of the solution in a Teflon trough sealed in a perspex box, with thin mylar windows for X-ray transmission. The box is hermetically tight to preclude evaporation, and consequent changes in the height of the solution, which in turn would affect the alignment of the sample over time. This factor may have been important in determining the self-limiting thickness of the films seen in these experiments.

A series of X-ray reflection measurements were taken and repeated over a period of 30 hours. Each set of measurements used the arm heights, slit widths and HT supply voltage and current listed in Table 4.1.

Table 4.1 *Parameters used for X-ray Reflection Measurements.*

Arm Heights	Voltage	Current	S_1	S_2	S_3	S_4
mm	kV	mA		μm		
0.8	50	10	10	10	30	50
1.6	50	10	30	30	55	85
3.2	50	10	120	120	220	330

4.3 Results

Reflection Theory

The analysis of the reflection data obtained is well documented elsewhere[16] and is discussed in Appendix Two. The principal approach utilises an exact formulation developed for optics,[17] which subdivides the profile into layers which are represented by a scattering length density (ρ) and a thickness (d). The scattering length density, ρ, for x-rays is defined as:

$$\rho = \sum_{atoms} N.Z.r_e$$

where N is the number of atoms per cubic angstrom, Z is the atomic number, therefore, NZ represents the number of electrons per unit volume, and r_e is the scattering length or power of an individual electron (2.82×10^{-5} Å). This is therefore a measure of the average scattering power of a layer or region of material.

Each discontinuity between layers contributes a reflectivity, given by the well known Fresnel coefficient, modified by a factor taking into account the roughness of the interface. The contributions from each interface are then combined using a matrix method. The usual procedure in fitting a reflectivity profile is to assume a model profile, and allow variation of parameters until a best fit of the calculated to real R(**Q**) is found. Extreme care must be taken to avoid local minima in the fitting procedures, and correlation between model parameters and the uniqueness of any model must be carefully studied since model fitting has been heavily criticised for its *posteriori* nature, and various model independent techniques have been suggested.[18]

Raw data from the reflection measurements were normalised to the incident beam spectrum, before being scaled to total reflection below the critical **Q** value for total reflection. Individual measurements at different angles were converted to **Q** and the overlaps joined to form a single reflectivity profile.

4.3.1 Reflectivity Data for Phosphatidylcholine Monolayer System

Measurements were taken over a period of several days, to follow the crystallisation process. Figure 4.3a shows the reflectivity profile for the initial measurement with a templating monolayer of phosphatidylcholine (PC) and Figure 4.3b shows the reflectivity profile after 48 hours.

These reflectivity profiles clearly indicate the evolution of fringes with time, and a more complex structure appearing at **Q** around 0.2 $Å^{-1}$ which signifies the thickening of the film at the air/water interface and as we shall demonstrate the evolution of the internal structure of silica.

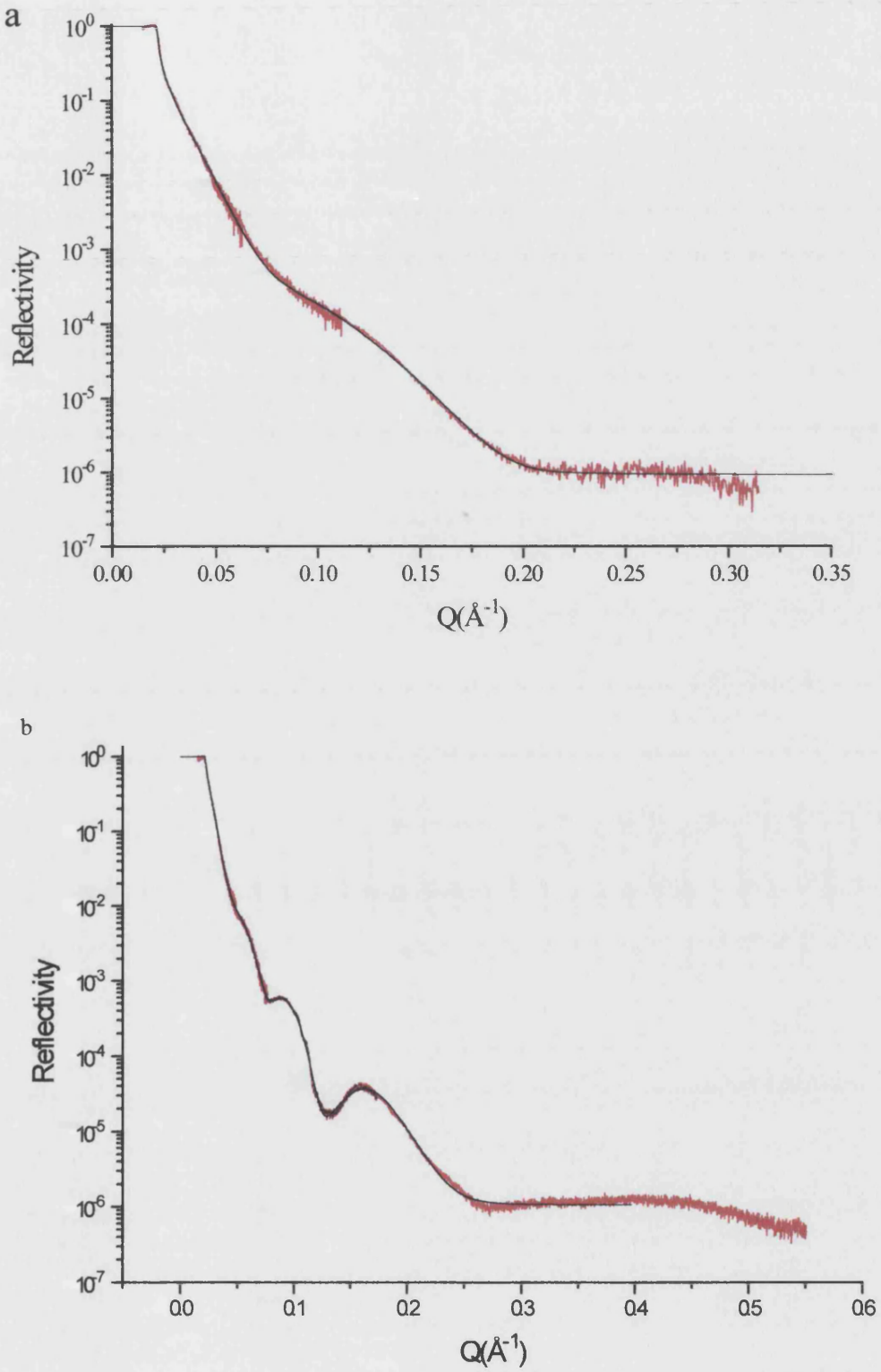

Figure 4.3 *Reflectivity profile (-) and fitted density (-) for MCM-41 films grown for a) 1 hour and b) 48 hours under a PC monolayer.*

In summary, the aim is to find a realistic scattering length density profile perpendicular to the air/water interface which will fit the observed reflectivity data. Superimposed upon Figures 4.3 a and b are the calculated best fits for the data. In these initial experiments we have concentrated on the static short- and long-time structural detail, but we have also made a preliminary study on the time-dependence of the Bragg peak showing evolution of internal structure within the growing film. Figure 4.4 shows the change in position of the Bragg peak appearing within the film.

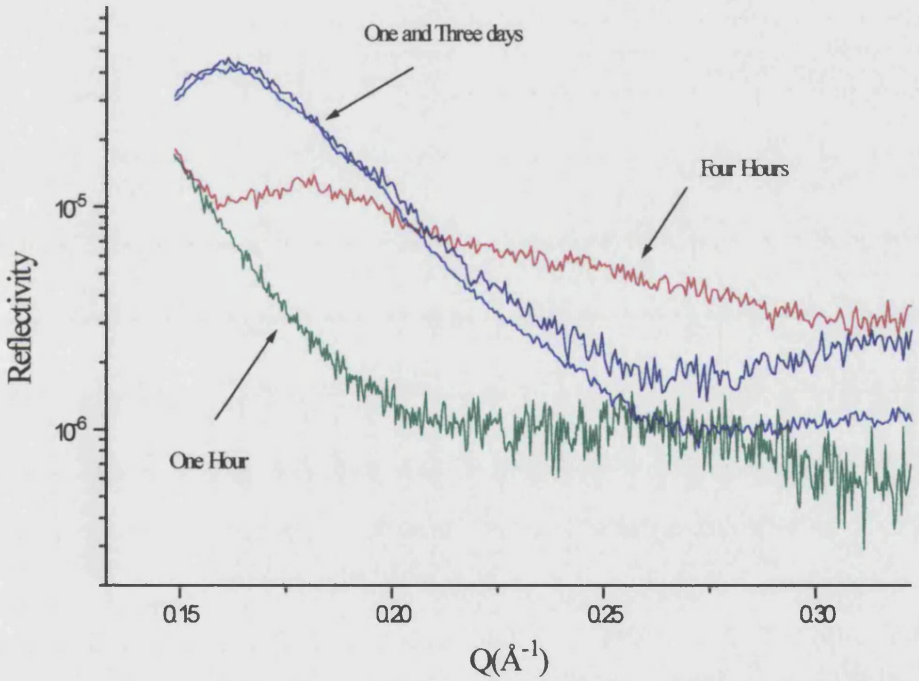

Figure 4.4 *Evolution of Bragg peak in reflectivity profile for MCM-41 film grown under a PC monolayer.*

The zero time measurements have no apparent repeat within the film, but very rapidly a peak evolves and within one day a Bragg reflection at 0.16 Å^{-1}, which corresponds to a 39 Å repeat distance, has been formed. This peak does not change in

position, width or intensity after a days growth, therefore suggesting that it represents the final structure reached over the entire period of the experiment. Small angle x-ray reflectivity (SAXR) measurements on powdered samples grown from identical solution compositions (Figure 4.5) have shown similar d-spacings as well as higher angle peaks, confirming the presence of an hexagonally close-packed mesoporous structure.[19]

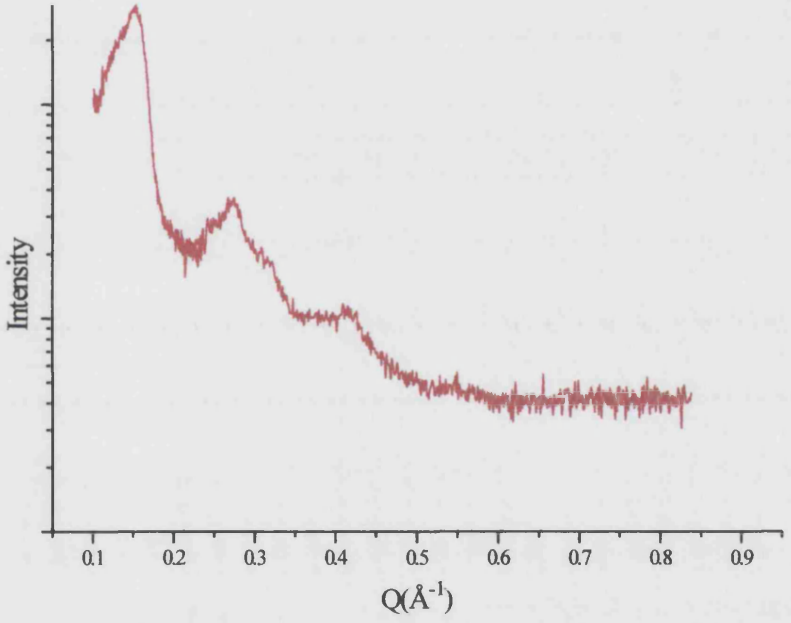

Figure 4.5 *SAXR spectra for powdered samples of MCM-41 film grown under a PC monolayer.*

4.3.2 Reflectivity Data for MCM System

Once again, measurements were taken over a period of several days, to follow the crystallisation process. Figure 4.6a shows the reflectivity profile for the initial measurement without a templating monolayer of PC and Figure 4.6b shows the reflectivity profile after 48 hours.

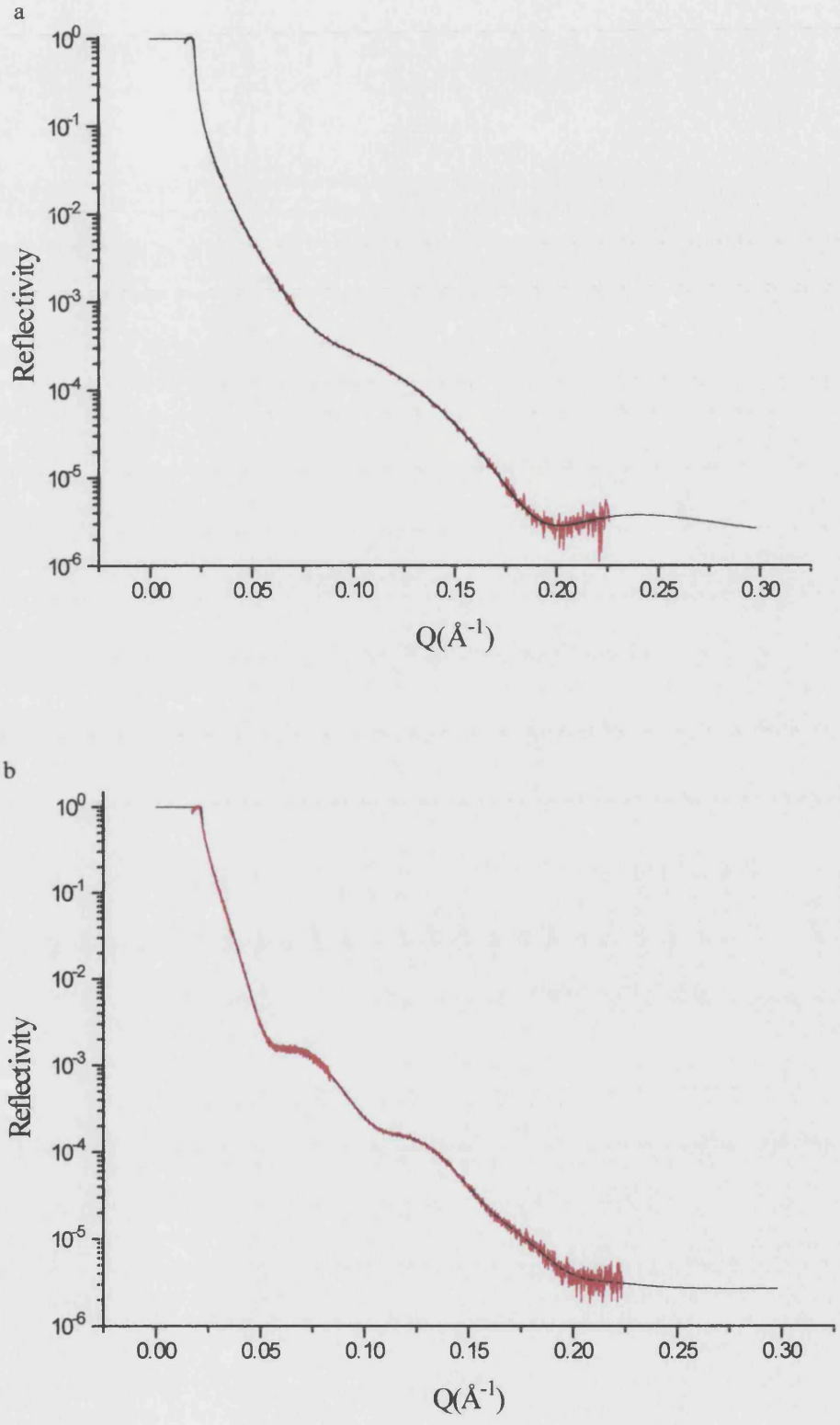

Figure 4.6 *Reflectivity profile (-) and fitted density (-) for MCM-41 film grown for a) 1 hour and b) 48 hours without the presence of a PC monolayer.*

4.3.3 Strategy for Analysing the Reflectivity Profiles

The profiles were analysed using two computer programs, XREF and MODELI, which are based on the optical matrix method (see Appendix Two) of determining reflection profiles from a model surface structure. The aim of both XREF and MODELI is to convert a graph of reflectivity versus **Q** to one of scattering length density versus distance from the surface, and hence elucidate the structure of the surface. Both programs compare experimental results with theoretical ones and then update the model of the surface until the best fit is obtained.

XREF requires the user to propose an initial structure for the surface and then fits the theoretical reflection profile to the experimental profile by changing the initial set of surface parameters. A knowledge of the system under study is useful in this case.

MODELI calculates the best fit to the experimental profile without any prior constraints, and produces a set of parameters for the structure of the surface being analysed. The parameters invariably lead to a theoretical reflection profile which fits well to the experimental profile. However, MODELI does not account for a degree of uncertainty in the model and therefore the suggested surface electron density profile may be chemically illogical. The MODELI program is useful as a starting point in cases where nothing about the surface composition is known, but XREF may lead to more accurate results if based on prior knowledge of the system.

Sometimes, with the trained eye, it is possible to estimate the surface structure using the equation, $d = 2\pi/\Delta\mathbf{Q}$ (Appendix Two). However, the reflection profiles described in sections 4.3.1 and 4.3.2 were analysed initially using MODELI, which suggested a structure which is then used as a starting point for the XREF fitting

procedure. The remainder of this section gives a general description of the best fit determination to the experimental data using the XREF computer model.

Each layer at the surface between the air and bulk phase is represented by two model parameters, one representing the electron density of the layer and one for thickness. Between each of the layers present there is also a parameter for the roughness of the interface. For example, a system containing two layers of different scattering length density (SLD) is represented by the following parameters (Table 4.2).

Table 4.2 *Table of parameters for a system containing two layers.*

Layer	*Parameter*
Layer 1	Thickness d (Å)
Layer 2	Thickness d (Å)
Air/Layer 1	Roughness d (Å)
Layer1/Layer2	Roughness d (Å)
Layer2/Bulk phase	Roughness d (Å)
Layer 1	Scattering Length Density ($Å^{-2}$)
Layer 2	Scattering Length Density ($Å^{-2}$)
	Background SLD ($Å^{-2}$)

These parameters are held constant with the exception of the background radiation. XREF then produces a theoretical reflectivity curve based on the model parameters listed above. XREF builds the theoretical reflectivity profile curve using the optical matrix method described in Appendix Two, whereby each layer is represented by a matrix and the product of all the layer matrices lead to the total reflectivity of the surface.

The theoretical reflectivity curve is then compared to the experimental one to see how closely the model parameters fit the surface under study. To improve the fit to the data the model parameters are allowed to vary. This process is achieved one step at a time in order for the effects of a particular parameter on the theoretical curve to be clearly seen. Usually one layer is dealt with at a time, and the layer that is expected to deviate most from the predicted model is the one that is selected. For example, let layer 2 be the layer which deviates the greatest from the parameter values it has been given, and similarly it is its thickness (as opposed to its electron density) which is more different to the predicted value.

XREF again plots a theoretical curve based on the parameters, allowing the thickness of layer 2 to vary. XREF uses a value for the layer 2 thickness which gives the best fit of the theoretical curve to the experimental one. This process is repeated allowing the electron density of layer 2 to vary. This means that the values of the thickness and electron density in the model are the ones which result in the closet fit between the theoretical and experimental reflectivity curves.

This procedure is repeated for layer 1, allowing its thickness and then electron density values to vary. Finally, the roughnesses at each interface are allowed to vary. The roughness values should be the same because the roughness at one interface will have a knock-on effect on the roughnesses at the other interfaces. Therefore, the parameter roughness values are allowed to vary but must be equal to each other. Throughout the fitting procedure it is possible to view the electron density profile versus distance from the air/layer 1 interface based on the model parameters for the surface. Hence, with all eight of the model parameters now varying, the values should result in a theoretical curve which most clearly resembles that of the experimental

reflectivity curve. The structure, based on the model parameter values, should be that of the actual surface and is in a direction normal to the interfaces.

In many cases, the theoretical reflectivity fit to the experimental reflectivity curve may not be reasonable, suggesting that some or all of the parameter values used by XREF are incorrect. In these circumstances, parameter values can be altered and then held constant to see their effect on the theoretical curve. If the theoretical fit to the experimental data is still not satisfactory, then it is possible that the number of layers at the surface is incorrect. A new set of parameters therefore needs to be used accounting for the thicknesses and electron densities of each of the layers and the roughnesses between them.

The fitting procedure, to some extent, involves trial and error, but with practice one is able to visualise and predict the affect of the parameters, of the surface model, on the theoretical reflectivity curve.

4.3.4 Model Calculations

The starting model used for model calculations was taken from the mechanism published by Yang *et al.*[8] Firstly, the scattering length density profiles for numerous possible surface structures, based upon hexagonally closed packed cylinders of various sizes and combinations of silica, micelles and water needs to be calculated. It is noted that we did not start with a layer of hemi-cylinderical micelles at the surface as suggested by Yang *et al.*[8] The first possible structure is based on a monolayer of silica encased micelles at the water surface, with no more layers below as shown in Figure 4.7. This monolayer of silica encased micelles can be subdivided into four layers which is also shown in Figure 4.7. This is necessary in order to obtain the input

parameters for MODELI and XREF to produce a scattering length density profile of the structure.

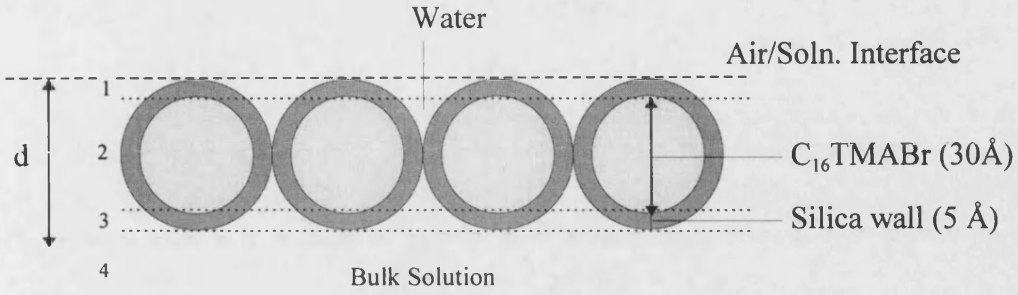

Figure 4.7 *Single monolayer of silica encased micelles at the water surface showing the number of layers present for modelling.*

Each cylinder has a simulated inner core of surfactant material with a radius of 15 Å, and an outer shell of amorphous silica with a thickness of 5 Å, therefore the total diameter of the silica encased micelle being 40 Å. The fractional contribution of each component as a function of distance (d) into the interface is shown in Figure 4.8. These values for each of the four layers (identified for the purpose of using MODELI and XREF) are then summed to give the scattering length density shown in Figure 4.9.

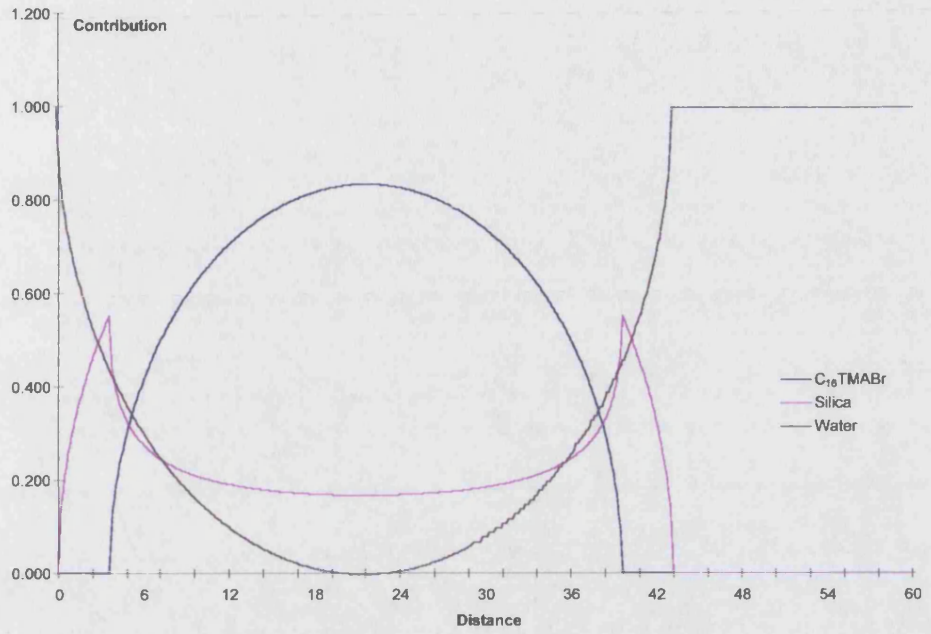

Figure 4.8 *Fractional contribution of a single silica encased micelle at the water surface.*

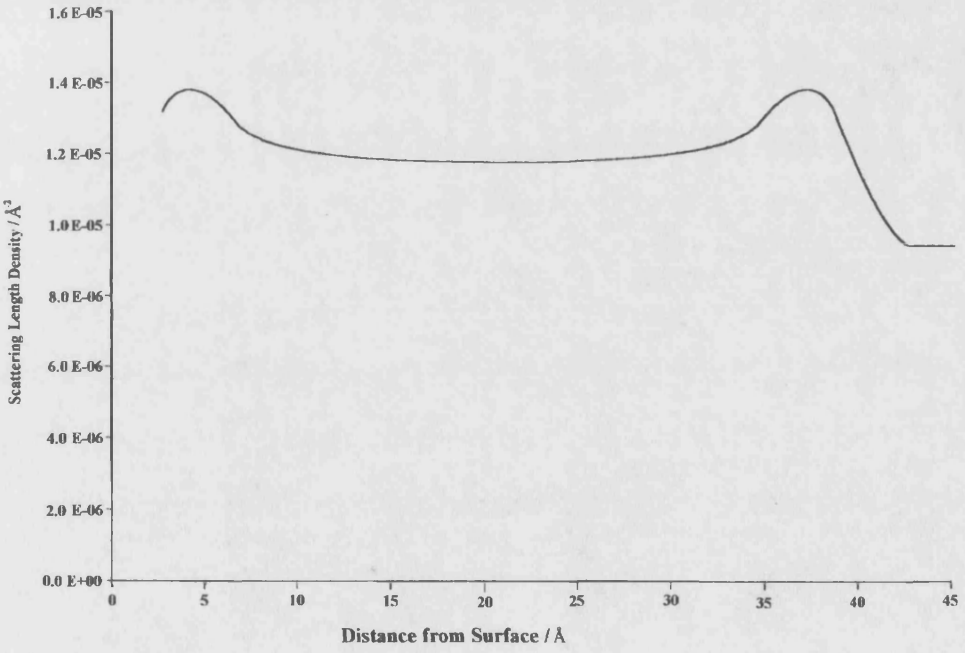

Figure 4.9 *Scattering length density for a monolayer of silica encased micelles.*

Figure 4.9 also illustrates the contribution of each of the components to the total SLD at each distance from the surface. The profile shows that the highest SLD occurs at 3.5 and 36.5 Å (SLD = 1.35×10^{-5} Å^{-2}) and the lowest at 20 Å (SLD = 1.15×10^{-5} Å^{-2}). These correspond to areas containing components of silica/water and silica/C_{16}TMABr, respectively. If the gaps between the micelles were filled with silica and not water, the shape of the profile changes slightly and the highest SLD area occurs between 0-3 Å (SLD = 1.86×10^{-5} Å^{-2}) and corresponds to a region of pure amorphous silica. The lowest SLD area is not affected by the change because it is composed of silica encased micelles only.

Now if more silica encased micelles are allowed to come into contact with the first monolayer, and lock into one another to form a perfect, hexagonally close packed array as illustrated in Figure 4.10, the fractional contribution plot would become more complicated as shown in Figure 4.11.

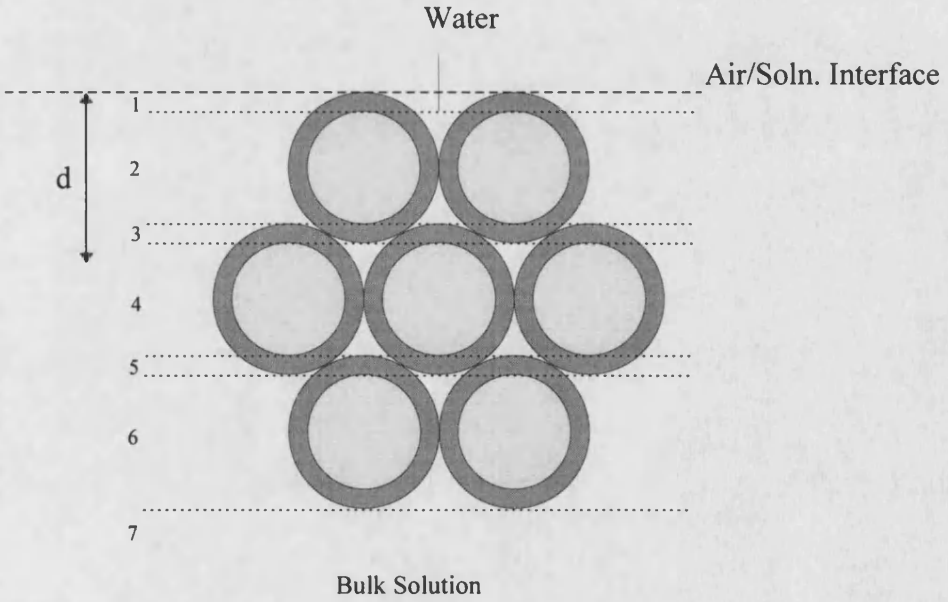

Figure 4.10 *Silica encased micelles at the water surface with second layer hexagonally close packed showing the number of layers present for modelling.*

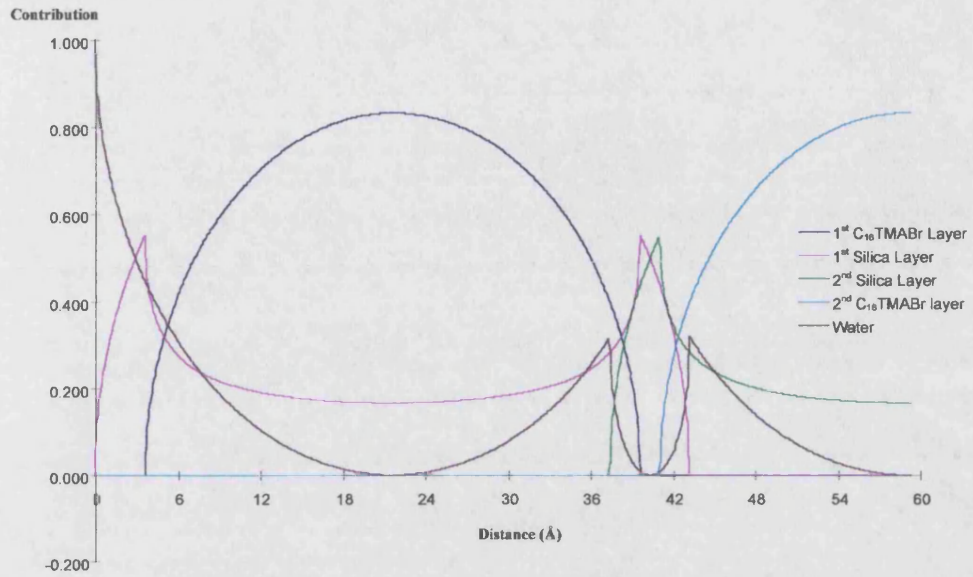

Figure 4.11 *Fractional contribution for a hexagonally close packed array of silica encased micelles at the water surface.*

The SLD profile for a hexagonally closed packed array of silica encased micelles is shown in Figure 4.12. When water is in the gaps between the hexagonally close packed micelles, the highest SLD occurs between 38-40 Å and has a value of 1.86×10^{-5} Å^{-2}. This is the region in which the second layer must be considered. The lowest SLD is the same value and position as in the case of the single monolayer of silica encased micelles because the second layer is not present at distances below ~30 Å.

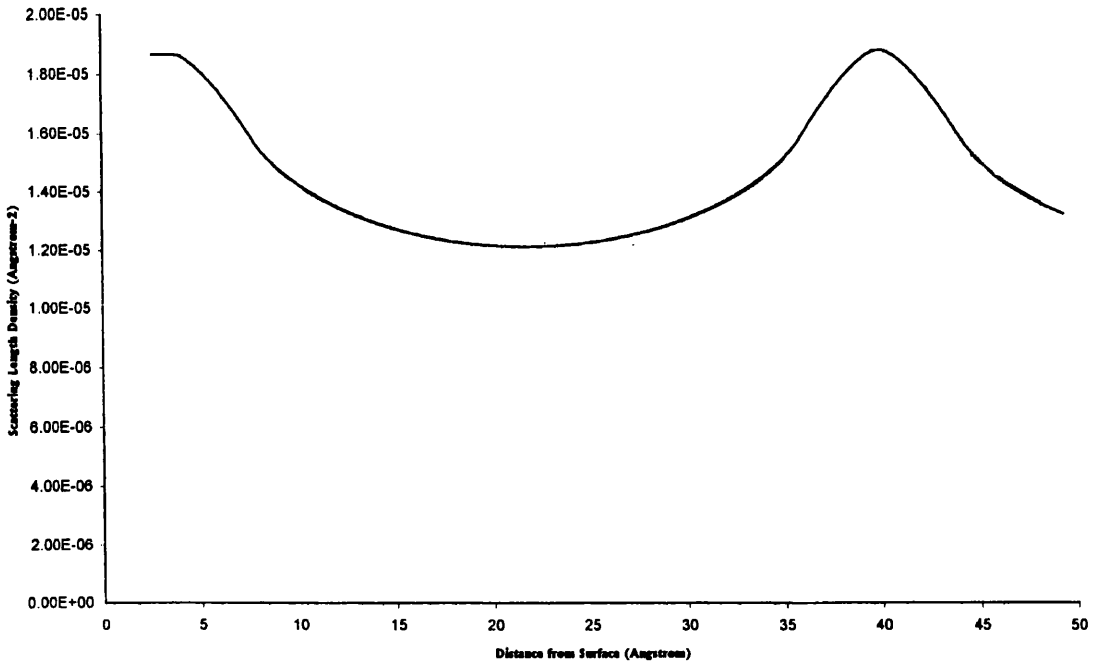

Figure 4.12 *Scattering length density for a hexagonally close packed array of silica encased micelles at the water surface.*

If the water is fully replaced with silica in the gaps, then the SLD profile will change slightly, as shown in Figure 4.13. There is only a small difference between this profile and the non-silicised film profile, with another high SLD at a depth of 33 Å corresponding to pure amorphous silica.

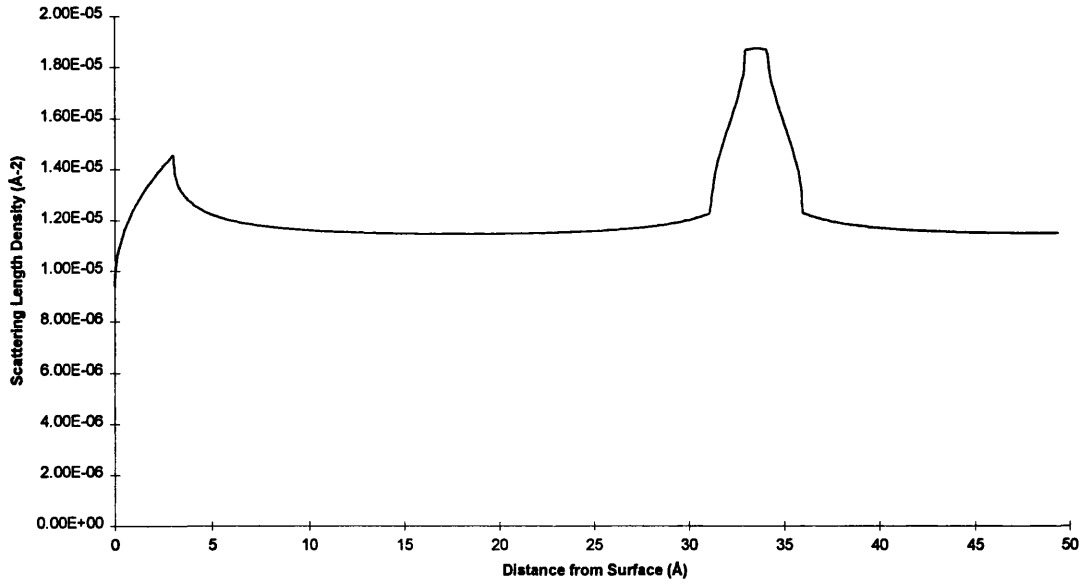

Figure 4.13 *Scattering length density for a fully silicised hexagonally close packed array of silica encased micelles.*

4.3.5 Data Fitting and Discussion

Phosphatidylcholine Monolayer System

The results of the MODELI fit on the PC system at one hour suggested the presence of three layers in the structure. Using this fit as a starting point, XREF was used to produce a more understandable fit, by restraining the thickness and scattering length density of each layer and the roughness between the layers in turn. XREF confirmed that three layers were present at the surface. A table of the 11 best fit parameters is shown in Table 4.3 and the subsequent SLD profile is shown in Figure 4.14.

Table 4.3 *Parameters leading to the best theoretical fit obtained from XREF to experimental data for PC system at one hour.*

Parameter	*Parameter Value*	*Uncertainty in Value (±)*
1st layer length (Å)	33.12	8.06
2nd layer length (Å)	1.08	4.20
3rd layer length (Å)	11.63	18.28
Roughness at air/layer 1 (Å)	8.57	2.83
Roughness at layer 1/2 (Å)	10.04	3.54
Roughness at layer 2/3 (Å)	13.56	9.16
Roughness at layer 3/bulk (Å)	35.93	2.21
1st layer SLD ($Å^{-2}$)	1.49×10^{-5}	0.74×10^{-5}
2nd layer SLD ($Å^{-2}$)	1.62×10^{-6}	2.50×10^{-5}
3rd layer SLD ($Å^{-2}$)	2.17×10^{-5}	0.14×10^{-5}
Background SLD ($Å^{-2}$)	8.43×10^{-7}	1.25×10^{-7}

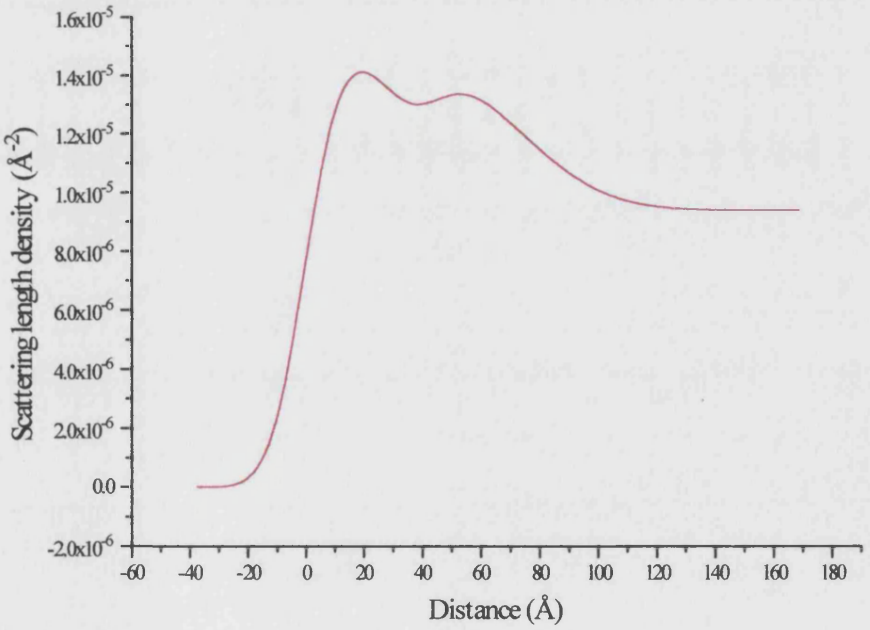

Figure 4.14 *Scattering length density profile at one hour for a MCM-41 film grown under a PC monolayer.*

From the SLD profile at one hour, it can be clearly seen that the silica film produced has a thickness of around 80 Å, and the plot shows the presence of two maxima, which are nearly symmetrical and have a SLD of about 1.45×10^{-5} Å^{-2}. By comparing this fit with the calculated SLD profile obtained from the monolayer of silica encased micelles at the surface given in Figure 4.8, it can be seen that despite the presence of two maxima, the data corresponds well with a single micelle layer at the surface. From this the two maxima are associated with the contribution of the lateral sum of the silica, rather than two micelles. The overall length of the calculated SLD profile is clearly shorter than the measured SLD profile. This is due to the presence of the PC molecules at the surface which will be somewhat disordered and hence shortened by the presence of the micelles. The uncertainty value for the 3rd layer length (Table 4.3) is larger than the actual thickness of the layer. This is due to the roughness of the interface between the 3rd layer and bulk solution. This roughness is shown in the SLD profile by the smaller gradient between 55-100 Å, compared with the roughness of the interface between layers 1 and 2, at a distance between 15-30 Å from the air/solution interface.

It is important to note that the model used to produce the theoretical reflectivity profile does not require the presence of any hemi-cylinderical micelles at the surface, although this has been previously proposed by Yang *et al.*[8] If a layer of hemi-cylinderical micelles at the surface was introduced to the model, the resulting theoretical reflectivity profile does not fit the experimental reflectivity profile.

The results of the MODELI fit on the PC system at 48 hours suggested the presence of nine layers at the air/water interface. Further fitting by use of XREF produced the 29 parameter fits tabulated in Table 4.4 and the subsequent SLD profile is shown in Figure 4.15.

Table 4.4 *Parameters leading to the best theoretical fit obtained from XREF to experimental data for PC system at 48 hours.*

Parameter	*Parameter Value*	*Uncertainty in Value (±)*
1st layer length (Å)	21.82	51.85
2nd layer length (Å)	16.70	52.53
3rd layer length (Å)	23.42	54.50
4th layer length (Å)	17.32	56.75
5th layer length (Å)	19.67	11.93
6th layer length (Å)	11.33	12.13
7th layer length (Å)	13.05	13.46
8th layer length (Å)	16.41	11.28
9th layer length (Å)	7.00	10.66
Roughness at air/layer 1 (Å)	16.03	4.92
Roughness at layer 1/2 (Å)	20.44	52.13
Roughness at layer 2/3 (Å)	19.53	16.66
Roughness at layer 3/4 (Å)	36.14	20.43
Roughness at layer 4/5 (Å)	8.86	1.21
Roughness at layer 5/6 (Å)	17.12	8.20
Roughness at layer 6/7 (Å)	16.46	6.21
Roughness at layer 7/8 (Å)	16.76	3.56
Roughness at layer 8/9 (Å)	16.80	1.23
Roughness at layer 9/bulk (Å)	14.99	1.73
1st layer SLD ($Å^{-2}$)	4.79×10^{-5}	8.26×10^{-5}
2nd layer SLD ($Å^{-2}$)	-2.05×10^{-5}	1.39×10^{-4}
3rd layer SLD ($Å^{-2}$)	5.35×10^{-5}	1.17×10^{-4}
4th layer SLD ($Å^{-2}$)	-1.26×10^{-5}	5.39×10^{-5}
5th layer SLD ($Å^{-2}$)	2.19×10^{-5}	3.44×10^{-5}
6th layer SLD ($Å^{-2}$)	-1.27×10^{-4}	2.23×10^{-4}
7th layer SLD ($Å^{-2}$)	1.63×10^{-4}	1.55×10^{-4}
8th layer SLD ($Å^{-2}$)	-1.18×10^{-4}	1.35×10^{-5}
9th layer SLD ($Å^{-2}$)	1.64×10^{-4}	2.50×10^{-4}
Background SLD ($Å^{-2}$)	1.05×10^{-6}	4.31×10^{-8}

From Table 4.4 it can be seen that there are negative input parameters for the generation of the SLD profile. This is attributed to the large roughness values between the various interfaces, and the limitations of the simple layer approach used for analysis of the reflectivity profiles.[20]

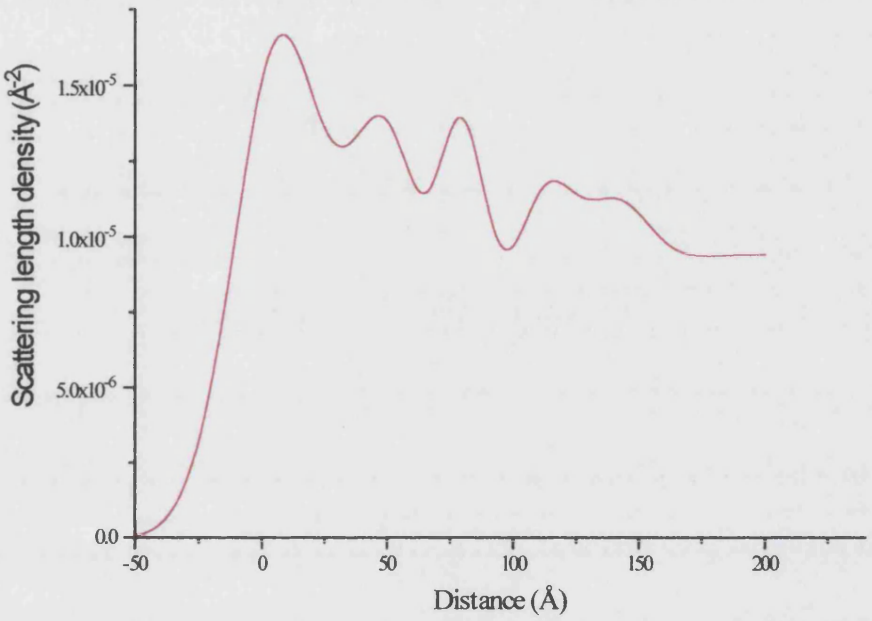

Figure 4.15 *Scattering length density profile for MCM-41 film grown for 48 hours under a PC monolayer.*

Significant differences begin to emerge when the film has started to grow. The thickness of the film is limited to *ca.* 200 Å and there is a Bragg peak showing a repeat distance of about 40 Å. From this it can be deduced that the film consists of 5 layers, but following further fitting by XREF, the SLD profile corresponds to four micellar layers. The profile also shows a gradual loss of scattering length density with distance from the surface, which suggests a loss of ordering into solution particularly after the second layer. It is not clear why there is a limiting value for the thickness of

the films produced from these experiments, although the gradual decrease of ordering maybe of some importance. It should be noted that in the experiments performed, there is no stirring of the subphase, but we do not expect that there is any limiting mass-transport effect, given the solution concentration and the time that the monolayer was left to crystallise over three days.

The SLD profile shown in Figure 4.15 is very complex and the caveat introduced in the reflectivity theory section (section 4.3) must be taken into account as there are likely to be different SLD profiles which fit this data. With this in mind, it is possible to approach the data analysis from a completely different direction assuming that no knowledge of the film structure is known. Therefore, in addition to the standard optical matrix method used so far for the analysis of the reflectivity profiles, it is possible to analyse the data using a model independent method as previously described by Hamley *et al.*[21] The method allows dampened variation of 50 coupled cubic splines which are appropriate for the resolution and **Q** range to model the SLD profile. A cubic spline is cubic polynomial function which is defined in Appendix Three. The 50 cubic splines are linked together, such that the adjacent splines are allowed to vary by a certain amount, thus giving a smoothing function.[20] The reflectivity is calculated by starting from a slab with no pretence to the final structure and so no shapes needs to be assumed for any interface. Variation techniques then lead to a minimised reflectivity profile and a best fit SLD profile. The SLD profile from the model independent method outlined above, is shown in Figure 4.16.

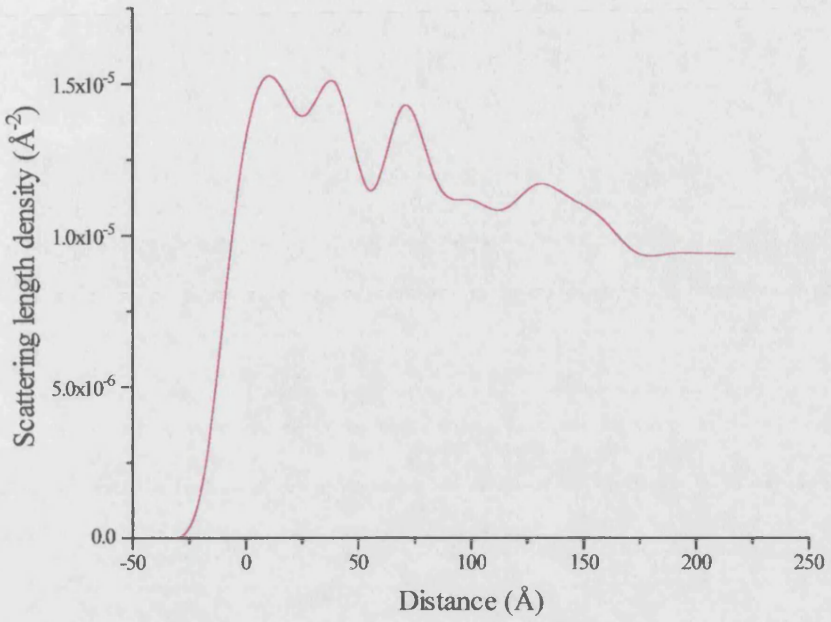

Figure 4.16 *Scattering length density profile for MCM-41 film grown for 48 hours under a PC monolayer as determined by the model independent method.*

Direct comparison of the SLD profiles obtained from the PC system at 48 hours (Figure 4.15) and the model independent method (Figure 4.16), shows remarkable similarity between the two. Both show five peaks and a gradual loss of SLD with distance from the surface, reflecting a loss of ordering into solution. This is particularly so after the second layer for the model independent method SLD profile.

It is believed that the model independent method SLD profile is strongly determined by the inter-relationship between the Bragg peak and the fringe structure. Forcing a repeat at around 40 Å, which the Bragg peak inevitably does, along with a well defined overall thickness appears to lead to the unique determination of the structure.[20]

MCM System

The results of the MODELI fit on the MCM system at one hour suggested the presence of three layers. Once again this was used as a starting point for XREF, which produced a more accurate fit. XREF produced a list of the 11 best fit parameters which are tabulated in Table 4.5 and the subsequent SLD profile is shown in Figure 4.17.

Table 4.5 *Parameters leading to the best theoretical fit obtained from XREF to experimental data for the MCM system at one hour.*

Parameter	*Parameter Value*	*Uncertainty in Value (±)*
1st layer length (Å)	32.08	2.76
2nd layer length (Å)	1.51	1.98
3rd layer length (Å)	3.06×10^{-2}	0.47
Roughness at air/layer 1 (Å)	5.76	2.46
Roughness at layer 1/2 (Å)	6.78	1.83
Roughness at layer 2/3 (Å)	15.89	7.41
Roughness at layer 3/bulk (Å)	21.55	3.54
1st layer SLD ($Å^{-2}$)	1.36×10^{-5}	7.95×10^{-7}
2nd layer SLD ($Å^{-2}$)	1.62×10^{-6}	9.39×10^{-6}
3rd layer SLD ($Å^{-2}$)	4.32×10^{-4}	7.49×10^{-4}
Background SLD ($Å^{-2}$)	2.23×10^{-6}	3.55×10^{-6}

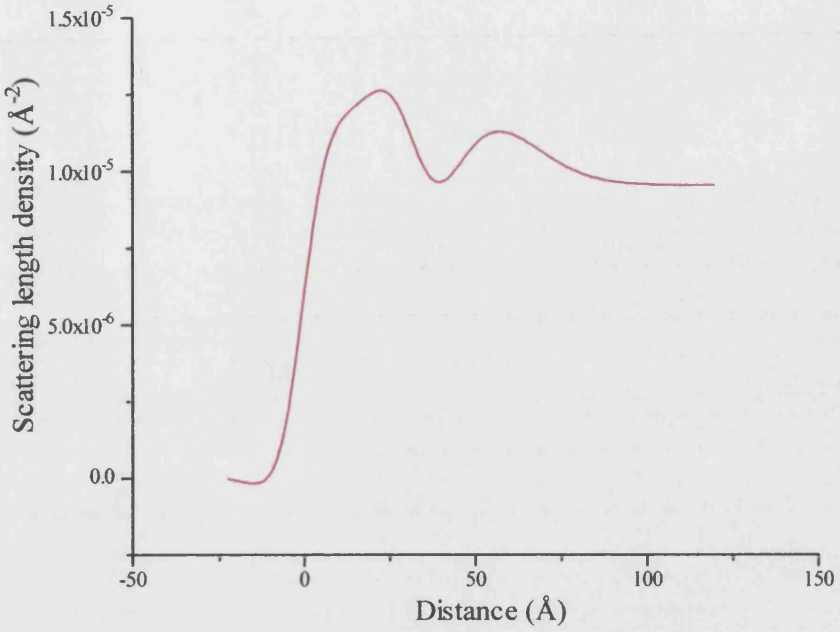

Figure 4.17 *Scattering length density profile for MCM-41 silica solution at one hour without the presence a PC monolayer.*

The SLD profile of the MCM system at one hour (Figure 4.17) is very similar to the SLD profile for the PC system (Figure 4.14) at the same time, indicating the presence of single micelle layer. The main difference that becomes apparent by the comparison of the two SLD profiles, in that the peak values in the SLD profile for the MCM system (1.25×10^{-5} and 1.1×10^{-5} Å^{-2}, respectively) are lower than the peak values obtained from the SLD profile for the PC system. This difference in peak values suggests that the PC monolayer induces a closer packing of the silica encased micelles at the surface than in a system without a PC monolayer. The fact that both SLD profiles appear similar suggests that the processes involved in the formation of these structures are very similar, with the MCM system producing a slightly more disordered initial structure.

The MODELI fit on the MCM system at 48 hours suggests the presence of nine layers. Once again this fit was used as a starting point for XREF to produce a more understandable fit. XREF produced a list of the 29 best fit parameters which are tabulated in Table 4.6 and the subsequent SLD profile shown in Figure 4.18.

Table 4.6 *Parameters leading to the best theoretical fit obtained from XREF to experimental data for the MCM system at 48 hours.*

Parameter	*Parameter Value*	*Uncertainty in Value (±)*
1st layer length (Å)	20.99	13.44
2nd layer length (Å)	18.02	15.69
3rd layer length (Å)	23.30	24.89
4th layer length (Å)	15.23	29.49
5th layer length (Å)	14.14	17.63
6th layer length (Å)	10.44	5.93
7th layer length (Å)	12.42	9.27
8th layer length (Å)	14.96	21.61
9th layer length (Å)	5.86	7.96
Roughness at air/layer 1 (Å)	14.25	6.21
Roughness at layer 1/2 (Å)	19.62	18.02
Roughness at layer 2/3 (Å)	17.99	20.26
Roughness at layer 3/4 (Å)	31.32	17.83
Roughness at layer 4/5 (Å)	10.71	4.84
Roughness at layer 5/6 (Å)	16.65	10.02
Roughness at layer 6/7 (Å)	16.76	5.89
Roughness at layer 7/8 (Å)	17.25	0.67
Roughness at layer 8/9 (Å)	16.90	2.61
Roughness at layer 9/bulk (Å)	15.71	0.80
1st layer SLD ($Å^{-2}$)	4.47×10^{-5}	1.18×10^{-4}
2nd layer SLD ($Å^{-2}$)	-2.55×10^{-5}	6.51×10^{-5}
3rd layer SLD ($Å^{-2}$)	5.31×10^{-5}	1.46×10^{-4}
4th layer SLD ($Å^{-2}$)	-1.46×10^{-5}	3.21×10^{-5}
5th layer SLD ($Å^{-2}$)	2.54×10^{-5}	1.08×10^{-4}
6th layer SLD ($Å^{-2}$)	-1.27×10^{-4}	1.24×10^{-4}
7th layer SLD ($Å^{-2}$)	1.70×10^{-4}	1.07×10^{-4}
8th layer SLD ($Å^{-2}$)	1.23×10^{-4}	1.38×10^{-4}
9th layer SLD ($Å^{-2}$)	1.61×10^{-4}	2.93×10^{-4}
Background SLD ($Å^{-2}$)	2.68×10^{-6}	1.83×10^{-6}

Once again negative input parameters were used for the generation of the SLD profile. This again is attributed to the large roughness values between the various interfaces and the limitations of the simple layer approach used.[20]

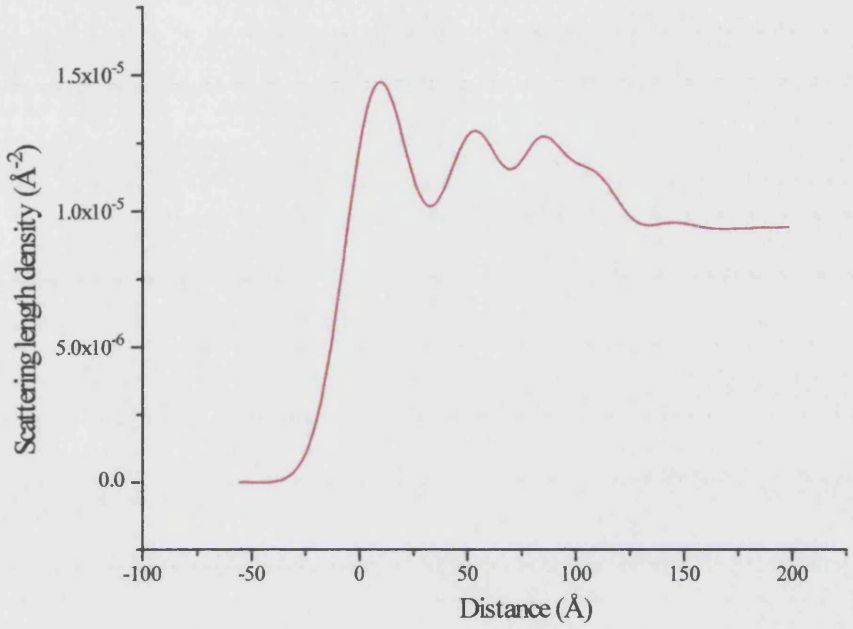

Figure 4.18 *Scattering length density profile for MCM-41 film grown for 48 hours without the presence of a PC monolayer.*

The SLD profile for the MCM system at 48 hours clearly shows the presence of three micellar layers. Once again there is a gradual loss of scattering length density with distance from the surface, reflecting a loss of ordering into solution.

4.3.6 Time Dependence Crystallisation

It is not within the remit of this chapter to present a full analysis of the structure as it evolves with time. We have presented a rather rapid change in the Bragg peak in Figure 4.4, and here in Figure 4.19 we simply show the change in thickness of the film as a function of time for the two systems investigated.

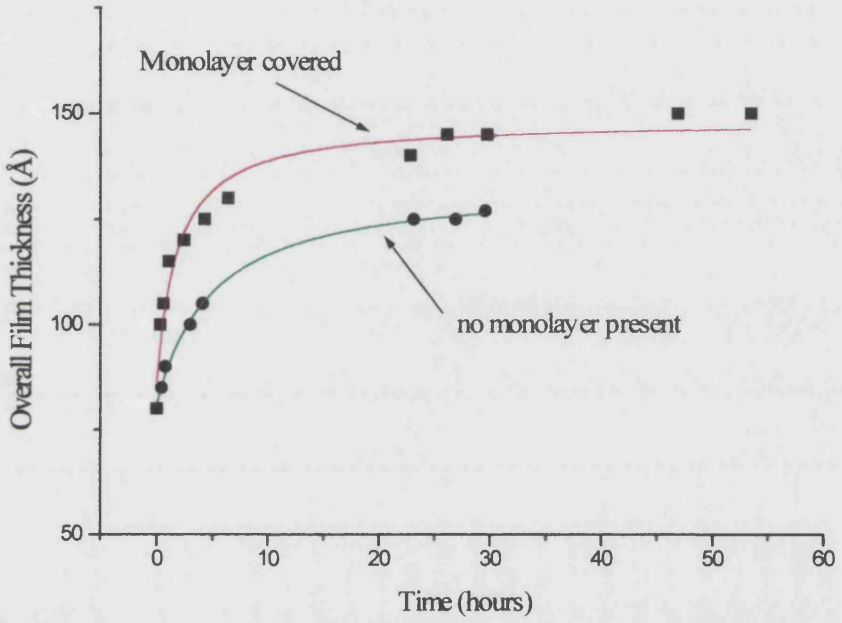

Figure 4.19 *Plot of film thickness versus time for MCM-41 deposition from a PC monolayer-covered and uncovered reaction solutions.*

Superimposed on each is a fit to the Langmuir isotherm equation for adsorption (Appendix Four), with *b* values for the MCM system and PC monolayer covered films of 0.2 and 0.55 respectively. Although this equation is derived for adsorption at idealised gas/solid surfaces, the *b* values in this case do not reflect the more rapid growth of the monolayer covered film, and the increased limited film thickness in this case.

The data must be regarded with some caution at short times, because the measuring time of *ca.* one hour to determine accurate fringe parameters is comparable to the rate of change of the distance. It is hoped that high intensity synchrotron radiation measurements will be able to resolve more detail in the rapid first phase growth.

4.4 Conclusions and Future Work

The results presented in this chapter have demonstrated that it is possible to obtain detailed information on the growth and structure of mesostructured MCM-41 silica films at the air/water interface using X-ray reflection. Spreading of a PC monolayer at the air/water interface enhances the rate of formation and quality of the thin films, suggesting that interactions between the lipid headgroups and molecular or supramolecular silica/surfactant species facilitate the assembly of the first layer of the film. Further work using a range of lipids and their associated phase behaviour is underway to elucidate these interfacial processes.

Interestingly, the data obtained from the reflectivity experiments could not be fitted with a model corresponding to a primary surface layer hemi-cylinderical micelles, as has been recently proposed by Yang *et al.*[8] as the initial stage in the nucleation of MCM-41 films from acidic solutions. Thus, under alkaline conditions, silica encased micelles are considered to constitute the first layer of MCM-41 film formed at the air/water or monolayer/solution interfaces.

There are several clear needs in extrapolating the results of this chapter. Firstly, the need to investigate changes in the sample environment which will overcome the self-limiting film thickness. This clearly means changing the saturation

conditions in order to change the rate of mass-transport to the interface. Also, it may be worth considering agitating the solution. The results presented in this chapter have followed the rate of growth of the films as a function of time, therefore other experiments that need to be undertaken are to follow the rate of crystallisation as a function of solution concentration, surfactant morphology and surface pressure of monolayer. Some of the structural ambiguity can be resolved by performing neutron reflection measurements. Using contrast variation it is possible to alter the scattering length density of the aqueous subphase by exchanging H_2O (a weak scatterer) for D_2O which scatters neutrons more strongly. Therefore it is possible to distinguish fully silicised layers from hexagonally close packed micelles. The density of the film may be related to the in-plane packing of the silica encased micelles, therefore by undertaking Brewster angle microscopy[22] measurements during the growth phase, it is possible to visualise any large scale density fluctuations in the monolayer. Further research on the structural relationship between the templating monolayer and the surfactant micelles needs to be undertaken. It is clear from the preliminary results presented in this chapter that there is some degree of ordering induced by the monolayer, but that this is only a perturbation on the overall growth pattern. Therefore, by increasing the strength of interaction between the monolayer and surfactant in the crystallising solution, *via* head group charge and size ratios, we will be able to more carefully modify the crystallisation behaviour.

4.5 References

1. Kresge, C.T., Leonowicz, M.E., Roth, W.J., Vartuli, J.C., and Beck, J.S. (1992). Ordered mesoporous molecular sieves synthesised by a liquid-crystal template mechanism, *Nature*, **359 (6397)**, 710-712.

2. Beck, J.S., Vartuli, J.C., Roth, W.J., Leonwicz, M.E., Kresge, C.T., Schmitt, K.D., Chu, C.T., Olsen, D.H., Sheppard, E.W., McCullen, S.B., Higgins, J.B., and Schlenker, J.L. (1992). A new family of mesoporous molecular sieves prepared with liquid-crystal templates, *Journal of the American Chemical Society*, **114 (27)**, 10834-10843.

3. Firouzi, A., Kumar, D., Bull, L.M., Besier, T., Sieger, P., Hue, Q., Walker, S.A., Zasadzinski, J.A., Glinka, C., Nicol, J., Margolese, D., Stucky, G.D., and Chemelka, B.F. (1995). Co-operative organisation of inorganic-surfactant and biomimetic assemblies, *Science*, **267 (5201)**, 1138-1143.

4. Huo, Q.S., Marglose, D.I., Ciesla, U., Demuth, D.G., Feng, P.Y., Gier, T.E., Sieger, P., Firouzi, A., Chmelka, B.F., Schüth, F., and Stucky, G.D. (1994). Organisation of organic molecules with inorganic molecular species into nanocomposite biphase arrays, *Chemistry of Materials*, **6 (8)**, 1176-1191.

5. Khushalani, D., Kuperman, A., Ozin, G.A., Tanaka, K., Garces, J., Olken, M.M., and Coombs, N. (1995). Metamorphic materials - Restructuring siliceous mesoporous materials, *Advanced Materials*, **7 (10)**, 842.

6. Koegler, J.H., Zandbergen, H.W., Harleveld, J.L.N., Nieuwenhuizen, M.S., Jansen, J.C., and Vanbekkum, H. (1994). Orientated coating of silicate-1 of gas sensor applications, *Studies in Surface Science and Catalysis*, **84 (part A-C)**, 307-314.

7. Jansen J.C., and Vandrosmalen, G.M. (1994). Orientated growth of silica molecular sieve crystals as support films, *Journal of Crystal Growth*, **128 (1-4)**, 1150-1156.

8. Yang, H., Coombs, N., Sokolov, I., and Ozin, G.A. (1996). Free-standing and orientated mesoporous silica films grown at the air/water interface, *Nature*, **381 (6583)**, 589-592.

9. Yang, H., Kuperman, A., Coombs, N., Mamiche-Afara, S., and Ozin, G.A. (1996). Synthesis of orientated films of mesoporous silica on mica, *Nature*, **379 (6567)**, 703-705.

10. Yang, H., Coombs, N., Sokolov, I., and Ozin, G.A. (1997). Registered growth of mesoporous silica films on graphite, *Journal of Materials Chemistry*, **7 (7)**, 1285-1290.

11. Yang, H., Coombs, N., and Ozin, G.A. (1997). Mesoporous silica with micrometer-scale designs, *Advanced Materials*, **9 (10)**, 811-814.

12. Thomas, R.K., and Penfold, J. (1996). Neutron and X-ray reflectrometry of interfacial systems in colloid and polymer chemistry, *Current Opinion in Colloid and Interface Science*, **1 (1)**, 23-33.

13. Sinha, S.K. (1996). Surface structure reflectometry with x-rays, *Current Opinion In Solid State and Materials Science*, **1 (5)**, 645-652.

14. Richardson, R.M., and Roser, S.J. (1987). X-ray reflectivity from insoluble monolayers spread on aqueous subphases, *Liquid Crystals*, **2 (6)**, 797-814.

15. Williams, N.A. (1996). X-ray reflection, BSc (Hons) Final Year Project, University of Bath.

16. Roser, S.J., Felici, R., and Eaglesham, A. (1994). Energy dispersive x-ray reflection from a liquid-liquid interface, *Langmuir*, **10 (10)**, 3853-3856.

17. Abélès, F. (1948). Sur la propagation des ondes electromagnétiques dans les milieux stratifiés, *Ann. Phys.*, **34**, 505-520.

18. Pedersen, J. (1992). Model-Independent determination of the surface scattering-length-density from specular reflectivity data, *Journal of Applied Crystallography*, **25 (2)**, 129-145.

19. Sims, S.D. (1997). Template directed synthesis of hybrid silica materials, PhD thesis, University of Bath.

20. Personal communication from Roser, S.

21. Hamley, I.W., and Pedersen, J. (1994). Analysis of neutron and X-ray reflectivity, *Journal of Applied Crystallography*, **27 (1)**, 29-35.

22. Meldrum, F.C., and Fendler, J.H. (1996). Construction of organised particulate films by the Langmuir-Blodgett technique. **In**: *Biomimetic materials chemistry* (Mann, S. ed.), pp 175-217. Cambridge: VCH Publishers (UK) Ltd.

CHAPTER FIVE

CADMIUM SULPHIDE BIONITES

5.1 Introduction

Within the field of biomimetics - in which scientists try to emulate natural processes for the fabrication of highly organised compounds, scientists are now turning to biology for novel and innovative ideas on how to fabricate these compounds. Nature has proved to be an extraordinary manufacturer of materials, from the bones in our hands to the seashells on a beach. Slowly, scientists are learning to mimic nature's processes.

Part of this imitation of nature's processes involves studying biomineralisation - the process by which hard bones emerge from soft tissues. In bone, an organic gel forms a lattice in which mineral crystals of hydroxyapatite take hold, giving rise to light, but strong skeletons. Therefore with the help of insights from biomineralisation, scientists may be able to fabricate materials with a wide variety of potential uses including sensing devices, electronics, magnetism, and so called intelligent materials, which can adapt to their changing environment.

Recent advances in the area of biotechnology by Mendelson[1] have provided new tools for the manipulation of biological materials and the fabrication of novel composite materials.[2,3] The basic idea put forward by Mendelson[1] is to employ bacterial cell walls *in situ* as a matrix for mineralisation and to draw the products into fibre-like materials. The use of mutant bacteria (which in general helps us to digest the food we eat, decompose waste and enrich soil) to fabricate materials is a new area of research, whilst mineralising the bacteria is novel. Due to the size of the bacterial cells, which are usually in the range of microns, scientists have not explored the

potential of bacterial cells, especially their cell walls for the fabrication of materials, or as models for material design. Mendelson quoted[4] "the bacterial cell wall is one of the most successful structures in the biological world. The question I am interested in is this: Can we make this material into something, and if so, what would its properties be? And are there any material design properties we can learn from these bacterial cells".

With this in mind the mutant bacterial cell wall can provide a very useful model of a self-organising, self-assembling system of a natural material. Bacteria make their cell walls from a curious material. Electrically active and physically resilient, the spongy, porous gel can shrink or swell, bend, twist, stretch, or shear, then resume its normal shape. An affinity for charged particles enables the wall to retain mineral deposits and form crystalline structures. By using the cell wall as a matrix for biomineralisation, hence acting as a "structural backbone", Mendelson termed these mineralised bacteria "bionite". The bacterium studied by Mendelson and employed in this study is a mutant form of *Bacillus subtilis*.

5.2 *Bacillus subtilis:* Structure and Composition

The bacterium *Bacillus subtilis* (Figure 5.1) is a rod shaped, Gram (+) organism. The cells are about 0.8 μm in diameter and up to 4 μm in length.[5] The bacterial cells are encased within a cell wall which is about 30-40 nm in thickness and gives shape and form to the organism and acts as a protective layer between the cell and its environment.[6] The cell wall consists of three regions: an inner layer, central zone and the outer fibrous surface. The cell wall provides constraints on form and size, as well as mechanical strength. The wall acts as a pressure vessel that restrains

the expansion, and potential rupture of the delicate cell membrane beneath it, caused by turgor pressure.[7] The cell wall is a dynamic structure, with new material being continually formed at the inner surface and shed at the outer surface. All metabolites, such as essential metals, organic nutrients and waste materials, must pass through this wall.

Figure 5.1 *SEM micrograph of individual Bacillus subtilis bacteria collected on a cellulose nitrate filter (courtesy of S.A. Davis, University of Bath).*

5.2.1 Cell wall Structure

The *Bacillus subtilis* cell wall is a gel-like viscoelastic material composed primarily of two cross-linked polymers: peptidoglycan, also called murein,[8] (an unusual polymeric material found only in bacteria, and is the main structural component in gram (+) bacterial cell walls), and teichoic acid[9] which is covalently linked to the peptidoglycan. The backbone of peptidoglycan consists of repeating dimers of β-(1,4)-linked *N*-acetyl-glucosamine (GlcNAc) and *N*-acetyl-muramic acid (MurNAc) arranged such as [...GlcNAc-MurNAc-GlcNAc-MurNAc...]. Each *N*-acetyl-muramic acid residue carries a peptide moiety (Figure 5.2a),[10] consisting of L-alanine, D-glutamic acid, *meso*-diaminopimelic acid and two D-alanine residues (L-Ala-D-Glu-*meso*-Dpm-D-Ala-D-Ala). Glycan chain lengths of 100 dimers are the building blocks of the cell wall. Individual peptides on adjacent polysaccharides strands can form direct linkages between the *meso*-diaminopimelic acid in position 3 from one peptide and the D- alanine in position 4 on another (Figure 5.2b).[11] Because the backbone is twisted, the peptides radiate at all angles creating the potential for cross-linking glycans into a complex network.[12] Approximately 35% of the glycan strands are cross-linked in this manner, creating a supra-molecular three-dimensional network around the whole cell, with unique mechanical properties.

The secondary polymer found in *Bacillus sublilis* is teichoic acid (Figure 5.2c). It is a linear glycerol polymer, substituted with D-glucose and occasionally D-alanine, and is joined together *via* phosphodiester linkages. The teichoic acid is covalently bonded to a number of peptidoglycan muramic acid residues and constitutes 50% of the weight of the cell wall. The teichoic acid is distributed on the

external surface of the cell wall, with about half of the molecules exposed and the remainder firmly embedded within the peptidoglycan matrix.[13]

Both peptidoglycan and the accessory polymer, teichoic acid are charged polymers. The peptide moiety of peptidoglycan carries both positively and negatively charged groups, whereas the teichoic acid polymer is negatively charged.

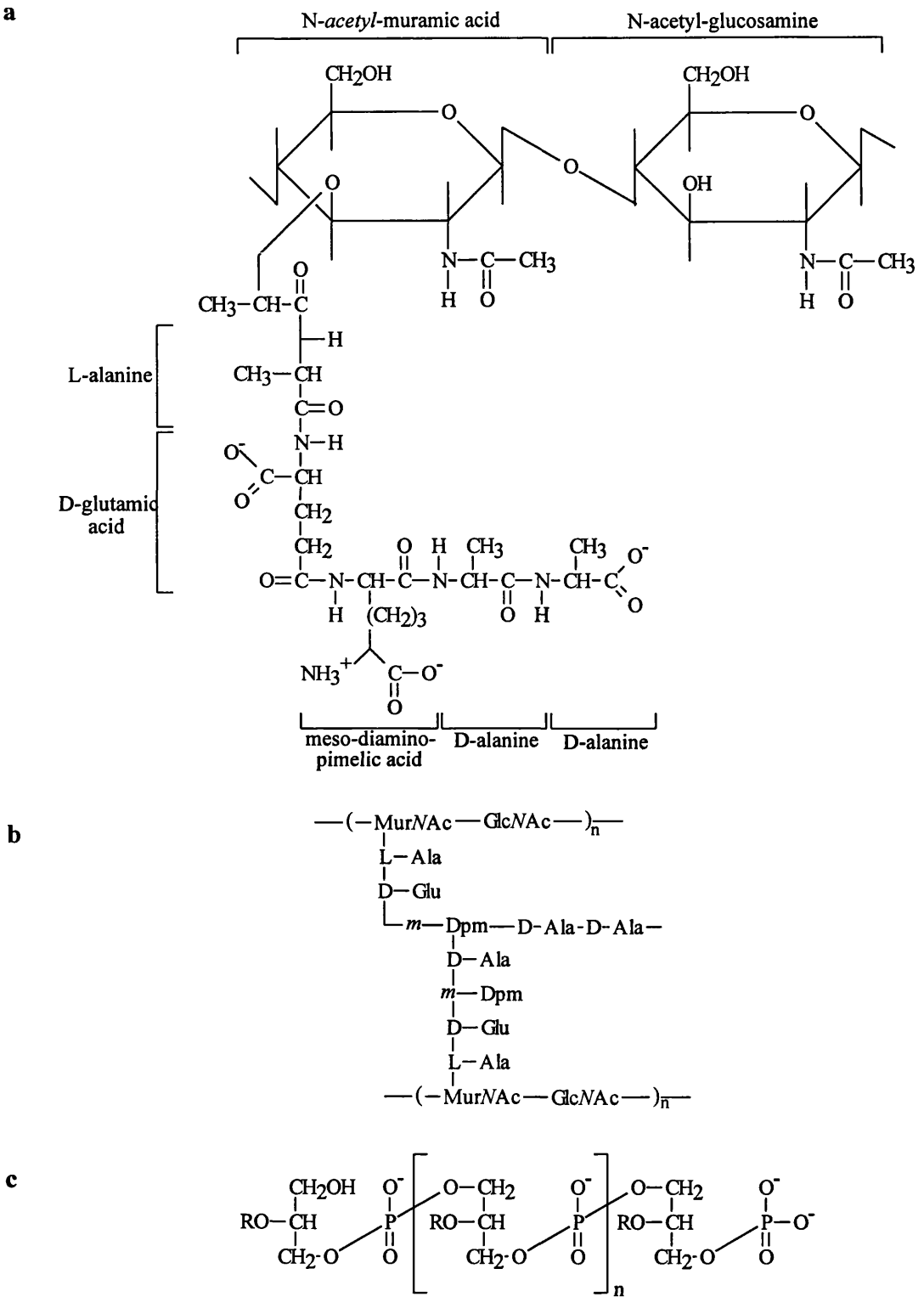

Figure 5.2 a) *The structure of Bacillus subtilis peptidoglycan, b) peptide cross-link between adjacent glycan strands, c) the structure of glycerol teichoic acid (R=H, D-alanine or D-glucose).*[10]

5.2.2 Metal Binding Properties

The two cell wall polymers of *Bacillus subtilis:* peptidoglycan and teichoic acid are thought to be the sites of metal binding. The overall negative charge density of the cell wall is conferred largely by the carboxylate groups of the peptidoglycan and the phosphate groups of the teichoic acid residues. Peptidoglycan also contain hydroxyl and amino functional groups. Each non-crosslinked peptide has three free carboxyl groups (present on D-Glu, *m*-Dpm and the terminal D-Ala) and a free amino group (on *m*-Dpm). Cross-linked peptides have five free carboxyl groups and one free amino group, they lack an amino group from the *m*-Dpm involved in cross-linking and a carboxyl group from the terminal D-Ala liberated on cross-linking.[11]

Due to the nature and bonding of the peptidoglycan and teichoic acid polymers, the cell wall has a porous open structure with a corresponding high surface area. The cell wall has an isoelectric point of approximately pH 3-4. Hence, the cell wall is electronegative at neutral pH.[14] The overall distribution of charge for most isolated *Bacillus subtilis* cells is symmetrical over the inner and outer walls. (Studies on peptidoglycan showed that it had the properties of an amphoteric polyelectrolyte, therefore by the titration of ionisable groups[15] or changing the ionic strength of the surrounding solution,[16] the polymer gel could be made to shrink or swell).

This high negative charge density of *Bacillus subtilis* cells is responsible for its strong metal binding capacity. The binding capacity of cations in the cell walls is usually very high. Values as high as those from numerous commercial ion exchange resins (3.5 milliequivalents per gram) have been reported by Marquis *et al.*[8] In order for the living cell to stabilise the cell walls, counterions must balance the charge of the anionic groups. Beveridge and Murray[17] determined a metal binding affinity series for

Bacillus subtilis cell walls. This series indicated that metal cations such as Mg^{2+}, Fe^{3+}, Cu^{2+}, Na^{+} and K^{+} are preferentially bound, whilst cations such as Mn^{2+}, Zn^{2+}, Ca^{2+}, Au^{3+} and Ni^{2+} are bound in somewhat smaller amounts. In certain cases, for example in the case of iron and gold, the final amount bound was in excess of the amount expected on the basis of stoichiometry. This is due to the formation of precipitates which can build up on and within the cell wall. Within the living cells, the surface precipitates are generally larger than those that develop within the constrained environment of the cell wall.

The metal binding capacity is reduced at low pH, as protons compete with the metal cations for the same site.[14] Protons are continuously pumped in to the cell wall as part of the metabolic process in living cells. Therefore, the number of metal binding sites available is far greater for dead cells than it is for metabolising cells.[18,19] Even though peptidoglycan and teichoic acid contribute to metal binding sites,[14] it is the carboxylate groups of the peptide glutamic acid that seems to be the most important site for metal. Copper (II) preferentially binds to the electropositive amine groups present in the cell wall, as opposed to the carboxylate groups on peptidoglycan because it forms an anionic complex in water.[11] In general the metal binding properties of Gram (+) bacteria are about ten-fold greater than Gram (-) bacteria such as Escherichia coli.[20]

5.3 Bacterial Filaments

Bacterial filaments of *Bacillus subtilis* are organised multi-cellular assemblies of bacterial cells. In order to produce these filaments, one needs to be able to get individual bacterial cells organised and connected to one another, rather than dispersed as single discrete cells. Mendelson decided rather than to attempt to construct these filaments by putting the individual cells together, he would prevent the normal cell separation mechanism from taking place within the cell. This was done by reducing the autolysin activity (specific enzymes which cleave peptidoglycan) within the mutant strain, so that cell separation is repressed. Therefore, by blocking cleavage of the cross-wall down its centre (which occurs as a part of the cell division cycle) it will force the cell not to separate, hence growth is *via* cylinder elongation at constant diameter.[21] After septation, no cell seperation occurs, resulting in the formation of long bacterial filaments (Figure 5.3). Because rod shaped cells grow only in length, filaments derived from them are long cylindrical objects. Every cell in the filament is aligned along the filament axis and can grow and divide into two progeny that will then repeat the process, and so on until other factors limit further growth.

The resulting filaments contain thousands of cylindrical individual cells[22] that have the ability to twist like a screw. The mutant strain of *Bacillus subtilis* is used in this way to produce two distinct types of fibre, bacterial macrofibres,[4] and bacterial thread. The two types of fibre are differentiated by the mode of organisation of the bacterial filaments: bacterial macrofibres are self-organising structures within the growth medium, whereas bacterial thread is a physically processed form.

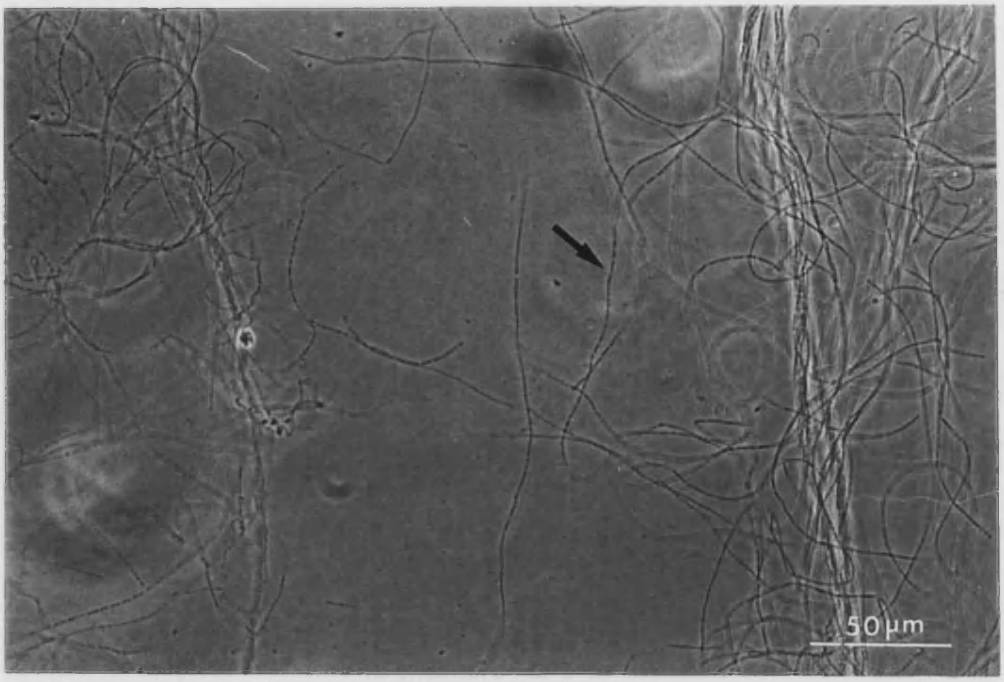

Figure 5.3 *Phase contrast micrograph of Bacillus subtilis showing multi-cellular filaments (arrow) (courtesy of S.A. Davis, University of Bath).*

5.3.1 Bacterial Macrofibres

The bacterial macrofibres are self-organising multi-cellular structures which consist of helically twisted bundles of bacterial filaments that can grow up to a centimetre in length,[23] but are usually only a few millimetres. They are produced by the individual bacterial filaments twisting, coiling, and bending back on themselves, so that the bacterial colonies create fibrous coils, which will eventually weave themselves into bacterial macrofibres. Twist is constantly produced throughout the

process by the geometry of cell growth. A multi-cellular filament writhes as it elongates, until eventually it touches itself. The loop so formed eventually twists on itself hereby creating a double-helix structure with a loop at one end and the two free tails at the other. When a filament touches itself, the turning motions associated with twist become impeded. The resulting forces serve to deform the cylindrical shape in the helix. A double-helical filament also grows, twists and writhes until it too touches itself. This in turn leads to the folding and twisting together of the double-helical filament into a four-stranded structure. Each time a structure folds and twists together it generates a new structure that contains an increased number of filament strands in its shaft. A summary of the process is shown in Figure 5.4[21] and a bacterial macrofibre is shown in Figure 5.5.

Chiral form and the degree of twist of the bacterial filaments is under genetic and physiological control.[24] Therefore, Briehl and Mendelson[25] showed it is possible to control the degree of twist and the growth of all bacterial macrofibres into the same helix hand by given environment conditions, and they perpetuate their state from generation to generation, so long as the environment remains constant.[25] Any given fibre can be made to change its twist state or invert its helix hand, simply by changing the environmental growth conditions, such as growth temperature or the concentration of ions in the growth medium. Once the new state has been achieved it will be passed from parent to progeny, if the environmental conditions are maintained. So in summary, the environment can be made to set the form of a bacterial macrofibre while the cell produces the detailed product: in this case some strains can be manipulated to display the entire range of macrofibre twist states from tight right handed to tight left handed bacterial macrofibres.

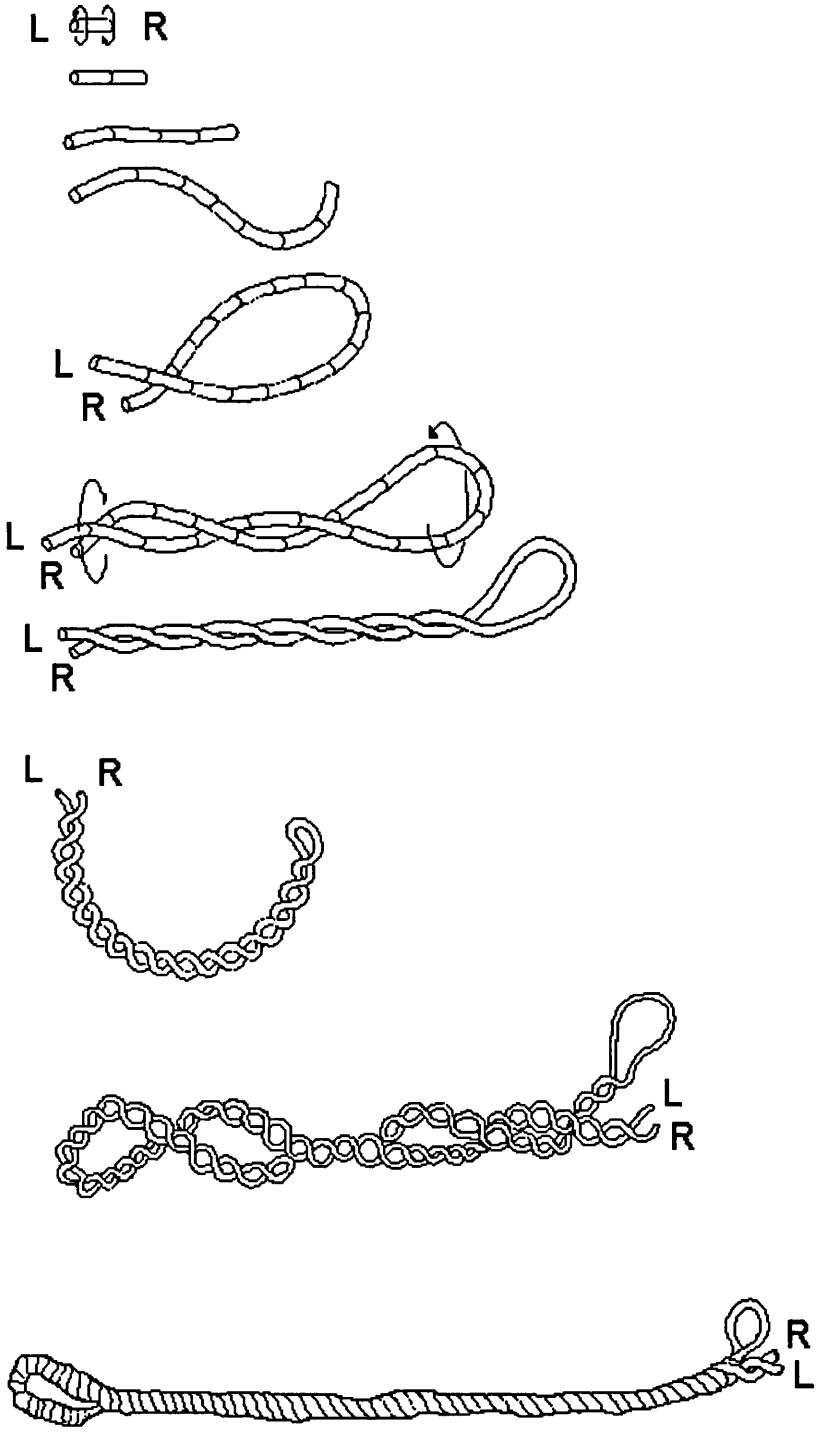

Figure 5.4 *Diagram of the initiation of macrofibre formation by writhing.*[21]

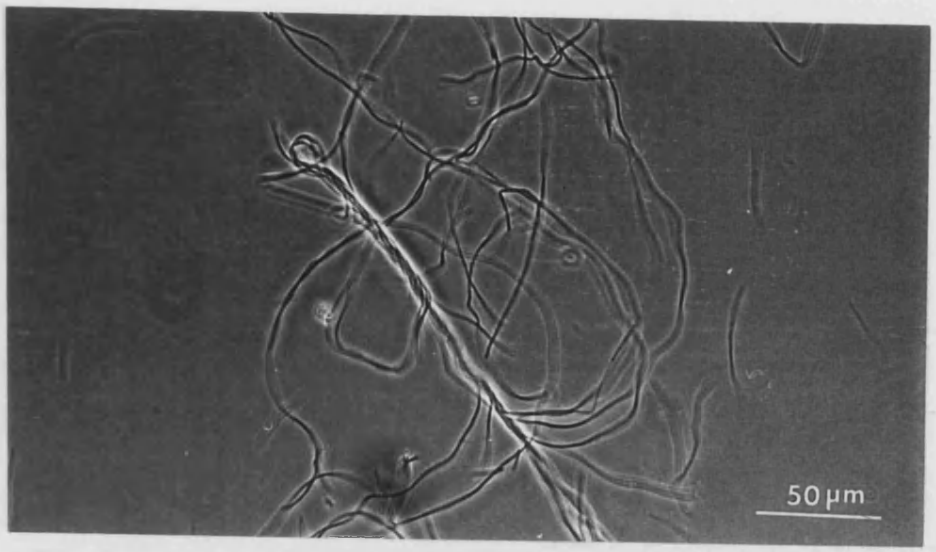

Figure 5.5 *Phase contrast micrograph of a bacterial macrofibre (courtesy of S.A. Davis, University of Bath).*

5.3.2 Bacterial Thread

The same *Bacillus subtilis* bacteria that produces the macrofibres described in section 5.3.1, can be cultured differently to yield individual filaments. Each of these filaments consist of about 300 cells along its length. The filaments in these cultures pass through a stage, where they do not fold or twist together, but rather form's a organised network resembling a textile web, visually shown in Figure 5.6.

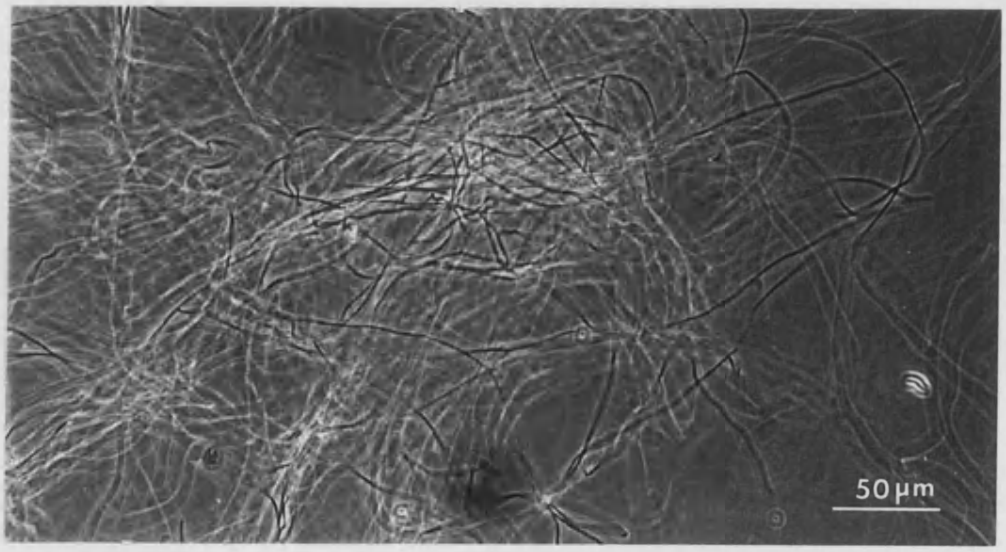

Figure 5.6 *Phase contrast micrograph of a textile web (courtesy of S.A. Davis, University of Bath).*

From these frothy web cultures, Mendelson has devised a technique to tease, delicate bacterial threads. With a gentle tug, it is possible to draw mechanically or manually, uniform metre long threads from a 10 cm^3 web culture at this stage of its growth. The individual fibres feed radially into a cone-shaped structure at the fluid/air interface of the culture medium, where they become compressed together into a thread upon drawing. The air-dried bacterial thread contains the bacterial filaments aligned parallel to the thread axis. A typical bacterial thread can contain about 50 000 cell filaments, arranged within a circular cross-section which is produced as the drawn thread dries[26] and it also has an excess of 10^{10} cells, arranged as a hierarchy of cylinders; cell-filament-thread.[27] Figure. 5.7 shows that along the fibre axis there is a high degree of alignment of the cellular filaments and the packing relationships of the cellular filaments within the interior, indicating that cell filaments in bacterial thread are tightly bound to one another. Figure 5.8 shows a bacterial thread viewed down a light microscope and Figure 5.9 shows the organised arrangement of the component multi-cellular filaments.

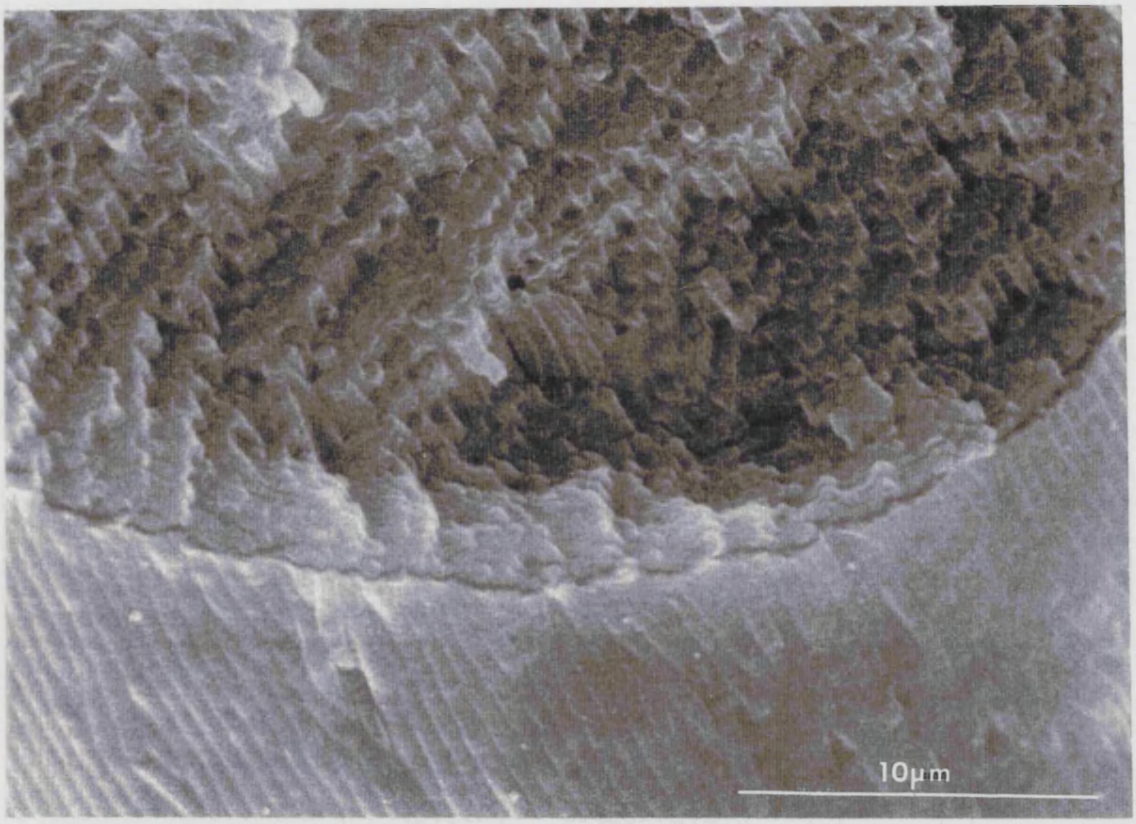

Figure 5.7 *SEM micrograph showing a cross-section of a bacterial thread.*[20]

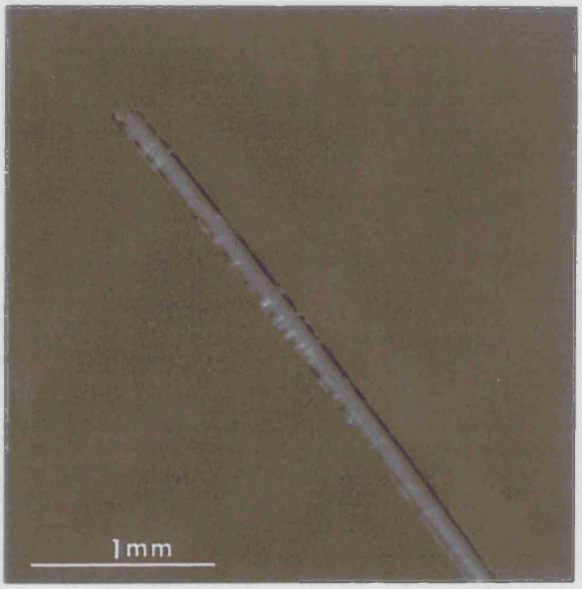

Figure 5.8 *Light micrograph of bacterial thread (courtesy of S.A. Davis, University of Bath).*

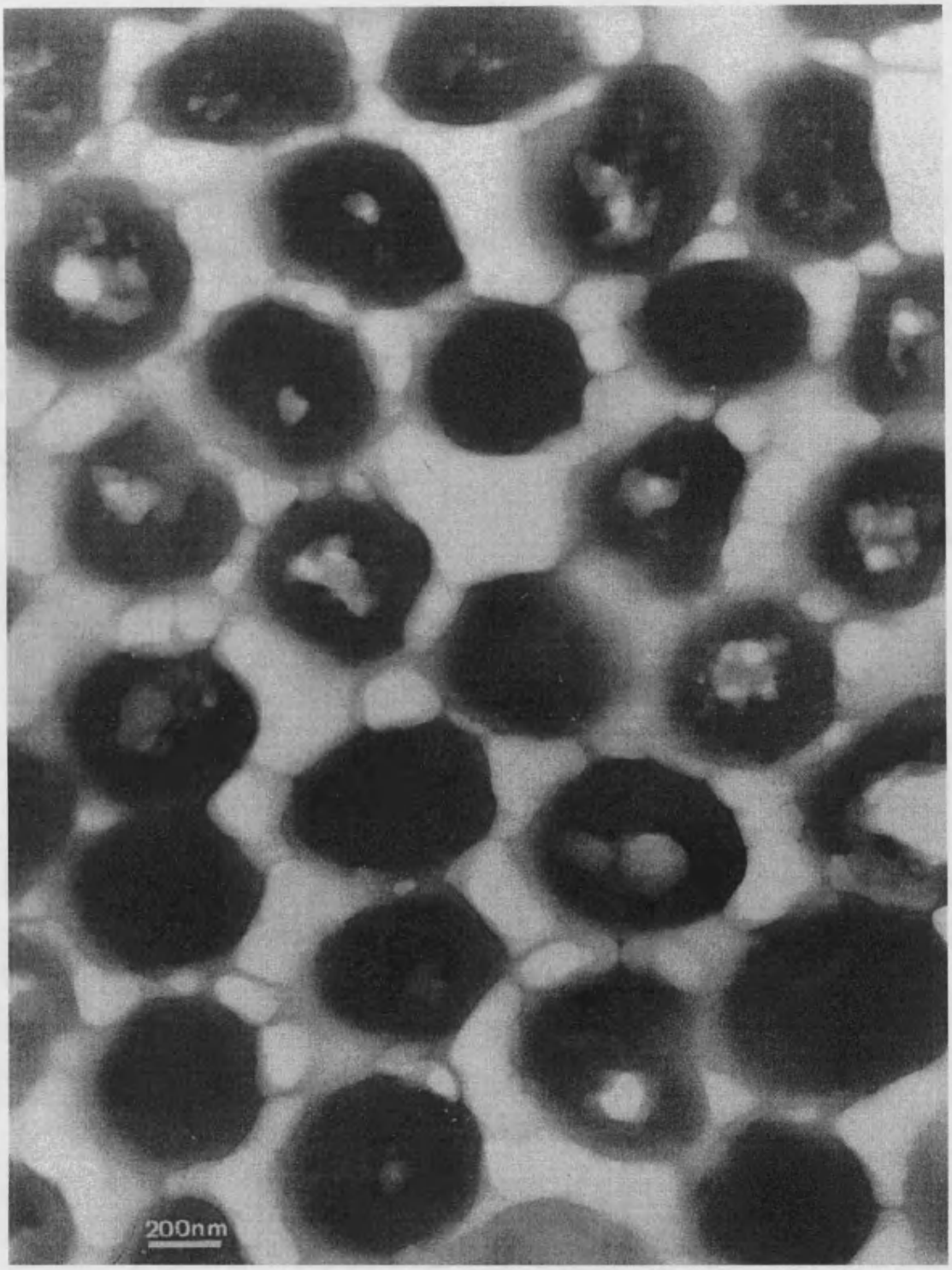

Figure 5.9 *TEM micrograph of a thin section of a bacterial thread of Bacillus subtilis (courtesy of S.A. Davis, University of Bath).*

When the bacterial thread is hydrated, it swells to approximately 1.4 times its dry length and 1.2 times its dry diameter. Although the individual filaments separate upon withdrawing the thread from solution, the "washed" filaments once again become compressed together on drying, to form the bacterial thread. However, if the bacterial thread is placed in organic solvents, it does not swell. The threads remain intact and can be recovered as fibres after removal from the solvent. With these observations it is feasible to do *in-situ* chemistry on cellular filaments that are organised into a bacterial thread.

5.4 Bionites

The production of mineralised bacterial threads, termed bionites is based on the electrostatic and porous nature of the bacterial cell wall. These properties enable counter-ions to build up within the cell wall gel and charged materials to bind to the wall. So the cell wall can serve as a molecular cage within which crystals can be grown, as well as a template on which deposition of solids can occur. The drawing process, where individual cell filaments assemble into a cohesive fibre serves to trap solution within the cell wall and this solution may bind to the outer wall surface of each filament cell in the form of a fluid film. Particulate material of appropriate size, entering at the cone at the fluid/air interface can also be drawn into the fibre to form inclusions between cell filaments in the final dried product. The drying process is important since the cell wall gel becomes compacted and the cell filaments become further compressed together into the fibre assemblage and crystallisation occurs in and on the fibre surface, depending upon which ions are present. The final appearance and

properties of the bionite are dependent upon the composition of the inorganic solid it carries within.

The bionites described previously by Mendelson[23] were produced using two methods. The first reported method added the soluble metal salts, such as $CaCl_2$, $FeCl_3$, or $CuCl_2$, directly to the washed web cultures of *Bacillus subtilis*. Then the web was drawn into a fibre and left to air dry. In second method, the addition of Ca and Fe salts to unwashed webs resulted in the formation of precipitates on the bacterial filaments within the web culture. When the web was drawn into a fibre, the mineral phase, $CaCO_3$ and Fe_2O_3, was found to be present throughout the fibre and the metal content of the composite was found to be 10-16 wt%. No precipitation was observed on the filaments, prior to drawing into the fibre when washed webs or copper salts were used. These bionites have a lower metal content compared to the first reported method. The mineral formed in these cases were produced solely by the dehydration of the entrapped salt solution.

5.5 Aims

The aim of this section of work is to investigate the potential for using the bacterial thread for the production of fibre-like composite materials. The primary interest is to exploit the underlying organisation of the bacterial thread as a template for producing composites with an extended, ordered microstructure. In order to achieve this, the potential for loading the bacterial thread with inorganic particles was investigated (cadmium in this case). Pre-formed bacterial thread was used, providing a different approach from Mendelson's previous studies and is described by Davis.[1,10,28] In terms of biomimetic strategies, the approach taken can be thought of as inorganic replication of a pre-formed, highly organised organic template.

5.6 Experimental

The following techniques were used to characterise the bacterial thread and the cadmium sulphide bionites, in addition to those described in chapter two.

X-Ray diffraction (XRD)

Whole bionite samples were analysed using a Phillips X-ray powder diffractometer with Cu K_α (λ = 1.5405 Å) radiation.

UV-vis absoportion spectroscopy

UV-vis measurements were carried out on a Lambda 11 UV-vis spectrometer with a holographic concave grating with 1053 lines mm^{-1} in the centre. The radiation source is a deuterium and halogen lamp (λ = 200-900 ± 0.5 nm).

Light microscopy (LM)

Samples were placed on the stage of an Zeiss Axioscope light microscope and viewed at various magnifications, with the images being recorded on an 35 mm camera.

Scanning electron microscopy (SEM) and elemental analysis (EDXA)

All samples were studied using a JEOL 6310 SEM operating at a voltage of 15 KeV. The SEM is fitted with a LINK Li drifted, silicon type light element detector which allows for semi-quantitative measurements of elements down to Z = 5-6 (B-C). Spectra are accumulated and then processed by a LINK AN1000 X-ray micro-analysis system. Samples were prepared in two ways:

(1) Air-dried samples were mounted onto aluminium stubs, using circular carbon sticky pads, to enable the surface texture of the sample to be studied. Energy dispersive x-ray analysis (EDXA) spectra were generally recorded from the surfaces of uncoated samples. Prior to obtaining micrographs, these samples were gold coated in an Edwards S150B sputter coater, for 4 minutes.

(2) Resin embedded samples, from which thin sections had been cut, were mounted onto aluminium stubs using colloidal graphite paste. This enabled the sample to be viewed in cross-section. To minimise the effects of charging, the samples were gold coated for 2 minutes. Then a colloidal graphite paste was applied to the resin blocks between the gold coat and the stub to enhance the electrical conductivity. Elemental analysis maps were generated and corresponding secondary electron images were obtained.

Transmission electron microscopy (TEM) and electron diffraction (ED)

Samples were prepared for TEM studies as follows. A portion of the bionite fibre was dehydrated for 1 hour in 50 cm^3 of 50:50 $MeOH/H_2O$ to which 0.5 cm^3 silane had been added, to aid adhesion between the resin and the sample. After air-drying the bionite fibre for 1.5 hours, it was transferred to a sample bottle, covered in premixed hardener 812 hard resin (supplied by TAAB Laboratory Equipment), and placed in a rotator for at least 12 hours, in order to allow infiltration of the resin into the fibre. The fibre was then placed in an embedding mould and covered with fresh resin, which was then allowed to polymerise in an oven at 60 $^{\circ}C$ for 2 days.

Sections were prepared using a freshly prepared glass knife on an OMU3 Ultramicrotome. Thin sections were cut perpendicular to the fibre axis to a thickness of typically 60-150 nm (silver-gold inference colours). TEM imaging and selected area electron diffraction studies were carried out on a JEOL 2000FX TEM, operating at an accelerating voltage of 200 KeV. Corresponding EDXA spectra were also obtained. All spectra contain copper peaks due to the support grid.

5.6.1 Preparation of *Bacillus subtilis* Bacterial Threads

Bacterial threads of *Bacillus subtilis* were supplied by Neil H. Mendelson (Department of Molecular and Cellular Biology, University of Arizona, Tucson, USA). They were cultured in the following way. Web cultures were grown at 20 °C in conical flasks containing 100 cm^3 of TB medium, which consists of 10 g l^{-1} tryptose; 3 g l^{-1} beef extract; and 5 g l^{-1} NaCl. This medium was supplemented with uracil[24] to give a final uracil concentration of 20 μg cm.[29] Cultures were inoculated by sterile pipette transfer from the previous fluid grown culture. *(Nb.* The initial fluid culture was inoculated from a culture grown in dishes on tryptose blood agar base (TBAB) medium). The cultures were then left to grow in web for 24-48 hours.

The web culture was then filtered through a 0.2 mm, 47 mm diameter cellulose nitrate membrane filter. The filter is then placed in a petri dish and the web was resuspended in 10 cm^3 of 0.1 M NaCl/0.015 M NaH_3 solution. Bacterial thread was produced by slowly drawing out the web from solution using tweezers or a thin wire hook, and then leaving the threads to air dry.

5.6.2 Preparation and Characterisation of Colloidal CdS

Preparation of Colloidal CdS

The following method was utilised to produce the CdS colloids[30] and was performed by Miss Gabriella Franco (PhD student, University of Bath); Cadmium acetate (2.712 g, 0.0118 moles), thiourea (0.263 g, 0.00346 moles) and thioglycerine 3-mercapto-1,2-propanediol (0.945 cm^3, 0.0113 moles) were mixed together with dimethylformamide (DMF) (200 cm^3) for approximately 1 hour, under a flow of argon. Then the mixture was heated (100-130 °C) for 20 minutes, then allowed to cool for 30 minutes, before it was heated once again. This heating-cooling cycle was repeated three times. On the third heating cycle, a white precipitate was seen to form. The heating process is of importance, since it serves to generate S^{2-} ions. The experiment is difficult to perform, and in order for success it is important to have clean glassware, an oxygen-free environment and the chemicals used are of the highest purity.[31] The precipitate was then separated by centrifugation, and then washed firstly with acetone, then diethylether and finally dried *in vacuo*. The washing procedure is of importance as it will wash away any residual Cd^{2+} ions.

Structure of the Colloidal CdS

In the preparation of the colloidal CdS, the cadmium source is from the cadmium acetate, and the sulphur source is the heated thiourea. The thioglycerine 3-mercapto-1,2-propanediol acts as a stabiliser, which protects the colloid by increasing the repulsive component of the free energy and hence avoiding flocculation. A schematic representation of the colloidal CdS and stabiliser is shown in Figure 5.10.

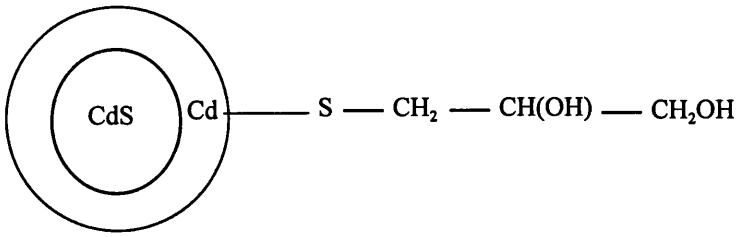

Figure 5.10 *Schematic representation of the colloidal CdS and stabiliser.*

The external Cd-S ligand has a strong covalent bond, hence not all of the Cd atoms on the surface will be capped, given the large size of the thiol,[32] causing an anisotropic capping of the colloid.[33] Furthermore it is important to note that the CdS ligand is responsible for the surface energy defects, which will be highlighted *via* absorption spectrum analysis.

It is important to note that the CdS nanoparticles prepared have a tendency to crystallise. XRD measurements of the nanoparticles obtained from the mother solution (Figure 5.11) showed that the CdS nanoparticles adopt a zinc blende structure, by the (111), (200), (220) and (311) reflections.[33] The broadening of the peaks is attributed to the small size of the particles.

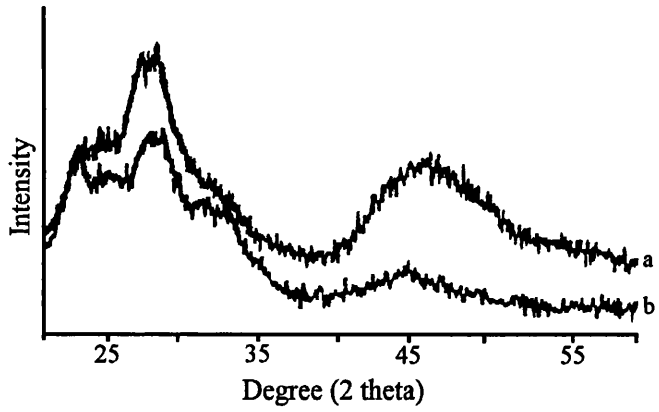

Figure 5.11 *XRD pattern of colloidal CdS nanoparticles (a) as a powder and (b) as a film (redrawn from Chemseddine, A.).*[33]

Characterisation of Colloidal CdS

UV-vis absorption measurements were used to characterise the colloid. Firstly the colloid was redissolved in DMF, and then deposited in quartz cuvette. Absorption measurements were taken between 250-600 nm at a scan speed of 30 nm min^{-1} and the resulting spectra is shown in Figure 5.12.

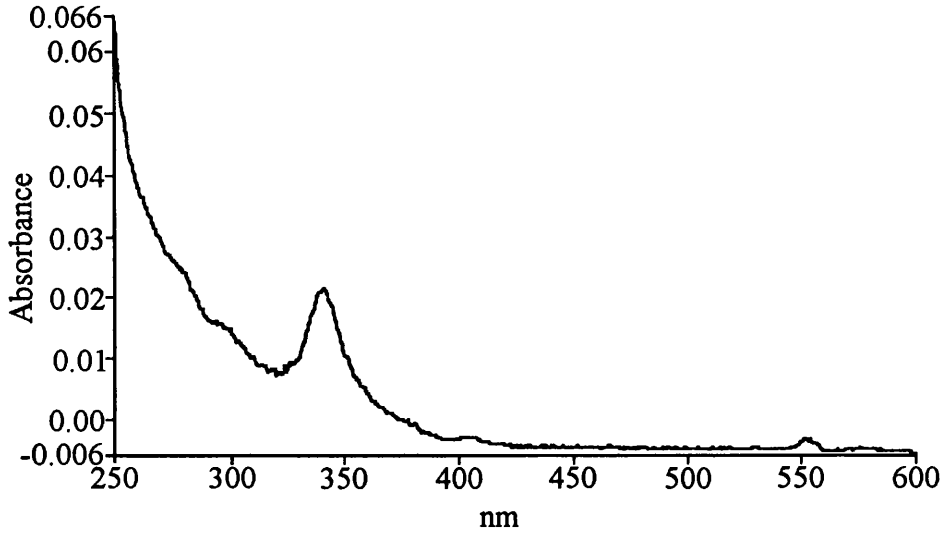

Figure 5.12 *Uv-vis absorption spectra for the colloidal CdS nanoparticles.*

From the above absorption spectra, by knowing the onset energy of the absoption band at 335 nm, the radius of the colloid can be calculated. The radius of the colloid was found to be 3.7 ± 0.7 nm as calculated by Miss Gabriella Franco.

The overall charge on the CdS colloidal particles is negative at neutral pH, due to the presence of the mercapto entity on the surface of the CdS. The colloidal CdS sol used in the experiments has a pH of 9.45, which is above the point zero charge (pzc) of the colloidal CdS particles (pH at 5.7).[31]

5.6.3 Preparation of *in-situ* CdS Bionite

Bacterial threads produced from the mutant strain of *Bacillius subtilis* were provided by N.H. Mendelson (Department of Molecular and Cellular Biology, University of Arizona, Tucson, USA). These threads were cultured in a tryptose blood agar based medium containing 20 mg ml^{-1} of uracil[10] for 18 hours at 20 °C. A 2 inch piece of bacterial thread, firmly held at one end by a pair of tweezers, was dipped into a vial containing purite water for 1 hour. After an hour the bacterial thread was drawn from the water and allowed to dry for a further hour. Once the bacterial thread was dry, it was rehydrated in a 1.0 M $CdCl_2$ solution (supplied by Aldrich) for 2 hours. After this time the bacterial thread or bionite was once again redrawn, this time from the cadmium solution and allowed to dry overnight. Care must be taken to draw the bacterial thread out of each solution as a thread rather than a ball.

Once the $CdCl_2$-loaded bionite was allowed to dry, it was placed on a carbon coated SEM stub. This stub in turn was placed in an dessicator, together with a glass vial containing a 1 cm^3 piece of Na_2S (supplied by Aldrich) and 5 cm^3 of purite water. Then 0.5 cm^3 of dilute HCl was pipetted into the glass vial and the lid placed on to the dessicator and left to stand. Every two days the amount of Na_2S and dil. HCI were replenished in order for the $CdCl_2$-bionite to be exposed to a constant supply of H_2S gas. The Cd-bionite was left in an environment of H_2S for 7 days.

5.6.4 Preparation of Colloidal CdS Bionite

The bacterial threads were washed as stated in section 5.6.3 and left to dry. Once the bacterial thread was dry, it was dipped into the colloidal CdS solution where it was left for 2 hours. After this time the bacterial thread was withdrawn from the

solution and allowed to air dry for a further hour. Care must be taken to draw the bacterium out of the solution as a thread rather than a ball.

5.7 Results and Discussion

Firstly, a full characterisation of the unmineralised bacterial thread provided by N.H. Mendelson was undertaken, as well as a characterisation for the washed bacterial thread, before analysis of the two CdS bionites was performed.

5.7.1 Characterisation of Unmineralised Bacterial Thread

The bare dry bacterial threads are off-white in colour and have a diameter of 10-20 μm. SEM and EDXA analysis (Figures 5.13, and 5.14, respectively) of the threads show that potassium, chloride and phosphorous ions are present in large quantities.

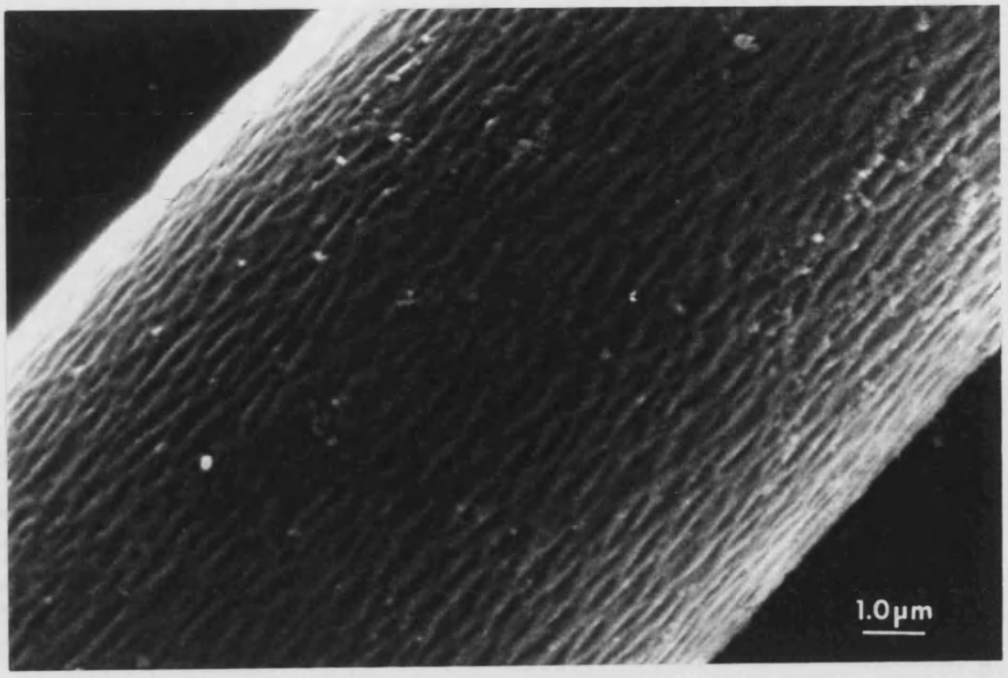

Figure 5.13 *SEM of a bare bacterial thread.*

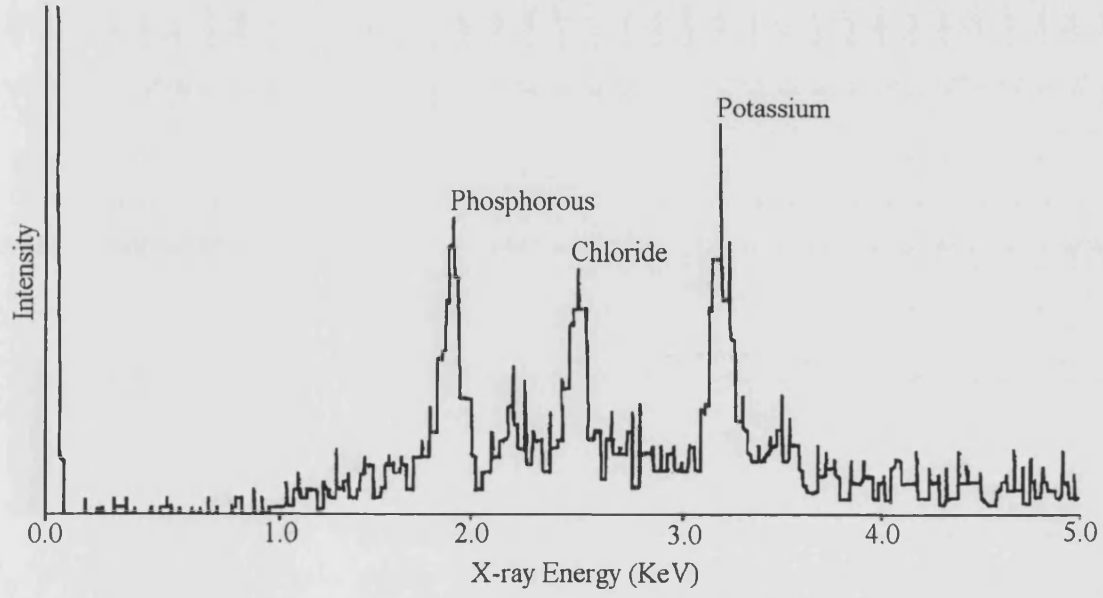

Figure 5.14 *EDXA spectra of a bare bacterial thread.*

The phosphorous ions can be attributed to the glycan backbone of the bacterial cell wall, while the potassium and chloride ions are present in the thread from the culture medium in which the threads were grown. The potassium and chloride ions appear to have coated the surface of the bare bacterial thread, since the bacterial. filaments on the surface of the thread cannot be seen.

5.7.2 Characterisation of washed, Unmineralised Bacterial Thread

Once the bare bacterial thread is washed, by placing the thread in water for 3 hours and re-drawn, the SEM and EDXA analysis (Figure 5.15 and Figure 5.16, respectively) show that the potassium and chloride ions are still present, but in reduced quantities.

Figure 5.15 *SEM of the washed bacterial thread.*

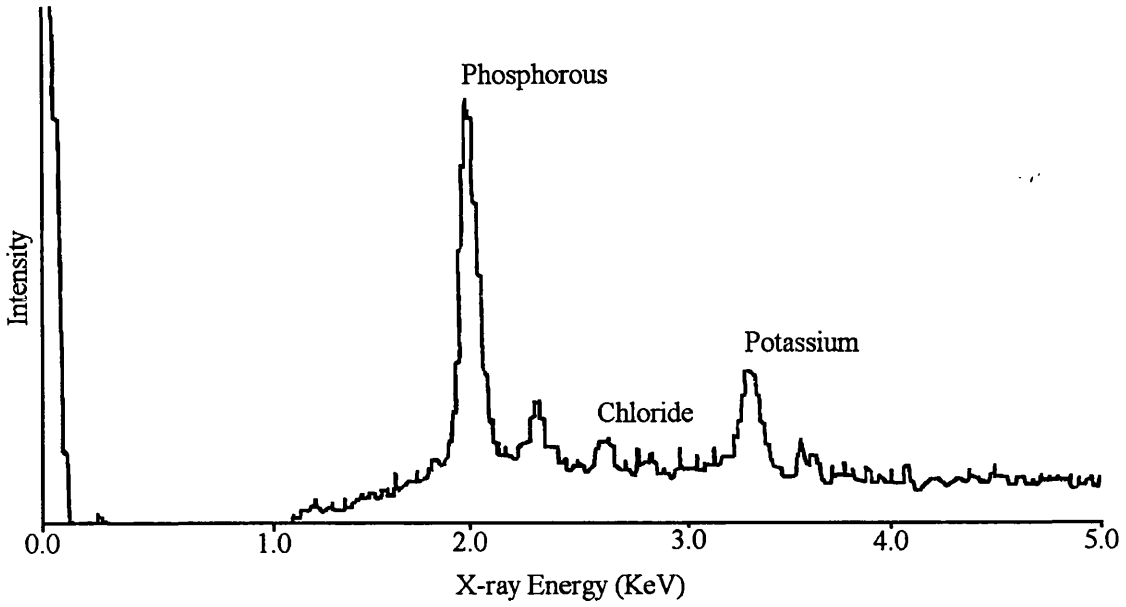

Figure 5.16 *EDXA spectra of the washed bacterial thread.*

The SEM micrograph of the washed bacterial thread shows that the potassium and chloride ions which coated the surface of the thread have been washed away and the bacterial cellular filaments and the individual bacterium cells are now visible. Therefore, extensive washing of the bare bacterial thread removes some of the potassium and chloride ions, but does not remove it completely as some is still bound to the charged groups of the bacterial filament cell walls. The phosphorous concentration remained constant as one would expect.

5.7.4 Characterisation of *in-situ* CdS Bionite

Once the bare bacterial thread is washed and allowed to dry, it is rehydrated by dipping into a 1 M $CdCl_2$ solution. After dipping for 2 hours, the thread dries to form a brittle, brilliant-white fibre (now termed a Cd-bionite) of similar diameter to the bare bacterial thread. SEM and EDXA analysis (Figures 5.17 and 5.18,

respectively) of the surface of the Cd-bionite shows that it has been loaded with $CdCl_2$.

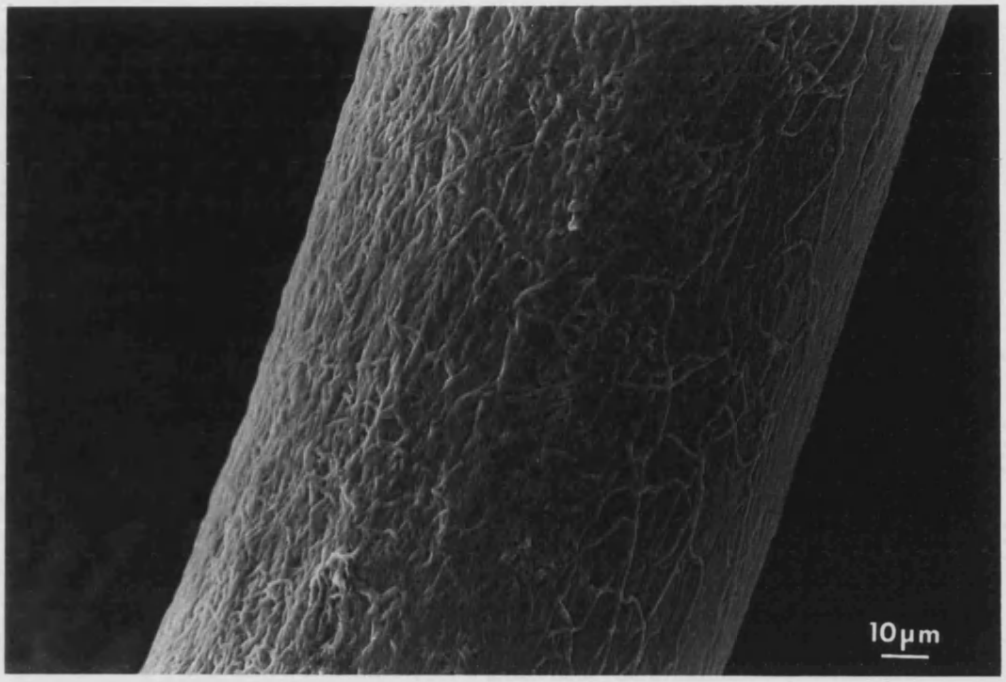

Figure 5.17 *SEM of the Cd-bionite.*

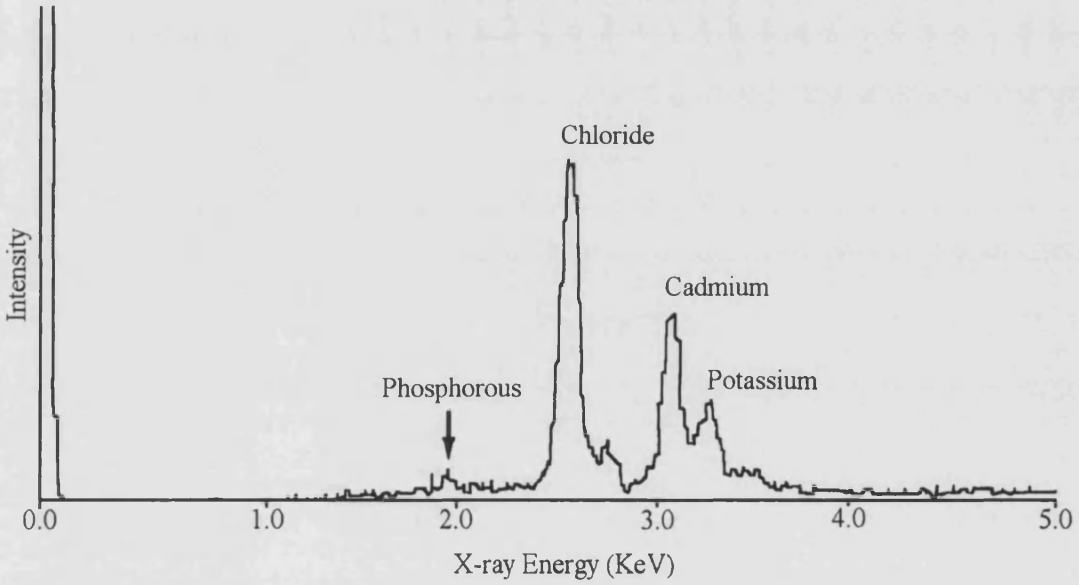

Figure 5.18 *EDXA spectra of the Cd-bionite.*

The appearance of the fibre in cross-section seemed to indicate the presence of $CdCl_2$ throughout the interior of the bacterial thread and the technique of x-ray mapping, qualitatively confirmed that $CdCl_2$ is present throughout the width of the Cd-bionite with a thicker coating on the outer surface (Figure 5.19).

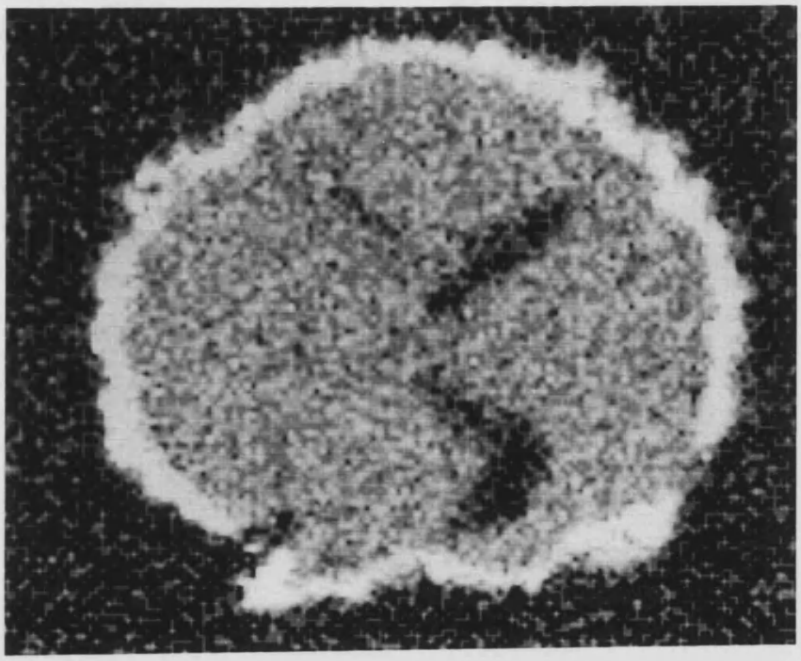

Figure 5.19 *Qualitative elemental map of cadmium obtained from a cross-section through a Cd-bionite (areas containing cadmium appear bright).*

When the dry bacterial thread is dipped into 1 M $CdCl_2$ solution, it swells due to rehydration as the solution penetrates into the thread. The component cellular filaments unravel and are exposed to the cadmium ions. These ions adhere to the highly charged groups present in the bacterial cell wall, which are known to act as metal binding sites. On drying the cellular filaments, coated with cadmium ions pack together to form a fibrous composite with the inorganic phase filling all available space between the filaments.

Once the Cd-bionite was exposed to H_2S, the brilliant-white Cd-bionite turned yellow due to the formation on the surface of CdS (Figure 5.20).

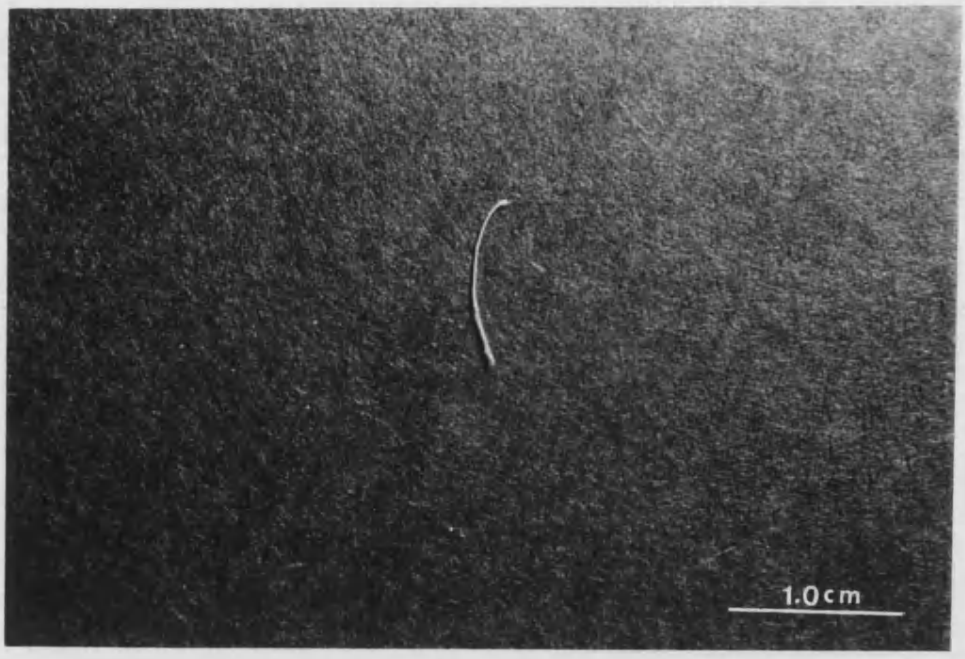

Figure 5.20 *Photograph of the CdS bionite.*

The bionite colour change observed was due to the reaction between $CdCl_2$ and H_2S gas taking place on the surface, and maybe within the Cd-bionite. SEM and EDXA analysis (Figures 5.21 and 5.22, respectively) of the surface of the CdS-bionite shows the Cd-bionite has been coated with CdS.

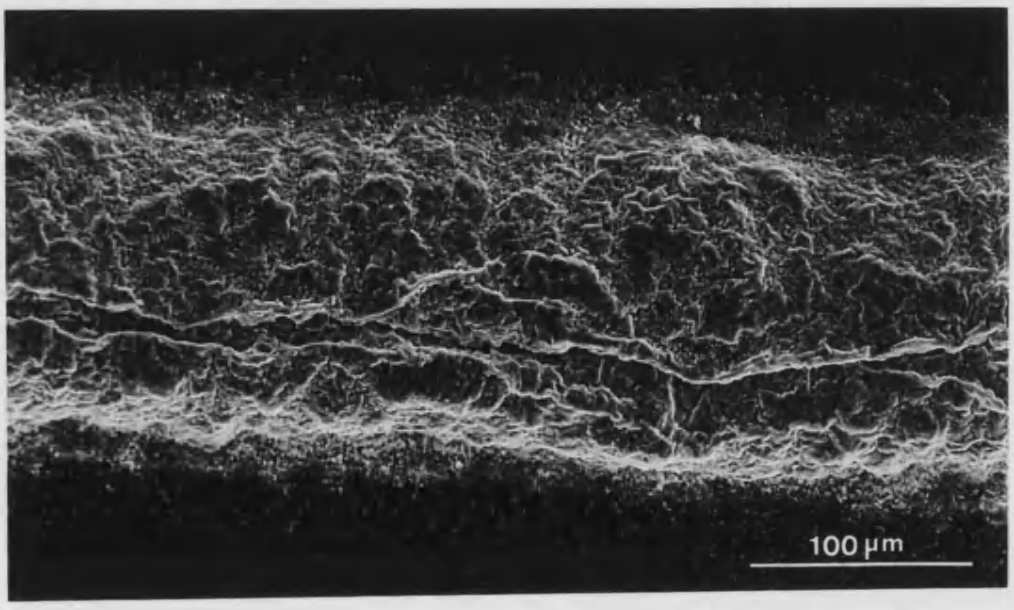

Figure 5.21 *SEM of the CdS bionite.*

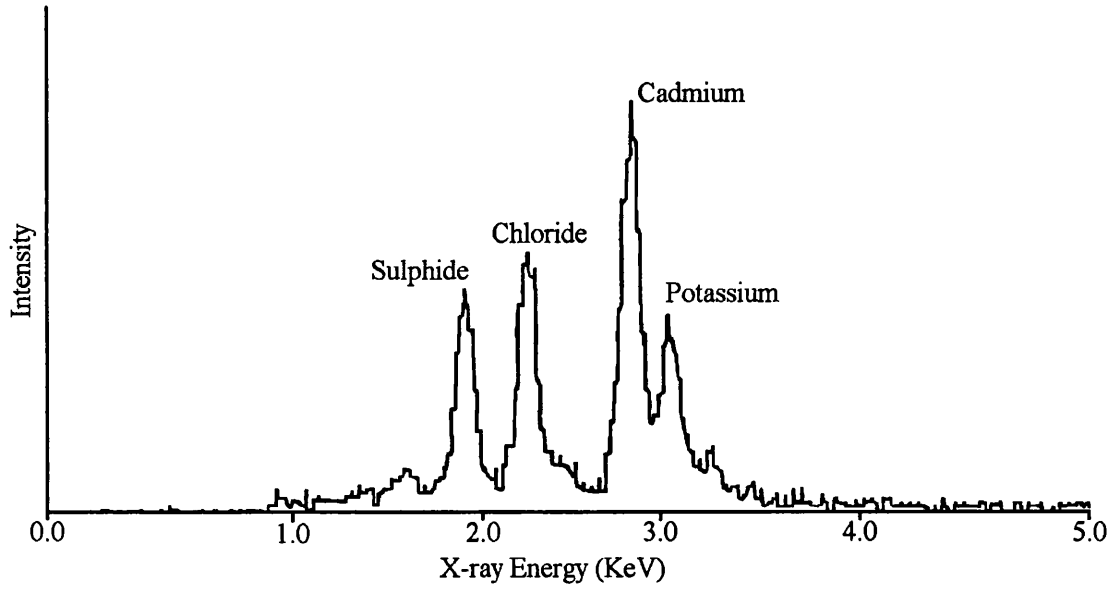

Figure 5.22 *EDXA spectra of the CdS bionite*

The final appearance of the CdS bionite and the corresponding EDXA spectrum of the surface seem to indicate that a CdS bionite has been produced. The CdS crystals appear as a "crust" on the surface of the bionite. Further examination of the "CdS-crust" shows that the surface consists of plate-like crystals and smaller discrete crystals. When the CdS bionite was viewed along the axis of elongation, it showed the plate-like crystals but also showed needle-like crystals overhanging what appear's to be pores (Figure 5.23).

These pores maybe the holes left by the bacterial filaments at the end of the bionites after being attacked by the hydrochloric acid, which is produced as a by product of the transformation from $CdCl_2$ to CdS, since the size of the pores is commensurate with the cell diameter. If this is the case, the hydrochloric acid attacks the bacteria and will ultimately destroy the bacterial backbone within the CdS bionite. Further work on this aspect of the CdS bionites needs to be undertaken.

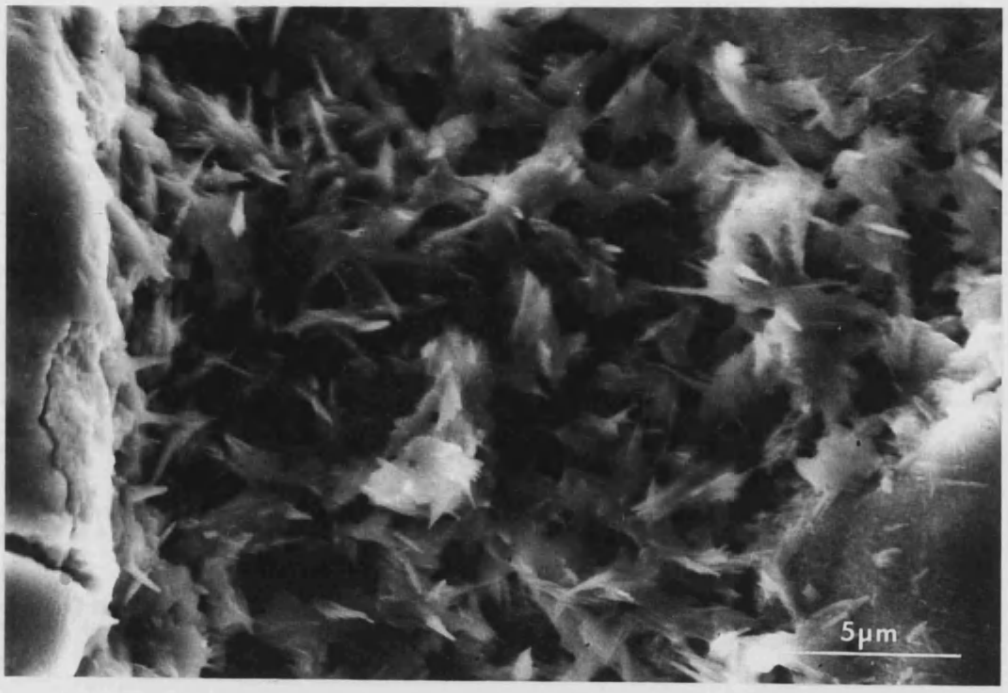

Figure 5.23 *SEM of the CdS bionite viewed down the axis of elongation.*

Further characterisation of the CdS bionite was needed to show whether the H_2S has just attacked the surface of the Cd-bionite forming a CdS coating over the bionite, or has it penetrated the width of the Cd-bionite, hence producing CdS throughout the resulting bionite. A simple experiment was undertaken to see which is the case. In the experiment a piece of Cd-bionite was placed upright on a carbon-coated SEM stub and exposed to H_2S as before. Once again the brilliant white Cd-bionite turned yellow as expected. Then the tip of the CdS bionite was broken off by a pair of tweezers. SEM and EDXA analysis at the centre of the bionite (Figures 5.24 and 5.25, respectively) shows that CdS is present throughout the bionite, therefore the H_2S gas does penetrate the entire Cd-bionite.

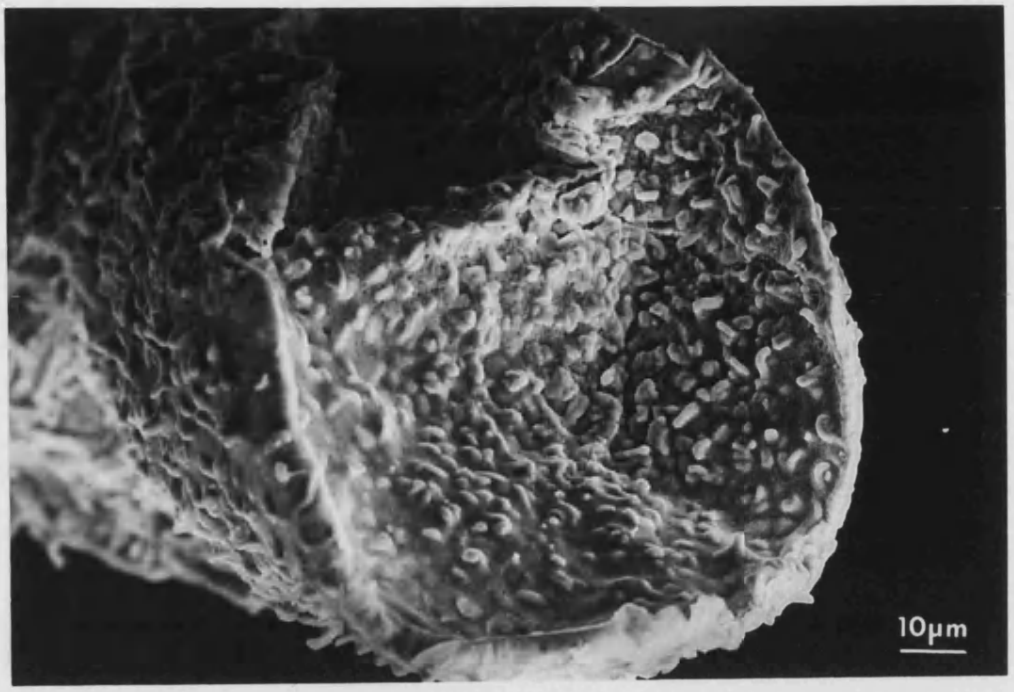

Figure 5.24 *SEM of the interior of the CdS bionite.*

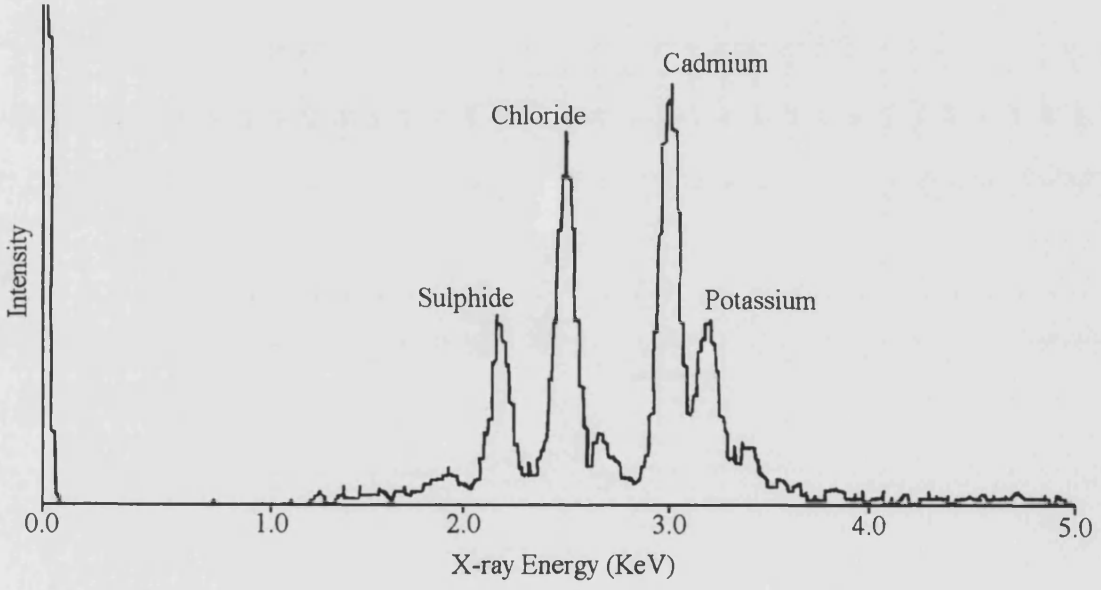

Figure 5.25 *EDXA spectra of the interior of the CdS bionite.*

In order to provide further evidence that CdS is present throughout the bionite, the technique of X-ray mapping was once again utilised. The results shown in Figure 5.26, show that there is an higher concentration of sulphide at the surface than there is at the centre of the bionite. Comparison with the Cd-elemental map (Figure 5.19) shows that once the H_2S attacks the Cd-bionite it will penetrate in to the bionite as well as attacking the outer surface. But after a while, the outer surface becomes covered with CdS and this will limit any further penetration of the H_2S gas into the bionite due to the impermeable nature of the CdS crust.

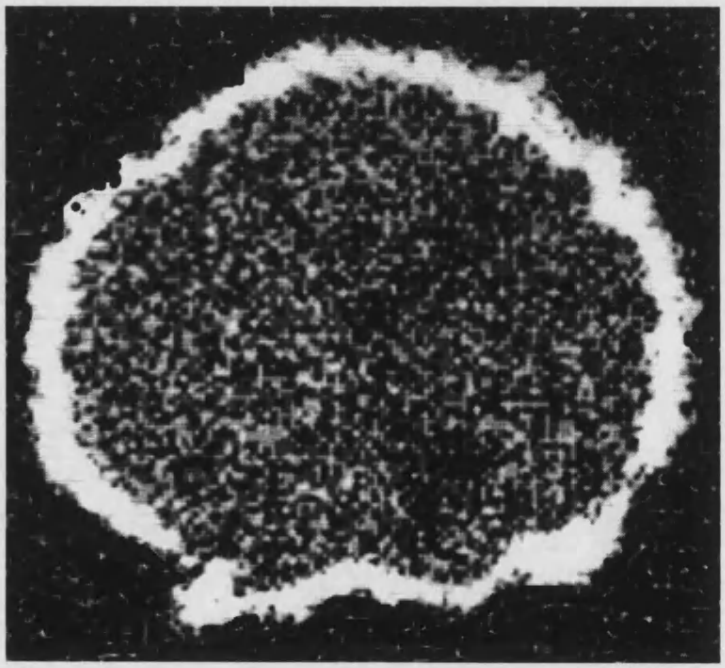

Figure 5.26 *Qualitative elemental map of sulphur obtained from* a *cross-section through a CdS bionite (areas containing sulphur appear bright).*

X-ray diffraction (XRD) of the *in-situ* CdS bionite (Figure 5.27) indicates the presence of a crystalline phase which was identified as the zinc blende structure of CdS, by the identification of the seven lines, as shown in Table 5.1.[34]

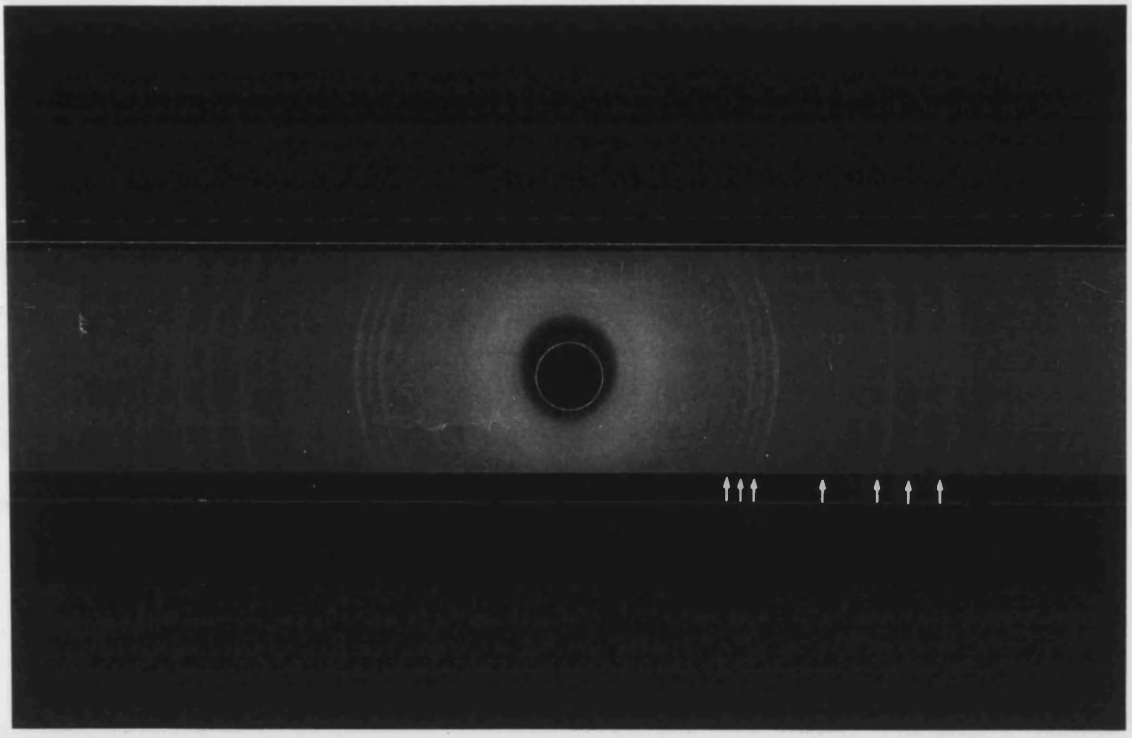

Figure 5.27 *XRD pattern for in-situ CdS bionite.*

Table 5.1 *XRD data for in-situ CdS bionite.*

d-value for *in-situ* CdS bionite (Å)	d-value for zinc blende structure of CdS (Å)
3.57	3.58
3.35	3.36
3.16	3.16
2.43	2.450
2.065	2.068
1.89	1.898
1.75	1.761

TEM and EDXA analysis of thin sections of *in-situ* CdS bionites (Figures 5.28 and 5.29, respectively) show that the bacterial filaments are all close packed together and CdS is present at the centre of the bionite.

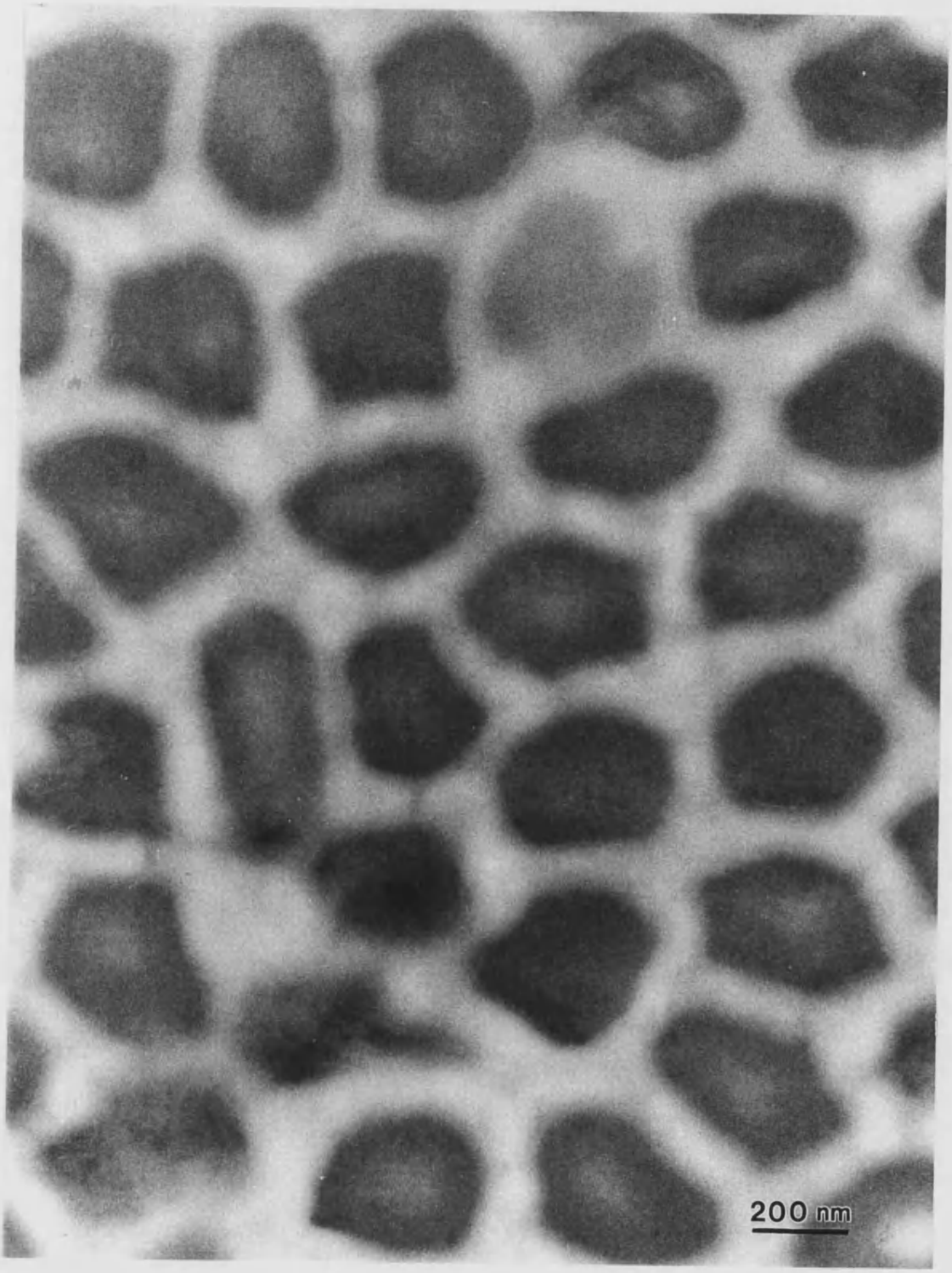

Figure 5.28 *TEM micrograph of thin section of in-situ CdS bionite.*

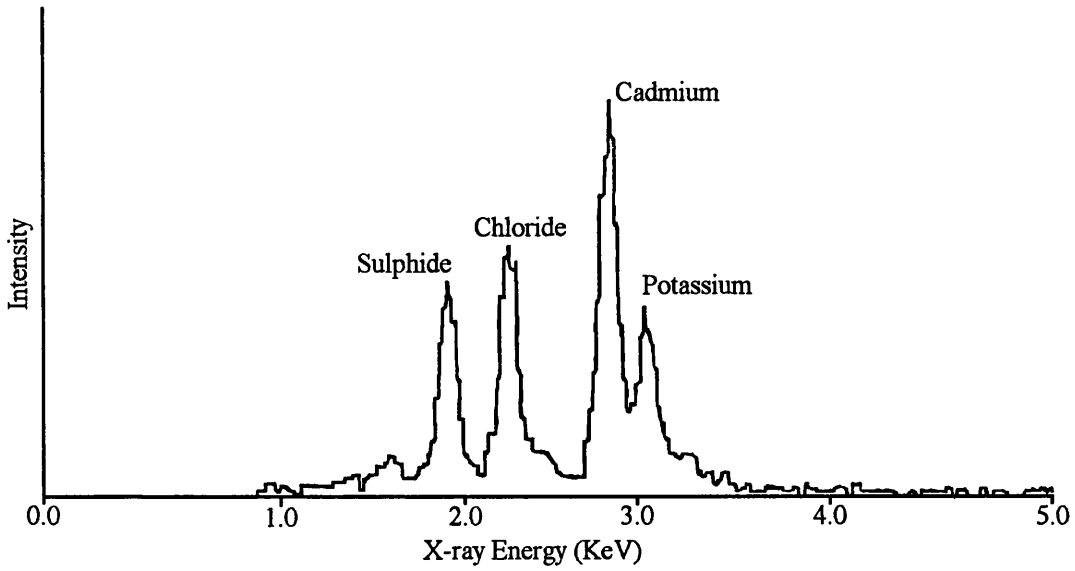

Figure 5.29 *EDXA spectra of a thin section of a in-situ CdS bionite.*

SAED of this area gave very diffuse rings which were unable to be resolved. Therefore, the technique of x-ray mapping showed that the majority of CdS was to be found at the surface or outer edge of the CdS bionite (Figure 5.26). TEM and EDXA analysis of the outer edge of the CdS bionite (Figure 5.30 and 5.31, respectively) show that the outer edge is indeed covered with a layer of CdS.

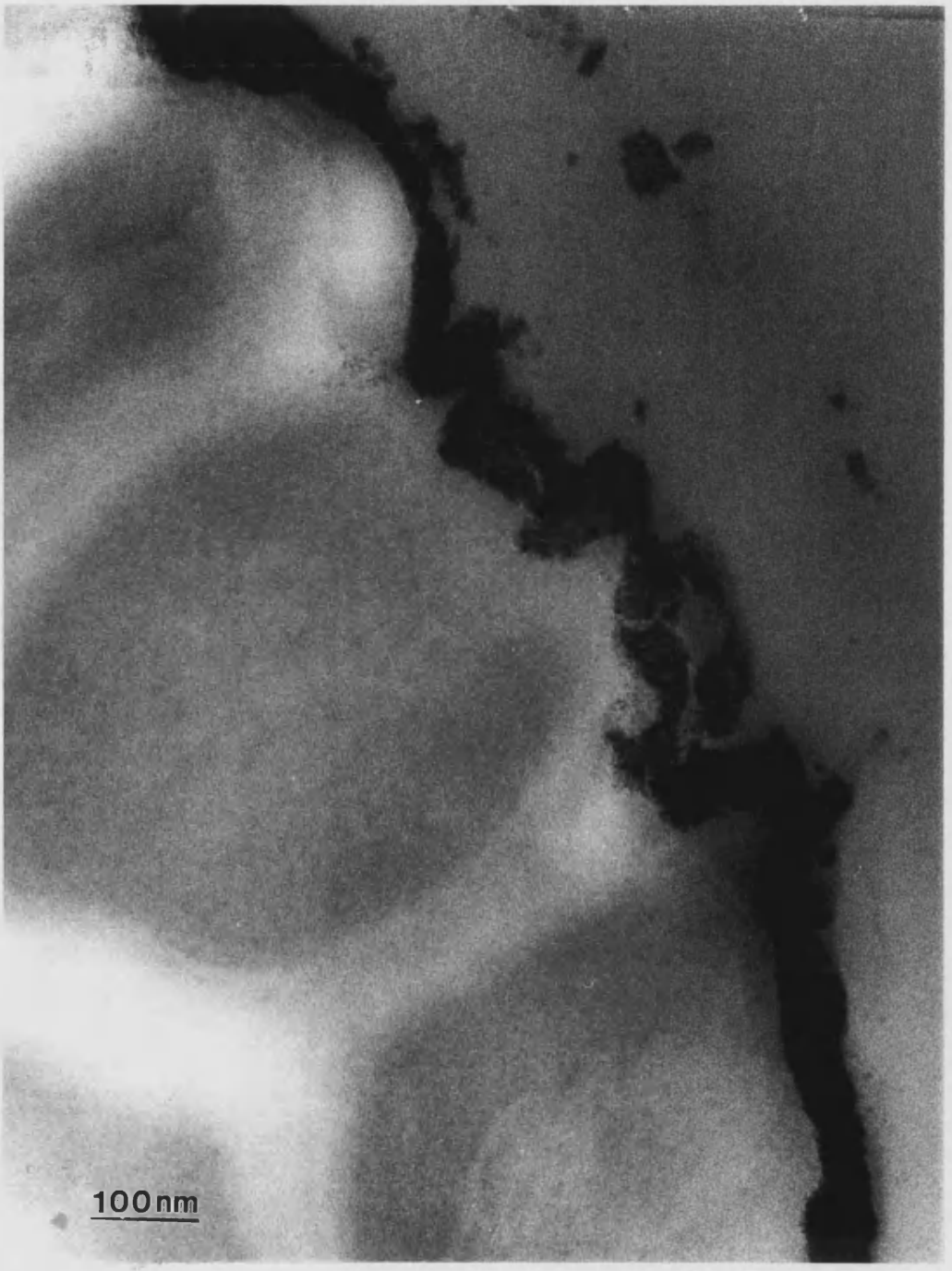

Figure 5.30 *TEM micrograph of outer edge of in-situ CdS bionite.*

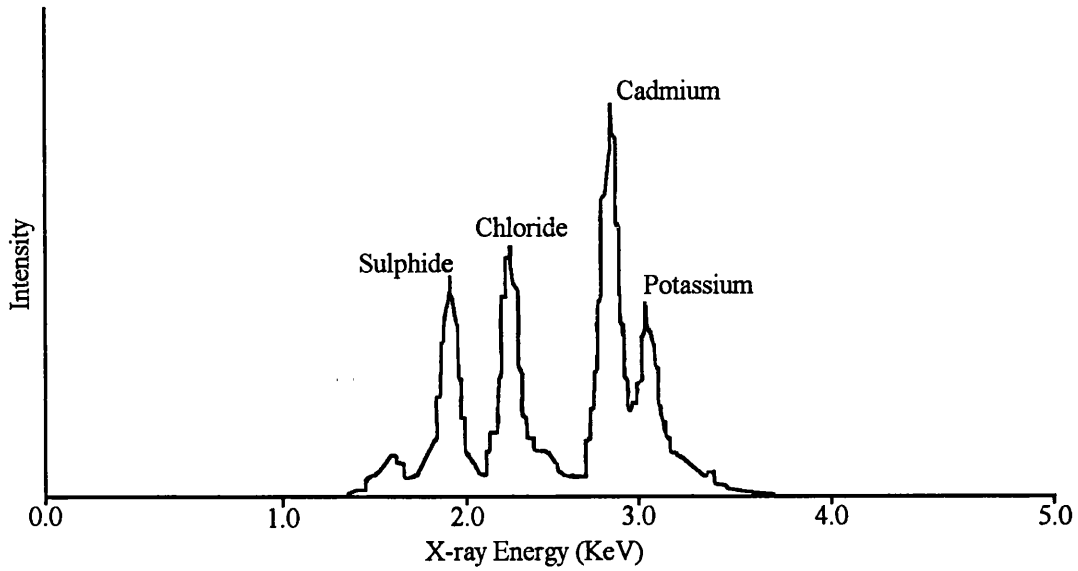

Figure 5.31 *EDXA spectra of the outer edge of the in-situ CdS bionite.*

SAED of the outer edge was performed and this time three ring are present as shown in Figure 5.32. These rings were resolved and the data shown in Table 5.2.[34] Upon closer inspection of the rings it is possible to see some "smudged" dots which may indicate that there is some sort of order in the CdS particle formed in this manner. This is as yet only a suggestion which needs to be further validated by more work. This suggests that the CdS on the outer edge of the bionite is crystalline, and the CdS at the centre is assumed to be crystalline, but there is not enough material to generate a electron diffraction pattern.

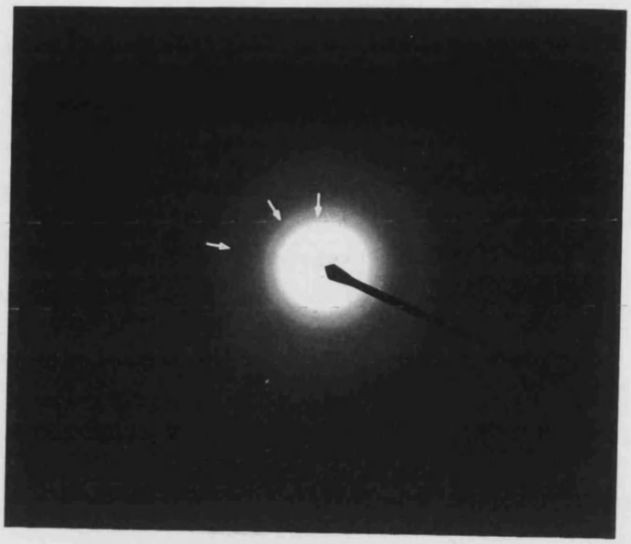

Figure 5.32 *SAED pattern for outer edge of in-situ CdS bionite.*

Table 5.2 *ED data for outer edge of in-situ CdS bionite.*

d-value for *in-situ* CdS bionite (Å)	d-value for zinc blende structure of CdS (Å)
3.34	3.36
-	2.90
2.09	2.058
1.75	1.753
-	1.680

5.7.4 Characterisation of Colloidal CdS Bionite

Once the bare bacterial thread is washed and allowed to dry, it is dipped into the colloidal CdS solution for 2 hours and subsequently dried for another hour. SEM microscopy of the colloidal CdS bionite at low magnification and EDXA analysis (Figures 5.33 and 5.34, respectively) shows that the bacterial filaments on the surface are now all disorganised.

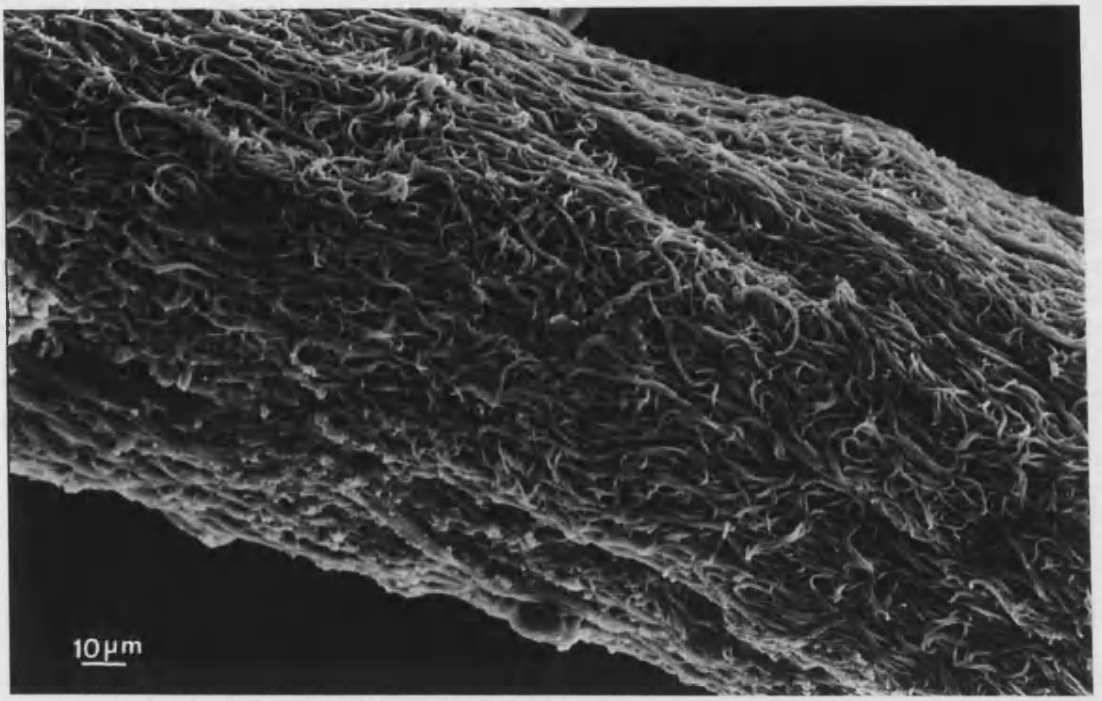

Figure 5.33 *SEM of the surface of the colloidal CdS bionite.*

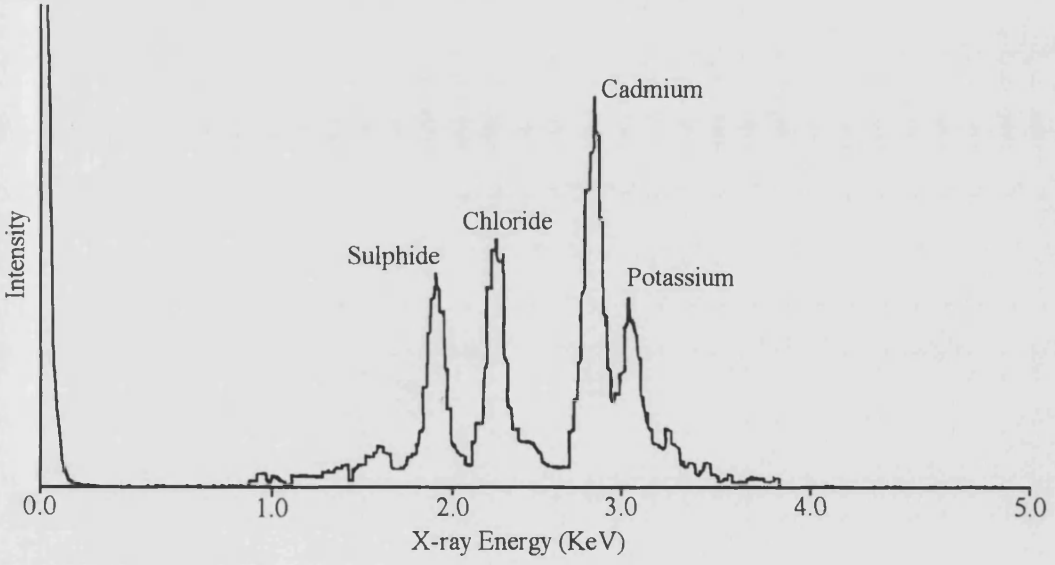

Figure 5.34 *EDXA spectra of the surface of the colloidal CdS bionite.*

The disorganised bacterial filaments may have arisen from the redrawing process of the thread from the colloidal solution. On closer inspection of the colloidal CdS bionite (Figure 5.35) the colloidal particles seem to aggregate together in discrete areas as opposed to an homogeneous surface coating.

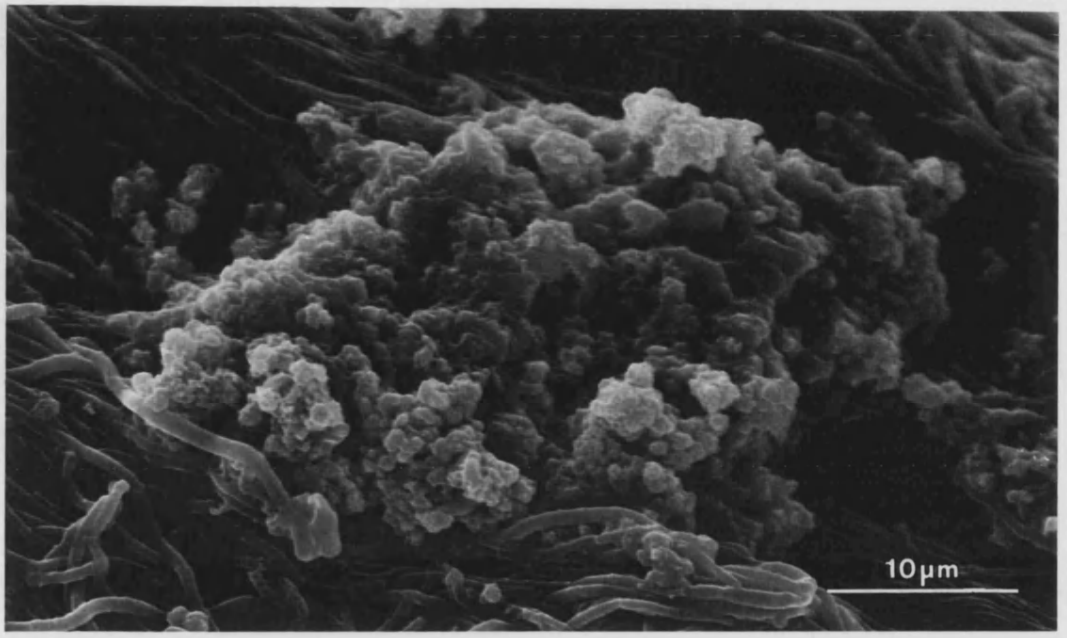

Figure 5.35 *SEM of colloidal CdS aggregates on the bionite surface.*

Once again a simple experiment was undertaken to see if the colloidal CdS was present throughout the entire colloidal CdS bionite. The tip of the colloidal CdS bionite was broken off with a pair of tweezers, as before and the corresponding SEM and EDXA analysis (Figures 5.36 and 5.37, respectively) data was obtained from the centre of the colloidal CdS bionite show that the colloidal CdS has packed throughout the entire bionite.

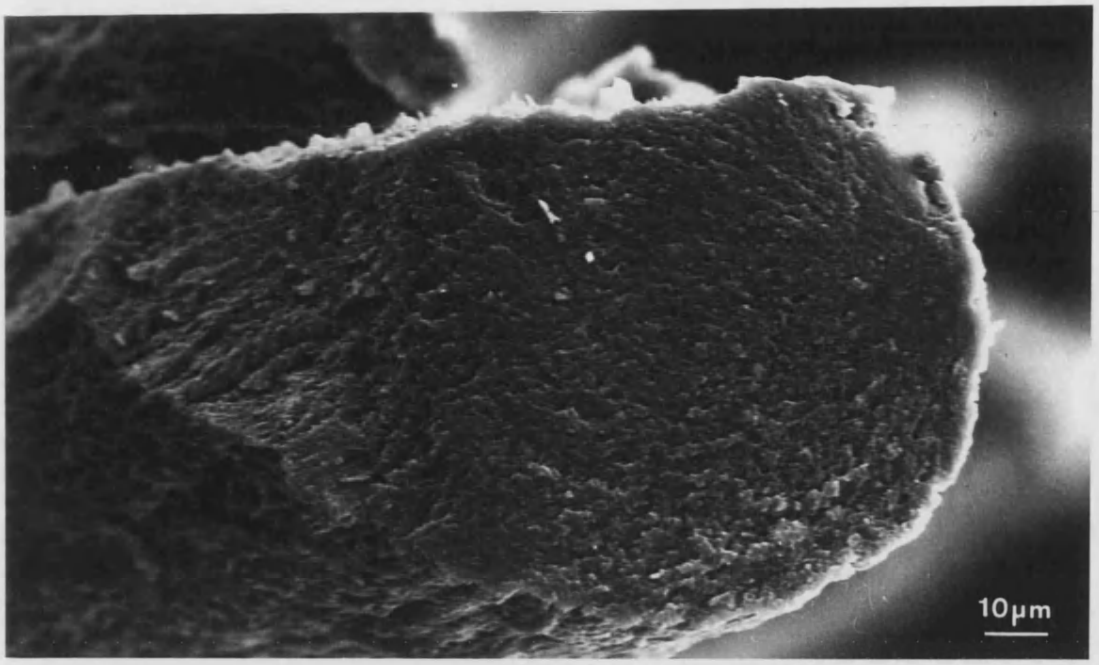

Figure 5.36 *SEM of the interior of the colloidal CdS bionite.*

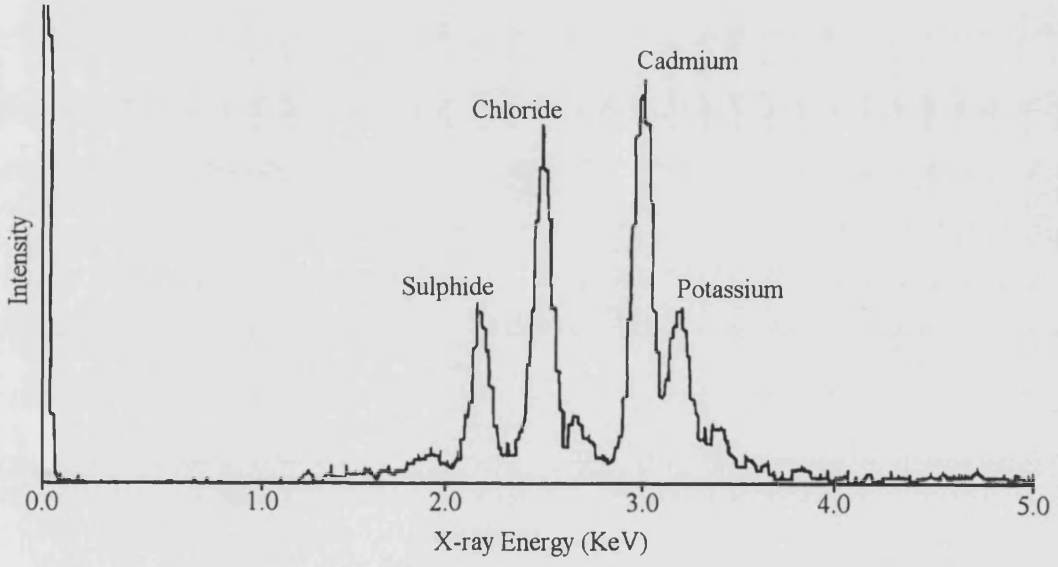

Figure 5.37 *EDXA spectra of the interior of the colloidal CdS bionite.*

X-ray mapping was once again utilised to provide further evidence that the colloidal CdS particles have penetrated the entire bionite. The results shown in Figure 5.38 conclusively show that the particles are present throughout the entire bionite, and are more evenly dispersed throughout the entire bionite.

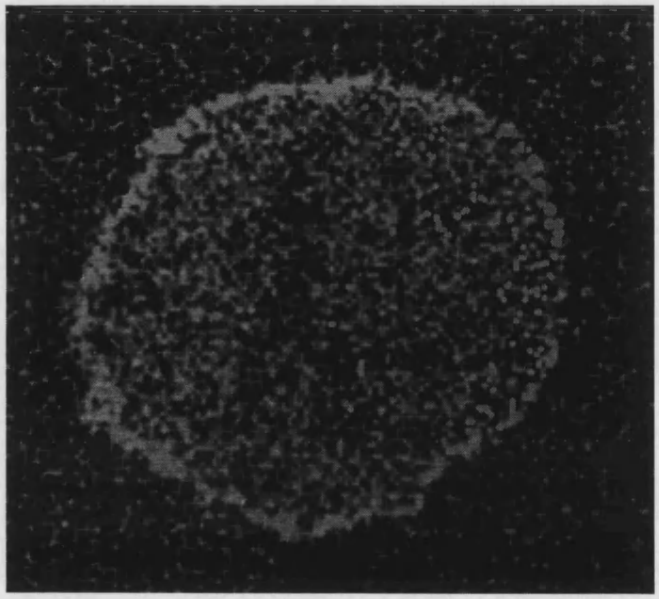

Figure 5.38 *Qualitative elemental map of sulphide obtained from a cross-section through a colloidal CdS bionite (areas containing sulphur appear bright).*

TEM micrograph of a thin section through a colloidal CdS bionite (Figure 5.39) shows that the bacterial filaments are organised in the centre of the colloidal CdS bionite as opposed the outer surface where they were disorganised and tangled up together. High resolution TEM micrographs of the bacterial filaments in the bionite (Figure 5.40) show an electron dense region around each of the filaments which is attributed to the colloidal CdS particles. SAED patterns of the colloidal CdS bionites gave no rings which was attributed to the poor crystallinity of the colloidal particles.

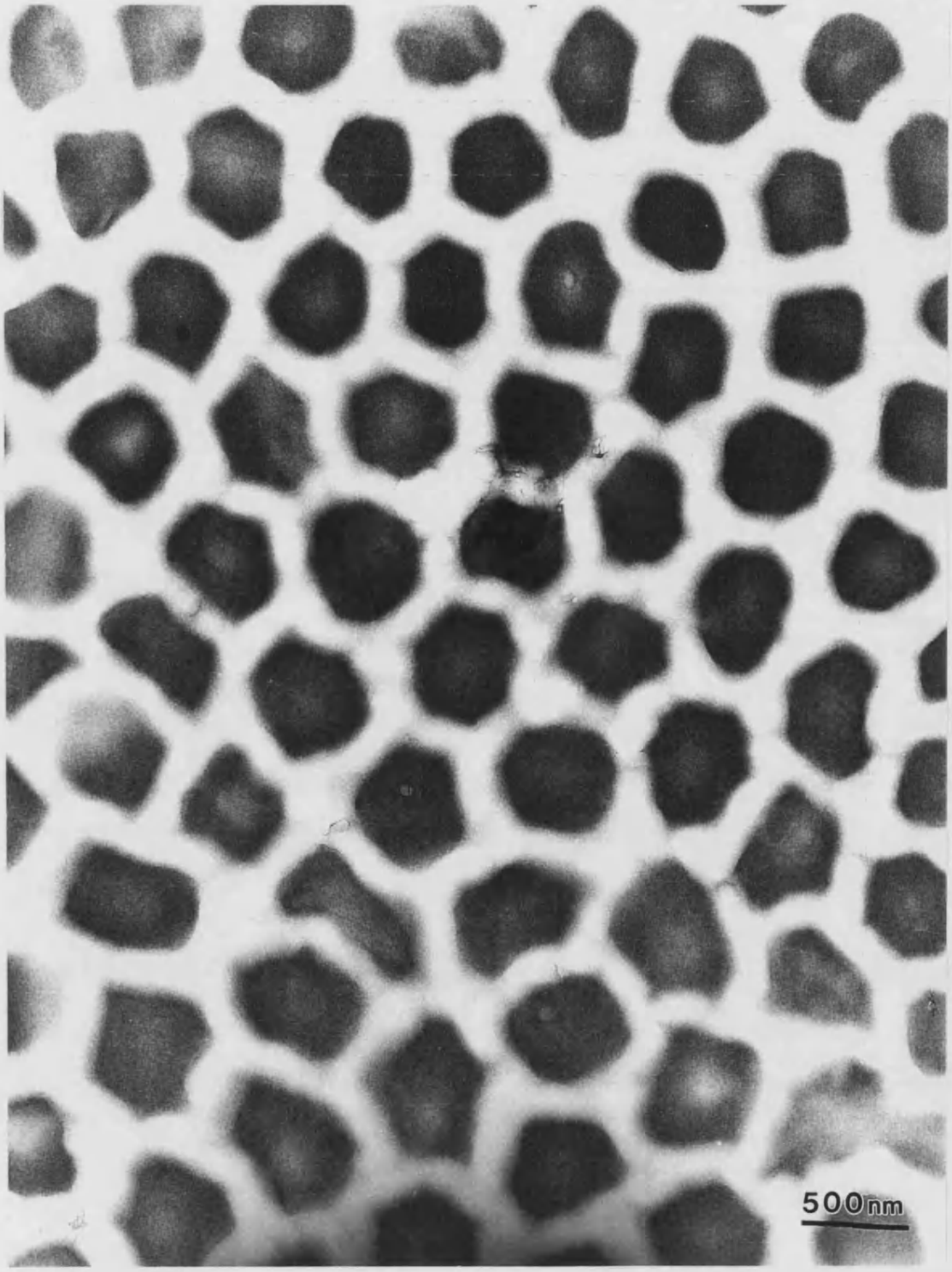

Figure 5.39 *TEM micrograph of a thin section through a colloidal CdS bionite.*

Figure 5.40 *High resolution TEM micrograph through a colloidal CdS bionite showing the colloidal CdS particles.*

5.8 Conclusions

The experiments performed in this chapter highlight the use of a bacterial thread as an organised matrix for the deposition of *in situ* inorganic and pre-formed particles. The technique of utilising templates for the precipitation of ordered materials is now well established. Static templates are used generally in the biomimetic processing of composite materials. For example, ceramic composites have been fabricated using self-assembled, bilayer tubules of phospholipid for the deposition of colloidal silica particles,[35] and the precipitation of aluminium hydroxide.[36] Also, the interlamellar space of synthetic bilayer membranes, which are structures formed *via* the self-assembly of double chain ammonium amphiphiles have been utilised for the production of planar multilayer magnetite,[37] and spherical multilayer silica composites.[38] One exception to the use of an static template and of great importance is the preparation of the hexagonal MCM-41 silica materials.[39,40]

In this chapter the reversible swelling properties of the bacterial thread or super-cellular template in aqueous solutions was exploited to facilitate infiltration of the inorganic phase (in this case cadmium). The microstructure of the biocomposites produced will depend on the initial properties of the two components.

For the *in-situ* CdS bionite, the very simple dipping technique has proved very adequate for loading the inorganic phase throughout the bacterial thread. When a dry bacterial thread is dipped into the cadmium solution, it swells as the solution penetrates into the thread and thereby exposing the multi-cellular bacterial filaments to the cadmium ions. On removal of the thread from the solution and subsequent drying, the filaments pack together to form the fibrous composite, with the inorganic $CdCl_2$ phase filling the space between them forming a micro-skeletal array. The

transformation of the Cd-bionite to the CdS-bionite *via* the exposure to H_2S gas was successful in that the gas penetrated the entire Cd-bionite and allowed the transformation to CdS, rather than just forming an outer coating of CdS. Therefore, by using this method we are able to produce a fibrous composite of CdS by utilising the charged groups present on the bacterial cell wall. So in summary, here we report on the formation of an inorganic bacterial composite and have successfully chemically processed this inorganic bionite by the exposure to H_2S. Therefore, this illustrates that there is some flexibility as regards to further processing of the initial inorganic bionite.

Using colloidal CdS particles, two distinctive types of bionite can be produced by the simple dipping technique; a surface coated bacterial thread or a infiltrated bacterial thread. In this study, the primary aim was to infiltrate the bacterial thread with the colloid. This was determined by the surface charge on the colloid. Colloids with a positive surface charge will tend to be deposited only on the surface of the macroscopic bacterial thread, whilst colloids with a negative surface charge will penetrate the interior bacterial thread and form an organised inorganic phase between the component multi-cellular filaments.[10] The CdS colloid used in this study has a negative surface charge, therefore it would be expected to infiltrate the bacterial thread. Indeed this is the case as results show that the colloidal CdS is present throughout the entire bionite. The CdS colloid was retained when the bionite was re-immersed in solution, which was part of the process of preparing thin sections. The degree of infiltration of the colloid depends on concentration of the sol, ionic strength and pH. The further the sol penetrates into the thread, the more depleted it becomes

of particles. However, if the particles are sufficiently concentrated, all the bacterial filaments will be coated throughout the width of the thread.

From the work carried out by Davis[10] and highlighted by this work, the following mechanism is proposed; when the bacterial thread is dipped into colloid it will swell as the sol penetrates through the thread. The thread increases its width and length by 1.2 and 1.4 times respectively in pure water, but does not unravel totally, therefore the component multi-cellular filaments are exposed to a finite volume of sol. Since both the bacterial filaments and the colloidal particles have a negative charge associated with them, it is these repulsive forces that allow the particles to infiltrate into the thread as opposed to being deposited on the surface of the thread. When the thread is redrawn from the sol, particles trapped between, or adhering to, the bacterial filaments are retained. On drying the bionite produced can be considered to be a two phase system. The idealised structure would consist of a well ordered, close packed array of uniform diameter bacterial filaments that are separated by an interpenetrating, continuous inorganic phase of uniform thickness.

In reality, only small areas within the bionite have such an idealised structure. The other areas are affected by various factors which result in the formation of more disordered domains. An example of this is when the bacterial thread is dipped into water and redrawn, the washed thread is less well organised.[27] Therefore, by this rationale a similar effect will be seen when the bacterial thread is dipped into the colloidal solution. This is manifested as a lowering in packing density of the bacterial component, with the most dense being hexagonally close packed, and a corresponding reduction in the periodicity.

Regarding potential applications, an important area is the minimal variation of pore size, with the major contributor being the discontinuities within the cell wall structure. These discontinuities in the micro-skeletal arrangement of the inorganic phase of the bionite arise from incomplete wall formation and fracture of weak, poorly developed walls on drying. The variation in actual pore size arising from the bacterial component is minor. The wide distribution of bacterial filament diameters and shapes ranging from round to ellipitical, seen in some TEM micrographs are artefacts of the bacterial filaments lying slightly oblique to the plane of section. Although the observed diameter of the cells appears to vary, the actual diameter is constant.[10]

There are a number of established synthetic methods for the preparation of highly ordered framework structures, one being the formation of M41S family of materials. Another example is two step fabrication of the metal nanohole array by Masuda and Fukuda.[41] The first step involves the production of a polymethacrylate 'negative' of porous alumina which was subsequently used as a template for the deposition of metal by electrolysis plating. The second stage involves removal of the template to leave the 'positive' metal nanohole array. At present the order of these materials is better than those obtained from the use of bacterial threads as templates. But an advantage of using bacterial threads as an template is that they offer access to micron scale pores, under ambient conditions. However it is clear that further studies need to be undertaken to determine the reaction conditions for optimum infiltration of the inorganic phase, particularly focusing on the role pH plays on the swelling of the bacterial thread. In conclusion, it is clear that this combination of preparative techniques in biotechnology and materials chemistry offers a large scope for the fabrication of composite materials.

5.9 References

1. Mendelson, N.H. (1992). Production and initial characterisation of bionites - Materials formed on a bacterial backbone. *Science,* **258 (5088)**, 1633-1636.

2. Abelson, P.H. (1983). Biotechnology - An overview. *Science,* **219 (4585)**, 611-613.

3. Koshland, J. (1992). The microbial wars, *Science,* **257 (5073)**, 1021-23.

4. Lipkin, R. (1994). The face is familiar, *Technology Review,* **97 (8)**, 11-13.

5. Nanninga, N., Kooper, L., and de Vries-Tijssen, F. (1981). *Acta Histochemica,* The interpretation of chemically fixed and freeze-fractured bacterial nucleoplasm, **S23**, 39-53.

6. Graham, L.L., and Beveridge, T.J. (1994). Structural differentation of the *Bacillus subtilis* 168 cell wall. *Journal of Bacteriology*, **176 (5)**, 1413-1421.

7. Clements, K., and Bullivant, S. (1991). An unusual symbiont from the gut of surgeonfishes may be the largest known prokaryote. *Journal of Bacteriology*, **173 (17)**, 5359-5362.

8. Marquis, R.E., Mayzel, K., and Carstensen, E..L. (1976). Cation exchange in the cell walls of gram-positive bacteria. *Canadian Journal of Microbiology,* **22**, 975-982.

9. Beveridge, T.J., (I989). "Metal-Microbe Interactions", p65-83. Edited by Poole, K., and Gadd, G. IRL Press, New York.

10. Davis, S.A. (1996). Biomineralisation and biomimetic synthesis, PhD thesis, University of Bath.

11. Beveridge, T.J., and Murray, R.G.E. (1980). Sites of metal deposition in the cell walls of *Bacillus subtilis. Journal of Bacteriology,* **141**, 876-887.

12. Rogers, H., Perkins, H., and Ward, J. (1980). "Microbial Cell Walls and Membranes", Chapman and Hall, London and New York.

13. Doyle, R.J., McDannel, M.L., Helman, J.R., and Streips, U.N. (1975). Distribution of teichoic acid in the cell walls of *Bacillus subtilis. Journal of Bacteriology,* **122**, 152-158.

14. Doyle, R.J., Matthews, T.H., and Strieps, U.N. (1980). Chemical basis for selectivity of metal ions by the *Bacillus subtilis* cell wall, *Journal of Bacteriology*, **143**, 471-480.

15. Ou, L-T., and Marquis, R.E. (1970). Electro-mechanical interactions in cell walls of gram-positive cocci, *Journal of Bacteriology*, **101**, 92-101.

16. Marquis, R.E. (1968). Salt-induced contraction of bacterial cell walls, *Journal of Microbiology*, **95**, 775-781.

17. Beveridge, T.J., and Murray, R.G.E. (1976). Uptake and retention of metals by the cell walls of *Bacillus subtilis*, *Journal of Bacteriology*, **141**, 1502-1518.

18. Mera, M.U., Kemper, M., Doyle, R.J and Beveridge, T.J. (1992). The membrane-induced proton motive force influences the ability of *Bacillus subtilis* cell walls, *Applied and Environmental Microbiology*, **58 (12)**, 3837-3844.

19. Kemper, M.A., Urrutia, M.M., Beveridge, T.J., Koch, A.L., and Doyle, R.J. (1993). Proton motive force may regulate cell wall associated enzymes of *Bacillus subtilis*, *Journal of Bacteriology*, **175 (17)**, 5690-5696.

20. Hughes, M.N., and Poole, R.K. (1989). **In**: *Metals and Micro-organisms*. pp 334-338. London: Chapman and Hall.

21. Mendelson, N.H., and Thwaites, J.J. (1990). Bending, folding, and buckling processes during bacterial macrofibre morphogenesis. *Materials Research Society Symposium Proceedings,* **174**, 171-178.

22. Mendelson, N.H. (1996). Bacterial fibers and their mineralised products: bionites. **In**: *Biomimetic materials chemistry* (Mann, S. ed.), pp 279-310. Cambridge: VCH Publishers (UK) Ltd.

23. Mendelson, N.H. (1992). Self-assembly of bacterial macrofibres - A system based upon hierarchies of helices. *Materials Research Society Symposium Proceedings,* **255**, 43-54.

24. Mendelson, N.H. (1990). Bacterial macrofibres - The morphogenesis of complex multicellular bacterial forms. *Science Progress (Oxford),* **74**, 425-441.

25. Briehl, M., and Mendelson, N. H. (1987). Helix hand fidelity in *Bacillus subtilis* macrofibres after spheroplast regeneration. *Journal of Bacteriology,* **169 (12)**, 5838-5840.

26. Thwaites, J.J, and Mendelson, N.H. (1985). Biomechanics of bacterial walls - Studies of bacterial thread made from *Bacillus subtilis. Proceedings of the National Academy of Science USA,* **82 (7)**, 2163-2167.

27. Mendelson, N.H., and Thwaites, J.J. (1989). Cell wall mechanical properties as measured with bacterial thread made from *Bacillus subtilis*. *Journal of Bacteriology,* **171 (2)**, 1055-1062.

28. Mendelson, N.H., Thwaites, J.J., Kessler, J.O., and Li, C. (1995). Mechanics of bacterial macrofiber initiation, *Journal of Bacteriology*, **177 (24)**, 7060-7069.

29. Mendelson, N.H. (1976). Helical growth of Bacillus subtilis: a new model of cell growth. *Proceedings of the National Academy of Science USA,* **73**, 1740-1744.

30. Chemseddine, A., and Fearheiley, M.L. (1994). Improved CdS buffer window layers for thin-film solar-cells, *Thin Solid Films*, **247 (1)**, 3-7.

31. Personal communication from Chemseddine, A.

32. Ozin, G.A. (1992). Nanochemistry - Synthesis in diminishing dimensions, *Advanced Materials*, **4 (10)**, 612-649.

33. Chemseddine, A. (1993). Fibrous and orientated quantum dots - Synthesis and characterisation, *Chemical Physics Letters*, **216 (3-6)**, 265-269.

34. Joint Committee on Powder Diffraction Standards. (1983). Card number 10-454.

35. Baral, S., and Schoen, P. (1993). Silica-deposited phospholipid tubules as a precursor to hollow submicron-diameter silica cylinders, *Chemistry of Materials*, **5 (2)**, 145-147.

36. Chappell, J.S., and Yager, P. (1992). Formation of mineral microstructures with a high aspect ratio from phospholipid bilayer tubules, *Journal of Materials Science Letters*, **11 (10)**, 633-636.

37. Okada, H., Sakata, K., and Kunitake, T. (1990). Formation of oriented iron oxide particles in cast multibilayer films, *Chemistry of Materials*, **2 (2)**, 89-91.

38. Tanev, P.T., and Pinnavia, T.J. (1996). Biomimetic templating of porous lamellar silica's by vesicular surfactant assemblies, *Science*, **271 (2553)**, 1267-1269.

39. Kresge, C.T., Leonowicz, M.E., Roth, W.J., Vartuli, J.C., and Beck, J.S. (1992). Ordered mesoporous molecular sieves synthesised by a liquid-crystal template mechanism, *Nature*, **359 (6397)**, 710-712.

40. Beck, J.S., Vartuli, J.C., Roth, W.J., Leonwicz, M.E., Kresge, C.T., Schmitt, K.D., Chu, C.T., Olsen, D.H., Sheppard, E.W., McCullen, S.B., Higgins, J.B., and Schlenker, J.L. (1992). A new family of mesoporous molecular sieves prepared with liquid-crystal templates, *Journal of the American Chemical Society*, **114 (27)**, 10834-10843.

41. Masuda, H., and Fukuda, K. (1995). Ordered metal nanohole arrays made by a two step replication of honeycomb structures of anodic alumina, *Science*, **268**, 1446-1468.

CHAPTER SIX

FULLERENE MALONIC ACID

6.1 Introduction

Ever since their first detection[1] and bulk production,[2] the fullerenes have gained a primary role within the scientific community, reaching their climax when the 1996 Nobel Prize for Chemistry was awarded to Kroto, Curl, and Smalley for their seminal discovery. The unique chemical and physical properties of the fullerenes led numerous scientists to predict a vast number of technological applications. However this created disappointment when it was clear that fullerene based materials would not be ready for the market due to its expensive synthesis and relatively low chemical reactivity. But, to date several dozens of researchers have found that buckminsterfullerene and its relatives undergo a variety of chemical reactions and in most cases, the new derivatives retained the main properties of the original fullerene, for example its rich electronic and electrochemical behaviour. With these new derivatives, it is now likely that some of the functionalised fullerenes may find useful applications within the field of materials science.

In 1990, Krästschmer *et al.*[2] developed an efficient way of synthesising macroscopic amounts of buckminsterfullerene (C_{60}), the most abundant representative of the fullerene family, by resistive heating of graphite. This discovery led to an extraordinary explosion of research not only from academics, but also from industry which has led to the discovery of several interesting physical properties, along with a careful definition of the chemical reactivity of the fullerenes.[3-10] Examples of the findings are that C_{60} was found to become a superconductor in M_3C_{60} species, where

M = alkali metal,[11-14] a relatively stable hexa-anion in cyclic voltammetry,[15,16] an organic soft ferromagnet in $TDAE^{+\cdot}C_{60}^{-\cdot}$ where TDAE = tetrakisdiethylaminoethylene,[17] and an interesting material with non-linear optical properties.[18,19]

It was clear that a novel molecular material had been unearthed with huge potential within several different disciplines and once again generated huge expectations. However, the difficulty in processing fullerenes has represented a major problem in the frantic search for practical applications. The most serious obstacle of C_{60} was that it is insoluble or only sparingly soluble in most solvents and aggregates very easily.[20] This could, at least in part be overcome with the help of the 'functionalisation chemistry of the fullerenes'.[21-29] The organic derivatisation of C_{60} has put forward a number of compounds, which retain most of the properties of the original fullerene, and make it much easier to handle.

6.1.1 Basic Principles of Fullerene Chemistry

The surface of C_{60} is made up of 20 hexagons and 12 pentagons. All of these rings are fused and all of the double bond are conjugated. X-ray crystallography studies on C_{60} and its derivatives have proved the existence of two different bond types. The first bond type being 'short bonds' or 6,6 junctions, shared by two adjacent hexagons (*ca.* 1.38 Å long) and the second type being 'long bonds' or 5,6 junctions, fusing a pentagon with an hexagon (*ca.* 1.45 Å long). The geometric demand of the spherical cage is such that all the double bonds in C_{60} deviate from planarity.[13] This pyramidalisation of the sp^2-hydridised carbon atoms confers an excess of strain to C_{60} which is responsible for the enhanced reactivity of the fullerene.

A release of strain is in fact associated with the change of hybridisation from sp^2 to sp^3 that accompanies most chemical reactions.[21]

The chemical reactivity of C_{60} is typical to that of an electron-deficient olefin. It reacts readily with nucleophiles and in cycloadditions it is a reactive 2π component.[4] The greatest number of reactants will attack the 6,6 ring junction position as opposed to the 5,6 ring position because the 6,6 ring junction possess more electron density. Insertions into 5,6 bonds occur, but only as rearrangements following a 6,6 junction attack.

The main objective of fullerene chemistry is the production of well-defined, stable and characterisable adducts. In this respect, several different approaches have given excellent results. These reactions can be of a widely different nature, but the single-addition products can be classified into a few broad categories, based on the structure which is obtained. In particular, with relation to the geometrical shape built on a 6,6 junction of C_{60}, there can be: an open structure; a three-membered ring, which also includes carbon or nitrogen insertion into a 5,6 ring junction; a four membered ring: a five membered ring: a six membered ring (Figure 6.1).[22]

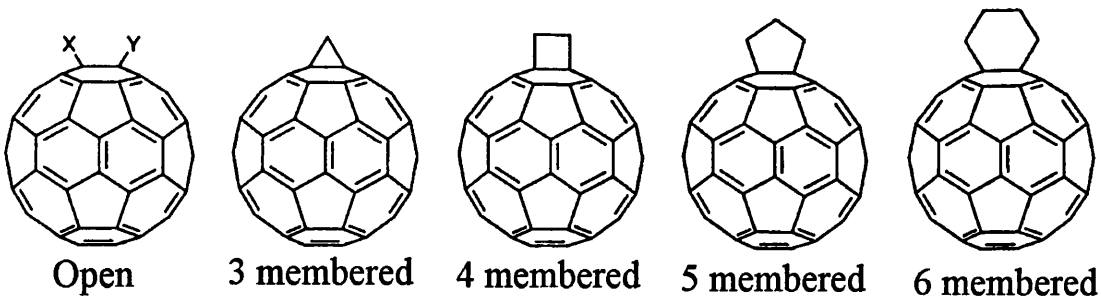

Figure 6.1 *Geometrical shapes built onto a 6,6 ring junction of C_{60} (redrawn from Prato, M.).*[22]

Buckminsterfullerene (C_{60}) can be chemically modified by a large variety of addition reactions[23-25] which allows the combination of its properties with those of other classes of materials. It has been shown by various groups of researchers[26-29] that some fullerene derivatives exhibit biological activity. Two properties of C_{60} are of special significance. Firstly, is its spherical shape which can be used for molecular recognition and secondly, the ability of the fullerene core to efficiently photosensitise the conversion of triplet to singlet oxygen.[30-32] A very important requirement for the investigation of the biological activity of a fullerene derivative is water solubility. This can be achieved by the attachment of polar functional groups. Lamparth and Hirsch[33] report on the synthesis of water-soluble malonic acid derivatives of C_{60} by the hydrogenolysis of stereochemically defined diethyl malonates. This derivative was termed fullerene malonic acid, and is of main interest in this study.

For the synthesis of fullerene malonic acid, $C_{60}[C(COOH)_2]$, Lamparth and Hirsch[33] chose the di(ethoxycarbonyl)methylene adduct, $C_{60}[C(COOEt)_2]$ which was synthesised by the reaction of fullerene with diethyl bromomalonate in the presence of base,[34-37] as the starting material. Fullerene malonic acid was obtained by stirring the corresponding diethyl malonate (100 mg) dissolved in toluene (50 cm^3) under N_2 in the presence of a twenty-fold molar excess of NaH for 3 hours at 60 °C. After this the NaH was almost homogeneously suspended in toluene while the diethyl malonate was unaffected. The transformation of the malonate was accompanied by a vigorous gas evolution and the quantitative precipitation of the sodium salt of the fullerene malonic acid took place after the addition of methanol (1 cm^3). The formation of the acids occurred, presumably, by the hydrogenolysis of the -OEt bonds. After centrifugation and the removal of the liquid phase, the precipitate was washed in toluene, followed

by 2 mol dm^{-3} sulphuric acid, then water and finally dried under vacuum at 60 °C for 12 hours. A schematic diagram of fullerene malonic acid is shown in Figure 6.2.

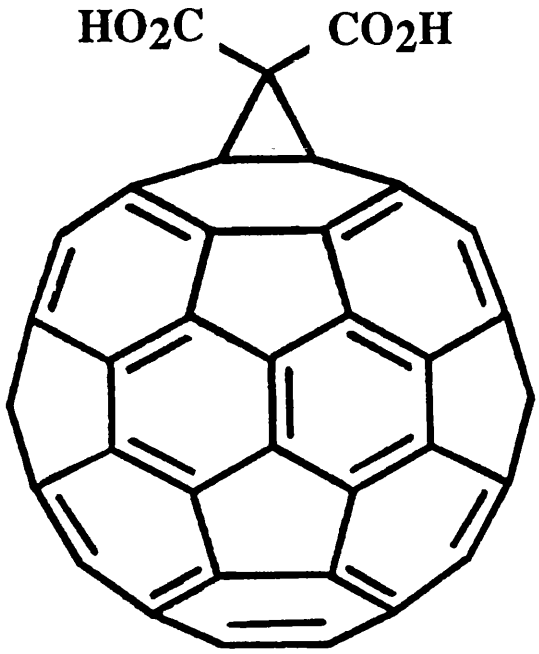

Figure 6.2 *Fullerene malonic acid.*

This monoadduct of malonic acid is soluble in solvents such as tetrahydrofuran and methanol, and it is moderately soluble in basic water (pH>9). The specific C_{2v} symmetry of this molecule suggests that it might be sufficiently amphiphilic to be spread at the air/water interface, in the form of compressed Langmuir monolayers.

6.2 Langmiur Monolayers of Fullerene Malonic Acid

In order to fully explore the potentials of fullerenes and their derivatives in material science, it is very important to fabricate fullerene systems in which the location and organisation of the fullerenes are controlled precisely. Well ordered thin films of fullerene molecules have been fabricated using the epitaxial growth method on various substrates including silicon and alkali halide single crystals.[38-42] These thin films have been reported to have closed-packed structures, such as hexagonal-close-packing (hcp) and/or face-centred-cubic (fcc) structures. But, one of the most powerful tools to construct organic monolayer films whose structures are controlled at the molecular level is the Langmuir-Blodgett (LB) technique. Also with LB technology, it makes possible the fabrication of multilayer films onto various solid substrates.

The formation of organised films of derivatised fullerene molecules could be important in the development of molecular systems based on fullerene properties. In addition, amphiphilic fullerene derivatives may show biological behaviour since they could be strongly coupled to lipid membranes.

Floating layers of unmodified fullerene molecules at the air/water interface were first reported upon by Obeng and Bard[43] in 1992. They showed the limiting area per molecule to be 96 $Å^2$. The limiting area per molecule is consistent with the value deduced from the crystallographic data of C_{60} molecules spaced at 10 Å in a hexagonal unit cell,[1] (Limiting area per molecule = $a^2 \sin 60°$). Since the Obeng and Bard[23] report, various groups have attempted to produce monolayers of unmodified C_{60}. For example, Nakamura *et al.*[44] and Long *et al.*[45] reported the limiting area per molecule for unmodified C_{60} to be 20 $Å^2$ and 31 $Å^2$ respectively. The explanation for

such small limiting area per molecule values obtained by these research groups, compared to the ideal value of 100 $Å^2$ was attributed to the formation of two-dimensional crystalline islands of C_{60} immediately after spreading the solution on to the pure water surface. Therefore, upon compression the film formed is a bi- or multi-layer rather than an ideal monolayer.

Interesting observations were noted firstly by Williams *et al.*[46] who reported that a diluted spreading solution produces a more expanded isotherm than the original spreading solution. Secondly, Maliszewskyj *et al.*[47] noted that considerable care needs to be taken when depositing droplets from being placed on top of one another, which will result in multilayer formation even before compression.

6.2.1 Experimental

Fullerene malonic acid was provided by A. Hirsch (Institut für Organische Chemie, Universität Erlangen, Henkestrasse 42, Erlangen, Germany).

Procedure for the Measurement of Isotherms

Water was purified by double distillation and upgraded using a Purite Standard Stillplus with bacterial filter, activated carbon filter, and ion-exchange system. A Radiometer Copenhagen digital PHM 84 Research pH meter and BDH glass plus electrode were calibrated at pH 4.0 and 7.0 using phthalate and phosphate buffers supplied by Fisons, respectively. Isotherm measurements were made using a NIMA Technology System 2001 trough with computer interface control. The pressure sensors, trough area and barrier speeds were calibrated prior to use. Purified water was employed as the subphase, and the trough was filled with about 0.8 dm^3 of this

solution and surface-cleaned twice with suction *via* a Pasteur pipette. 200 μl of fullerene malonic surfactant was spread at the air/water interface as approximately a 0.08 mg cm^{-3} solution in tetrahydrofuran (Fisons HPLC grade). After solvent evaporation, the pressure sensors were zeroed, and compression was initiated at a standard rate of 50 cm^2 min^{-1}.

Control isotherms were carried out on the water subphase, in the absence of a spread monolayer, to establish whether the subphase components influenced the surface tension. Checks were also made for any surface activity due to contamination in the tetrahydrofuran solvent.

Characterisation of Monolayers

The prepared monolayer was transferred onto a hydrophobic surface using the horizontal dipping method. Silicon and quartz wafers, treated hydrophobically with hexamethyldisilazane, supplied by Aldrich, were used for FT-IR and UV-visible absorption spectroscopy, respectively.

UV-visible absorption spectra were obtained by using a Perkin-Elmer UV-visible Lambda II spectrometer. FT-IR spectra were obtained by the standard transmission method using a Nicolet 510P FT-IR spectrometer. Electron micrographs of the monolayer film were obtained using a JEOL JEM - 1200 FX II transmission electron microscope (TEM), operating at 120.0 kV, and JEOL JEM 6310 scanning electron microscope (SEM), operating at 15 kV. Energy dispersive X-ray analysis (EDXA) spectra were obtained using a Link Li-drifted silicon type detector attached to the JEOL JEM 6310 SEM. A Link ANI0000 X-ray microanalysis system accumulated and processed the data to produce a spectra.

6.2.2 Results and Discussions

In initial experiments, three or four 50 μl drops of the $C_{60}[C(COOH)_2]$/THF solution were added in quick succession to the air/water interface. Under these conditions, surface pressure-area (π - a) isotherms were recorded but the limiting area per molecule varied between 5 and 25 $Å^2$, as shown in Figure 6.3.

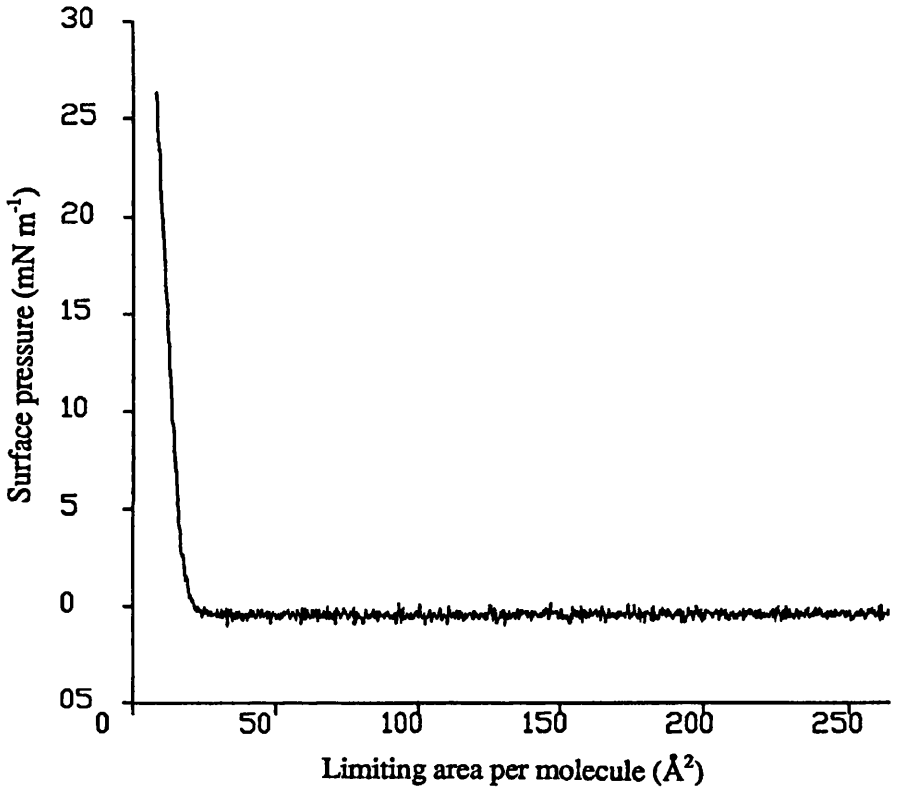

Figure 6.3 *π - a Isotherm of $C_{60}[C(COOH)_2]$ in THF (0.08 mg cm^{-3}, 200 μl) on a purite water subphase at 290 K.*

These values are clearly too small compared with the predicted value of 86 $Å^2$ for close packed fullerene molecules with intermolecular distances of 10 Å. Similar low limiting areas per molecule have been reported for C_{60} [44,45] and indicate multilayer formation. However, if a single drop of the THF solution was allowed to evaporate for at least 5 minutes prior to addition of the next drop, then a stable monolayer of

$C_{60}[C(COOH)_2]$ could be routinely achieved, as shown in Figure 6.4. The isotherms showed an initial increase in surface pressure at 200 $Å^2$, a well-established expanded liquid phase, and a distinct phase transition to the fully compressed solid domain. The limiting area per molecule was extrapolated to be 100 ± 4 $Å^2$. Assuming a close packed hexagonal lattice, this value corresponds to an interheadgroup spacing (limiting area per molecule = a^2 sin 60°, where a is the interheadgroup spacing of $C_{60}[C(COOH)_2]$) of 10.75 Å. Further compression resulted in a collapse pressure of 40 mN m^{-1} followed by multilayer formation. The monolayer was sufficiently stable, that it was possible to hold this system at constant area without any loss of pressure for at least 48 hours.

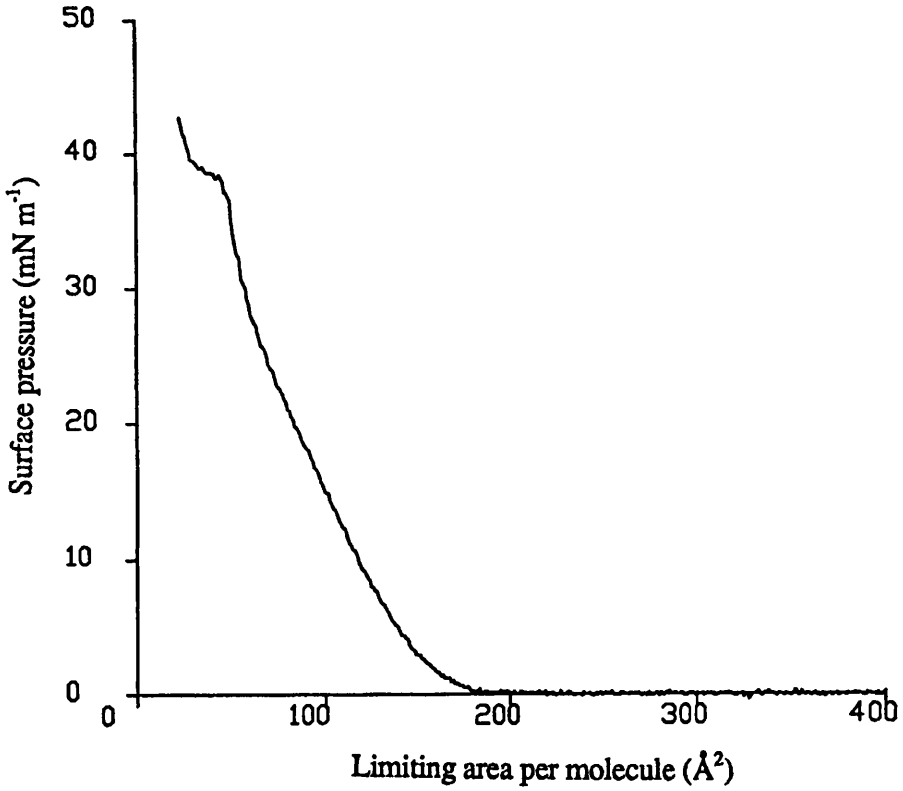

Figure 6.4 *π - a Isotherm of $C_{60}[C(COOH)_2]$ in THF (0.08 mg cm^{-3}, 200 μl) on a purite water subphase at 290 K.*

The UV-visible spectrum of a multilayer film of $C_{60}[C(COOH)_2]$ (shown in Figure 6.5), which consists of five transfers on to a hydrophobic quartz wafer showed the characteristic bands at 220, 272, 330, 370, and 450 nm for the C_{60} moiety.

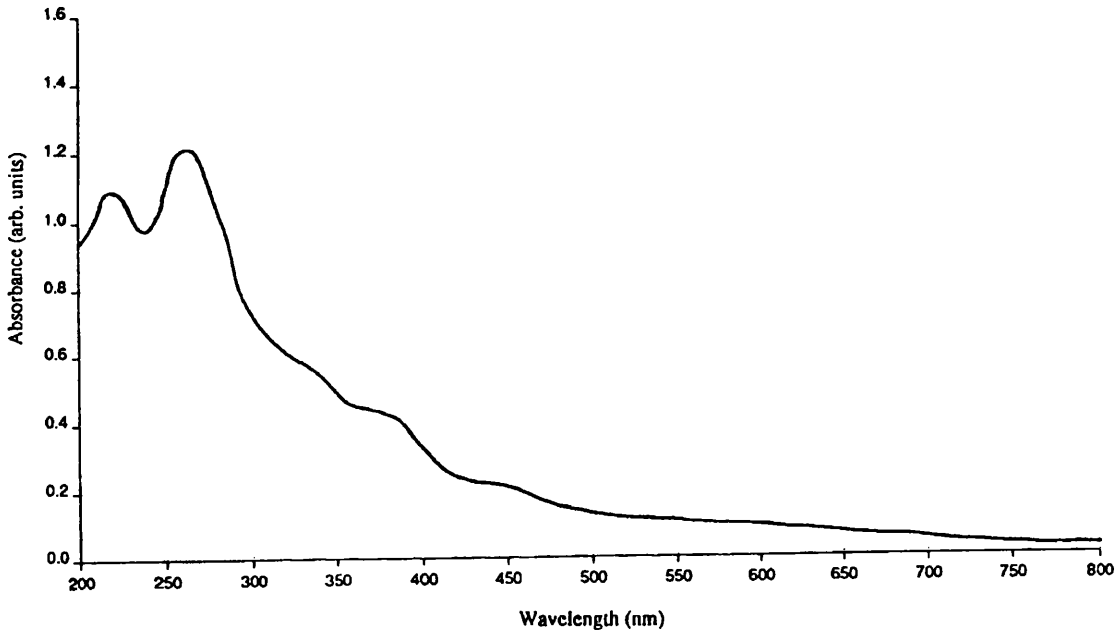

Figure 6.5 *UV-visible absorption spectra of a multilayer film of $C_{60}[C(COOH)_2]$ from pure water on a hydrophobic quartz substrate.*

TEM micrographs of the monolayer (Figure 6.6) and multilayer (Figure 6.7) films showed inhomogeneous films due to breakage of films during the transfer onto electron microscope grids.

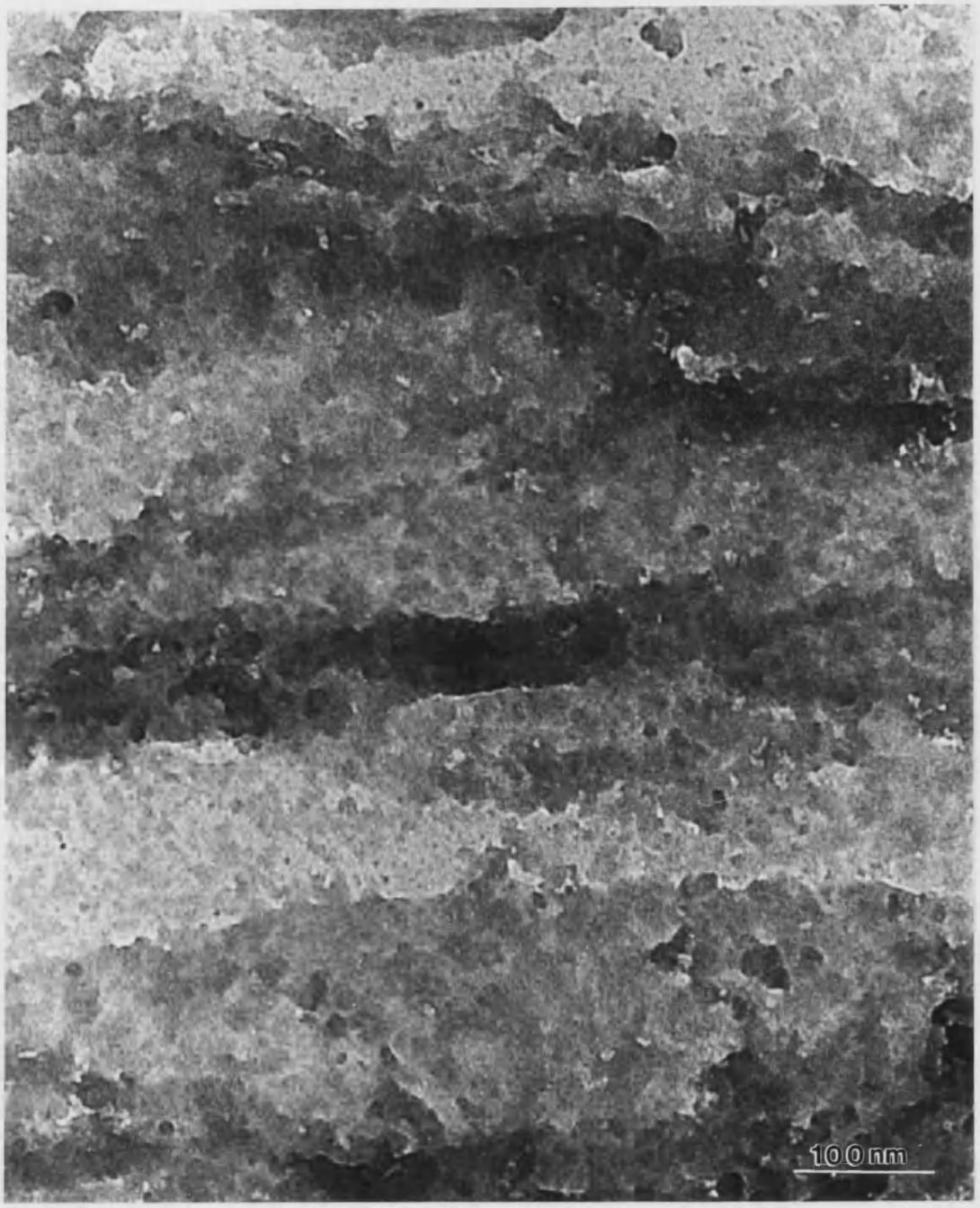

Figure 6.6 *TEM micrograph of a inhomogeneous monolayer film.*

Figure 6.7 *TEM micrograph of a inhomogeneous multilayer film.*

6.2.3 Conclusions

Here we show for the first time, provided extreme care is taken, the formation of self-assembled monolayers of buckminsterfullerene malonic acid, $C_{60}[C(COOH)_2]$, at the air/water interface. The isotherm on pure water afforded a limiting area per molecule of 100 ± 4 Å^2 which is consistent with crystallographic data of a hexagonal close packed lattice of C_{60} molecules. It also showed a well-established liquid phase, and a distinct phase transition to a fully compressed solid domain. Upon further compression, a collapse pressure of 40 mN m^{-1} was recorded which indicates that the monolayer film is stable. Further compression resulted in the formation of multilayers. The UV-visible spectra showed the characteristic bands of the C_{60} moiety, therefore it is possible to transfer the monolayer from the air/water interface to a substrate. Once again extreme care is needed to transfer the monolayer to the substrate, since TEM micrographs show inhomogeneous films due to film breakage on the transfer process.

6.3 Fullerates: Interaction of Cations with Fullerene Malonic Acid

With the bi-functionality of the polar head groups and the associated C_{2v} symmetry of the fullerene malonic acid molecule, and the fact that it can be spread at the air/water interface due to its amphiphilic nature, the next area of research was to explore to potential of the malonic acid subsituent of the C_{60} cage for metal-ion binding and the formation of salt-like "fullerates". Together these properties suggest that cations could be incorporated into organised multilayer assemblies of fullerenes derivatised with appropriate pendent groups.

6.3.1 Experimental

The trough experiments were set up as stated in section 6.2.1, except that experiments were performed on the following subphases; 10 mM solutions of $CdCl_2$ and $CaCl_2$. Characterisation of the monolayers were also performed as stated in section 6.2.1.

6.3.2 Results and Discussion

Surface π - a isotherms for $C_{60}[C(COOH)_2]$ spread on aqueous subphases containing 1 mM Ca^{2+} or Cd^{2+} divalent cations showed well-formed expanded monolayer (Figures 6.8 and 6.9 respectively). The onset of the liquid phase occurs at significantly higher areas of about 300 $Å^2$, than on pure water. This suggests that association of the metal cations with the carboxylate headgroups of $C_{60}[C(COOH)_2]$ is established even in the apparently uncompressed state.

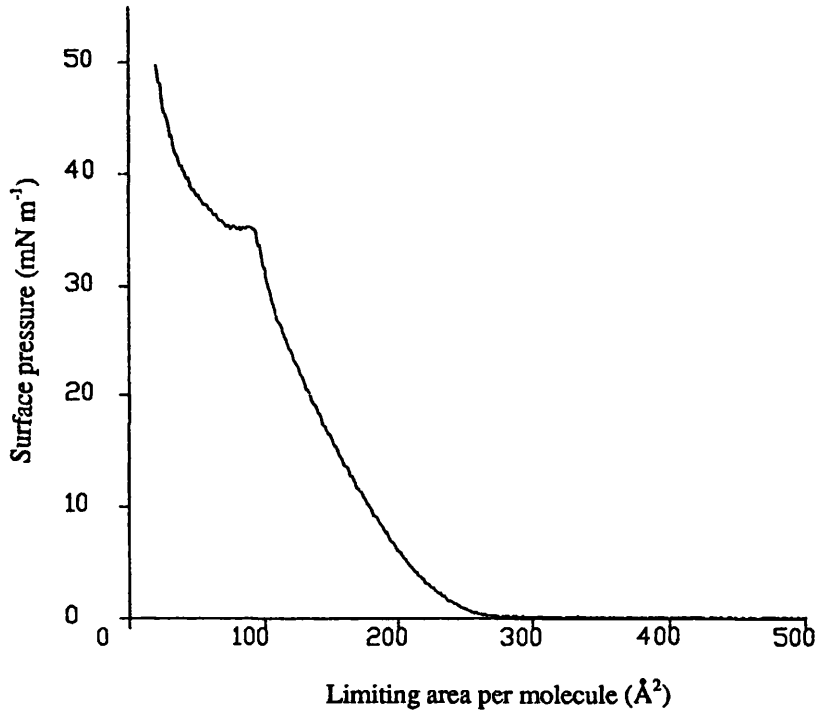

Figure 6.8 *π - a Isotherm of $C_{60}[C(COOH)_2]$ in THF (0.08 mg cm^{-3}, 200 μl) on a 1 mM $CaCl_2$ subphase (pH 5.3) at 290 K.*

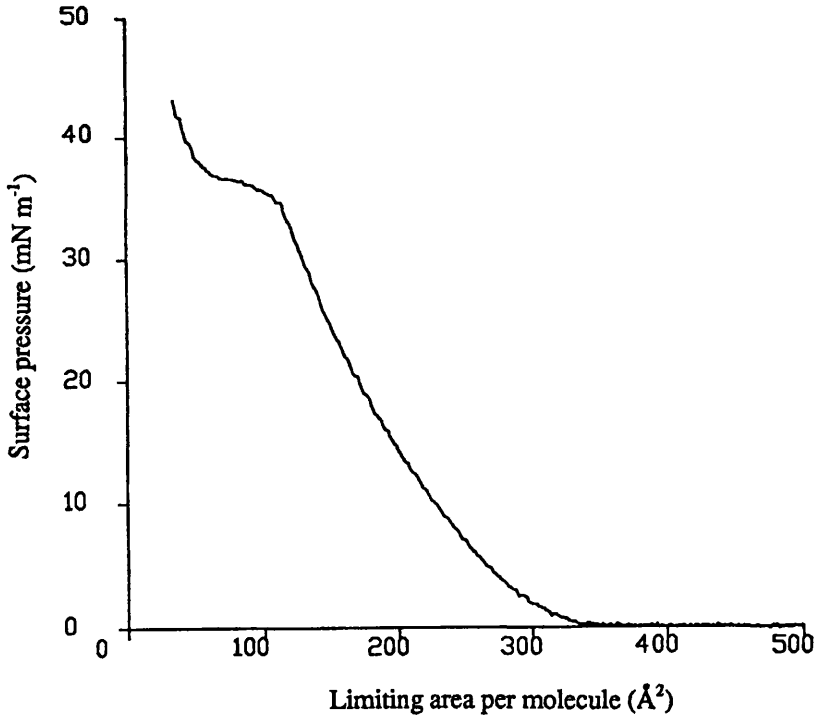

Figure 6.9 *π - a Isotherm of $C_{60}[C(COOH)_2]$ in THF (0.08 mg cm^{-3}, 200 μl) on a 1 mM $CdCl_2$ subphase (pH 6.4) at 290 K.*

Compression resulted in well defined liquid phases but only monolayers spread on Ca^{2+} solutions showed a distinct transition to a solid phase. Limiting areas per molecule of 160 $Å^2$ and 230 $Å^2$ were determined for Ca^{2+} and Cd^{2+} subphases, respectively. In both cases further compression resulted in a distinct phase change at a surface pressure of 35 mN m^{-1}, followed by an increase in pressure with a limiting area per molecule of 100 $Å^2$, similar to that for pure water.

These results suggest that the divalent cations intercalate between the head groups of $C_{60}[C(COOH)_2]$ to give expanded films that can be compressed to solid phases, but which on further compression revert to close packed monolayers depleted of the metal cations. In this regard, EDXA showed the presence of calcium in an expanded monolayer transferred onto a formvar substrate, shown in Figure 6.10.

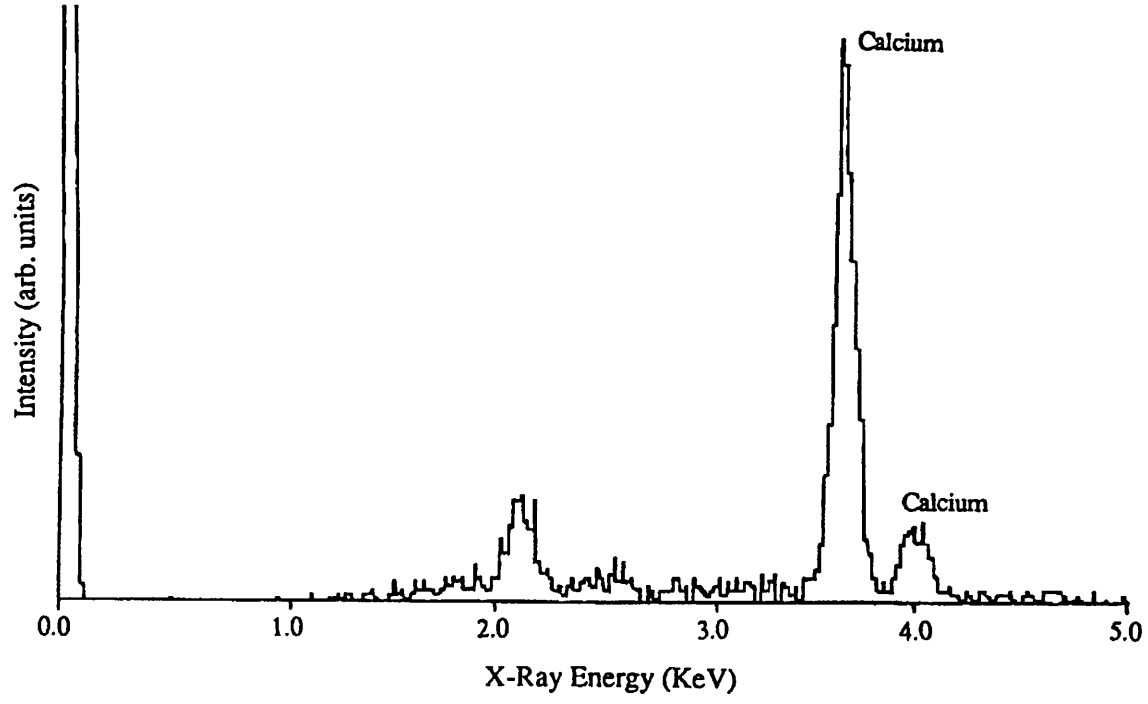

Figure 6.10 *EDXA spectra of a monolayer formed on a $CaCl_2$ subphase.*

In the corresponding monolayer formed on a $CdCl_2$ subphase, no cadmium was detected as shown by EDXA analysis (spectra shown in Figure 6.11).

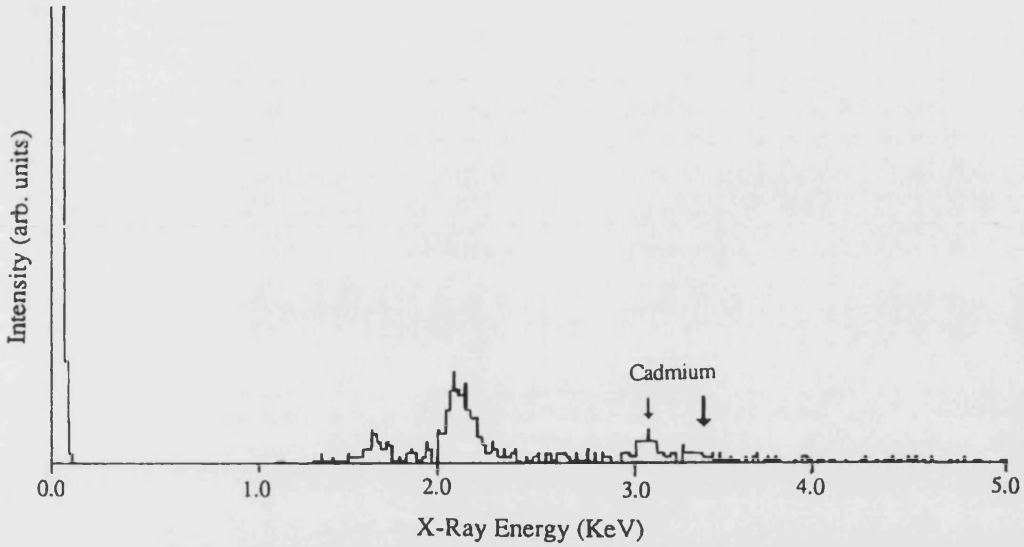

Figure 6.11 *EDXA spectra of a monolayer formed on a $CdCl_2$ subphase.*

The results of SAED patterns of the fullerene monolayer on 1 mM $CaCl_2$ are shown in Figure 6.12 and tabulated in Table 6.1.

Figure 6.11 *SAED of monolayer on 1 mM $CaCl_2$ subphase.*

Table 6.1 ED results for fullerene monolayer on 1 mM $CaCl_2$.

Radius (mm)	d-spacing (Å)	Assignments
2.35	2.84	calcite
3.58	1.86	calcite
6.63	1.01	calcite
10.67	0.63	carbon support
12.15	0.55	carbon support

These results suggests that calcium ions are present on the monolayer, and upon exposure to CO_2 in the air the calcium will transform to calcite (calcium carbonate). This was further validated by the TEM micrograph of the calcite crystals shown in Figure 6.12.

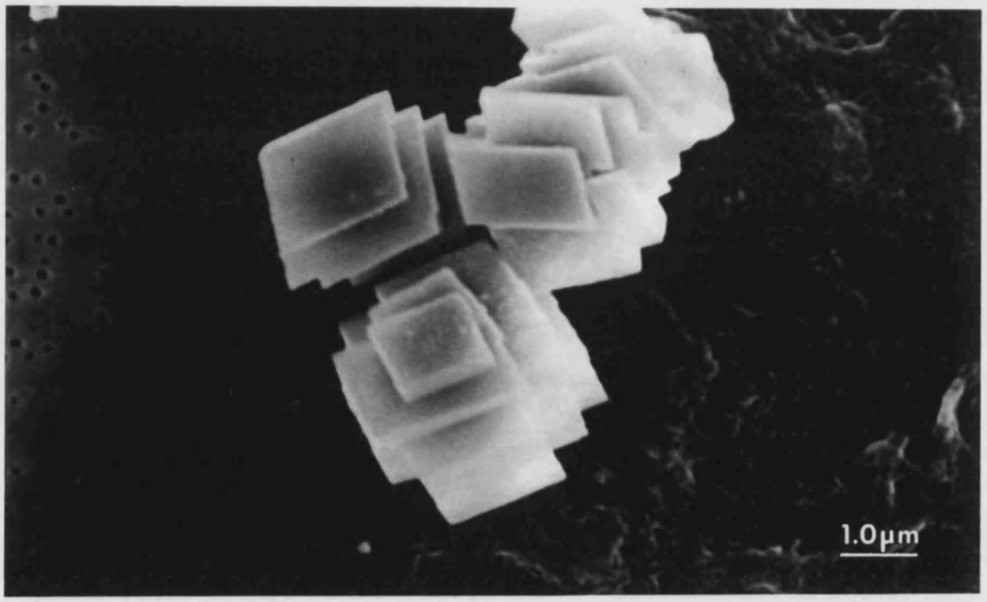

Figure 6.12 *TEM micrograph of the calcite crystals found on the fullerene monolayer after exposure to air.*

The data suggests that there is a stronger interaction between Ca^{2+} and the ionised carboxylate headgroups of the fullerene malonic acid than for Cd^{2+}, which is presumably lost from the expanded monolayer on transfer.

Multilayers consisting of up to ten transfers were formed by transfer on to hydrophobic silicon substrates of solid phase monolayers of $C_{60}[C(COOH)_2]$ spread on Ca^{2+} or Cd^{2+} subphases. EDXA analysis showed the multilayer films contained calcium (Figure 6.13), but no cadmium (Figure 6.14).

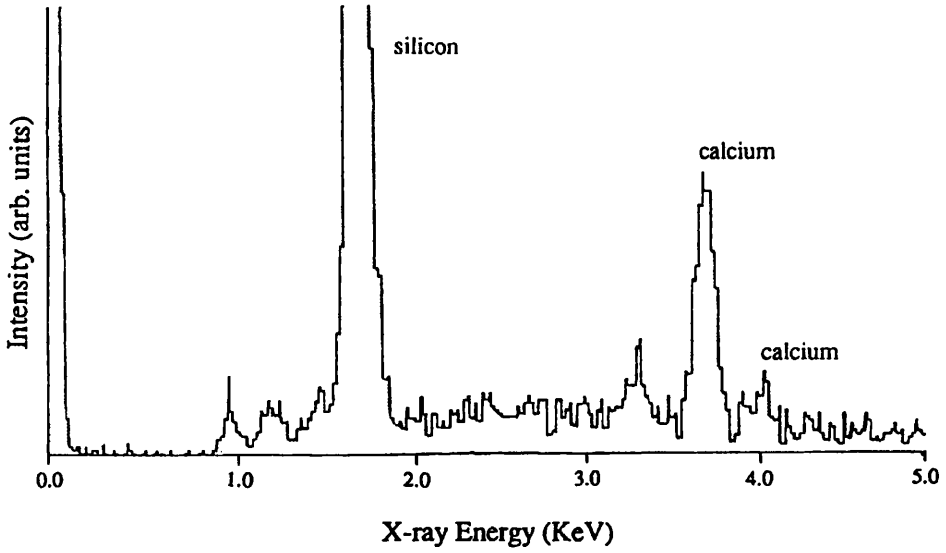

Figure 6.13 *EDXA of multilayers of $C_{60}[C(COOH)_2]$ spread onto a Ca^{2+} subphase.*

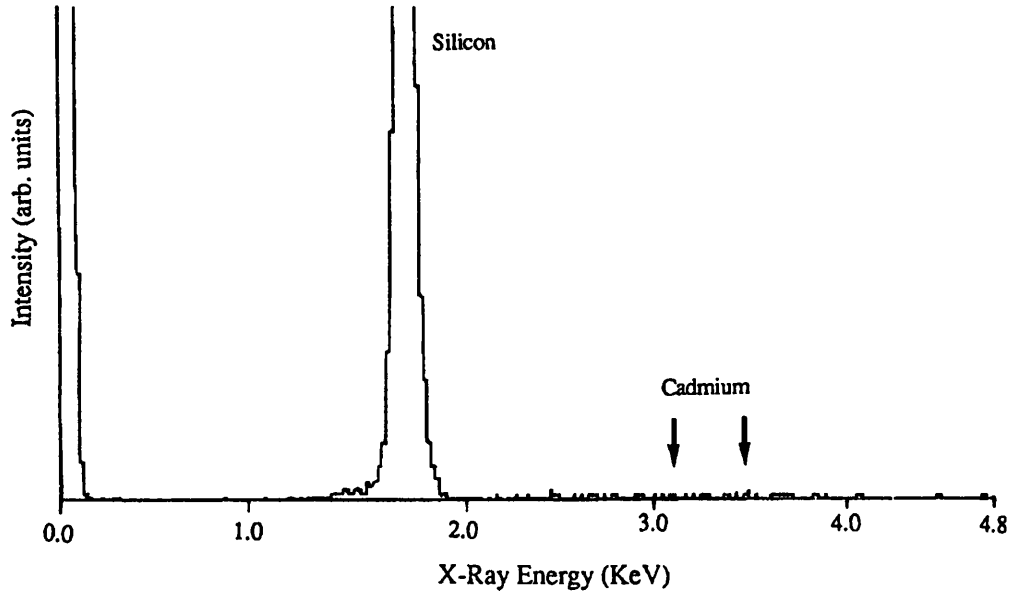

Figure 6.14 *EDXA of multilayers of $C_{60}[C(COOH)_2]$ spread onto a Cd^{2+} subphase.*

6.2.3 Conclusions and Future Work

Stable monolayers of $C_{60}[C(COOH)_2]$ can be produced on subphases containing Ca^{2+} or Cd^{2+} salts. The presence of the divalent cations produces well-formed expanded monolayers, which suggests that the divalent cations intercalate between the monolayer headgroups of $C_{60}[C(COOH)_2]$. The expanded films can be compressed to solid phases, with the monolayer on Ca^{2+} cations showing a distinct transition to a solid domain. On further compression the isotherms revert to close packed monolayers depleted of the metal ions. EDXA showed the presence of calcium in the expanded monolayers, but no cadmium was detected in the corresponding monolayer. This suggests that there is stronger interaction between the ionised carboxylate headgroups of $C_{60}[C(COOH)_2]$ and Ca^{2+}, than for Cd^{2+}. The limiting area per molecule of 160 $Å^2$ for the expanded Ca^{2+}-bound monolayer corresponds to an interheadgroup spacing of 13.5 Å, assuming a hexagonal lattice. This increase of 2.75 Å compared with the monolayer of $C_{60}[C(COOH)_2]$ on pure water is commensurate with the intercalation of Ca^{2+} ions between carboxylates of adjacent malonate headgroups such that a metal-ion bridged network is established at the monolayer/solution interface as represented in Figure 6.15.

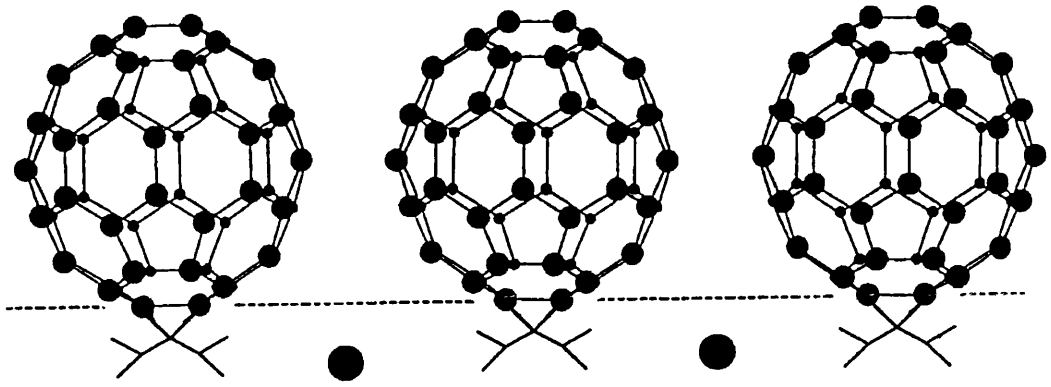

● Calcium

Figure 6.15 *Graphical representation of the intercalated Ca^{2+} cations and the ionised carboxylate headgroups of $C_{60}[C(COOH)_2]$.*

EDXA results for the multilayer films show that calcium is present but no cadmium in the corresponding multilayers, suggesting that calcium can be readily intercalated with close packed molecules of $C_{60}[C(COOH)_2]$ and co-assembled in organised arrays. Further experiments are underway to investigate the structure and properties of these metal-fullerene thin films.

This study highlights how self-assembled monolayers of functionalised fullerenes can be produced by careful manipulation of the spreading conditions. This aspect of the experimental methodology, although straight-forward it is of significant value because it allows the ability to organise fullerene molecules into assembled arrays which is an important requirement in the full realisation of the potential use of fullerenes as electrical, conducting and super-conducting nanostructured materials. This study also reports on the interaction of aqueous metal ions with functionalised fullerenes organised in mono-molecular or multilayer films. The ability to transfer

metal ion containing monolayers to produce multilayers is novel and leads the way towards organised fullerene composites.

Work to be undertaken is to provide evidence that the carboxylate groups on the $C_{60}[C(COOH)_2]$ are ionised when spread onto a Ca^{2+} subphase, *i.e.* that there is clear evidence of interaction between the -COOH groups and Ca^{2+}. FT-IR spectroscopy has already been utilised for this purpose. The multilayer film on a Ca^{2+} subphase was transferred onto a hydrophobic silicon wafer and analysed by reflective FT-IR spectroscopy. To date the data produced is inconclusive, possibly due to the limitations of the technique used. One possible method is once the monolayer is compressed fully, the resulting film is skimmed onto a 40 mesh stainless steel gauze. The skimmed films are then dried over P_2O_5 at room temperature for 1-4 days before being analysed.

Another area of research is to attempt to crystallise a C_{60}-malonic salt. A possible route is to dissolve the $C_{60}[C(COOH)_2]$ in basic water and titrate against a $CaCl_2$ solution of the same pH. The resulting precipitate will then be analysed *via* FT-IR and chemical analysis. If no precipitate is formed, then the resulting solution will be allowed to evaporate slowly to form crystals, which will then be analysed.

With regard to the characterisation of the multilayers, studies need to focus on the ion binding of Ca^{2+} to the multilayer. Another area of research to be explored is to attempt to incorporate other ions into the multilayers. Ions of interest are Mn^{2+}, Cu^{2+} and other transition metals, all of similar size to the Ca^{2+} cation. Mn^{2+} is of particular interest since it can display magnetic properties, hence the possibility exists to fabricate magnetic fullerene multilayers.

6.4 $CaCO_3$ Crystallisation under Fullerene Malonic Acid Monolayers

It is well known that the crystallisation of inorganic solids on rigid substrates often proceeds in an orientated fashion.[48] In many instances, the crystallographic relationships between the overgrowth and inorganic substrate can be explained by the epitaxial matching of lattice spacings of specific crystal planes at the crystal/crystal interface.[49] Although relatively large degrees of lattice mis-matching can occur,[49] geometric factors are generally considered to be of fundamental importance.

Similar epitaxial mechanisms have been proposed for the nucleation of oriented inorganic minerals in biological systems.[50-54] However, in these systems the substrate is often an organic polymeric framework of complex composition. The possibility that organised organic surfaces are capable of mediating inorganic crystallisation reactions is of great importance because these substrates, unlike inorganic surfaces, can be extensively tailored by specific chemical modifications of functional groups. Thus the potential scope for controlled, oriented inorganic crystallisation, is high.

A number of different experimental strategies have been developed to elucidate the mechanisms of inorganic crystallisation at organised organic templates. A biological approach has been to isolate the matrix components of mineralised tissue such as bones, teeth and shells, and examine the formation of insoluble Ca salts in the presence of these macromolecules.[55-57] Difficulty encountered with these studies showed that the details of the surface structure cannot be assessed because of the complexity of the macromolecules used. Furthermore, *in vitro* conformation of such molecules may be very different from their *in vivo* counterparts.

In this study we have adopted a different approach using simplified organised surfaces which can be characterised and systematically modified. The method involves the use of compressed monomolecular surfactant films formed at air/water interfaces in a Langmuir trough as substrates for inorganic crystallisation from supersaturated subphases. Landau *et al.*[58-60] have compressed resolved amino acid monolayers as templates for the nucleation of inorganic and chiral inorganic crystals. Recent studies[61-62] have shown that the crystallisation of $CaCO_3$ under stearic acid monolayers resulted in dramatic changes in the crystallochemical properties of the product. Whereas crystallisation in the absence of films gave rise to uncontrolled intergrowth of calcite of rhombohedral morphology, crystals nucleated in the presence of the negatively charged monolayer were discrete organised crystals of the metastable polymorph, vaterite. Furthermore, the vaterite crystals were orientated with their *c* axis perpendicular to the monolayer suggesting that stereochemical and electrostatic interactions were responsible for nucleation on this specific face.

Another aspect of carrying out research in the field of "controlled crystallisation" under macromolecular organic monolayers is that the interfacial adsorption of organic macromolecules is relevant to understanding mineralisation processes in living systems. Proteins are thought to control the crystallisation of biominerals from aqueous solutions at interfacial sites inside, or on the surface of the cell. Formation of biominerals is under strict genetic control and information is often laid down at a interface of organic macromolecules,[63] thus the interaction between these organic macromolecules and the biomineral is crucial to the understanding of the biomineralisation process.

6.4.1 Calcium Carbonate ($CaCO_3$) Systems

Calcium carbonate has three different crystalline polymorphs; calcite, aragonite and vaterite (Figure 6.16). Calcite and aragonite are the most common forms, and both are of particular significance in the context of biomineralisation, where they are used extensively by many organisms.[64]

Calcite

The crystalline structure of calcite is comprised of approximately close-packed layers of calcium and planar carbonate ions alternating along the *c* axis of the hexagonal unit cell.[65] The C_3 axis of the trigonal carbonate ion is orientated parallel to the crystallographic *c* axis, with the C_2 axis of the anions pointing in opposite directions in alternate layers. Calcite crystals can exhibit a greater variety of forms and habits than any other mineral. Synthetic calcite is, however, dominated by the rhombohedral form.

Aragonite

The crystalline structure of aragonite is similar in form to that of calcite. Calcium ions lie in the positions of a hexagonally close packed (hcp) structure deformed by compression along the six-fold axis. Layers of calcium ions lie perpendicular to the c axis of the orthorhombic unit cell,[66] alternating with layers of carbonate ions. However, unlike the calcite structure where there is a single plane of arranged carbonate ions, there are two staggered planes, aligned in different directions. Aragonite morphology can be acicular or columnar, but synthetically is more often multi-crystalline aggregates of fibrous crystals.

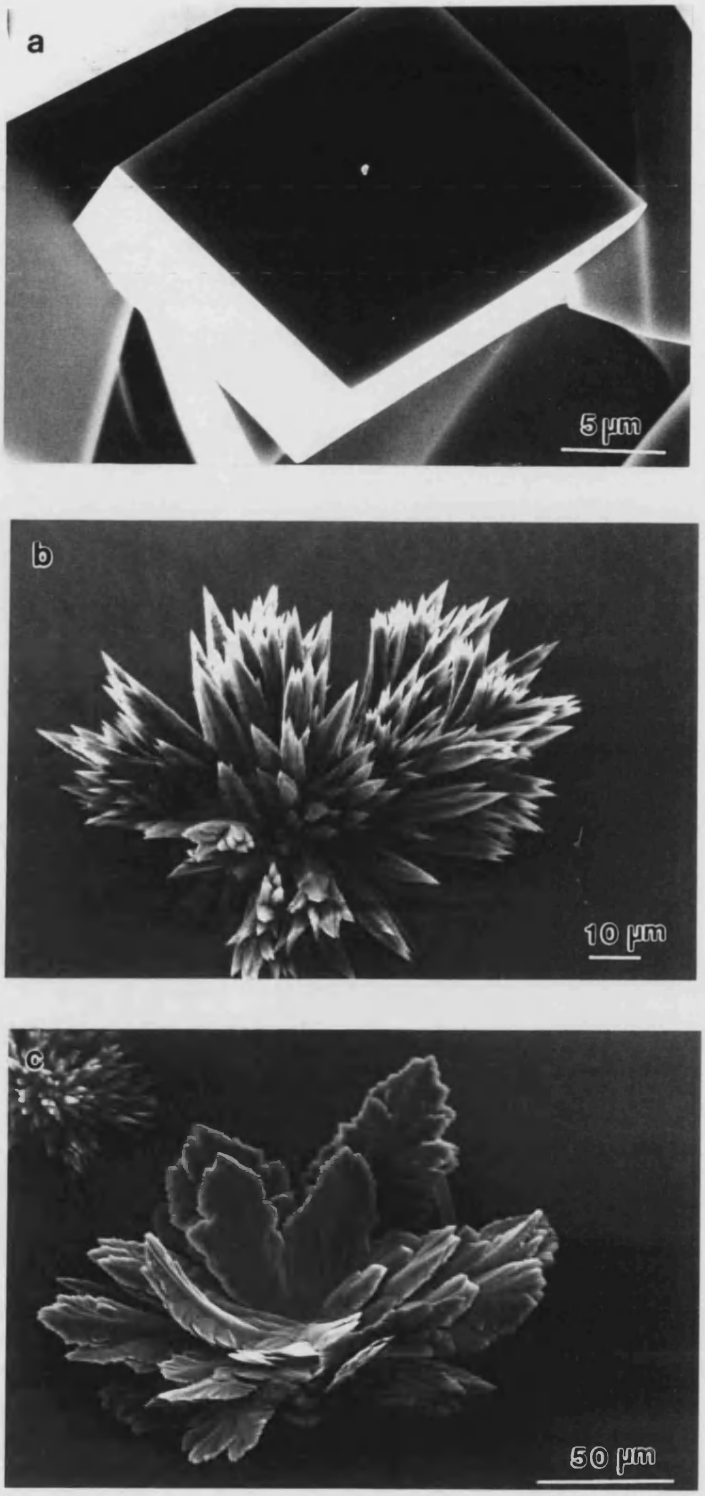

Figure 6.15 *SEM micrographs of a) calcite, b) aragonite and c) vaterite polymorphs of* $CaCO_3$.

6.4.2 Experimental

In this section the above work has been extended to use microscopy to study the formation of $CaCO_3$ crystals under compressed monolayer films of fullerene malonic acid. The objective of this work was to investigate the role of headgroup charge and Ca on the structure, morphology and organisation of $CaCO_3$ crystals under the fullerene malonic acid monolayer.

Preparation of Synthetic Calcium Carbonate

The supersaturated calcium bicarbonate solution was prepared according to the procedure adopted by Kitano,[67] with some modifications. Calcium carbonate (BDH Analar grade) shown to be the polymorph, calcite *via* XRD analysis, was suspended (2.5 g dm^{-3}) in Purite™ distilled water. The suspension (pH 8.0-8.4) was then bubbled with carbon dioxide at a rate of 3 dm^3 min^{-1}, then scrubbed through twin Hirsch bottles (250 cm^3) containing Purite™ distilled water for an initial period of 1 hour, with mechanical stirring. The remaining calcium carbonate was then removed from the solution using Buchner filtration (Whatman filter paper number 42). A further period of 0.5 hour bubbling with carbon dioxide was then employed to dissolve any crystal nuclei that might be present. The resulting bicarbonate solution (pH 5.8-6.0) was then ready for crystal growth experiments.

EDTA Volumetric Analysis for Calcium[68]

A value of the total dissolved calcium (Ca_T) in an aqueous system was determined by pipetting the solution (25 cm^3) to be analysed into a conical flask with 2 mol dm^{-3} HCl (2 cm^3) and Purite™ distilled water (25 cm^3). This solution was then

boiled to completely remove carbonate and cooled. Then 8 mol dm^{-3} NaOH (4 cm^3) was added to adjust the pH to about 12-13. After allowing the solution to stand for a few minutes. Then 10% KCN (6 drops) and 10% hydroxylamine hydrochloride (6 drops) together with 2-hydroxy-1-(2-hydroxy-4-sulpho-1-naphthylazo)-3-naphthoic acid (0.05 g) indicator were introduced. This was then titrated with standardised EDTA solution of concentration appropriate to the expected level of calcium in solution. Colour change was from wine red (Ca-indicator complex) to dark blue (free indicator). All titration's were performed in duplicate.

Crystallisation Experiments

The bicarbonate solution, of Ca_T 9-10 mmol, was transferred into four clean Pyrex™ crystallisation dishes. One of the dishes was slightly covered with a piece of filter paper, but was left open to the atmosphere under ambient conditions. This dish acted as a control. The remaining three dishes had a monolayer of $C_{60}[C(COOH)_2]$ placed at the interface to produce a solid phase film. These were also covered with filter paper, but left open to the atmosphere. The reason the dishes were covered with filter paper was prevent and dust falling into the dishes and initiate crystallisation. The dishes had to be left slightly open to the atmosphere to allow the slow diffusion of CO_2 into the atmosphere and initiate slow crystallisation of $CaCO_3$.

In all experiments, crystallisation was governed by the slow loss of CO_2 gas from unstirred supersaturated solutions according to the reaction:

$$Ca^{2+}_{(aq)} + 2HCO_3^-{}_{(aq)} = CaCO_{3(s)} + CO_{2(g)} + H_2O_{(l)}$$

Characterisation of the $CaCO_3$ Crystals

Crystals nucleated at the monolayer/solution interface were studied by X-ray diffraction and microscopy. SEM examination of crystals mounted directly onto stainless steel stubs was undertaken by the method shown in Figure 6.16.

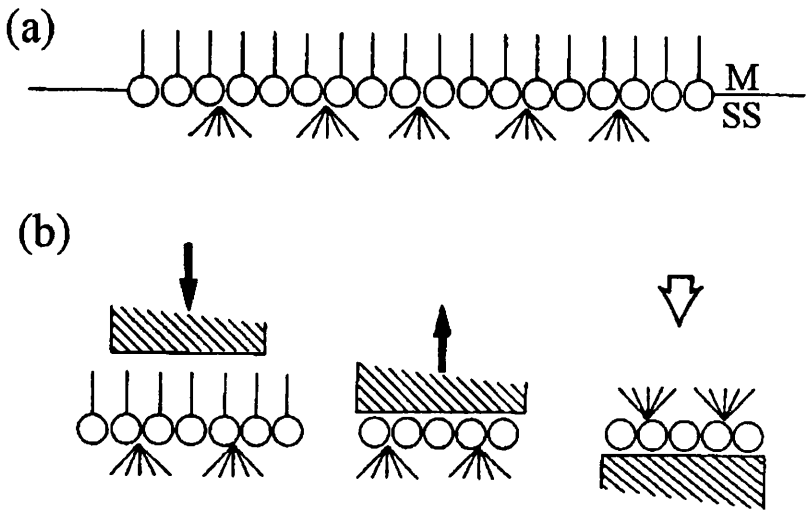

Figure 6.16 *Schematic showing techniques for removing crystals from monolayer surfaces for SEM microscopy (redrawn from Rajam, S. et al.).*[69]

From Figure 6.16, part (a) shows the crystals formed at the monolayer(M)/subphase(SS) interface. Part (b) shows how the stainless steel SEM stub is brought into close contact with the monolayer (↓) and the crystals adhere by surface tension on retraction (↑). The orientation of the crystals on the SEM support is now equivalent to a view from below the monolayer.

6.4.3 Results and Discussion

Control Experiments

Crystallisation of calcium carbonate from a supersaturated subphase in the absence of Langmuir films resulted in uncontrolled crystallisation at both the air/water interface and at the bottom of the reaction vessel. The crystals formed at the surface of the solutions were randomly intergrown calcite crystals of rhombohedral or truncated rhombohedral morphology (Figure 6.17).

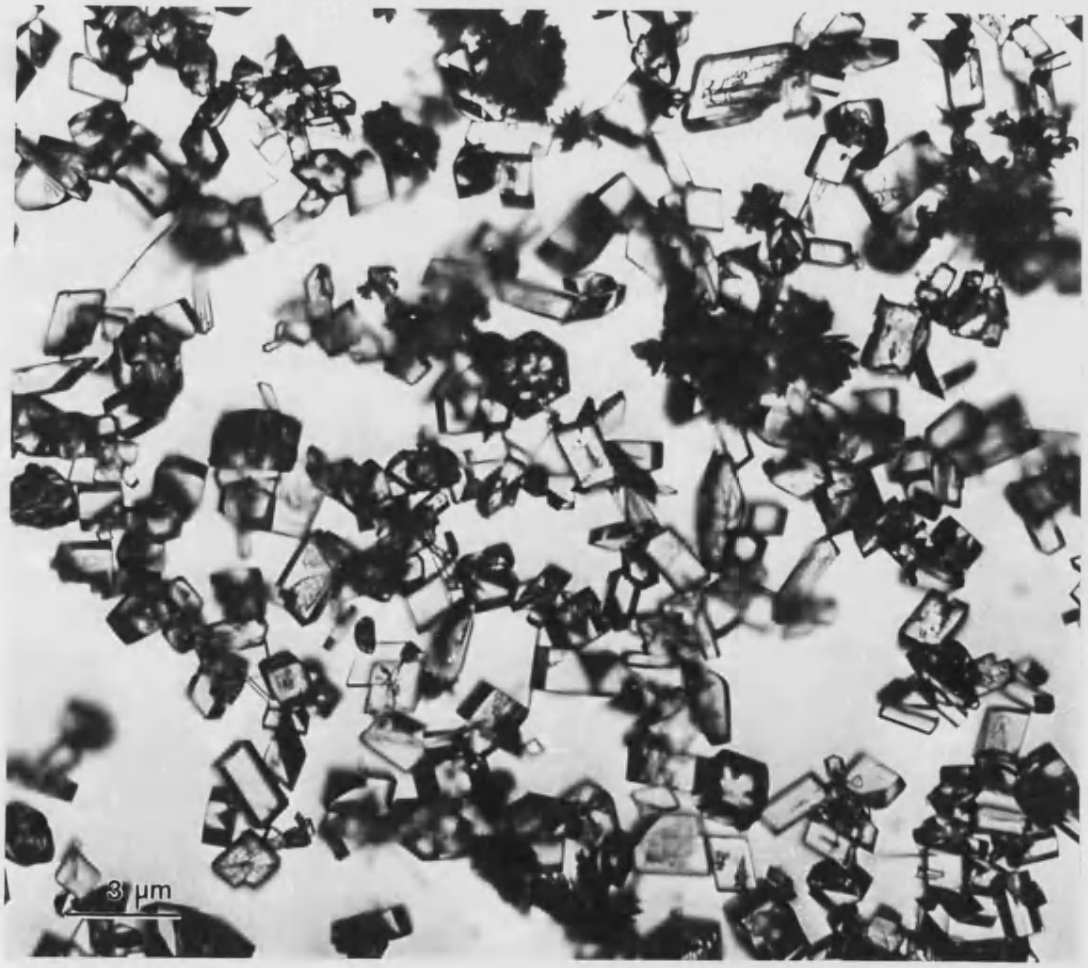

Figure 6.17 *Optical micrograph, viewed from above of rhombohedral calcite formed at the air/water interface.*

The crystals were non-orientated at the air/water interface. Some dendritic vaterite crystals were also present. Crystals formed at the bottom of the reaction vessel were discrete non-orientated calcite rhombohedral crystals (Figure 6.18).

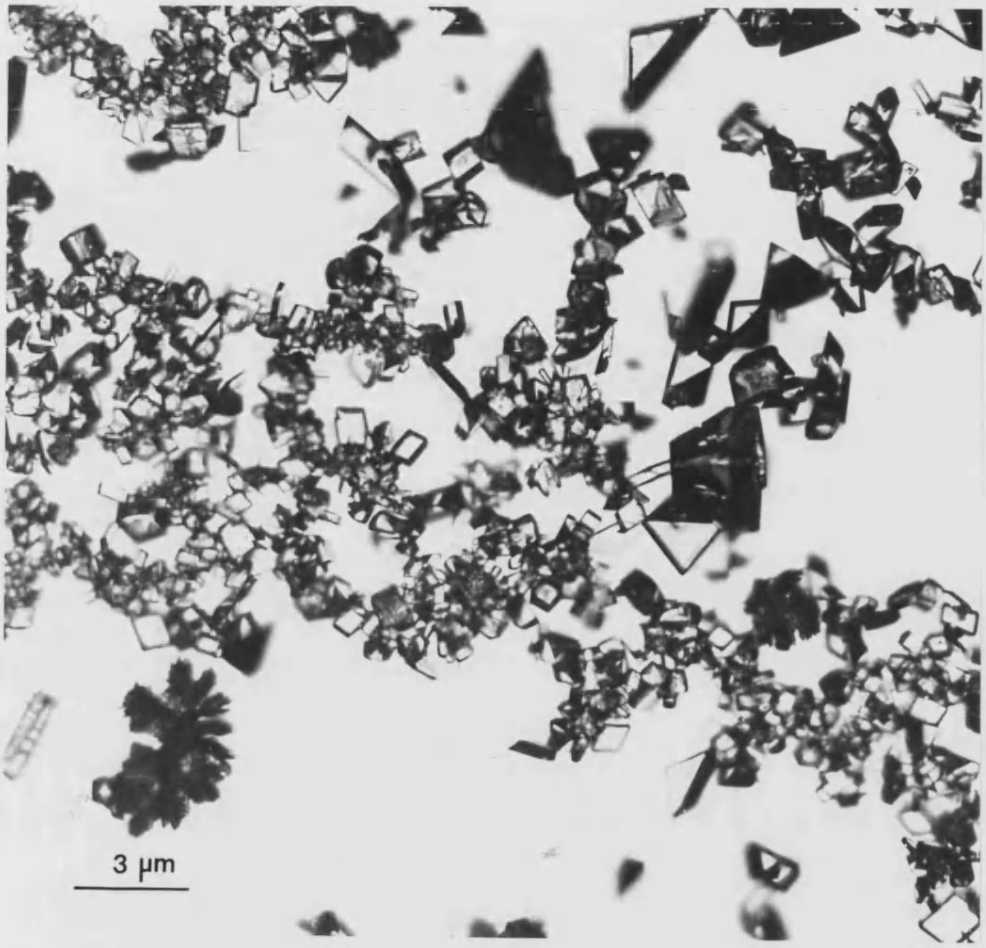

Figure 6.18 *Optical micrograph, viewed from above of rhombohedral calcite formed at the bottom of the reaction vessel.*

X-ray diffraction of the crystals collected at the air/water interface (Figure 6.19 and Table 6.2) showed that the crystals are predominately calcite with some vaterite crystals present, confirming the results obtained by optical microscopy.

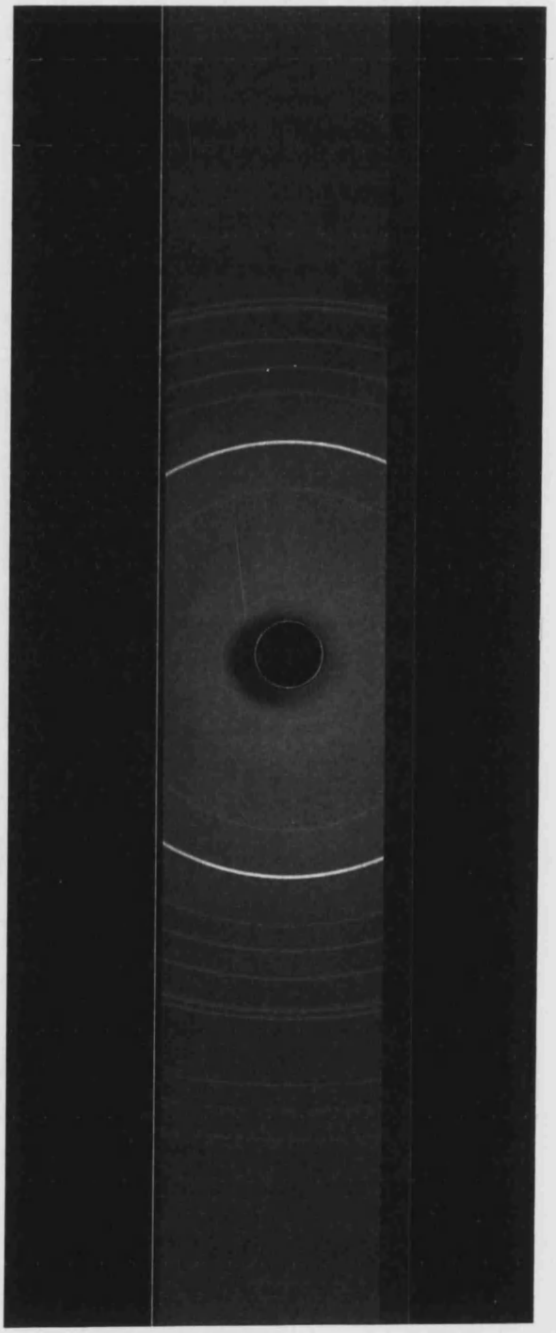

Figure 6.19 *XRD pattern for crystals collected at the air/water interface.*

Table 6.2 *XRD data for crystals collected at the air/water interface.*

d-value for $CaCO_3$ crystals (Å)	d-value for calcite[70] (Å)	d-value for vaterite[71] (Å)
3.87	3.86	-
3.04	3.035	-
-	2.845	-
2.50	2.495	-
2.29	2.285	-
2.10	2.095	-
-	1.927	-
1.92	1.913	-
1.87	1.875	-
1.65	-	1.6481
1.63	1.626	-
1.61	1.604	-
-	1.587	-
1.54	1.525	-
-	1.518	-
-	1.510	-
-	1.473	-
1.45	1.440	-
1.43	1.422	-
1.29	-	1.2881

SEM microscopy of the crystals collected onto a stubb, as shown in Figure 6.16b, show that the crystals are calcite rhombohedra (Figure 6.20).

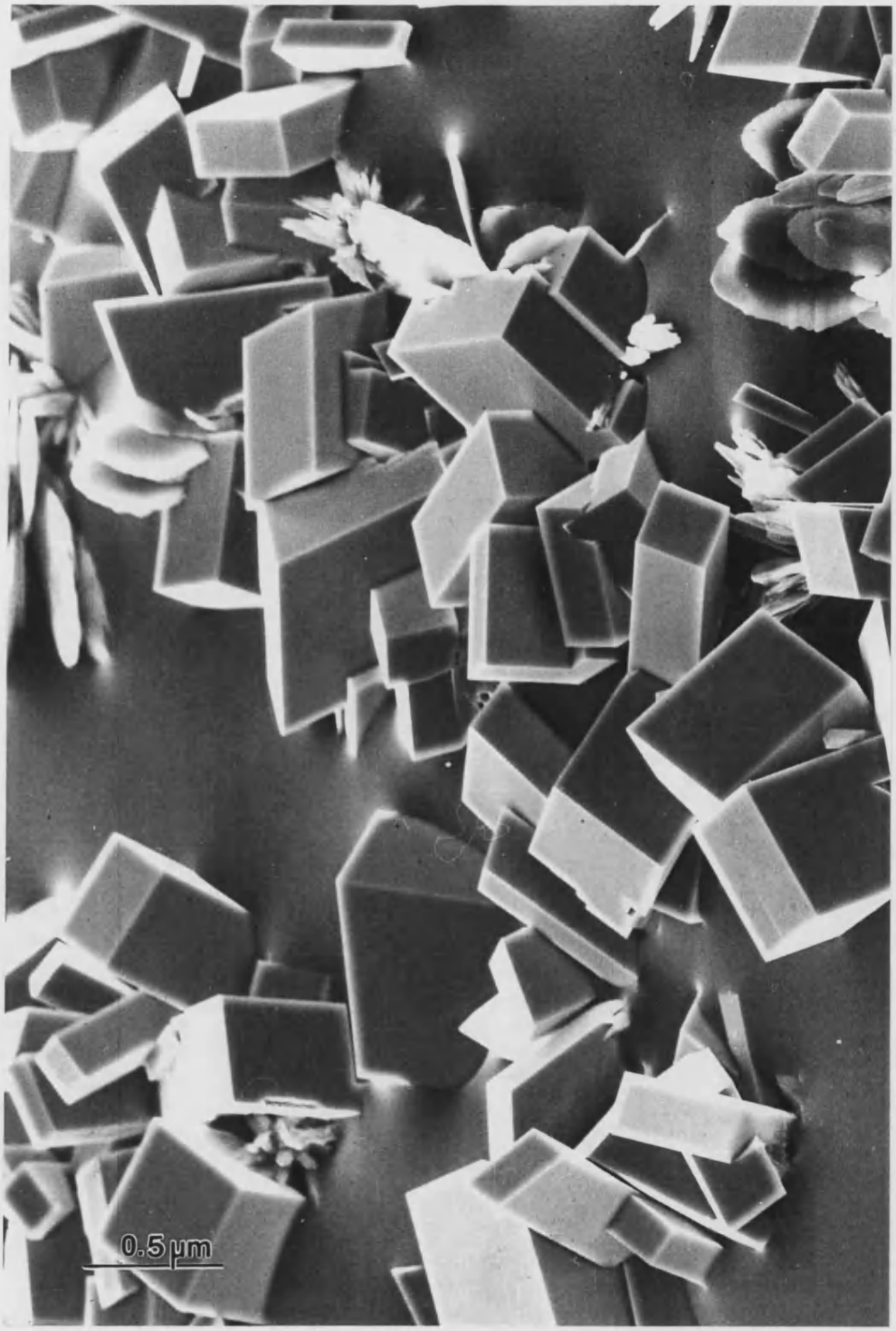

Figure 6.20 *SEM micrograph of crystals collected at the air/water interface.*

In total five optical micrographs were taken at random of the control sample. Distribution of the three different polymorphs of $CaCO_3$ grown at the air/water interface are tabulated in Table 6.3 and graphically shown in Figure 6.21.

Table 6.3 *Distribution of $CaCO_3$ morphology from control samples.*

Polymorph	% Distribution
Calcite	96
Vaterite	3
Aragonite	1

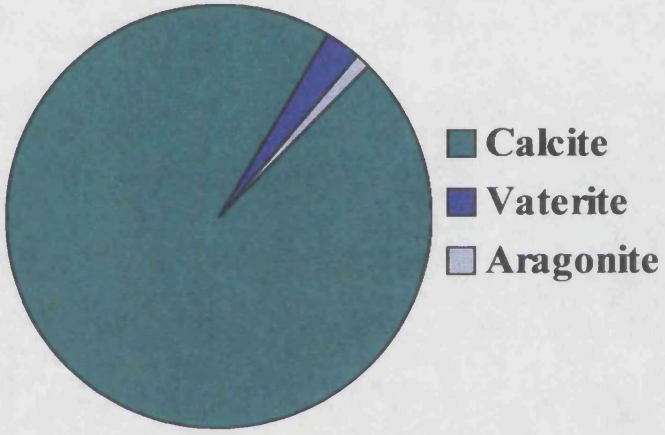

Figure 6.21 *Pie chart showing the distribution of each polymorph of crystals grown at the air/water interface.*

Fullerene Malonic Acid Experiments

Crystallisation of calcium carbonate from a supersaturated subphase under a compressed monolayer of $C_{60}[C(COOH)_2]$ resulted in the formation of non-orientated calcite crystals at the solution/monolayer interface and at the bottom of the reaction vessel. Viewed from above the monolayer surface by optical microscopy, the crystals were once again in the form of rhombohedra or truncated rhombohedra (Figure 6.22), as they were for the control sample.

Figure 6.22 *Optical micrograph, viewed from above of rhombohedral calcite formed at the solution/monolayer interface.*

Once again some dendritic vaterite was present as in the control sample. Crystals formed at the bottom of the reaction vessel were once again discrete non-orientated calcite rhombohedral crystals (Figure 6.23).

Figure 6.23 *Optical micrograph, viewed from above of rhombohedral calcite formed at the bottom of the reaction vessel.*

X-ray diffraction of the crystals formed at the solution/monolayer interface (Figure 6.24), is identical to the XRD pattern obtained for the control sample.

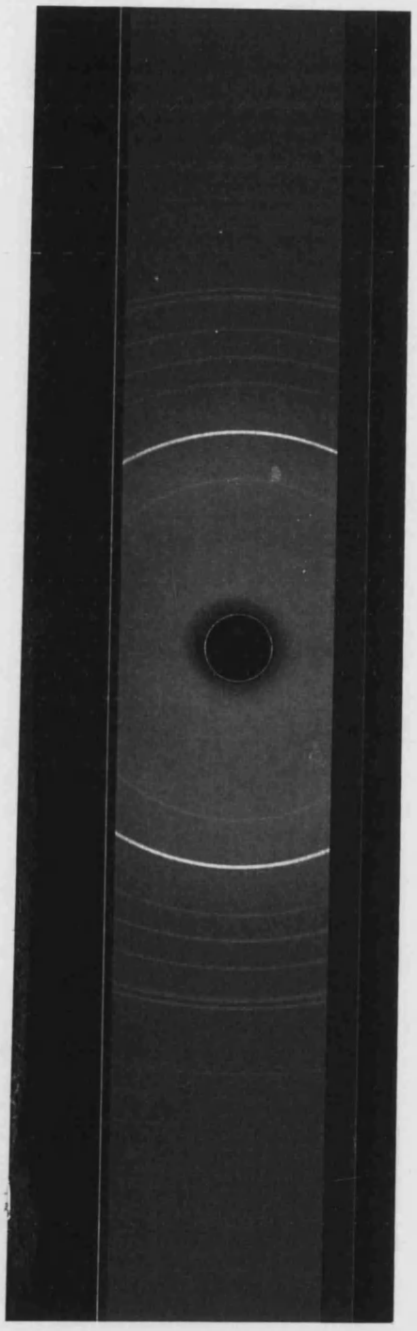

Figure 6.24 *XRD pattern for crystals collected at the solution/monolayer interface.*

The SEM micrograph (Figure 6.25) shows that the crystals collected are calcite. The overall percentage distribution of each polymorph taken once again from five random photographs is tabulated in Table 6.4 and graphically shown in Figure 6.26, revealing that calcite is once again the predominant polymorph.

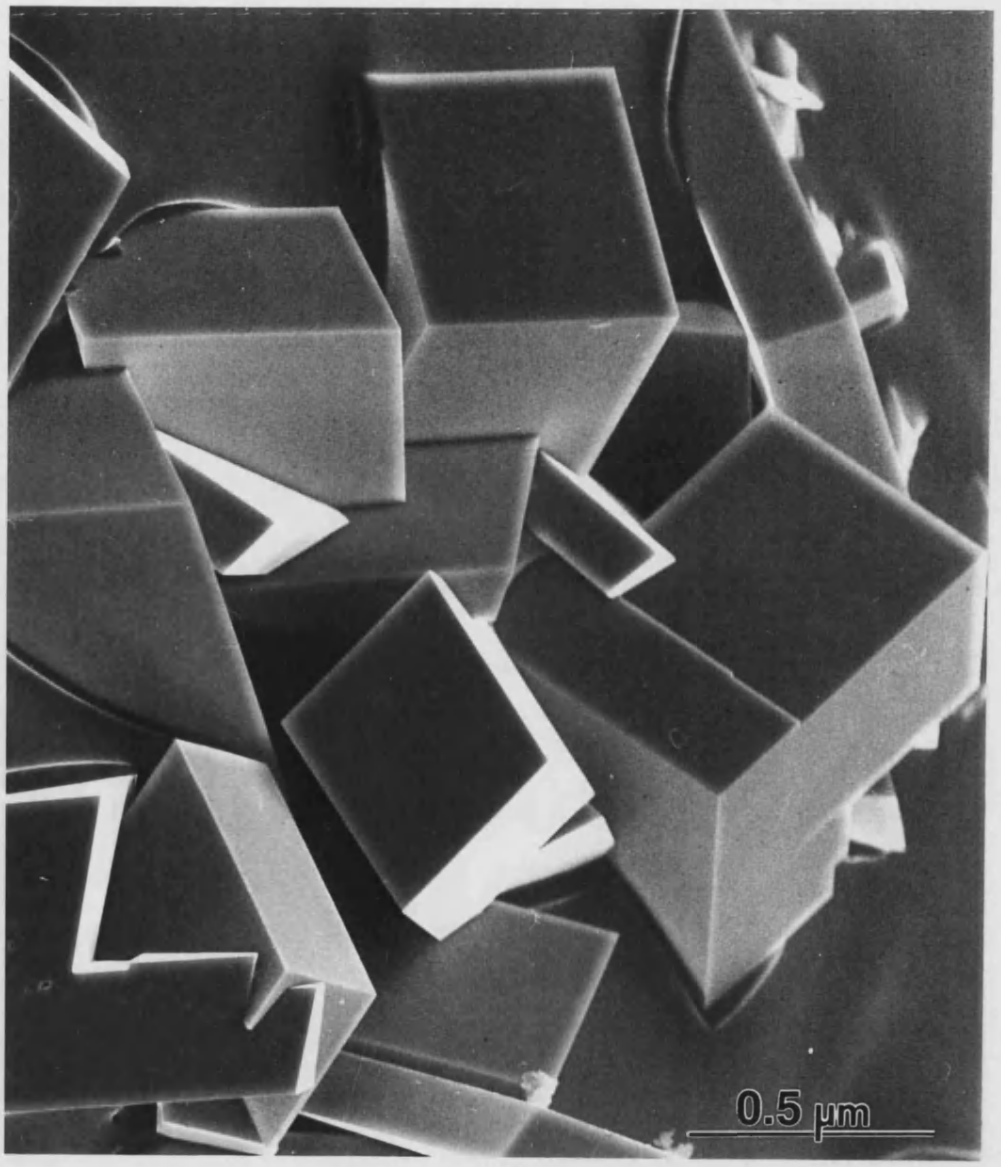

Figure 6.25 *SEM micrograph of crystals collected at the solution/monolayer interface.*

Table 6.4 *Distribution of $CaCO_3$ morphology from $C_{60}[C(COOH)_2]$ samples.*

Polymorph	% Distribution
Calcite	96
Vaterite	3
Aragonite	1

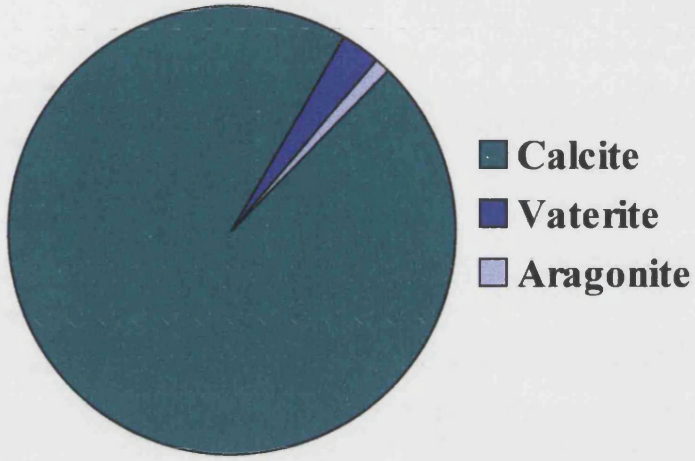

Figure 6.26 *Pie chart showing the distribution of each polymorph of crystals grown at the air/water interface under a $C_{60}[C(COOH)_2]$ monolayer.*

6.4.4 Conclusions

On comparison of the results obtained from the samples with and without the presence of the fullerene malonic acid monolayer, it is clear to see that there is no orientation of the $CaCO_3$ crystals, since both sets of results are almost identical. This suggests that there is no specific interaction between the malonic acid head groups of the C_{60} and the calcium ions in the supersaturated solution, therefore leading to non-orientated crystals. Even though this is a negative result in terms that no specific orientation of $CaCO_3$ crystals was seen, the study was worthy of inclusion since the next logical step after being able to produce an monolayer of fullerene malonic acid was to see if it does orientate $CaCO_3$ crystals in a specific manner.

6.5 Fullerene Malonic Acid Doped within Silica Sol-Gels

Among the most notable features of C_{60} are its optical properties[72] which make this molecule interesting from the point of view of non-linear optical materials[73] as is shown, for example, in optical limiting experiments.[74]

Sol-gel processing, mainly due to the relatively low temperatures at which inorganic or hybrid organic-inorganic glasses can be prepared,[75] offers an attractive possibility to satisfy other requirements for non-linear optical materials. The production of materials using sol-gel techniques has become evermore common in recent years. The sol-gel process is based around the formation of a glassy network by the polymerisation of a suitable monomeric unit. The most commonly used monomers are the metal alkoxide species, $M(OR)_n$.[75,76] Common metal alkoxides such as tetramethoxysilane (TMOS) or tetraethoxysilane (TEOS) are widely used in the production of silica gels.

The monomeric alkoxides hydrolyse and then condense to form M-O-M linkages *via* a series of reactions summarised in equations 6.1 and 6.2.

$$M(OR)_n + n\,H_2O \rightarrow M(OH)_n + n\,R\text{-}OH \qquad (6.1)\ \text{Hydrolysis}$$

$$M(OH)_n \rightarrow MO_{n/2} + n/2\,H_2O \qquad (6.2)\ \text{Condensation}$$

Since alkoxides and water are immiscible, a common solvent is generally incorporated to produce an initial homogeneous liquid. Common solvents usually are methanol or ethanol. The incorporation and entrapment of species within the gel framework is possible either by the diffusion of species into the porous hydrated gels,[77] or by direct inclusion into the alkoxide/water mixture,[78] used in the initial gel

formation. The transparent nature of the resulting gels has allowed the activity of the doped molecules to be probed using optical techniques, confirming their non-linear optical properties are unaffected by their presence in the gel.

The versatility of the sol-gel preparation of silica glasses allows the final dried glass to be processed in different ways, dependent on the final use. For example spin coating of silica sols allows the formation of thin single, or multi-layers of composite glasses. Alternatively large, fault free, glass monoliths can be produced. The most desirable features of sol-gels are: the possibility of obtaining thin films by simple methods, good control of refractive index, wave-guiding properties and good resistance to environmental degradation.

The idea of incorporating C_{60} in sol-gel derived materials is an obvious consequence of the above concepts. Sheng *et al.*[79] described the preparation of C_{70}-doped silica gel monoliths. Attempts to use C_{60} for the same purpose produced only powder gel. In a more recent paper, Zerda *et al.*[80] reported the diffusion of C_{60} in porous sol-gel silica glasses. The diffusion process was an attempt to avoid the non-homogeneous distribution of the fullerene in the precursor solution. It appears, however, that this method allows the introduction of only a small amount of C_{60} into the inorganic matrix. A solution to the problem of homogeneity is to increase the solubility of the fullerene in the sol-gel solution by suitable functionalisation of C_{60}.[81]

In this section, we report on the preparation of transparent sol-gel thin films containing fullerene malonic acid.

6.5.1 Experimental

Production of Silica gels

Silica sols were prepared by using tetramethyl orthosilicate (TMOS) supplied by Aldrich. Silica sols were formulated by preparing a solution of TMOS, H_2O and 0.04 M HCl ($TMOS:H_2O:HCl$ = 8.8:15.8:1 molar ratios). Phase separation occurs between these components, therefore sonication for about 5 minutes produces a homogeneous solution. 2 cm^3 of this solution was placed in a plastic vial, to which 1 cm^3 of the $C_{60}[C(COOH)_2]$ solution in THF was added. The vial was then shaken and 2 cm^3 of 0.05 M Na_2PO_4 (pH 6) was added to the vial. The purpose of the buffer solution was to increase the gelation rate for the gel from several days to 2 minutes. This was necessary since the $C_{60}[C(COOH)_2]$ molecules aggregated at the bottom of the reaction vial if the gel was allowed to form in its own time. Therefore the $C_{60}[C(COOH)_2]$ molecules are dispersed throughout the gel. Silica sol gels containing 0.15, 0.20, and 0.81 mg cm^3 of $C_{60}[C(COOH)_2]$ dissolved in THF were prepared, in addition to a silica gel containing no $C_{60}[C(COOH)_2]$ molecules (used as a control). The gels were left in the reaction vials for two weeks before they were analysed. It is important to note that the resulting gels need to be stored in a solution of water to prevent the gels from further shrinkage.

6.5.2 Results and Discussions

The photograph shown in Figure 6.27 shows the four sol gels prepared by the method stated above. The brownish colouration of the three sol-gels (sol-gels b-d) clearly shows that $C_{60}[C(COOH)_2]$ is present within the sol-gels, when compared to the control sol-gel (sol-gel a) which is opalescent. The photograph also shows that it is possible to incorporate varying concentrations of $C_{60}[C(COOH)_2]$. Here we have only shown a $C_{60}[C(COOH)_2]$ concentration in the sol-gels up to 0.81 mg cm^{-3}.

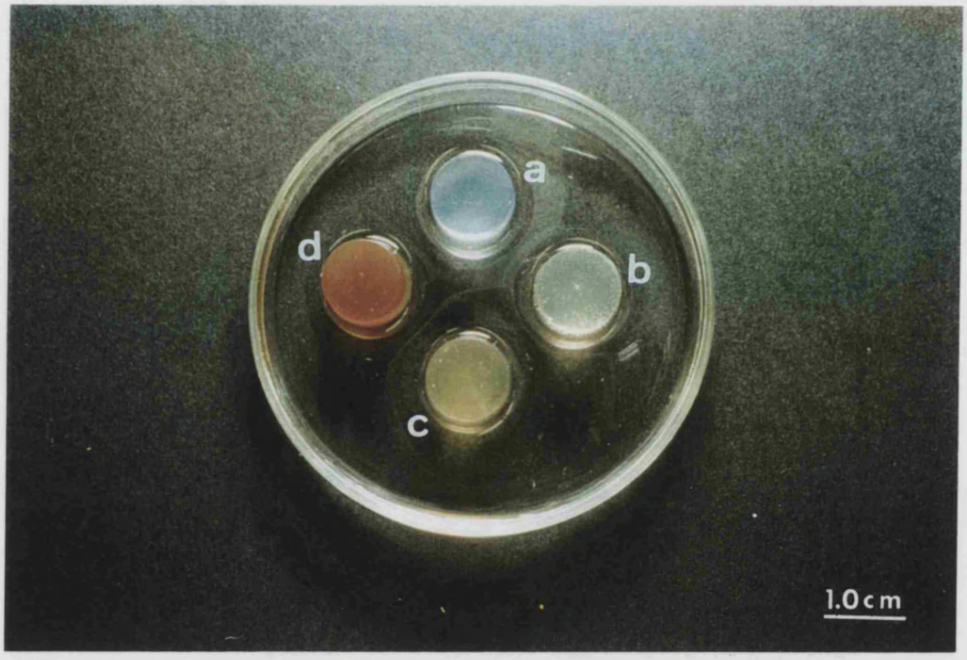

Figure 6.27 *Photograph of the four sol-gels prepared, a) control gel, b) 0.15, c) 0.20, and d) 0.81 mg cm^{-3} of $C_{60}[C(COOH)_2]$.*

Uv-visible spectroscopy of these prepared $C_{60}[C(COOH)_2]$ silica sol-gels failed to show the characteristic absorbance bands of the C_{60} moiety. This may be due to the fact that the $C_{60}[C(COOH)_2]$ sol-gels prepared are too thick to produce a characteristic uv-visible spectra for the C_{60} moiety. In order to solve this problem,

thinner $C_{60}[C(COOH)_2]$ sol-gels were prepared and the characteristic absorbance bands for the C_{60} moiety can be seen (Figure 6.28).

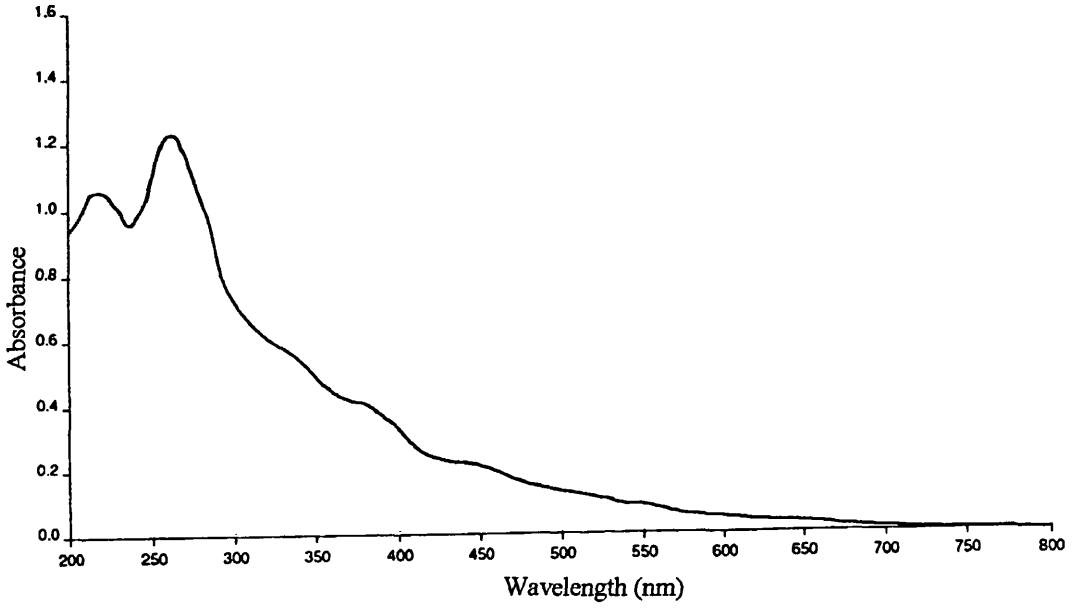

Figure 6.28 *Uv-visible spectra of a 0.81 mg cm^{-3} $C_{60}[C(COOH)_2]$ doped silica sol-gel, showing the characteristic C_{60} bands.*

One possibility to enhance the absorbance of the C_{60} bands is to spin coat the $C_{60}[C(COOH)_2]$ sol-gel mixture to produce very thin films. If we were to spin-coat the sol gel mixture, a slower gelation rate will be needed to allow enough time to spin the $C_{60}[C(COOH)_2]$ sol-gel before it hardens. This can be easily achieved by changing the pH of the buffer added to the sol-gel from 6 to a value of around 5.0-5.5.

6.5.3 Conclusions and Future Work

Here we show for the first time the incorporation of $C_{60}[C(COOH)_2]$ within a silica sol-gel medium. On forming these gels, the rate of gelation needs to be fast since otherwise there is a tendency for the $C_{60}[C(COOH)_2]$ molecules to aggregate at the bottom of the reaction vial. The brownish colour of the sol-gels show that the $C_{60}[C(COOH)_2]$ molecules are present in the gel and are evenly dispersed if compared with the control sol-gel with no $C_{60}[C(COOH)_2]$ incorporated which is transparent. Uv-visible spectroscopy shows the characteristic absorbance bands of the C_{60} moiety present within the gel.

Further characterisation of the $C_{60}[C(COOH)_2]$ sol-gels needs to be undertaken since the results shown here are in an early stage. For example, infra-red spectroscopy of the thin $C_{60}[C(COOH)_2]$ sol gel films will determine the nature of the carboxylate groups on C_{60}. For example, in the spectra we would expect to see characteristic bands for the silica, but also the carboxylate band will tell us if the group is bonded to the silica in any way (-COO-R) therefore being bonded to the silica network, or if it is protonated (-COOH) or not ($-COO^-$). This would be deduced by examining any shifts in this band.

Thermogravimetric analysis on the $C_{60}[C(COOH)_2]$ sol-gels will provide data as to the % weight of $C_{60}[C(COOH)_2]$ incorporated within the silica sol-gel.

6.6 Summary

In this chapter, it is shown that once buckminsterfullerene has been chemically modified, whilst still retaining some, if not all of its original properties, it can open up a number of avenues of research that will, hopefully one day realise the full potential of the C_{60} molecule. Therefore, if these avenues are opened by using this particular fullerene malonic acid molecule, then there are a vast number of avenues awaiting to be explored with other chemically modified fullerenes.

In this chapter, it is shown that the chemically modified fullerene can be spread at the air/water interface, easily and reproducibly to produce stable monolayers and how the limiting area per molecule is increased by the inclusion of cations leading to "salt-like" structures termed fullerates. The use of $C_{60}[C(COOH)_2]$ monolayers for the possible specific orientation of biominerals ($CaCO_3$ in this study) has also been highlighted, even though it was unsuccessful. Finally, we report on the doping of silica gels with $C_{60}[C(COOH)_2]$. This area of research is in an early stage, therefore more research needs to be undertaken to realise $C_{60}[C(COOH)_2]$ potential in this form.

6.7 References

1. Kroto, H.W., Heath, J.R., O'Brien, S.C., Curl, R.F., and Smalley, R.E. (1985). C_{60} - Buckminsterfullerene, *Nature*, **318 (6042)**, 162-163.

2. Krätschmer, W., Lamb, L., Fostiropolous, K., and Huffman, D. (1990). Solid C_{60} - A new form of carbon. *Nature,* **347 (6291)**, 354-358.

3. (1992). Acc Chem Res, **25**, special issue on buckminsterfullerene

4. Hammond, G.S., and Kuck, V.J. eds. (1992). *Fullerenes: Synthesis, properties and chemistry of large carbon clusters*. **In**: American Chemical Society Symposium series 481, Washington DC.

5. Billups, W.E., and Ciufolini, M.A. eds. (1993). *Buckminsterfullerenes*. New York: VCH Press.

6. Kroto, H.W., Fischer, J.E., and Cox, D.E. eds. (1993). *The Fullerenes*. Oxford: Pergamon Press.

7. Prassides, K. ed. (1994). *Physics and chemistry of the fullerenes*. NATO ASI Series C, **443**, Dordecht: Kluwer Academic.

8. Kuzmany, H., Fink, J., Mehring, M., and Roth, S. eds (1994). *Progress in fullerene research*. Singapore: World Scientific.

9. Kadish, K.M., and Ruoff, R.S. eds. (1994). *Recent advances in the chemistry and physics of fullerenes and related materials.* Pennington, NJ: Electrochemical Society Incorporated.

10. Andreoni, W. ed. (1996). *The chemical physics of fullerenes 10 (and 5) years later.* NATO ASI Series E, **316**, Dordecht: Kluwer Academic.

11. Hebard, A.F., Rosseinski, M.J., Haddon, R.C., Murphy, D.W., Glarum, S.H., Palstra, T.T.M., Ramirez, A.P., and Kortan, A.R. (1991). Superconductivity at 18 K in potassium-doped C_{60}, *Nature*, **350 (6319)**, 600-601.

12. Holczer, K., Klein, O., Huang, S.-M., Kaner, R.B., Fu, K.-J., Whetton, R.L., and Diederich, F. (1991). Alkali-fulleride superconductors - Synthesis, composition and diamagnetic shielding, *Science*, **252 (5009)**, 1154-1157.

13. Haddon, R.C. (1992). Electronic-structure, conductivity, and superconductivity of alkali metal doped C_{60}, *Accounts of Chemical Research*, **25 (3)**, 127-135.

14. Rosseinsky, M.J. (1995). Fullerene intercalation chemistry, *Journal of Materials Chemistry*, **5 (10)**, 1497-1513.

15. Xie, Q., Pérez-Cordero, E., and Echegoyen, L. (1992). Electrochemical detection of $C_{60}(6^-)$ and $C_{70}(6^-)$ - Enhanced stability of fullerides in solution, *Journal of the American Chemical Society*, **114 (10)**, 3978-3980.

16. Ohsawa, Y., and Saji, T. (1992). Electrochemical detection of $C_{60}(6^-)$ at low temperature, *Journal of the Chemical Society, Chemical Communications*, **10**, 781-782.

17. Allemand, P.-M., Khemani, K.C., Kock, A., Wudl, F., Holczer, K., Donovan, S., Gruner, G., and Thompson, J.D. (1991). Organic molecular soft ferromagnetism in a fullerene C_{60}, *Science*, **253 (5017)**, 301-303.

18. Tutt, L.W., and Kost, A. (1992). Optical limiting performance of C_{60} and C_{70} solutions, *Nature*, **356 (6366)**, 225-226.

19. Kajzar, F., Taliani, C., Danieli, R., Rossini, S., and Zamboni, R.., (1994). Wave dispersed 3rd-order non-linear optical properties of C_{60} thin films. *Chemical Physics Letters,* **217 (4)**, 418-422.

20. Ruoff, R.S., Tse, D.S., Malhotra, R., and Lorents, D.C. (1993). Solubility of C_{60} in a variety of solvents, *Journal of Physical Chemistry*, **97 (13)**, 3379-3383.

21. Haddon, R.C. (1993). Chemistry of the fullerenes - The manifestation of strain in a class of continuous aromatic molecules, *Science*, **261 (5128)**, 1545-1550.

22. Prato, M. (1997). [60] Fullerene chemistry for materials science application, *Journal of Materials Chemistry*, **7 (7)**, 1097-1109.

23. Taylor, R., and Walton, D.R.M. (1993). The chemistry of fullerenes. *Nature,* **363 (6431)**, 685-693.

24. Hirsch, A. (1993). Dicyano polyynes - Formation of new rod-shaped molecules in a carbon plasma, *Angewandte Chemie, International Edition in English,* **32 (9)**, 1340-1342.

25. Hirsch, A. (1993). The chemistry of fullerenes - An overview. *Angewandte Chemie, International Edition in English,* **32 (8)**, 1138-1141.

26. Friedman, S.H., DeCamp, D.L., Sijbesma, R.P., Srdanov, G., Wudl, F., and Kenyon, G.L. (1993). Inhibition of the HIV-1 protease by fullerene derivatives - Model building studies and experimental verification. *Journal of the American Chemical Society,* **115 (15)**, 6505-6509.

27. Sijbesma, R.P., Srdanov, G., Wudl, F., Castoro, J.A., Wilkins, C., Friedman, S.H., DeCamp, D.L., and Kenyon, G.L. (1993). Synthesis of a fullerene derivative for the inhibition of HIV enzymes. *Journal of the American Chemical Society,* **115 (15)**, 6510-6512.

28. Tokuyama, H., Yamago, S., Nakamura, E., Shiraki, T., and Sugiura, Y. (1993). Photo-induced biochemical activity of fullerene carboxylic acid. *Journal of the American Chemical Society,* **115 (17)**, 7918-7919.

29. Anderson, J.L.., An, Y.Z., Rubin, Y., and Foote, C.S. (1994). Photophysical characterisation and singlet oxygen yield of a dihydrofullerene. *Journal of the American Chemical Society,* **116 (21)**, 9763-9764.

30. Arbogast, J.W., Darmanyan, A P., Foote, C.S., Rubin, Y., Diederich, F., Alvarez, M.M., Anz, S.J., and Whetton, R.L. (1991). Photophysical properties of C_{60}. *Journal of Physical Chemistry,* **95 (1)**, 11-12.

31. Arbogast, J.W., and Foote, C.S. (1991). Photophysical properties of C_{70}. *Journal of the American Chemical Society,* **113 (23)**, 8886-8889.

32. An, Y.Z., Anderson, J.L., and Rubin, Y. (1993). Synthesis of α-amino acid derivatives of C_{60} from 1,9-(4-hydroxycyclohexanol) buckminsterfullerene film. *Journal of Organic Chemistry,* **58 (18)**, 4799-4801.

33. Lamparth, I., and Hirsch, A. (1994). Water-soluble malonic acid derivatives of C_{60} with a defined 3-dimensional structure. *Journal of the Chemical Society., Chemical Communications,* **14,** 1727-1728.

34. Beck, R.D., Weis, P., Hirsch, A., and Lamparth, I. (1994). Laser-desorption mass-spectrometry of fullerene derivatives, *Journal of Physical Chemistry,* **98 (39),** 9683-9687.

35. Hirsch, A., Lamparth, I., and Karfunkel, H.R. (1994). Fullerene chemistry in 3-dimensions - Isolation of 7 regioisomeric *bis*-adducts and chiral *tris*-adducts of C_{60} and di(ethoxycarbonyl)methylene. *Angewandte Chemie, International Edition in English,* **33 (4),** 437-438.

36. Hirsch, A., Lamparth, I., Grösser, T., and Karfunkel, H.R. (1994). Regiochemistry of multiple additions to the fullerene core - Synthesis of a T-H-symmetrical hexakisadduct of C_{60} with bis(ethoxycarbonyl)methylene. *Journal of the American Chemical Society,* **116 (20),** 9385-9386.

37. Bingel, C. (1993). Cyclopropylation of fullerenes. *Chemische Berichte,* **126 (8),** 1957-1959.

38. Ren, S.L., Wang, Y., Rao, A., McRae, E., Holden, J., Hager, T., Wang, K., Lee, W., Ni, H., Selegue, J., and Eklund, P. (1991). Ellipsometric determination of the optical constants of C_{60} (Buckminsterfullerene) films. *Applied Physics Letters,* **59 (21),** 2678-2680.

39. Tong, W., Ohlberg, D., You, H., Williams, R., Anz, S., Alvarez, M., Whetton, R., Rubin, Y., and Diedrich, F. (1991). X-ray diffraction and electron spectroscopy of epitaxial molecular C_{60} films. *Journal of Physical Chemistry,* **95 (12),** 4709-4712.

40. Sakurai, M., Tada, H., Saiki, K., and Koma, A. (1991). Van der waals epitaxial growth of C_{60} film on a cleaved face of MoS_2. *Japanese Journal of Applied Physics,* **30 (N11A),** L1892-L1894.

41. Achiba, Y., Nakagawa, T., Matusi, Y., Suzuki, S., Shiromaru, H., Yamauchi, K., Nishiyama, K., Kainosho, M., Hoshi, LI., and Mitani, T. (1991). Visible, UV, VUV absorption-spectra of C_{60} thin films grown by the Molecular Beam Epitaxy (MBE) technique. *Chemistry Letters,* **7,** 1233-1236.

42 Ichihashi, T., Tanigaki, K., Ebbensen, T., Kuroshima, S., and Iijima, S. (1992). Structures of C_{60} thin films fabricated on alkali substrates by organic MBE. *Chemical Physics Letters,* **190 (3-4),** 179-183.

43. Obeng, Y.S., and Bard, A. (1991). Langmuir films of C_{60} at the air/water interface. *Journal of the American Chemical Society,* **113 (16),** 6279-6280.

44. Nakamura, T., Tachibana, H., Yumura, M., Matsumoto, M., Azumi, R., Tanaka, M., and Kawabata, *Y.* (1992). Formation of Langmuir-Blodgett films of a fullerene. *Langmuir,* **8 (1),** 4-6.

45. Long, C., Xu, Y., Guo, F., Li, Y., Xu, D., Xao, Y., and Zhu, D. (1992). Lattice imaging of C_{60} Langmuir-Blodgett films. *Solid State Communications*, **82 (5),** 381-383.

46. Williams, G., Penisson, C., Bryce, M., and Petty, M. (1992). Langmuir-Blodgett films of C_{60}. *Thin Solid Films,* **209 (2),** 150-152.

47. Maliszewskyj, H., Heiney, P., Jones, D., Strongin, R., Cichy, M., and Smith, A.(1993). Langmuir Films of C_{60}, $C_{60}O$, and $C_{61}H_2$. *Langmuir,* **9 (6),** 1439-1441.

48. Gebhard, H., and Neuhaus, A. (1972). *Epitaxie-Daten anorganischer und organischer Kristalle*. Berlin: Springer.

49. van der Merwe, J.H. (1949). *Discussions of the Faraday Society*, **5**, 201.

50. Neuman, W.F., and Neuman, M.W. (1958). *The chemical dynamics of bone mineralisation.* Illinos: University of Chicago Press.

51. Bachra, B.N. (1973). *Biological mineralisation* (Zipkin, I. ed.), pp 845-881. New York: Wiley.

52. Towe, K.M. (1982). Anomalous C_{13} depletion in precambrian organic-carbon, *Nature*, **295 (5845)**, 171-172.

53. Weiner, S., and Traub, W. (1980). *FEBS Letters*, **111**, 311.

54. Lowenstam, H.A., and Weiner, S. (1989). *On biomineralisation.* Oxford: Oxford University Press.

55. Addadi, L., and Weiner, S. (1985). Interactions between acidic proteins and crystals - stereochemical requirements in biomineralisation, *Proceedings of the National Academy of Science, USA*, **82 (12)**, 4110-4114.

56. Addadi, L., and Weiner, S. (1986). Interactions between acidic macromolecules and structured crystal surfaces - stereochemistry and biomineralisation, *Molecular Crystals and Liquid Crystals*, **134 (1-4)**, 305-322.

57. Fisher, L.W., and Termine, J.D. (1985) Non-collagenous proteins influencing the local mechanisms of calcification, *Clinical Orthopaedics*, **200**, 362.

58. Landau, E.M., Levanon, M., Leiserowitz, L., Lahav, M., and Sagiv, J. (1985). Transfer of structural information from Langmuir monolayers to 3-dimensional growing crystals, *Nature*, **318 (6044)**, 353-356.

59. Landau, E.M., Popovitz-Biior, R., Leiserowitz, L., Lahav, M., and Sagiv, J. (1986). Langmuir monolayers designed for the orientated growth of glycine and sodium chloride crystals at air/water interfaces, *Molecular Crystals and Liquid Crystals*, **134 (1-4)**, 323-325.

60. Landau, E.M., Grayer Wolf, S., Leiserowitz, L., Lahav, M., and Sagiv, J. (1989). Stereochemical studies in crystal nucleation - orientated crystal - growth of glycine at interfaces covered with Langmuir and Langmuir-Blodgett films of resolved α-amino acids, *Journal of the American Chemical Society*, **111 (4)**, 1436-1445.

61. Mann, S., Heywood, B.R., Rajam, S., and Birchall, J.D. (1988). Controlled crystallisation of $CaCO_3$ under stearic acid monolayers, *Nature*, **334 (6184)**, 692-695.

62. Mann, S., Heywood, B.R., Rajam, S., Walker, J.B.A., Davey, R.J., and Birchall, J.D. (1989). Interfacial control of nucleation of $CaCO_3$ under organised stearic acid monolayers, *Proceedings of the Royal Society of London Series A - Mathematical and Physical Sciences*, **423 (1865)**, 457.

63. Williams, R.J.P. (1984). An introduction to biominerals and the role of organic molecules in their formation, *Philosophical Transactions of the Royal Society of London Series B - Biological sciences*, **304 (1121)**, 411-424.

64. Sims, S.D. (1994). Biomimetic approaches to the control of crystal morphology; a study on calcite, aragonite and gypsum, M. Phil. Report, University of Bath.

65. Hexagonal system ($a=b\neq c$, $\alpha=\beta=90°$, $\gamma=120°$). Calcite unit cell parameters: a(nm)=0.499, c=1.706.

66. Orthorhombic system ($a\neq b\neq c$, $\alpha=\beta=\gamma=90°$). Aragonite unit cell parameters: a(nm)=0.496, b=0.797, c=0.5746.

67. Kitano, Y. (1962). The Behaviour of various ions in the separation of calcium carbonate from bicarbonate solution. *Bulletin of the Chemical Society of Japan*, **35**, 1973-1980.

68. Vogel, A.I. (1978). **In**: *Textbook of quantitative inorganic analysis*, 4th edition, London: Longmans.

69. Rajam, S., Heywood, B.R., Walker, J.B.A., Mann, S., Davey, R.J., and Birchall, J.D. (1991). Orientated crystallisation of $CaCO_3$ under compressed monolayers. Part 1: Morphological studies of mature crystals, *Journal of the Chemical Society, Faraday Transaction*, **87 (5)**, 727-734.

70. Joint Committee on Powder Diffraction Standards. (1976). Card number 5-0586.

71. Joint Committee on Powder Diffraction Standards. (1974). Card number 24-309.

72. Wang, Y. (1992). Photoconductivity of fullerene doped polymers. *Nature,* **356 (6370)**, 585-587.

73. Kajzar, F., Taliani, C., Danieli, R., Rossini, S., and Zamboni, R.., (1994). Wave dispersed 3rd-order non-linear optical properties of C_{60} thin films. *Chemical Physics Letters,* **217 (4)**, 418-422.

74. Tutt, L.W., and Kost, A. (1992). Optical limiting performance of C_{60} and C_{70} solutions. *Nature,* **356 (6366)**, 225-226.

75. Hench, L., and West, J., (1990). The Sol-gel process. *Chemical Reviews,* **90 (10)**, 33-72.

76. Brinker, C., and Scherer, G. (1990). **In**: *Sol gel science.* Academic Press, San Diego.

77. Hummel, D., and Torriani, I. (1994). **In**: *Better ceramics through chemistry V.* San Francisco, MRS, Pittsburgh.

78. Levy, D., and Avnir, D. (1988). Effects of the changes in the properties of the silica cage along the gel/xerogel transition on the photochromic behaviour of trapped spiropyrans. *Journal of Physical Chemistry,* **92 (16)**, 4734-4738.

79. Sheng, D., Compton, R.N., Young, J.P., and Mamantov, G. (1992). Preparation of C_{70} doped solid-gel *via* sol-gel processes, *Journal of the American Ceramic Society,* **75 (10)**, 2865-2866.

80. Zerda, T., Brodka, A., and Coffer, J. (1994). Diffusion of C_{60} in porous sol-gel glass. *Journal of Non-Crystalline Solids,* **168 (1-2)**, 33-41.

81. Maggini, M., Scorrano, G., Prato, M., Brusatin, G., Innocenzi, P., Guglielmi, M., Renier, A., Signorini, R., Meneghetti, M., and Bozio, R. (1995). C_{60} derivatives embedded in sol-gel silica films. *Advanced Materials,* **7 (4)**, 404-406.

APPENDIX ONE

Operational Procedures in Transmission Electron Microscopy

The main components of the transmission electron microscope (Figure A1.1) are the illumination source (electron gun), vacuum system, lens systems (condenser, objective and projector), screen and camera. The basic principle of operation is that the electron gun produces a beam of electrons projected onto a specimen by the condenser lens system. The condenser aperture controls the number of electrons in the beam and hence the intensity of illumination. The vacuum system prevents scattering of the beam by gas molecules, and in conjunction with the anti-contamination device filled with liquid nitrogen, prevents contamination of the specimen, lenses and apertures by dust and gases which will lead to loss of resolution. The first focused image is produced by the objective lens system and is magnified to final size by the projector lenses. Image contrast is produced using the objective lens aperture which separates scattered and unscattered electrons. The final image is viewed on a fluorescent screen and can be recorded using the camera system in the base of the microscope.

Routine operation of the TEM requires a number of procedures to be carried out prior to use.[1] Firstly, the cold trap or anti-contamination device (ACD) had to be filled with liquid nitrogen. The next requirement was the alignment of all the various lenses and apertures in the column so as to be optically centred relative to each other. This was necessary in order to minimise the effects of circuit instability which cause aberrations due to electrons that are not coincident with the optical axes of the lenses. Lastly, it is important that residual astigmatism is eliminated from the lenses.

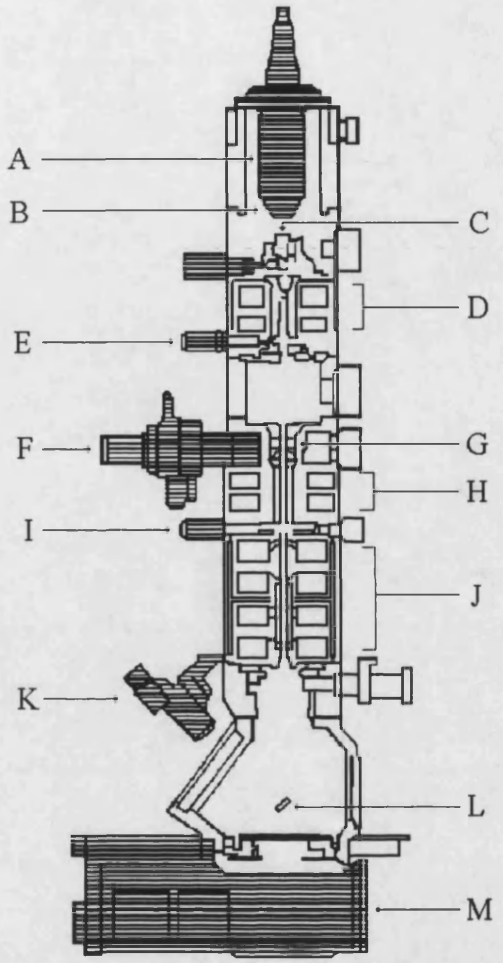

A	Electron Gun	**E**	Condenser Aperture	**I**	Selected Area Aperture
B	Wehnelt Cap	**F**	Goniometer	**J**	Projector Lenses
C	Anode	**G**	Objective Aperture	**K**	Viewing Port
D	Condenser Lenses	**H**	Objective Lenses	**L**	Fluorescent Screen
M	Photographic Chamber				

Figure A1.1 *Schematic diagram of a transmission electron microscope.*

Alignment and the correction for lens asymmetry were carried out in the following way:

(a) Adjusting the heating current in the filament (electron source) such that the electron gun was operating at its optimum level (saturation point). This enables the illumination to be sufficiently bright to view objects at the highest magnification, whilst not overworking the filament, and so reducing its life. When undersaturated, the filament can be aligned with respect to the gun axis using the gun tilt control.

(b) Positioning the electron source on the condenser lens axis to ensure an even illumination of the specimen, as the intensity of the beam is varied, *via* focusing and defocusing of the condenser lens.

(c) Checking the astigmatic condition of the condenser lens to produce a symmetrical beam as it is focused or defocused.

(d) Centring the condenser aperture to prevent illumination.

(e) Alignment of the projector lenses and objective aperture by positioning the caustic spot and the shadow of the aperture at the centre of the fluorescent screen

(f) Establishing specimen eucentricity such that the focal plane of the objective lens is coincident with the tilting axis of the specimen stage. This is done after the insertion of the sample or carbon-formvar grid.

(g) Determining the current and voltage centre. Minute electrical disturbances in the lens current and the accelerating voltage cause image movement which is relatively insignificant near the optical axis, but a problem causing loss of resolution at larger distances from the axis. Voltage centration is performed by finding a point in a focused image which remains stationary when the voltage is varied (wobbled), whilst keeping the current fixed. Current centration involves varying the current whilst keeping the voltage constant.

(h) Lastly, checking the astigmatic condition of the objective lens. This was ascertained by viewing the carbon grains deposited on the formvar support at a magnification of 400-500 K and corrected using the astigmators, where appropriate.

The accuracy of alignment could be assessed by the value of the objective lens current (200 KeV : 7.08 mA ; 120 KeV : 5.22 mA).

References

1. Wischitzer, S. (1981). **In**: *Introduction to electron microscopy*, 3rd edition, pp 81-95. New York: Pergamon Press.

APPENDIX TWO

X-Ray Reflection Theory[1-3]

The following appendix describes the analysis of reflection profiles by the optical matrix method.

Two Layers - One Interface

Consider a perfectly smooth, infinitely sharp solid surface:

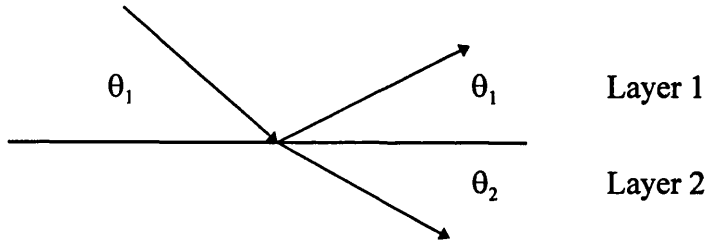

At a particular angle, θ_1, the amount of incident X-ray radiation that is transmitted and reflected depends only on the refractive index difference between the two layers. The angle of refraction, θ_2, is determined by **Snells Law**:

$$n_1 \cos\theta_1 = n_2 \cos\theta_2$$

where n_1 and n_2 are the refractive index values of layers 1 and 2 respectively, and θ_1 and θ_2 are the incident and transmitted angles, as shown. θ_c is the critical angle, below which all the X-ray radiation is reflected. This is known as Total External Reflection. When $\theta_2 = 0$, then $\cos\theta_c = n_2$, if $n_1 = 1$, *i.e.* the refractive index of air.

The refractive index of a material for X-rays is given by the formula

$$n = 1 - \left(\frac{\lambda^2}{2\pi}\right) NZr_e$$

Thus (equation A):

$$\cos\theta_c = 1 - \left(\frac{\lambda}{2\pi}\right) NZr_e$$

where λ is the wavelength of the incident X-ray radiation, N is the number of atoms per $Å^3$, Z is the atomic number and r_e is the classical radius of an electron, typically 2.82×10^{-5} Å. NZ represents the number of electrons per unit volume and r_e the scattering power of one electron, so the higher the electron density of a material, the greater its ability to scatter X-rays.

The number density, N, is usually found by (units $Å^{-3}$):

$$N = \left(\frac{\rho}{M}\right) N_a \times 10^{-24}$$

where ρ is the density (g cm^{-3}), M is the molar mass (g mol^{-1}) and N_a is the Avagadro constant. If the refractive index for a liquid or solid is only slightly less than 1, then the critical angle will be very small. Thus the following series expansion can be used[4]

$$\cos\theta_c = 1 - \left(\frac{\theta c^2}{2}\right) + \left(\frac{\theta c^4}{4}\right) + \left(\frac{\theta c^6}{6}\right) + \ldots\ldots\ldots$$

and since θ_c is small (equation B):

$$\cos\theta_c = 1 - \left(\frac{\theta_c^2}{2}\right)$$

Comparing Equations A and B leads to:

$$\frac{\theta_c}{\lambda} = \left(\frac{NZr_e}{\pi}\right)^{1/2}$$

Hence the angle below which no refraction occurs and all the incident beam is reflected, can be calculated. Above the critical angle, the amount of scattering falls off according to **Fresnels Law** for a perfectly smooth, infinitely sharp interface:

$$\text{Reflectivity } R = r_{12}\, r_{12}^*$$

where r_{12} is the Fresnel coefficient and is defined as:

$$r_{12} = \frac{(n_1 \sin\theta_1) - (n_2 \sin\theta_2)}{(n_1 \sin\theta_1) + (n_2 \sin\theta_2)}$$

and r_{12}^* is the complex conjugate of r_{12}. If r_{12} is real, in that it contains no I value, then the reflectivity at a given angle is:

$$R = r_{12}^2$$

Experimentally, a graph of the $\log_{10}$ of the intensity of reflected X-rays (I_R) relative to the intensity of the incident X-rays (I_I) is plotted against the momentum transfer **Q**. This is known as a reflectivity profile.

$$R = \frac{I_R}{I_I}$$

The momentum transfer, **Q**, is the difference between the reflected and incident wavevectors ($\mathbf{Q} = k_I - k_R$) and since for specular reflection the angle of the incident X-Ray beam is the same as that of the reflected beam, the direction of **Q** is normal to the interface and is given by:

$$Q = \frac{4\pi \sin\theta}{\lambda}$$

Hence the plot of $\log_{10}$ versus **Q** (Figure A2.1) is related to the change in refractive indices normal to the interface and thus yields information on the composition and change in electron densities at the surface.

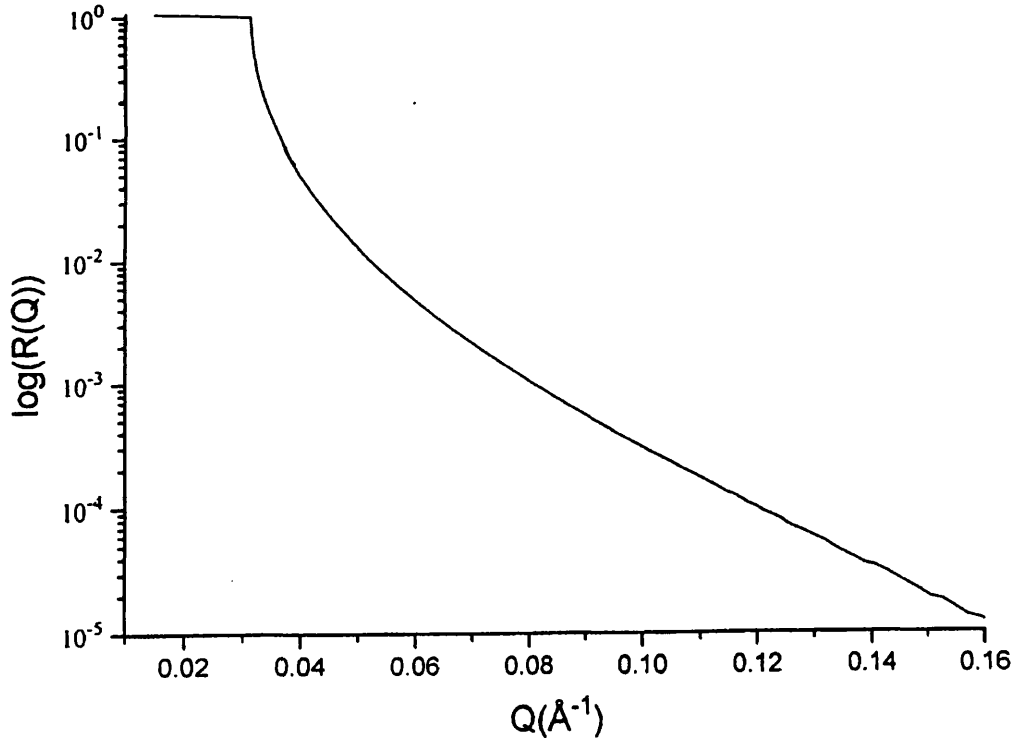

Figure A2.1 *Theoretical reflectivity profile for a smooth flat air/silicon interface.*

Three Layers - Two Interfaces

Let us now consider a surface consisting of three layers:

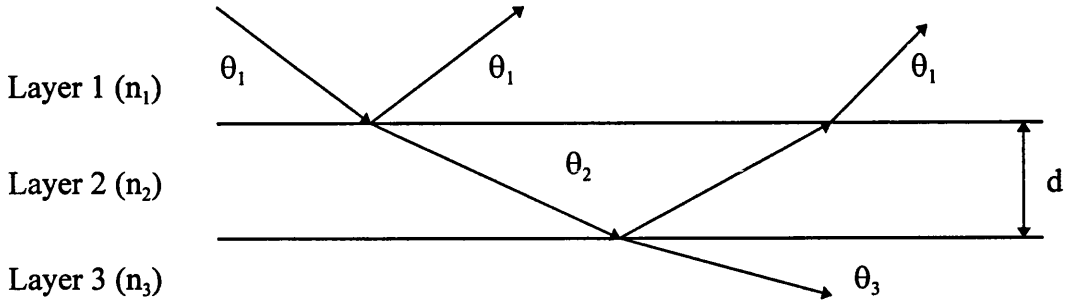

Reflection of the X-ray radiation will occur from the interface between layers 1 and 2, and from the interface between layers 2 and 3. An example of such a system would be a thin film on a solid substrate in air, with layer 1 representing air, layer 2 representing the thin film and layer 3 representing the solid substrate. Therefore what we have is essentially a single layer on a substrate in air, with two interfaces.

The total reflectivity of a particular wavelength at a given angle, is given by the Fresnel reflectivity formula:

$$R_f = \left(\frac{(r_{12} + r_{23} \exp(-2i\beta))}{(1 + r_{12} r_{23} \exp(-2i\beta))} \right)^2$$

where

$$r_{12} = \frac{(n_1 \sin\theta_1) - (n_2 \sin\theta_2)}{(n_1 \sin\theta_1) + (n_2 \sin\theta_2)}$$

$$r_{23} = \frac{(n_2 \sin\theta_2) - (n_3 \sin\theta_3)}{(n_2 \sin\theta_2) + (n_3 \sin\theta_3)}$$

and

$$\beta = 2\pi \, n_1 \, d \sin\theta_1$$

where d is the thickness of layer 2 (n_2).

In the X-ray reflection experiments, the angle of incidence is kept constant and the wavelength varied, therefore **Q** is proportional to $1/\lambda$. In order to achieve a wide **Q** range, the reflectivity of a surface is recorded at three different angles. X-ray reflection from a thin film will lead to interference between the reflected X-rays and therefore Bragg peaks in the reflectivity profile. The distance between the peaks corresponds to the thickness of the film. Reflected X-rays from thicker films will interfere constructively and destructively more often in **Q** than those from thinner films and therefore produce more interference fringes. Since

$$Q = \frac{4\pi \sin\theta}{\lambda}$$

and **Braggs Law** is:

$$\lambda = 2\, d \sin\theta$$

then

$$d = \frac{2\pi}{\Delta Q}$$

so the thickness of the film can be approximated from the reflectivity profile shown in Figure A2.2.

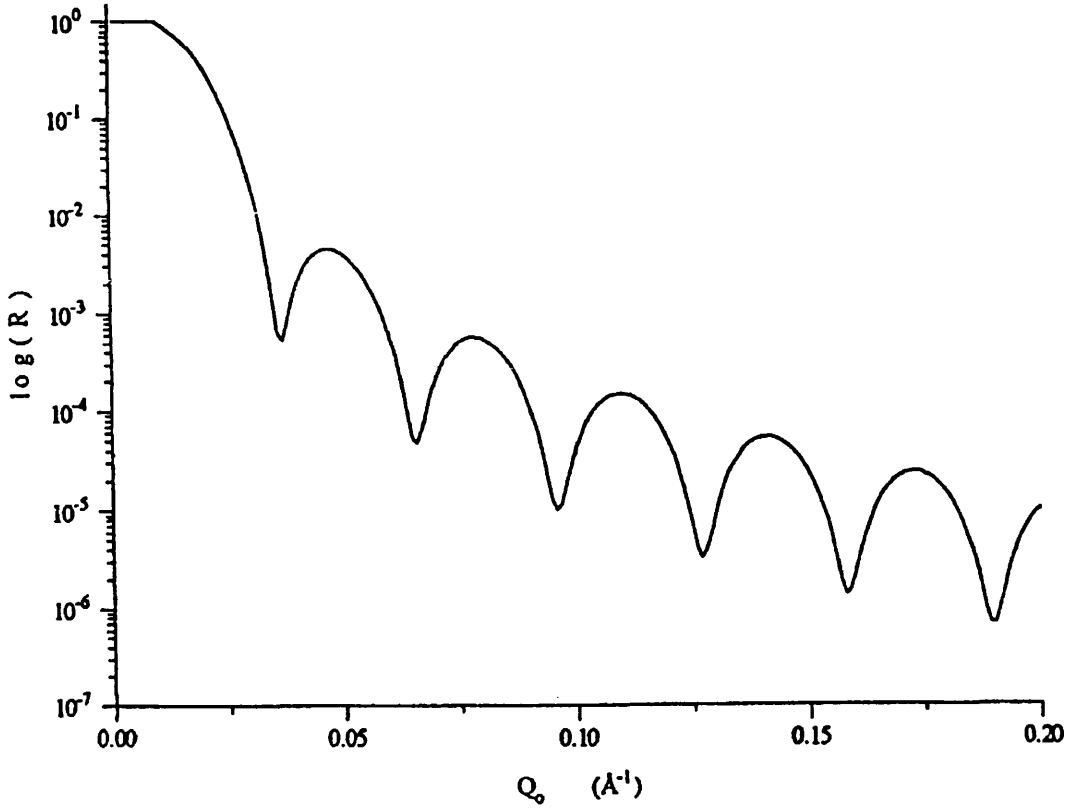

Figure A2.2 *Theoretical reflectivity profile for a thin film at the air/silicon interface (film thickness 200 Å).*

Application of Porods Law[4] ($R \propto Q^{-4}$ at high **Q** values), enables a graph of $R \times Q^4$ versus **Q** (known as the film factor) to be plotted. This removes the reflectivity decay curve, since the reflectivity varies linearly with Q^{-4}, leaving the interference fringes.

Rough Interfaces

In reality, interfaces are rarely perfectly smooth and all exhibit a density gradient in going from one to another. Long range undulations have the same effect as beam divergence and so can be considered as locally flat. If the surface is not

entirely smooth on the small scale, however, the local roughness will modify the specular reflectivity in a manner similar to that of a diffuse interface. This means the reflectivity will decrease more rapidly with **Q** that is expected. The Fresnel reflectivity equation can therefore be modified.[5]

$$R(Q) = R_F e^{-Q_i Q_j \langle\sigma\rangle^2}$$

Where $\langle\sigma\rangle$ and $\mathbf{Q}_j = 4\pi\sin(\theta_j)/\lambda$ is the root mean square Gaussian roughness. The value of σ is the width of the Gaussian and hence a comparative idea of roughness. Effectively, the roughness from a rough interface falls away more rapidly with increasing $\mathbf{Q}_o$ than in the case of the ideally smooth, sharp surface and thus Porod's law no longer applies.[4]

This treatment can be extended to thin films present at the interface,[6] thus modifying the Fresnel coefficients such that (equation c):

$$r_j = \frac{P_{j-1} - P_j}{P_{j-1} + P_j} e^{\frac{-Q_{j-1}Q_j\langle\sigma\rangle^2}{2}}$$

However, roughness cannot be applied to more that three layers using the matrix method, as the roughness factor cannot be substituted into the equations. A way of overcoming this is to use the Abélès method.[7] In this approach a characteristic matrix, C_j (where j = jth layer), per layer can be derived from the relationship between the electric vectors in successive layers, expressed in terms of Fresnel coefficients, such that

$$C_j = \begin{pmatrix} \frac{e^{i\beta_{j-1}}}{r_j e^{-i\beta_{j-1}}} & \frac{r_j e^{i\beta_{j-1}}}{e^{-i\beta_{j-1}}} \end{pmatrix}$$

The product matrix, C, for m multilayers is thus obtained by

$$C = \prod_{j=1}^{m+1} C_j$$

and the reflectivity is then given by

$$R = \frac{C_{21}\overline{C_{21}}}{C_{11}\overline{C_{11}}}$$

hence a roughened interface can be easily introduced at each boundary by using equation c.

References

1. Born, M., and Wolf, E. (1970). **In**: *Principles of optics: Electromagnetic theory of propagation, interference, and diffraction of light*. Pergamon Press, Oxford, U.K.

2. Richardson, R.M., and Roser, S.J. (1991). Neutron reflection studies of spread monolayers of docosanoic acid and pentadecanoic acid on water, *Langmuir*, **7 (7)**, 1458-1467.

3. Penfold, J., and Thomas, R.K. (1990). The application of the specular reflection of neutrons to the study of surfaces and interfaces, *Journal of Physics-Condensed Matter*, **2 (6)**, 1369-1412.

4. Lovell, M. (1996). An in-situ study of the Langmuir-Blodgett deposition of a model fatty acid, PhD thesis, University of Bath.

5. Névot, L., and Gasginer, P. (1981). Analysis and crystallographic structures of chromium thin films, *Physica Status Solidi A-Applied Research*, **66(2)**, 525-540.

6. Cowley, R.A., and Ryan, T.W. (1987). X-ray scattering studies of thin films and surfaces - Thermal oxides of silicon, *Journal of Physics, D-Applied Physics*, **20 (1)**, 61-68.

7. Abélès, F. (1948). Sur la propagation des ondes electromagnétiques dans les milieux stratifiés, *Ann. Phys.*, **34**, 505-520.

APPENDIX THREE

Cubic Splines[1]

When we are presented with the values u_o, u_1, ..., u_n at the points $x = 0, 1, \ldots, n$ and we wish to connect them together, the easiest method of all is to connect the points by straight lines, termed linear interpolation. A disadvantage with this method is that the slopes between each point change and become unreliable. A far better choice is to use *cubic splines*.[2]

A cubic spline is a polynomial cubic in which the function u and the slope

$$slope = \frac{du}{dx}$$

but also **the second derivative (d) is continuous**.

$$d = \frac{d^2u}{dx^2}$$

Physically it comes from bending a long thin beam to give it the correct heights u_o, ..., u_n at the interpolation points. At all other points the force is zero, the beam is free to choose its own shape, and the solution to the beam equation $d^4u/dx^4 = 0$ is an ordinary cubic.

References

1. Strang, G. (1986). **In**: *Introduction to applied mathematics*, Massachusetts: Wellesley-Cambridge Press.

2. The name and the idea come from naval architects.

APPENDIX FOUR

Langmuir Adsorption Isotherm[1]

The Langmuir adsorption isotherm is based on the assumption that every site is equivalent, and the ability of a particle to bind there is independent of whether or not nearby sites are occupied. The Langmuir adsorption isotherm is given by:

$$\theta = \frac{bp}{1+bp}$$

where θ is the fractional coverage and is expressed as the number of adsorption sites occupied / the number of adsorption sites available.

The constant b is expressed as:

$$b = \frac{k_a}{k_d}$$

where k_a and k_d are the rates of adsorption and desorption, respectively.

References

1. Atkins, P.W. (1986). **In**: *Physical chemistry*, 3rd Edition, Oxford: Oxford University Press.

Fullerates: interaction of divalent metal ions with Langmuir monolayers and multilayers of mono-substituted C_{60}–malonic acid

Harish M. Patel,[a] Jon M. Didymus,[a] Kim K. W. Wong,[a] Andreas Hirsch,[b] Andreas Skiebe,[b] Iris Lamparth[b] and Stephen Mann*[a]

[a] *School of Chemistry, University of Bath, Bath, UK BA2 7AY*
[b] *Institut für Organische Chemie, Universität Erlangen, Henkestrasse 42, 91054, Erlangen, Germany*

Stable Langmuir monolayers of $C_{60}[C(CO_2H)_2]$ are formed on pure water and on solutions containing Ca^{2+} or Cd^{2+} ions; cation–headgroup interactions result in expanded monolayers and the transfer of Ca^{2+}–fullerene multilayers onto quartz substrates.

There is continuing interest in the chemistry of chemically modified C_{60}. Previous studies have shown that floating monolayers of unmodified C_{60} molecules can be produced at the air/water interface[1] but that the highly hydrophobic nature of the molecules often results in multilayer films.[2,3] Several chemically modified C_{60} derivatives have been described recently and some of these materials, such as an *N*-acetylfulleropyrrolidine derivative,[4] an aliphatic carboxylic acid adduct[5] and a fullerene cryptate,[6] have sufficient amphiphilic character to give stable monolayer films at the air/water interface.

In this paper we describe the surface active and metal-ion binding properties of a recently synthesized malonic acid derivative of C_{60}, $C_{60}[C(CO_2H)_2]$ **1**.[7] Compound **1** is a stereochemically specific monoadduct in which the dicarboxylic acid group is directly coupled to the C_{60} cage at a single equatorial site. The bifunctionality of the polar side group and the associated C_{2v} symmetry of the molecule suggest that **1** might be sufficiently amphiphilic to undergo self assembly when spread at the air/water interface. Furthermore, the malonic acid substituent offers potential for metal-ion binding and the formation of salt-like 'fullerates'. Together, these properties suggest that cations could be incorporated into organized multilayer assemblies of fullerenes derivatized with appropriate pendent groups.

The fullerene malonic acid **1** was prepared as described in the literature,[7] and dissolved in tetrahydrofuran to a concentration of 9.73×10^{-5} mol dm^{-3}. Langmuir monolayers of **1** were formed on pure water or aqueous solutions of $CaCl_2$ or $CdCl_2$, buffered to pH 8 by sodium hydroxide solution (2.0 mol dm^{-3}).† Fig. 1 shows isotherms for $C_{60}[C(CO_2H)_2]$ spread on pure water at 290 K. The method of spreading of the thf solution of **1** was critical to the formation of high quality monolayers. In initial experiments, two or three 50 μl drops of the solution were added in quick succession to the air/water interface. Under these conditions, isotherms were recorded but the limiting area per molecule varied between 5 and 25 Å^2 [Fig. 1(*a*)]. These values are clearly too small compared with the predicted value of *ca.* 86 Å^2 for hexagonally close-packed fullerene molecules with intermolecular distances of *ca.* 10 Å. Similar low limiting areas have been reported for underivatized C_{60}[2,3] and derivatized fullerenes,[6] and indicate multilayer formation. However, if a single drop of the thf solution was allowed to evaporate for at least 5 min prior to addition of the next drop, then stable monolayers of **1** could be routinely achieved [Fig. 1(*b*)]. The isotherms showed an initial increase in surface pressure at 200 Å^2, a well established liquid phase, and a distinct phase transition to the fully compressed solid domain. The limiting area per molecule was extrapolated to be 100 ± 4 Å^2. Assuming a close-packed hexagonal lattice, this value corresponds to an inter-headgroup spacing of 10.75 Å. Further compression resulted in a collapse pressure of 40 mN m^{-1} followed by multilayer formation [Fig. 1(*b*)].

The UV–VIS spectrum of a multilayer film of **1** consisting of five monolayer transfers to a hydrophobic quartz wafer showed the characteristic bands at 220, 272, 330, 370 and 450 nm for the C_{60} moiety. TEM micrographs of either monolayers or multilayers showed inhomogeneous films possibly due to breakage during transfer to the electron microscope grids (Fig. 2).

Surface pressure–area isotherms for $C_{60}[C(CO_2H)_2]$ spread on aqueous subphases containing divalent cations showed well formed expanded monolayers (Fig. 3). At concentrations of 1 mmol dm^{-3} Ca^{2+} or Cd^{2+}, the onset of the liquid phase occurred at significantly higher areas (*ca.* 300 Å^2) than on pure water, suggesting that association of the metal cations with the carboxylate headgroups of **1** is established even in the apparently uncompressed state. Compression resulted in well defined liquid phases but only monolayers spread on Ca^{2+} solutions showed a distinct transition to the solid phase [Fig. 3(*a*)]. Areas per molecule of 160 and 230 Å^2 were determined for Ca^{2+} and Cd^{2+} subphases, respectively. In both cases, further compression resulted in a distinct phase change at a surface pressure of 35 mN m^{-1}, followed by an increase in pressure with a limiting area per molecule of 100 Å^2, similar to that for pure water.

These results suggest that the divalent cations intercalate between the monolayer headgroups of $C_{60}[C(CO_2H)_2]$ to give expanded films that can be compressed to solid phases, but which on further compression revert to close-packed mono-

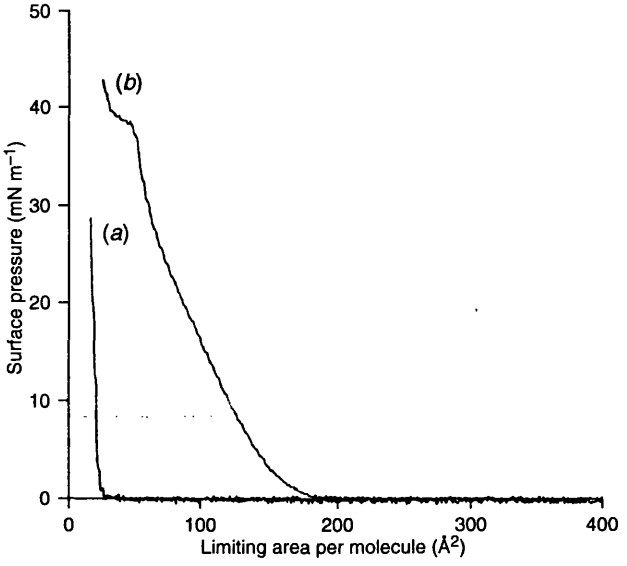

Fig. 1 Surface pressure–area isotherms for $C_{60}[C(CO_2H)_2]$ spread on pure water at 290 K, (*a*) from THF solution applied as a series of drops in quick succession, and (*b*) from THF as a series of single droplets but with solvent evaporation prior to addition of the next drop

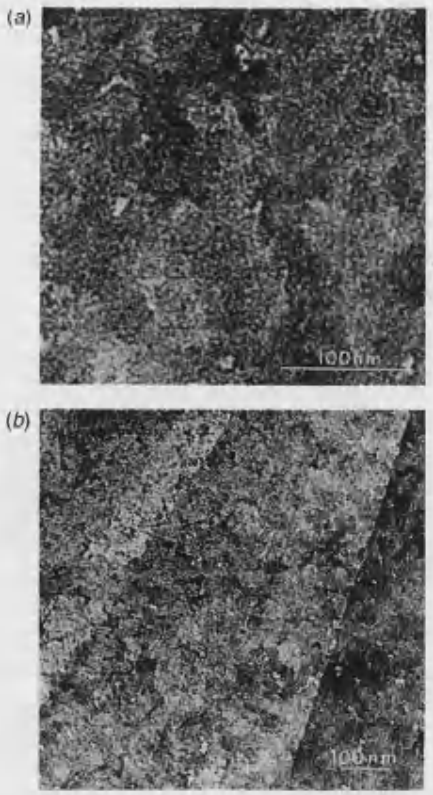

Fig. 2 TEM micrographs of (*a*) monolayer and (*b*) multilayer films of $C_{60}[C(CO_2H)_2]$. Scale bars = 100 nm.

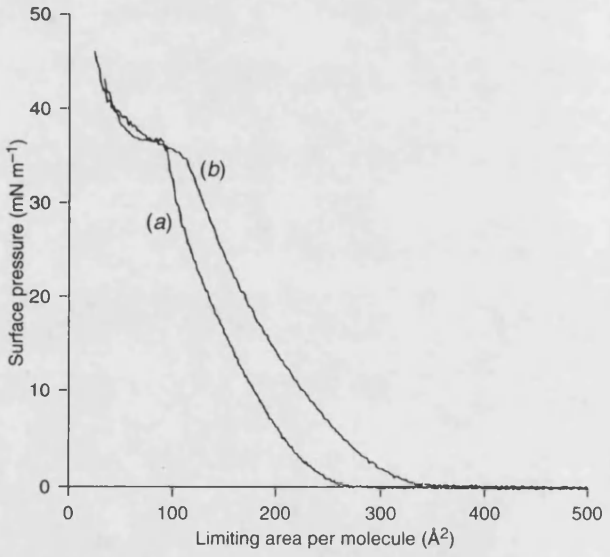

Fig. 3 Surface pressure–area isotherms at 290 K for $C_{60}[C(CO_2H)_2]$ spread on (*a*) 1 mmol dm^{-3} $CaCl_2$ subphase (pH 5.3) and (*b*) 1 mmol dm^{-3} $CdCl_2$ subphase (pH 6.3)

layers depleted of the metal ions. In this regard, EDXA showed the presence of Ca in an expanded monolayer transferred onto a formvar substrate (data not shown), but no Cd was detected in the corresponding monolayer formed on a $CdCl_2$ solution. The data suggest that there is a stronger interaction between Ca^{2+} and the ionised carboxylate headgroups of the C_{60} malonic acid derivative than for Cd^{2+}, which is presumably lost from the expanded monolayer on transfer. The limiting area per molecule of 160 $Å^2$ for the Ca^{2+}-bound monolayer corresponds to an inter-headgroup spacing of 13.5 Å, assuming a hexagonal lattice. This increase of 2.75 Å compared with the monolayer of

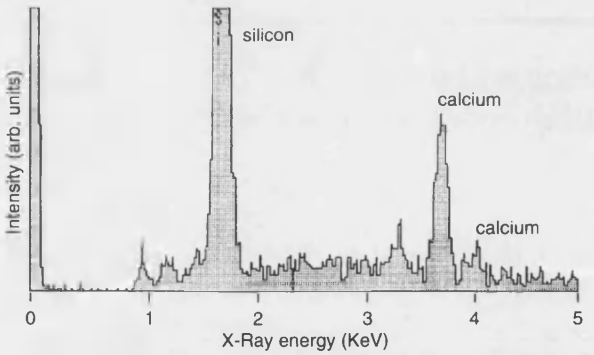

Fig. 4 EDXA spectrum of a multilayer thin film of $C_{60}[C(CO_2H)_2]$ transfered from a 1 mmol dm^{-3} $CaCl_2$ subphase onto an Si wafer, showing the presence of intercalated calcium

1 on pure water is commensurate with the intercalation of Ca^{2+} ions between carboxylates of adjacent malonate headgroups such that a metal-ion bridged network is established at the monolayer/solution interface.

Multilayers consisting of up to ten monolayers were formed by transfer on to hydrophobic quartz or silicon substrates of solid-phase monolayers of **1** spread on Ca^{2+} or Cd^{2+} subphases. TEM micrographs showed inhomogeneous films that contained calcium by EDXA (Fig. 4) but not cadmium. The results suggest that calcium can be readily intercalated with close-packed molecules of **1** and co-assembled in organized arrays. Further experiments are underway to investigate the structure and properties of these metal fullerate thin films.

Footnote

† Isotherm measurements were made using a NIMA Technology System 2001 trough with computer interface control. Purified water (0.8 dm^3) was employed as the subphase, and surface-cleaned twice with suction *via* a Pasteur pipette. 200 μl of a 0.08 mg cm^{-3} solution of **1** in thf was spread at the air/water interface and the solvent allowed to evaporate for at least 15 min prior to compression. Surface pressure *versus* area per molecule isotherms were measured at a compression speed of 50 cm^2 min^{-1}. In separate experiments, 1–5 mmol dm^{-3} aqueous solutions of $CdCl_2$ and $CaCl_2$ were employed as the subphase. Control isotherms were carried out on each subphase, in the absence of a spread monolayer. Checks were also made for any surface activity due to contamination in the thf solvent.

Silicon wafers, rendered hydrophobic by treatment with hexamethyldisilazane, were used for UV–VIS spectroscopy measurements of the LB multilayer films. The prepared films were transferred using a horizontal lifting method onto hydrophobic Si or quartz surfaces, or formvar-coated copper electron microscope grids, and studied by transmission electron microscopy (TEM) and energy dispersive X-ray analysis (EDXA).

References

1 Y. S. Obeng and A. Bard, *J. Am. Chem. Soc.*, 1991, **113**, 6279.
2 T. Nakamura, H. Tachibana, M. Yumura, M. Matsumoto, R. Azumi, M. Tanaka and Y. Kawabata, *Langmuir*, 1992, **8**, 4.
3 C. Long, Y. Xu, F. Guo, Y. Li, D. Xu, Y. Xao and D. Zhu, *Solid State Commun.*, 1992, **82**, 381.
4 M. Maggini, A. Karlsson, L. Pasimeni, G. Scorrano, G. Prato and L. Valli, *Tetrahedron Lett.*, 1994, **35**, 18, 2985.
5 M. Matsumoto, H. Tachibana, R. Azumi, M. Tanaka, T. Nakamura, G. Yunome, M. Abe, S. Yamago and E. Nakamura, *Langmuir*, 1995, **11**, 660.
6 U. Jonas, F. Cardullo, P. Belik, F. Diederich, A. Gügel, E. Harth, A. Herrmann, L. Isaacs, K. Müllen, H. Ringsdorf, C. Thilgen, P. Uhlmann, A. Vasella, C. A. Waldraff and M. Walter, *Chem. Eur. J.*, 1995, **1**, 243.
7 I. Lamparth and A. Hirsch, *J. Chem. Soc., Chem. Commun.*, 1994, 1727.

Received, 6th November 1995; Com. 5/07296D

X-Ray reflection studies on the monolayer-mediated growth of mesostructured MCM-41 silica at the air/water interface

Stephen J. Roser, Harish M. Patel, Michael R. Lovell, Jane E. Muir and Stephen Mann*†

Department of Chemistry, University of Bath, Bath, UK BA2 7AY

X-Ray reflection has been used to study the nucleation and growth of thin films of a silica–surfactant mesophase (MCM-41) at the air/water interface in the presence and absence of an insoluble lipid monolayer of phosphatidylcholine; the rate of self-assembly and structural order of films comprising up to four micellar layers were enhanced under the lipid monolayer.

One of the most promising routes to new silica-based mesostructured materials with pore diameters greater than those of conventional materials such as zeolites involves the co-operative assembly of inorganic precursors with supramolecular organic templates.[1–7] The resulting silica–surfactant liquid crystalline mesophases can have a range of symmetries, including hexagonal (MCM-41) or cubic (MCM-48), and can be processed to produce mesoporous replicas consisting of an ordered array of channels with 1 nm thick silica walls. Several studies have recently shown that thin films of MCM-41 materials can be formed under acidic conditions at the air/water,[8] mica/water,[9] or graphite/water interface,[10] as well as on Au substrates that had been chemically patterned.[11] In a recent study,[12] X-ray reflection (XRR) was used to investigate the time-dependent growth of MCM-41 under acidic conditions at the air/water interface. In this report we use X-ray reflectivity to probe the nucleation and growth of thin films of MCM-41 under alkaline conditions at the air/water interface in the presence of an insoluble lipid monolayer that acts as a secondary template in the self-assembly process.

MCM-41 silica was synthesised at room temperature from a dilute basic solution *via* condensation of tetraethoxysilane (TEOS) in the presence of hexadecyltrimethylammonium bromide (C_{16}TMABr).‡ The films were grown slowly at the air/water interface from a quiescent solution contained within a Teflon trough which was sealed in a Perspex box with thin Mylar windows for X-ray transmission. In experiments involving phosphatidylcholine (PC) monolayers, a known volume of PC in chloroform was spread onto the air/water interface prior to recording of the XRR data.§ Analysis of X-ray reflection data was performed according to established procedures.¶

Fig. 1 shows the fitted reflectivity profile and calculated scattering density (inset) for the initial measurements for MCM-41 films grown from alkaline solutions under a PC monolayer. The zero-time fit has a fringe periodicity which corresponds to a thickness of 4 nm and demonstrates that the electron density profile perpendicular to the surface has two maxima, both of which have similar electron density values. The presence of the fringes indicates that a single micellar layer of a silicate–surfactant film is nucleated under the lipid monolayer. Similar data were obtained for the zero-time measurements for MCM-41 grown at an unmodified air/water interface, except that the peak values of the scattering length density profiles were slightly lower, suggesting that the presence of the PC monolayer induced the nucleation of a more densely packed arrangement of silicated rod-like micelles. In both cases, the model used to fit the data was based on a layer of amorphous silica-coated cylindrical micelles with an overall diameter of 4 nm. Interestingly, the data could not be fitted with a model corresponding to a primary surface layer of hemispherical micelles, as has been recently proposed as the initial stage in the nucleation of MCM-41 films from acidic solutions.[8] Thus, under alkaline conditions, mineralized micellar cylinders are considered to constitute the first layer of MCM-41 nuclei formed at the air/water or monolayer/solution interfaces.

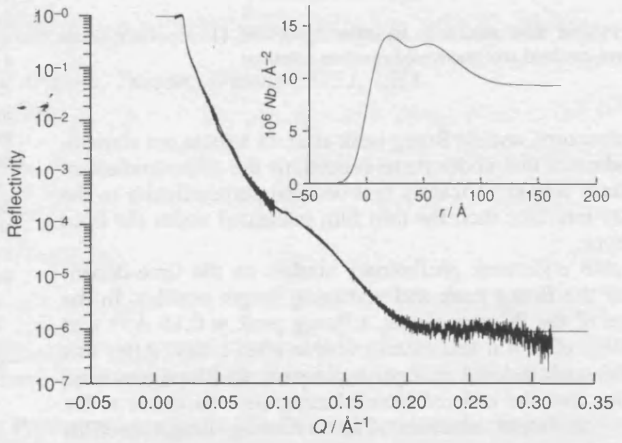

Fig. 1 Fitted reflectivity profile and calculated scattering length density (*Nb*, inset) for MCM-41 films grown for 1 h under a PC monolayer

Significant differences were observed in the XRR scattering length density profiles for thin films grown for 3 days under a PC monolayer (Fig. 2). The complex profile shows five distinct peaks with a repeat spacing of 3.9 nm in the density plot, leading to a broad Bragg peak centred at Q *ca.* 0.16 Å^{-1}. If the cylinders are hexagonally close packed, this corresponds to a film consisting of four silica–surfactant micellar layers, but with the scattering length density less than that expected from a perfectly ordered structure. The Bragg peak was consistent with small angle powder XRD and electron diffraction data of the retrieved thin films which confirmed the formation of the hexagonal mesophase.‖ In contrast, the MCM-41 silica prepared at the unmodified air/water interface showed a less well developed

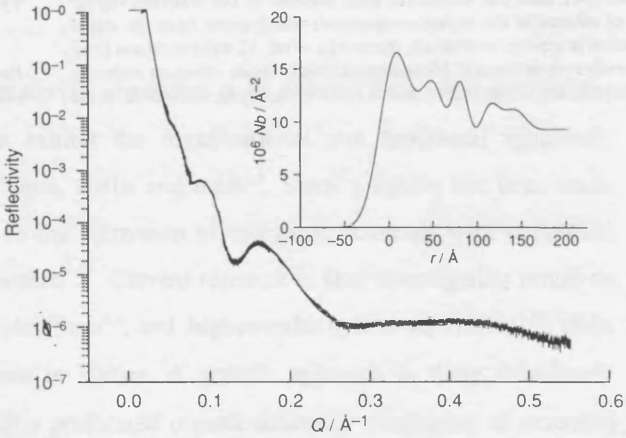

Fig. 2 Fitted reflectivity profile and calculated scattering density (inset) for MCM-41 films grown for 3 days under a PC monolayer

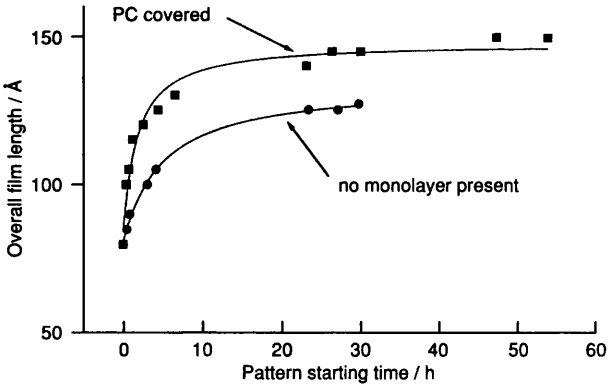

Fig. 3 Plot of film thickness *vs.* time for MCM-41 deposition from monolayer-covered and uncovered reaction solutions

fringe structure, and no Bragg peak after 48 h (data not shown). This indicates that under these conditions the silica–surfactant mesophase was significantly less ordered perpendicular to the air/water interface than the thin film nucleated under the lipid monolayer.

We also undertook preliminary studies on the time-dependence of the Bragg peak and scattering length profiles. In the presence of the PC monolayer, a Bragg peak at 0.16 $Å^{-1}$ was discernible after 4 h and clearly visible after 1 day. After this time, the peak did not change in position, width or intensity, indicating that the ordered internal structure was stable at the monolayer/solution interface. The scattering length profiles were used to determine the rate of growth in thickness of the MCM-41 films and clearly indicated that the presence of the PC monolayer results in faster growth and a more ordered mesophase (Fig. 3).

In conclusion, we have demonstrated that it is possible to obtain detailed information on the growth and structure of mesostructured MCM-41 silica films at the air/water interface using X-ray reflection. Spreading of a PC monolayer at the air/water interface enhances the rate of formation and quality of the thin films, suggesting that interactions between the lipid headgroups and molecular or supramolecular silica/surfactant species facilitate the assembly of the first layer of the nucleus. Further work using a range of lipids and their associated phase behaviour is underway to elucidate these interfacial processes.

Notes and References

† E-mail: s.mann@bath.ac.uk

‡ In a typical experiment, 0.16 g of C_{16}TMABr was dissolved in 318.0 g of H_2O and stirred continuously. 2.0 g of 1 M NaOH were added, followed by 0.828 cm^3 of TEOS, (molar composition = 0.001 C_{16}TMABr:0.11 NaOH:0.009 TEOS:40.2 H_2O). The solution was left to stir for 3 min before being placed in the Teflon trough of the X-ray reflectometer. Growth of the MCM-41 film was extremely slow because of the constant vapour pressure of ethanol in the sealed environment which arose from the initial condensation reactions. In contrast, the results of ref. 12 were obtained from an evaporative environment. Measurements were made using an in-house energy-dispersive X-ray reflectometer, and typically consisted of three separate runs at different angles, lasting in total for 1 h. Measurements of MCM-41 growth were taken over a period of several days.

§ 124 μl of a chloroform solution of PC (100 mg cm^{-3}) were spread at the air/water interface using a micro-syringe. The volume added was calculated to produce a solid phase monolayer after solvent evaporation.

¶ In general, each discontinuity in scattering length density ($Nb/Å^{-2}$) between thin layers lying parallel to the interface under investigation contributes to the X-ray reflectivity, given by the well known Fresnel coefficient. This is modified by a factor, which allows for the roughness of the interface. The contributions from each layer are then combined using a matrix method. The usual procedure in fitting a reflectivity profile is to assume a model profile, and allow variation of numerous parameters, until the best fit between the model and the real $R(Q)$ is found. The layer electron density in $Å^{-3}$ can be determined by dividing Nb by the scattering length of a single electron (2.8×10^{-5} Å). Thus, the experiment measures the change in electron density perpendicular to the air/water interface, but averages information in the plane of the surface. Further details can be found in ref. 13.

‖ Samples for SAXRD, electron diffraction, ^{13}C and ^{29}Si solid state NMR, FTIR and TGA were collected from the air/water or monolayer/water interfaces after growth for 3 days in an unsealed environment. Data for monolayer-mediated synthesis; SAXRD *d* spacings, 4.0, 2.31, 1.99, 1.51 nm (as-synthesized), 3.16, 1.97, 1.75 nm (calcined); ^{29}Si NMR, δ −89.7 (Q^2), −99.6 (Q^3), −109.4 (Q^4) (as-synthesized); ^{13}C NMR, δ 14.46, 23.25, 26.99, 30.68, 32.62, 54.04, 66.91 (as-synthesized); FTIR, ν(Si–O–Si) 1000–1200 cm^{-1}, $\nu(CH_2)$ 1460–1490, 2850–2950 cm^{-1}; CHN analysis, 32 mass% C (as-synthesized). Hexagonal arrays of 4 nm spaced lattice fringes were observed by TEM.

1 C. T. Kresge, M. E. Leonowicz, W. J. Roth, J. C. Vartuli and J. S. Beck, *Nature*, 1992, **359**, 710.
2 J. S. Beck, J. C. Vartuli, W. J. Roth, M. E. Leonwicz, C. T. Kresge, K. D. Schmitt, C. T. Chu, D. H. Olsen, E. W. Sheppard, S. B. McCullen, J. B. Higgins and J. L. Schlenker, *J. Am. Chem. Soc.*, 1992, **114**, 10834.
3 A. Firouzi, D. Kumar, L. M. Bull, T.Besier, P. Sieger, Q. Hue, S. A. Walker, J. A. Zasadzinski, C. Glinka, J. Nicol, D. Margolese, G. D. Stucky and B. F. Chemelka, *Science*, 1995, **267**, 1138.
4 Q. S. Huo, D. I. Marglose, U. Ciesla, D. G. Demuth, P. Y. Feng, T. E. Gier, P. Sieger, A. Firouzi, B. F. Chmelka, F. Schüth and G. D. Stucky, *Chem. Mater.*, 1994, **6**, 1176.
5 D. Khushalani, A. Kuperman, G. A. Ozin, K. Tanaka, J. Garces, M. M. Olken and N. Coombs, *Adv. Mater.*, 1995, **7**, 842.
6 J. H. Koegler, H. W. Zandbergen, J. L. N. Harleveld, M. S. Nieuwenhuizen, J. C. Jansen and H. Vanbekkum, *Stud. Surf. Sci. Catal.*, 1994, **84**, 307.
7 J. C. Jansen and G. M. Vandrosmalen, *J. Cryst. Growth*, 1994, **128**, 1150.
8 H. Yang, N. Coombs, I. Sokolov and G. A. Ozin, *Nature*, 1996, **381**, 589.
9 H. Yang, A. Kuperman, N. Coombs, S. Mamiche-Afara and G. A. Ozin, *Nature*, 1996, **379**, 703; I. A. Aksay, M. Trau, S. Manne, I. Hunma, N. Yao, L. Zhou, P. Fenter, P. M. Eisenberger and S. M. Gruner, *Science*, 1996, **273**, 892.
10 H. Yang, N. Coombs, I. Sokolov and G. A. Ozin, *J. Mater. Chem.*, 1997, **7**, 1285.
11 H. Yang, N. Coombs and G. A. Ozin, *Adv. Mater.*, 1997, **9**, 811.
12 A. S. Brown, S. A. Holt, Thien Dam, M. Trau and J. W. White, *Langmuir*, 1997, **13**, 6363.
13 J. Penfold and R. K. Thomas, *J. Phys: Condens. Matter.*, 1990, **2**, 1369.

Received in Cambridge, UK, 1st December 1997; revised manuscript received 28th January 1998; 8/00777B

Preprint of "Brittle bacteria: A biomimetic approach to the formation of fibrous composite materials", submitted for publication to *Chemistry of Materials*, April 1998.

BRITTLE BACTERIA: A BIOMIMETIC APPROACH TO THE FORMATION OF FIBROUS COMPOSITE MATERIALS

Sean A. Davis[†], Harish M. Patel[†], Eric.L. Mayes[†], Neil.H. Mendelson,[#] Gabriella Franco[†] and Stephen Mann*[†]

Department of Chemistry, University of Bath, Bath, BA2 7AY, U.K., and Department of Molecular and Cellular Biology, University of Arizona, Tucson, Arizona 85721, USA.

* To whom correspondence should be addressed.

[†] University of Bath.

[#] University of Arizona

ABSTRACT

Organized bacterial superstructures have been used as 3-D templates for the fabrication of ordered inorganic-organic fibrous composites. Preformed magnetic (Fe_3O_4) and semiconducting (CdS) inorganic nanoparticles were incorporated into macroscopic threads of *Bacillus subtilis* by reversible swelling of the superstructure in colloidal sols. The air-dried mineralized fibres consisted of a close packed array of 0.5 μm diameter multicellular bacterial filaments, each of which was coated with a 30 to 70 nm thick layer of aggregated colloidal particles. Inorganic patterning of the interfilament spaces was influenced by the surface charge of the nanoparticles used. Whereas negatively charged magnetite colloids gave good infiltration and replication of the bacterial superstructure, the neutral ligand-capped CdS colloid, although internalized to some extent, was preferentially localized at the surface of the thread. Positively charged sols of TiO_2 in contrast, did not penetrate the swollen fibre but produced coherent surface coatings with uniform thickness. Attempts to pattern the deposition of CdS using molecular precursors by exposing a Cd(II)-containing bacterial fibre to H_2S gas produced an uneven surface coat of CdS particles. Removal of the bacterial component from the magnetic composite by heating at elevated temperatures resulted in structural collapse.

INTRODUCTION

A central objective of biomimetic materials chemistry is to develop new strategies for the synthesis of materials and composites that exhibit the organizational and functional specificity exemplified by biological minerals such as bones, shells and teeth[1,2]. Some progress has been made towards developing biomimetic approaches to the formation of inorganic materials with controlled size, shape, orientation and polymorphic structure[3,4]. Current research is also investigating routes to the synthesis of inorganic materials with complex form[5,6], and higher-order hybrid assemblies[7-10], often reminiscent of the hierarchical structures seen in Nature. A generic approach to these biomimetic materials involves the inorganic replication of a preformed organic assembly possessing an extended and patterned architecture. In this paper we develop this strategy by using a bacterial template with

reversible swelling properties to fabricate fibrous bioinorganic composites consisting of organized arrays of magnetic or semiconducting nanoparticles.

Bacterial threads can be produced from a mutant strain of the bacterium *Bacillus subtilis* which has a cylinder-shaped cell, 0.8μm in diameter and 4μm in length. In fluid cultures, the mutant strain, which exhibits suppressed cell separation, can only grow by elongation at constant diameter along the cylinder axis to produce long multi-cellular filaments that intertwine to form web-like structures (Figure 1). Drawing these web structures from the culture medium results in compaction of the individual filaments at the fluid-air interface to give a macroscopic bacterial thread, often several decimetres long and 0.1 to 0.2 mm wide[11,12]. The air-dried thread consists of a superstructure of multi-cellular filaments aligned parallel to the thread axis, and arranged in a pseudo-hexagonal packed configuration, reminiscent of the organization of cylindrical surfactant micelles in the H_I liquid-crystal lyotropic phase, albeit on a length scale two orders of magnitude greater. A typical bacterial thread can contain in excess of 10^{10} cells and 50, 000 filaments arranged as a cell → filament → thread hierarchy of cylindrical building units[13].

The strong metal-binding ability of the cell wall of *B. subtilis* [14] has been utilized for the mineralization of multicellular bacterial filaments prior to drawing of the macroscopic composite fibre[15]. For example, addition of soluble metal salts of iron and calcium directly to unwashed web cultures resulted in the formation of precipitates on the filaments within the web culture[16]. Analysis of fibres drawn from these mineralized web structures indicated a metal content of 10-16 wt% deposited in the form of mineral phases such as $Fe_2O_3$and $CaCO_3$. However, no precipitation was observed on the filaments prior to drawing into a fibre when washed webs or copper salts were used. The corresponding drawn fibres contained mineral deposits formed by solution evaporation but the metal loadings were significantly reduced. The internal microstructure of the composite fibres produced from mineralized webs (both washed and unwashed) was not systematically studied.

In recent studies, we have been investigating an alternative method to the fabrication of organized bacterial-mineral composites that is based on reversible swelling of unmineralized threads in the presence of preformed inorganic nanoparticles[17]. Our objective is to exploit the underlying organization of the thread as a template for producing composites with an extended, ordered microstructure. This was achieved by loading the bacterial thread with colloidal suspensions of ceramic nanoparticles, followed by air-drying to consolidate the inorganic mineral and replicate the interfilament spaces in the form of a continuous inorganic framework. Moreover, removal of the bacterial template by calcination produced a silica fibre with ordered macroporous channels. We also infiltrated the organic superstructure with a colloidal dispersion of a surfactant-templated mesostructured silica phase (MCM-41) to illustrate how bacterial templates could be used in hierarchical processing. An ordered macroporous fibre with channel walls of periodic mesoporous silica was obtained after calcination[17]. Here we describe the use of preformed bacterial thread for the production of a fibre-like composites containing Fe_3O_4, CdS or TiO_2 nanoparticles.

EXPERIMENTAL SECTION

Production of Bacterial Thread.

The cultures of *Bacillus subtilis* strain FJ7(II) were grown at 20°C in 100 mm diameter plastic petri dishes containing 16 ml of tryptose blood (TB) medium, consisting of tryptose (10 g/l), beef extract (3 g/l), and NaCl (5 g/l), and was supplemented with uracil (20 mg/l)[18]. Decimetre long bacterial threads were produced by slowly pulling the web from solution using a thin wire hook withdrawn at 22 mm min^{-1} by a rate-controlled motor, and were left to dry in air.

Synthesis of Magnetite (Fe_3O_4) Nanoparticles.

A magnetite colloid was prepared in alkaline media according to the general procedure described elsewhere[19]. An aqueous solution containing iron (III) chloride hexahydrate (4 ml, 0.0085 moles) and ammonium iron (II) sulfate hexahydrate (1 ml, 0.0043 moles, in 2M HCl) was added to 50 ml of 1M tetramethylammonium hydroxide. The resulting black suspension was stirred for one hour at room temperature and then placed in an ultrasonic bath for an hour. The colloid produced was centrifuged at 20000g for one hour. The supernatant was decanted and the sediment resuspended in 20ml water by sonication. The black dispersion obtained was filtered through a 0.2μm pore cellulose nitrate membrane filter. The particle size of the approximately spherical particles was 9.1 ± 2.4 nm as determined by transmission electron microscopy (TEM). Electron diffraction data (d_{hkl} = 0.500 nm (111), 0.305 nm (220), 0.259 nm (311), 0.216 nm (400)) were consistent with magnetite.

Synthesis of Cadmium sulfide (CdS) Nanoparticles.

A CdS colloid was prepared by the following procedure[20]: cadmium acetate (2.712 g, 0.0118 moles), thiourea (0.263 g, 0.00346 moles) and 3-mercapto-1,2-propanediol (0.945 cm^3, 0.0113 moles) were mixed together with dimethylformamide (200 cm^3) for approximately 1 hour, under a flow of argon. The mixture was then heated to 100-130°C for 20 minutes and allowed to cool for 30 minutes. This heating-cooling cycle, which decomposes the thiourea and generates S^{2-} ions, was repeated and on the third heating cycle a white precipitate of CdS formed. The precipitate was isolated by centrifugation, washed with acetone followed by diethylether (to remove residual Cd(II) ions) and finally dried in vacuo. The particle diameter determined by TEM was 3.4 ± 0.7 nm. XRD measurements of films and powders prepared from the dispersion indicated that the CdS nanoparticles adopt the ZnS blende structure (d_{hkl} = 0.336 nm (111), 0.290 nm (200), 0.206 nm (220), 0.175 nm (311)).

Synthesis of Titania (TiO_2) Colloid.

Colloidal titania was prepared by hydrolysis of titanium tetraisopropoxide under a nitrogen atmosphere using the procedure described previously[21]. Titanium(IV) isopropoxide (1.25 ml, 0,00424 moles) was added to 0.25 ml isopropanol in a syringe. This mixture was added dropwise over five minutes to 10 ml distilled, deionized water whilst stirring vigorously. Ten minutes after the final alkoxide addition, 0.05 ml 70% nitric acid was added. The hydrolysis mixture was then stirred for 8

hours at 80°C to remove the isopropanol. The mean particle diameter from TEM studies was 8.2 ± 2.2 nm. Electron diffraction indicated that the major phase present was the anatase polymorph of TiO_2 ($d_{(hkl)}$ = 0.355 nm (101), 0.238 nm (004), 0.231 nm (112), 0.191 nm (200), 0.169 nm (105)). A small amount of brookite, also a polymorph of TiO_2, was also detected ($d_{(hkl)}$ = 0.292 nm (121)).

Preparation of mineralized bacterial composites from preformed nanoparticles.

Fibre composites were prepared by dipping 5 cm long samples of prewashed bacterial thread into a colloidal dispersion of inorganic nanoparticles (Fe_3O_4, CdS or TiO_2) for between five and 120 minutes. Samples were then carefully removed from the colloid-containing solution and allowed to dry in air for at least 24 hours prior to analysis. Reverse tweezers were used to hold the bacterial thread throughout the process. During the dipping process, the tweezers were held so that the tip was not immersed in the dispersion, and the portion of bacterial thread being held remained dry which aided the recovery of the composite fibre. Consequently, a portion of the loaded thread remained bare and this was removed from the air-dried samples before further analysis.

A portion of a magnetite-bacterial thread composite was placed in a crucible and heated in air to 600°C in an oven. The temperature was increased in 50°C increments at 30 minute intervals. The oven was turned off after 2 hours and allowed to cool to room temperature before the product was recovered.

Preparation of mineralized bacterial composites by in situ deposition.

A 5 cm long portion of a prewashed bacterial thread was dipped into a 1.0 M cadmium chloride solution for 2 hours, redrawn and allowed to dry in air overnight. The Cd-containing bacterial thread was then placed in a dessicator and exposed to a constant supply of H_2S, generated from the reaction of $Na_2S_{(s)}$ with $HCl_{(aq)}$, for 7 days.

Characterization.

Scanning electron microscopy (SEM) and energy dispersive X-ray analysis (EDXA) were performed using a JEOL 6310 SEM operated at 15keV. Samples were prepared for analysis using one of two different methods. Firstly, air-dried uncoated samples were mounted onto aluminium stubs using circular carbon adhesive pads for EDX analysis and then gold coated in an Edwards S150B sputter coater for 4 minutes for imaging studies. Secondly, resin-embedded samples were mounted onto aluminium stubs using a carbon 'gum' and gold coated for 2 minutes after which a carbon paste was applied between the gold coat and the stub to enhance the electrical conductivity of the resin blocks. Elemental distribution maps were generated by EDX analysis and corresponding secondary electron images obtained.

Thin sections of the composite fibres were prepared for transmission electron microscopy (TEM) analysis by dehydrating a 1 cm length of the material for one hour in 50ml of 50:50 MeOH/H_2O containing 0.5ml silane to aid adhesion between the sample and resin. After drying in air for 90 minutes, the fibre was transferred to a sample bottle, covered in TAAB hard resin, and placed in

a rotator for at least 12 hours to allow infiltration of the resin into the fibre. The sample was then placed in an embedding mould and covered with fresh resin which was polymerized in an oven at 60^{o}C for 2 days. Sections were prepared using a diamond knife on an OMU3 ultramicrotome. Thin sections were cut perpendicular to the fibre axis to a thickness of typically 50-100 nm (silver-gold interference colours). Sections were collected on formvar-covered, carbon coated, 3 mm slotted copper grids and left unstained. TEM imaging, selected area electron diffraction studies and EDXA were performed on a JEOL 2000FX analytical TEM operated at an accelerating voltage of 200keV.

X-ray diffraction data were recorded from whole samples, using a Phillips X-ray powder diffractometer with Cu K_{α} (l=1.5405Å) radiation.

RESULTS

Bacterial-magnetite fibrous composites.

Dipping of bacterial threads into a ferrofluid of magnetite nanoparticles resulted in visible swelling of the biological superstructure without loss of structural integrity. The swollen fibre was withdrawn through the air/liquid interface to produce a compact black fibre that was initially pliable due to a high moisture content. Drying in air gave a consolidated, brittle fibre of similar size to the unmineralized bacterial thread. The iron loading in the dried sample was 19 wt.%, as determined by atomic absorption spectrometry. The mass loading of magnetite in the composite was calculated as 26 wt%, by assuming a chemical composition of Fe_3O_4. The composite fibres were sufficiently magnetic that they responded and tracked to an external magnetic field, and could be suspended vertically under the poles of a bar magnet (Figure 2). Further details on the superparamagnetic properties of the composite fibres are reported elsewhere[22].

The surface and internal texture of the individual composite fibres (Figure 3) was significantly different to that of the unmineralized bacterial thread. A thin mineral coating, which gave peaks for iron by energy dispersive X-ray analysis (data not shown), obscured the underlying bacterial cells. The fibres appeared uniformly dark in cross-section indicating that the mineral phase was not restricted to the surface of the fibre. This was confirmed by mapping the iron distribution of a sample in cross-section (Figure 4), as well as TEM imaging of the central region of thin transverse sections (Figure 5). The TEM data showed that discrete magnetite nanoparticles were concentrated around and between the multicellular filaments of the bacterial superstructure to produce an extended and interconnected micro-skeletal framework. The thickness of the mineral walls was typically between 50 to 70 nm.

Removal of the bacterial template by high temperature curing produced an intact but extremely brittle black fibre. Any attempt to manipulate the sample resulted in collapse of the structure.

Bacterial-CdS fibrous composites.

Dipping bacterial thread into an aqueous suspension of CdS nanoparticles produced a fibre that was not significantly different in appearance to the original bacterial thread. SEM microscopy of the composite fibre revealed that the fibre surface consisted of partially disorganised filaments and discrete, randomly distributed micron-scale mineral aggregates (Figure 6), which contained Cd and S (EDX data not shown). Thus, the CdS colloid produced localized aggregates rather than a uniform coating at the fibre surface. However, elemental mapping indicated that the inorganic phase was dispersed throughout the bacterial thread (Figure 7), although a higher concentration was observed near to the edge of the fibre due to the surface aggregates. TEM micrographs of transverse thin sections (Figure 8) showed that the bacterial filaments were comparatively well-ordered in the centre of the fibre, in contrast to their surface organization. Higher magnification images (Figure 8b) revealed 30-40nm thick electron dense regions surrounding individual filaments that were attributed to closely packed arrays of the CdS nanoparticles. No electron diffraction patterns could be recorded from these areas due to the low localized concentration of the colloidal particles.

In-situ mineralization of CdS in bacterial thread.

Dry fibres, produced after dipping bacterial thread into aqueous $CdCl_2$ solution, were white in colour and of similar diameter to the native material. Although Cd was detected by EDX analysis (data not shown), no mineral phases, such as a $CdCl_2$ evaporite, were observed by SEM examination of the fibre surface, which consisted of disorganized bacterial filaments. The Cd-containing bacterial thread developed a yellow colouration when exposed to H_2S. Examination of the fibre by SEM revealed an uneven surface coating which consisted of a mass of plate-like, and smaller discrete crystals (Figure 9). Elemental mapping indicated that Cd and S were not evenly distributed throughout the fibre, but were concentrated near the surface (Figure 10). X-ray diffraction (XRD) of the composite fibre indicated the presence of a crystalline CdS phase with the ZnS blende structure ($d_{(hkl)}$ = 0.335 nm (111), 0.298 nm (200), 0.206 nm (220)). TEM imaging of thin sections clearly showed the presence of a surface coating about 60 nm thick (Figure 11). Electron diffraction data recorded from this area were consistent with the XRD data. Cadmium sulfide particles were also identified at much lower loadings in the centre of the thread by EDX analysis (data not shown).

Bacterial-titania fibrous composites.

A pale white fibre was produced by dipping bacterial thread into an aqueous dispersion of titania nanoparticles. Examination of the surface of the fibre by SEM revealed a distinct mineral coating (Figure 12), which appears smooth and of quite uniform thickness. The apparent plate-like morphology originated from shrinkage of a thin mineral film during drying which caused extensive cracking predominantly perpendicular and parallel to the fibre axis. The characteristic texture of the underlying bacterial thread was visible between some of the mineral plates. X-ray analysis indicated the presence of Ti and P (data not shown). Lattice spacings obtained by XRD of the composite fibre

were the same as those obtained from the TiO_2 colloid (d = 0.350 nm, 0.304 nm, 0.238 nm, 0.190 nm, 0.168 nm, 0.148 nm). The mineral phase was therefore identified as being predominantly anatase.

The distinct surface coating was clearly discernible by SEM examination of a sample in cross-section (Figure 13). When compared with the corresponding elemental distribution map for titanium it was clear that the mineral phase was present only at the surface of the macroscopic thread. No infiltration into the centre of the thread was observed. The thickness of the surface coating was estimated as 0.5 to 5 μm. TEM studies of different regions of transverse thin sections of the fibre indicated a densely consolidated surface coat (Figure 14) and negligible infiltration of TiO_2 between the co-aligned bacterial filaments.

DISCUSSION

The technique of utilising organic templates for the fabrication of fibrous hybrids is currently being explored in a number of systems. Often, preformed static templates are surface-coated to produce biomimetic composite materials; for example, composite magnetite-textile polyester fibres[23] and magnetic spider silk threads[24] have been prepared by absorbing magnetite particles onto the surface of the (bio)polymers. Similarly, hollow ceramic cylinders have been fabricated by calcining silica[25] or aluminium hydroxide[26]-coated phospholipid tubules.

In contrast, the work described here illustrates that organized organic superstructures with reversible swelling properties can be exploited in the preparation of mineral-infiltrated fibrous composites, provided that the surface charge of the inorganic phase is appropriately tailored. The bacterial filaments are negatively charged due to the predominance of carboxylate groups on the cell membrane. Thus, colloids with a net positive surface charge, such as TiO_2, tend to deposit only on the external surface of the macroscopic bacterial thread to give uniform coatings, whereas a negatively charged colloid, such as magnetite or silica[17], penetrates into the interior of the thread to produce an organized inorganic phase that is patterned within the interspaces between the multi-cellular filaments. Presumably in this case, repulsive forces between the nanoparticles and cell membranes give rise to infiltration, as opposed to surface absorption, when the superstructure swells during permeation of the sol into the thread. When the thread is redrawn from the sol, particles trapped between or adhering to the bacterial filaments are retained and consolidated within the interfilament spaces on drying. The idealised structure would therefore consist of a well-ordered, close-packed array of uniform diameter bacterial filaments that are separated by an interpenetrating, continuous inorganic phase of uniform thickness. In reality, only small areas within the composite have such an idealised structure because the superstructure is disordered to some extent by the hydration and air-drying process.[12] This is manifested as a lowering in packing density of the bacterial component and a corresponding reduction in the long range periodicity. Furthermore, the formation of a continuous wall structure requires particle-particle aggregation and fusion into an extended network; although this was observed for amorphous silica nanoparticles[17], the crystalline magnetite domains remain only loosely associated such that calcination of the composite did not produce a stable porous inorganic replica of the bacterial superstructure.

The extent of infiltration of the CdS nanoparticles was less than that observed for the magnetite colloid, but greater than for the TiO_2 system. This is consistent with the surface structure of the CdS colloid which is capped with hydroxylated ligands. The *in situ* deposition of CdS can be described based on a similar mechanism to that proposed above. When the dry bacterial thread is dipped into $CdCl_2$ solution it swells as the solution penetrates into the thread. The component multicellular filaments separate and are exposed to the Cd(II) ions that adhere to the highly charged groups present in the bacterial cell wall, which are known to act as metal binding sites[14]. To some extent, these interactions disrupt the superstructure as shown by changes in the surface texture of the threads after air-drying. Subsequent reaction with H_2S gas is diffusion-limited because of the preferential formation of a crust of CdS particles at or near the external surface of the bacterial thread. Although, there is only partial transformation to CdS near the centre of the fibre, it should be possible to control the diffusion processes to prepare fully mineralized composites by this *in situ* method.

CONCLUSIONS

The results presented in this paper indicate that bacterial superstructures with reversible swelling properties can be used as 3-D templates for the fabrication of ordered inorganic-organic fibrous composites containing nanoparticles with magnetic (Fe_3O_4) or semiconducting (CdS) properties. Further studies are in progress to establish the optimum conditions for mineral infiltration with different types of inorganic nanoparticles. In the longer term, we aim to integrate biotechnological and materials chemistry processes for the fabrication of a wide range of hybrid materials exhibiting patterned microstructures and morphological complexity.

ACKNOWLEDGEMENTS

We thank BNFL (S.A.D and E.L.M), Leverhulme Trust (S.A.D), EPSRC (H.M.P), the Arizona Agricultural Experimental Station Hatch (N.H.M) and the University of Bath (G.F) for financial support. We also thank K.K.W. Wong for assistance with TEM studies of CdS systems, T. Douglas for help with web cultures and magnetite preparations, and D.J. Riley for helpful discussions.

REFERENCES

(1) Sarikaya, M.; Aksay, I. A. *Biomimetics: Design and Processing of Materials,* AIP Series in Polymers and Complex Materials, AIP Press, New York, 1995.

(2) Mann, S. *Biomimetic Materials Chemistry*, VCH Publishers, New York, 1996.

(3) Mann, S. *J. Mat. Chem.* **1995**, *5*, 935.

(4) Heuer, A.H.; Fink,D.J.; Laraia,V.J.; Arias,J.L.; Calvert,P.D.; Kendall,K.; Messing, G.L.; Blackwell, J.; Rieke,P.C.; Thompson, D.H.; Wheeler, A.P.; Veis, A.; Caplan, A.I. *Science*, **1992**, *255*, 1098-1105.

(5) Mann, S.; Ozin, G.A. *Nature*, **1996**, *382*, 313-318.

(6) Mann, S. *J. Chem. Soc. Dalton Trans.* **1997**, 3953.

(7) Aksay, I. A.; Trau, M.; Manne, S.; Hunma, I.; Yao, N.; Zhou, L.; Fenter, P.; Eisenberger, P. M.; Gruner, S. M. *Science*, 1996, **273**, 892.

(8) Antonietti, M.; Göltner, C. *Angew. Chem. Int. Ed. Engl.* **1997**, *36*, 910.

(9) Mann, S.; Burkett, S.L.; Davis, S.A.; Fowler, C.E.; Mendelson, N.H.; Sims, S.D., Walsh, D.; Whilton, N.T. *Chem. Mater.* **1997**, *9*, 2300.

(10) Combs, N.; Khushalani, D.; Oliver, S., Ozin, G. A.; Shen, G. S.; Sokolov, I.; Yang, H. *J. Chem. Soc. Dalton Trans.* **1997**, 3941.

(11) Mendelson, N.H.; Thwaites, J.J. *MRS Symp. Proc.* **1990**, *174*, 171.

(12) Thwaites, J.J.; Mendelson, N.H. *Proc. Natl. Acad. Sci. U.S.A.* **1985**, *82*, 2163.

(13) Mendelson, N.H.; Thwaites, J.J. *J. Bacteriol.* **1989**, *171*, 1055.

(14) Beveridge, T.J.; Murray, R.G.E. *J. Bacteriol.* **1976**, *127*, 1502.

(15) Mendelson, N.H. *Science* **1992**, *258*, 1633.

(16) Mendelson, N.H.. In *Biomimetic Materials Chemistry*; Mann, S. (ed.), VCH Publishers, New York, 1996, pp 279-313.

(17) Davis, S.A.; Burkett, S.L.; Mendelson, N.H.; Mann, S. *Nature* **1997**, *385*, 420.

(18) Mendelson, N.H. *Proc. Natl. Acad. Sci. U.S.A.* **1976**, *73*, 1740.

(19) Massart, R. *IEEE Trans. Magnet.* **1981**, *17*, 1247.

(20) Chemseddine, A.; Feaheiley, M.L. *Thin Sol. Films* **1994**, *247*, 3.

(21) O'Regan, B.; Moser, J.; Anderson, M.; Gratzel, M. *J. Phys. Chem.* **1990**, *94*, 8720.

(22) Smith, C.J.; Field, M.; Coakley, C.J.; Awschalom, D.D.; Mendelson, N.H.; Mayes, E.L.; Davis, S.A.; Mann, S. *IEEE Trans. Mag.* **1998** in press.

(23) Forder, C.; Armes, S.P.; Simpson, A.W.; Maggiore, C.; Hawley, M. *J. Mat. Chem.* **1993**, *3*, 563.

(24) Mayes, E. M.; Vollrath, F.; Mann, S. *Adv. Mater.* **1998** in press.

(25) Baral, S.; Schoen, P *Chem. Mater.* **1993**, *5*, 145.

(26) Chappell, J.S.; Yager, P. *J. Mat. Sci. Lett.* **1992**, *11*, 633.

Preprint of "Brittle bacteria: A biomimetic approach to the formation of fibrous composite materials", submitted for publication to *Chemistry of Materials*, April 1998.

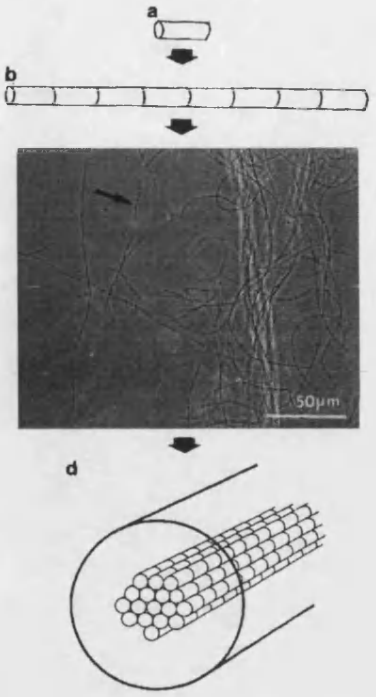

Figure 1
Different levels of cellular organization in bacterial thread. (a) individual rod shaped cells of *B. subtilis*, (b) growth at constant diameter to produce multicellular filamens, (c) optical micrograph of cultured bacteria showing intertwined filaments with web-like structures, and (d) withdrawing of multicellular filaments through the air-water interface produces macroscopic bacterial thread with organized internal superstructure.

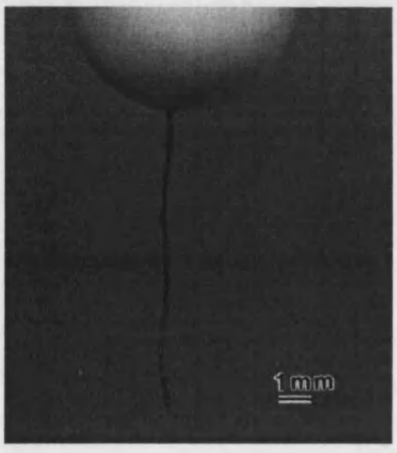

Figure 2
A bacterial-magnetite fibrous composite attracted to, and vertically suspended from a permanent bar magnet.

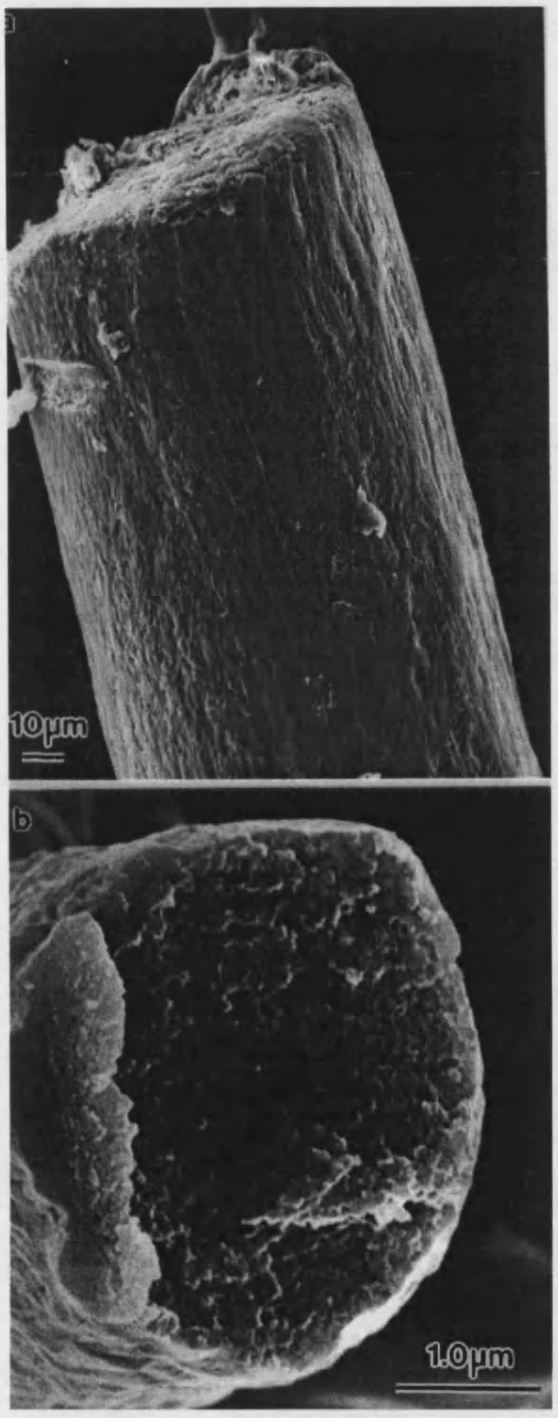

Figure 3
SEM images of (a) external surface, and (b) cross-section, of a bacterial-magnetite fibrous composite.

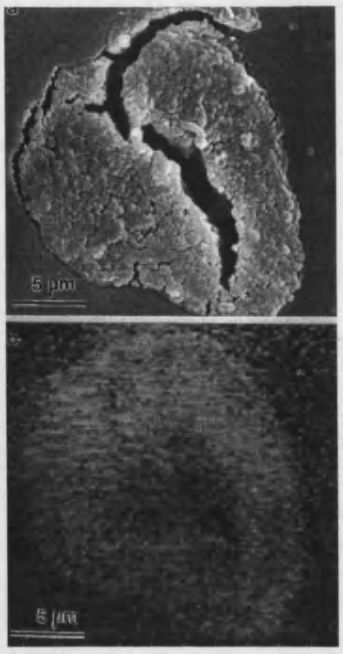

Figure 4
(a) SEM image of a resin embedded bacterial-magnetite composite imaged in cross-section. (b) Corresponding elemental distribution map for iron.

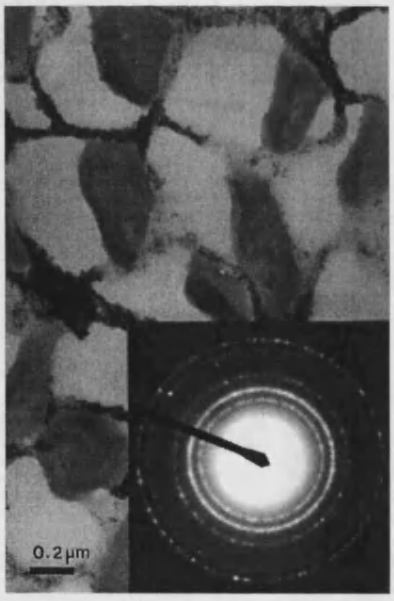

Figure 5
(a) TEM image of a transverse thin section of a bacterial-magnetite composite fibre showing aggregated Fe_3O_4 nanoparticles (darkest areas in the micrograph) within the interfilament spacings. Inset: associated selected-area diffraction patterns confirming the presence of magnetite (d_{hkl} : 0.492 nm (111), 0.300 nm (220), 0.253 nm, 0.212 nm).

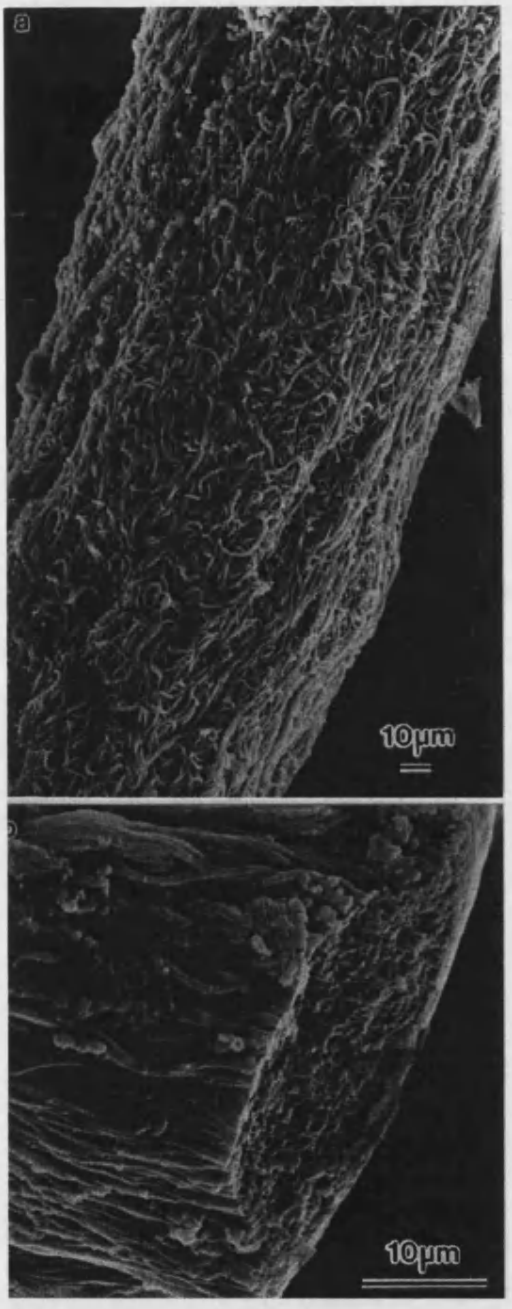

Figure 6
(a) SEM of the surface of a bacterial-CdS composite fibre. (b) Higher magnification image showing detail of a fracture surface.

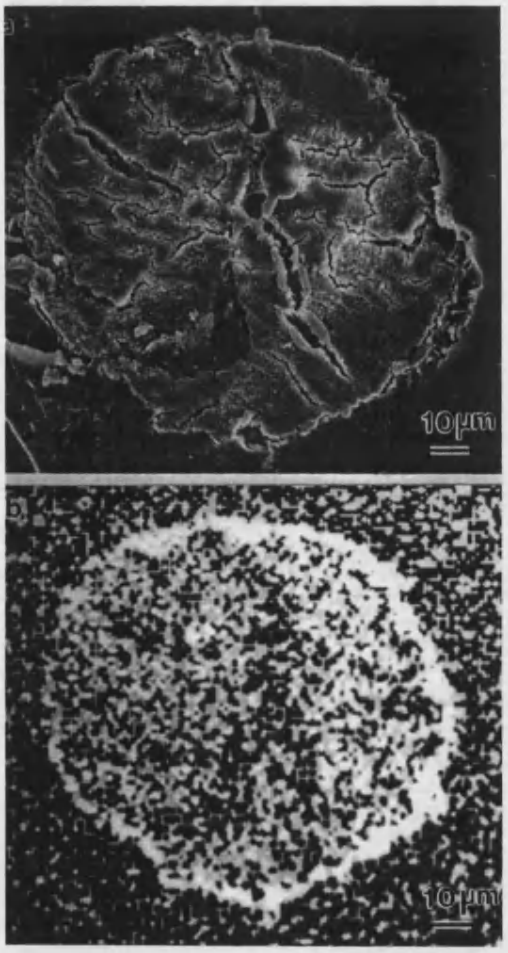

Figure 7
(a) SEM of a bacterial-CdS composite imaged parallel to the fibre axis. (b) Corresponding elemental distribution map for Cd.

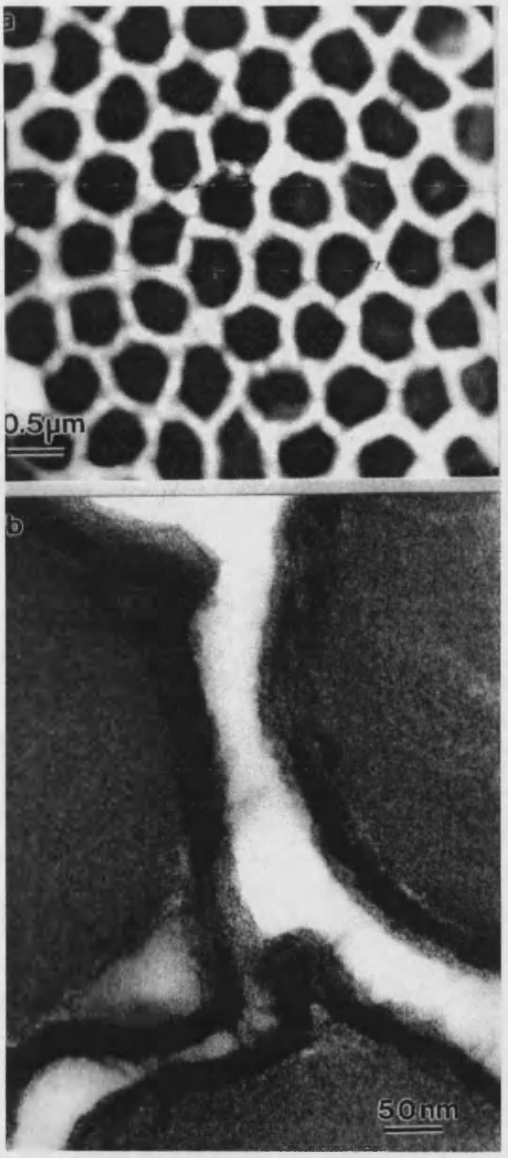

Figure 8
(a) Low magnification TEM micrograph of a transverse thin section of a bacterial-CdS composite showing the ordered arrangement of the bacterial filaments near the centre of the fibre. (b) Higher magnification image of individual bacterial filaments showing a densely packed array of CdS nanoparticles on the cell walls.

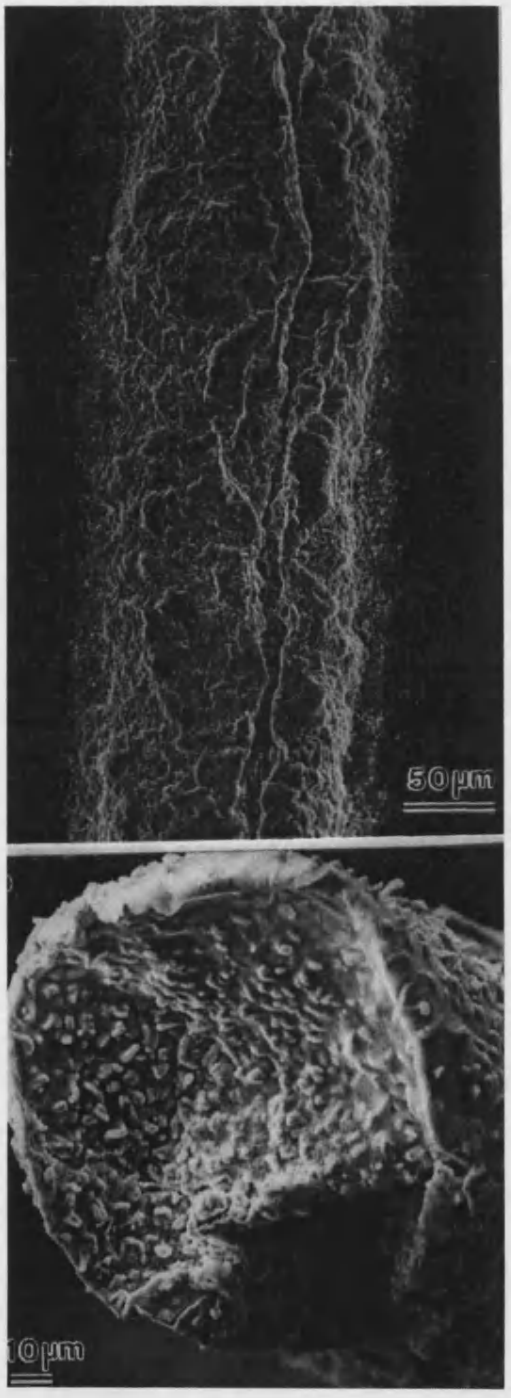

Figure 9
(a) SEM of the surface of a bacterial thread mineralized *in situ* with CdS. (b) Higher magnification image of the tip of a composite fibre.

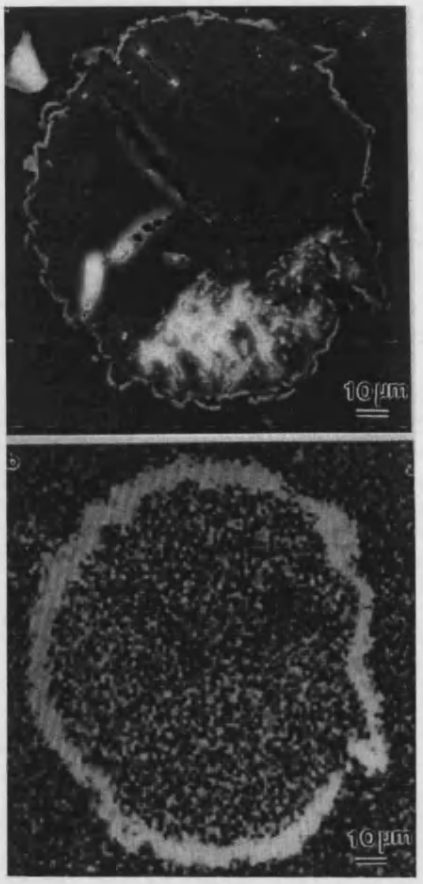

Figure 10
(a) SEM image of an *in situ* mineralized bacterial-CdS composite fibre viewed in cross-section. (b) Corresponding elemental distribution map for S.

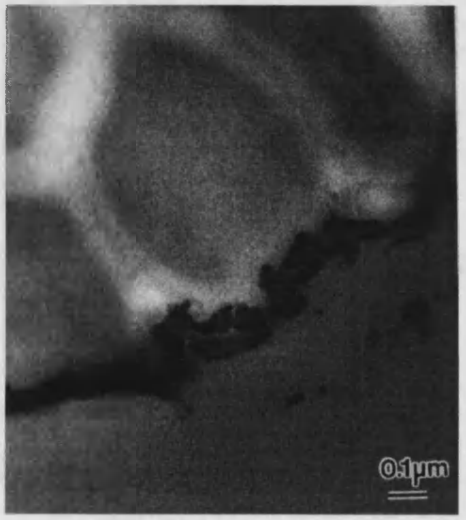

Figure 11
TEM image of the outer edge of a bacterial-CdS composite fibre mineralized *in situ*. The mineral phase forms a distinct surface coating.

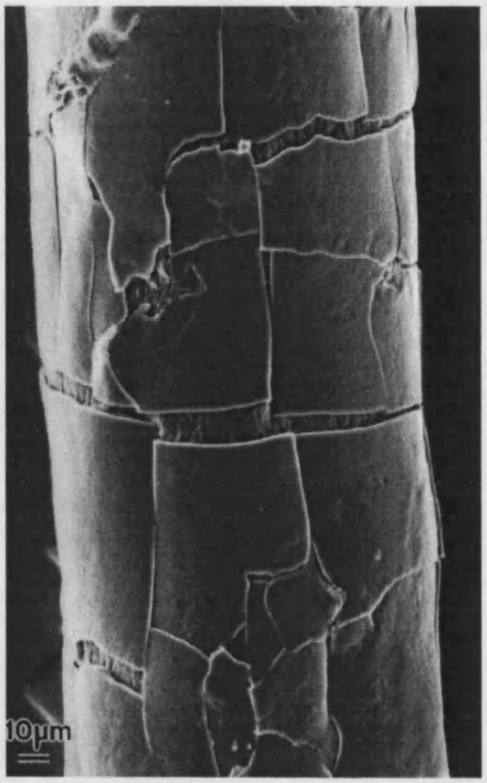

Figure 12
SEM image of the surface of a bacterial-titania composite fibre.

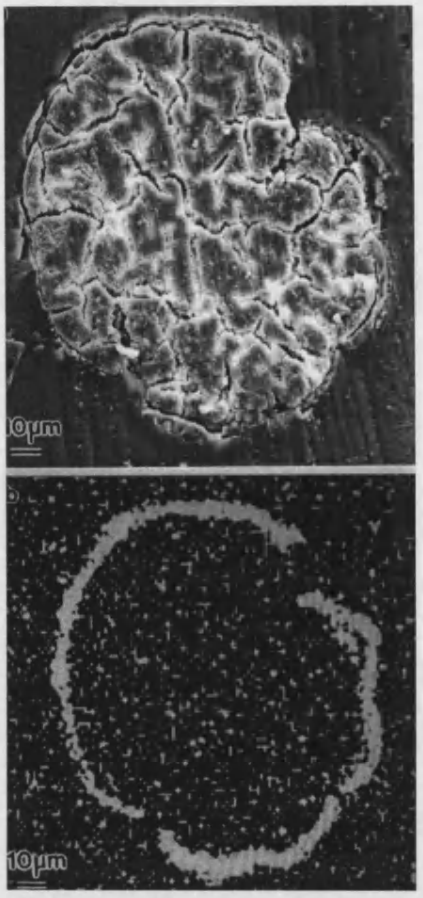

Figure 13
(a) SEM of a bacterial-titania composite embedded in resin and cut perpendicular to the fibre axis. (b) Corresponding Ti distribution map.

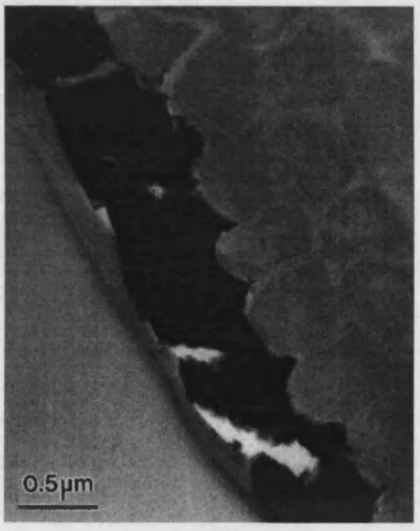

Figure 14
TEM image of a transverse thin section of a bacterial-titania composite fibre showing a uniform consolidated mineral coating at the fibre surface.